UNIVERSITI TEKNOLOGI MARA

XEROGEL IMMOBILIZED N/S/O-DOPED CARBON QUANTUM DOTS FROM SHRIMP SHELLS BASED CHITOSAN FOR CO_2 ADSORPTION

NUR AINAA BINTI MOHD HASYIM CHAN

MSc

June 2026

UNIVERSITI TEKNOLOGI MARA

XEROGEL IMMOBILIZED N/S/O-DOPED CARBON QUANTUM DOTS FROM SHRIMP SHELLS BASED CHITOSAN FOR CO_2 ADSORPTION

NUR AINAA BINTI MOHD HASYIM CHAN

Thesis submitted in fulfilment
of the requirements for the degree of
Master of Science
(Chemical Engineering)

Faculty of Chemical Engineering

June 2026

CONFIRMATION BY PANEL OF EXAMINERS

I certify that a Panel of Examiners has met on 3 December 2025 to conduct the final examination of Nur Ainaa Binti Mohd Hasyim Chan on her Master of Science thesis entitled "Xerogel Immobilized N/S/O-Doped Carbon Quantum Dots from Shrimp Shells Based Chitosan for CO_2 Adsorption" in accordance with Universiti Teknologi MARA Act 1976 (Akta 173). The Panel of Examiners recommends that the student be awarded the relevant degree. The Panel of Examiners was as follows:

Nornizar Anuar, PhD
Associate Professor
Faculty of Chemical Engineering
Universiti Teknologi MARA
(Chairman)

Azil Bahari Alias, PhD
Associate Professor
Faculty of Chemical Engineering
Universiti Teknologi MARA
(Internal Examiner)

Sumathi Sethupathi, PhD
Professor
Faculty of Engineering and Green Technology
Universiti Tunku Abdul Rahman
(External Examiner)

PROFESSOR DR HJH ZURAEDA IBRAHIM
Dean
Institute of Postgraduates Studies
Universiti Teknologi MARA

Date: 9 June 2026

AUTHOR'S DECLARATION

I declare that the work in this thesis was carried out in accordance with the regulations of Universiti Teknologi MARA. It is original and is the results of my own work, unless otherwise indicated or acknowledged as referenced work. This thesis has not been submitted to any other academic institution or non-academic institution for any degree or qualification.

I, hereby, acknowledge that I have been supplied with the Academic Rules and Regulations for Postgraduate, Universiti Teknologi MARA, regulating the conduct of my study and research.

Name of Student	:	Nur Ainaa Binti Mohd Hasyim Chan
Student ID. No.	:	2023672804
Programme	:	Master of Science (Chemical Engineering) – CEEH750
Faculty	:	Chemical Engineering
Thesis Title	:	Xerogel Immobilized N/S/O-Doped Carbon Quantum Dots from Shrimp Shells Based Chitosan for CO_2 Adsorption
Signature of Student	:	
Date	:	June 2026

ABSTRACT

Rising CO_2 emissions underscore the need for sustainable and efficient capture materials. This study develops N/S/O-doped carbon quantum dots (CQDs) derived from shrimp-shell chitosan and stabilized within xerogel matrices (N/S/O-CCQD-X) to overcome the common limitations of CQDs such as aggregation, instability, and moisture sensitivity. The aims of the work were to (i) evaluate the role of xerogel immobilization in improving CQD stability, (ii) synthesize N/S/O-doped CQDs using varying chitosan:thiourea:KOH ratios, (iii) assess CO_2 adsorption performance under different process conditions, and (iv) analyse adsorption behaviour through isotherm, kinetic, and thermodynamic models. CQDs were synthesised by hydrothermal treatment with varying chitosan:thiourea:KOH ratios and immobilised in xerogels at different CQD-to-solution ratios. Characterisation included FTIR, XPS, CHNS, HRTEM, BET, FESEM and fluorescence spectroscopy to confirm functionalisation, particle morphology and pore structure. CO_2 adsorption performance was measured in a continuous fixed-bed breakthrough rig. Initial screening used 30 °C, 5 vol% CO_2 and 100 mL·min^{-1}, additional tests varied temperature (30–110 °C), CO_2 concentration (2–10 vol%) and flow rate (60–140 mL·min^{-1}). Adsorption data were analysed by isotherm, kinetic and thermodynamic modelling. Xerogel-immobilised CQDs maintained dispersion and active sites, the 1:50 xerogel formulation was selected after initial screening for detailed doping ratio studies. BET and FESEM indicated a microporous xerogel network supporting gas diffusion and preserving N/S/O functionalities confirmed by FTIR, XPS and CHNS. Synthesis and screening of doping ratios identified CQD-X 133 as the best performing doped sample (breakthrough capacity 234.93 mg·g^{-1} under initial screening). HRTEM showed well-dispersed CQDs with an average diameter of 4.27 ± 1.06 nm. Under optimised conditions the material reached 358.80 mg·g^{-1} at 30 °C, 100 mL·min^{-1}, 5 vol% CO_2, and the highest measured uptake was 402.12 mg·g^{-1} at 30 °C, 100 mL·min^{-1}, 2 vol% CO_2. Temperature, flow rate and CO_2 concentration influenced breakthrough and capacity, with optimal adsorption conditions identified in the parameter study. Equilibrium data fit best to the Redlich–Peterson model (mixed monolayer–multilayer on a heterogeneous surface), kinetics followed a pseudo-second-order model, and thermodynamics gave $\Delta G < 0$, $\Delta S < 0$ and $\Delta H = -9.49$ kJ·mol^{-1} indicating spontaneous, exothermic adsorption dominated by physisorption with complementary localized chemisorptive sites. Xerogel immobilisation stabilises biomass-derived, heteroatom-doped CQDs and preserves active N/S/O sites that enhance CO_2 affinity. CQD-X 133's superior performance demonstrates that precursor ratio design can tune both adsorption capacity and thermal resilience. Overall, this study demonstrates the novelty and practical potential of combining waste-derived CQDs with a xerogel matrix to create a stable, functionalised, and scalable adsorbent for low-energy CO_2 capture applications.

ACKNOWLEDGEMENT

First and foremost, all praise is to Allah SWT for His countless blessings, granting me the strength, patience, and opportunity to complete this challenging yet rewarding journey of my master's degree. Without His guidance, none of this would have been possible.

To my dearest family, my loving mother, and my father, Mohd Hasyim Chan Abdullah, this achievement is dedicated to you. Your sacrifices, prayers, and belief in education have shaped who I am today. Your vision and determination continue to inspire me every day. To my supportive sister, Siti Aishah Mohd Hasyim Chan, and brother, Muhammad Amin Mohd Hasyim Chan, thank you for always cheering me on and reminding me of my purpose.

I extend my deepest gratitude to my dedicated supervisors, whose wisdom and encouragement shaped this research. To my main supervisor, Dr. Norhusna Mohamad Nor, thank you for your unwavering guidance, insightful critiques, and constant motivation throughout this journey. My sincere appreciation also goes to my co-supervisors, Dr. Muhammad Zahiruddin Ramli and Professor Dato' Seri Ir. Abdul Rahman Mohamed, for their invaluable expertise, constructive feedback, and support in refining this work.

To my incredible research partner and lab mate, Aimi Solihah Zaul Kapri, words cannot express how grateful I am for your companionship. Our countless discussions, shared lab sessions, and collaborative problem-solving made this journey not only productive but also enjoyable. Many of the breakthroughs in this research were achieved because of your support and teamwork, thank you for being an irreplaceable part of this experience.

My heartfelt appreciation goes to my beloved housemates, Riza Lydia Liyana Rizalmen, Siti Hawa Mat Yaman, and Ellisa Natasya Rosli for being my pillars of strength. Your companionship during late-night lab work, words of encouragement during stressful times, and endless laughter kept me grounded. This thesis is a testament to your unwavering friendship and moral support.

A special note of thanks to the faculty staff and lab assistants for their technical assistance, facility access, and patience in guiding me through experiments. Their contributions were instrumental in the success of this project.

Finally, to all my friends, colleagues, and mentors who contributed directly or indirectly to this journey, thank you. This milestone is not mine alone, but a collective achievement made possible by the kindness and support of so many. Alhamdulillah, for everything.

TABLE OF CONTENTS

LIST OF TABLES

LIST OF FIGURES

LIST OF PLATES

LIST OF SYMBOLS

Symbols

Φx	Fluorescence Quantum Yield
η	Refractive Index

LIST OF ABBREVIATIONS

Abbreviations

CCQDs	Chitosan Derived Carbon Quantum Dots
CQDs	Carbon Quantum Dots
CQD-X	Xerogel Immobilized Carbon Quantum Dots
CSS	Chitosan-Based Shrimp Shells
DA	Degree Of Acetylation
FTIR	Fourier-Transform Infrared Spectroscopy
HT	Hydrothermal Treatment
N/S/O	Nitrogen/Sulfur/Oxygen
N/S/O-CCQD-X	N/S/O-Heteroatoms Hybridized Carbon Quantum Dots Derived From Chitosan-Based Shrimp Shells Immobilized In Xerogel
PL	Photoluminescence
QY	Quantum Yield

LIST OF NOMENCLATURE

Nomenclatures

A	Absorbance
I	Integrated Fluorescence Intensity

CHAPTER 1
INTRODUCTION

1.1 Research Background

In recent years, rising CO_2 emissions from industries like power generation, transportation, and petrochemicals have sparked global concern. Fossil fuel-based power plants and transportation are major contributors, while refining and flaring in oil and gas sectors further exacerbate the issue (Tuo et al., 2022). Between 1990 and 2023, global GHG emissions surged, with fossil CO_2 up 72.1%, methane 28.2%, and nitrous oxide 32.4%, driven by high consumer demand and slow adoption of low-carbon alternatives (Martin, n.d.; Minx et al., 2021). In 2024, global CO_2 emissions are projected to hit 41.6 billion tonnes, up from 40.6 billion in 2023, with fossil fuels accounting for 37.4 billion tonnes. Land-use changes, like deforestation, contribute the rest (*Global Carbon Budget | Fossil Fuel CO_2 Emissions Increase Again in 2024*, n.d.). China, the U.S., India, the EU, Russia, and Brazil are the top emitters, responsible for 62.7% of global GHG emissions (Martin, n.d.; Minx et al., 2021; *(Open Access) Long-Term Trend in Global CO2 Emissions (2011) | J G.J. Olivier | 40 Citations*, n.d.).

Despite some decarbonization in Europe and North America, global emissions continue to rise, highlighting the need for stronger policies and faster transitions to sustainable practices (Bahman et al., 2023; Friedlingstein et al., 2010; Lamb et al., 2021; Minx et al., 2021). These emissions intensify the greenhouse effect, trapping heat and driving climate change, which leads to higher global temperatures, extreme weather, and environmental disruptions. To address this, global regulations are being implemented to reduce CO_2 emissions. Malaysia, committed to the Paris Climate Accord, aims to cut carbon emission intensity by 45% by 2030 relative to GDP, targeting a 1.5°C temperature limit. The plan focuses on innovation, industry restructuring, and reducing household emissions. As a developing nation, Malaysia is committed to climate action under the Paris Agreement, prioritizing transparency, financial support, and technology transfer despite not having binding emission reduction targets under the Kyoto Protocol. It updates its National Determined Contribution (NDC) every five years to track progress and refine strategies (Syahindah et al., 2023).

Various CO_2 removal technologies, including post-combustion capture (chemical absorption, adsorption, membrane separation, cryogenic distillation), pre-combustion capture, and oxyfuel combustion, are widely used. Chemical absorption, the most established, captures around 50 million tons of CO_2 annually (Astuti et al., 2024). AI and machine learning are optimizing CO_2 reduction strategies (Sahane et al., 2024) while CO_2 conversion into fuels is gaining traction for emission reductions and resource recycling (Z. Feng, 2024). Among these technologies, adsorption stands out for its efficiency, scalability, and sustainability, avoiding the energy-intensive and corrosive nature of chemical absorption. Adsorption methods include physical, chemical, and hybrid processes, with physical adsorption relying on surface forces and chemical adsorption involving reactions (J. Cui, 2022). In the realm of adsorbents for CO_2 removal, various adsorbents have been extensively studied for their effectiveness in removing CO_2 from gas streams. Adsorbents like activated carbon, zeolites (e.g., NaY, NaX), and MOFs are studied for CO_2 capture. Zeolites excel at low pressures, while MOFs, like amine-MIL, show promise but need cost optimization. While activated carbon is a cost-effective option, zeolites and MOFs demonstrate significantly higher adsorption capacities for CO_2 (Rashid & Rafey, 2023; J. Shen et al., 2023; K. Zhang & Wang, 2024). Advanced materials, such as CQDs, are crucial for improving efficiency and reducing costs (Shamiri & Shafeeyan, 2022).

1.1.1 Carbon Quantum Dots (CQDs)

Carbon Quantum Dots (CQDs) are a class of zero-dimensional carbon nanomaterials (<10 nm) with exceptional properties, including high photoluminescence, tunable surface chemistry, biocompatibility, and strong chemical stability. Their unique structure, composed of sp^2/sp^3 hybridized carbon cores and oxygen/nitrogen-rich functional groups, enables diverse applications in bioimaging, sensing, catalysis, and environmental remediation (Khan et al., 2024; Patekar et al., 2024). In CO_2 capture, CQDs offer advantages such as high surface area, abundant active sites, and the ability to be functionalized with heteroatoms (i.e., N, S, O, etc.), enhancing adsorption capacity and selectivity. CQDs can be synthesized via top-down (e.g., laser ablation, electrochemical oxidation) or bottom-up (e.g., hydrothermal, microwave-assisted) methods. The hydrothermal method is widely preferred due to its

simplicity, cost-effectiveness, and ability to control doping and surface functionalization.

CQDs can be derived from a variety of carbon-rich precursors, ranging from synthetic chemicals to sustainable biomass. Conventional sources include citric acid, urea, and graphene oxide, which yield highly luminescent CQDs with controlled properties. However, recent research has shifted toward eco-friendly alternatives, particularly biomass waste such as fruit peels, agricultural residues, and chitosan—a natural biopolymer obtained from shrimp and crab shells. Chitosan stands out as an excellent precursor due to its inherent nitrogen content, biodegradability, and abundant hydroxyl/amine groups that facilitate heteroatom doping and surface functionalization (Chakravarty & Edwards, 2022; Sarbon et al., 2015). Other biomass-derived sources, such as plant leaves, grass, and food waste, have also gained attention for their low-cost, renewable nature and ability to produce CQDs with competitive optical and adsorption properties. This sustainable approach not only reduces reliance on petroleum-based precursors but also aligns with circular economy principles by valorizing waste materials into high-value nanomaterials for CO_2 capture and other applications.

1.1.2 Modification of CQDs for CO_2 Removal

CQDs derived from chitosan-based shrimp shells (CSS) are a potential solution for CO_2 removal but face challenges in adsorption efficiency and sustainability. The native structure of CSS contains functional groups such as hydroxyl (-OH), amine ($-NH_2$), and acetyl ($-COCH_3$) groups, which provide some interaction sites for CO_2 but are often insufficient in number or activity to achieve high adsorption performance (Ali Said Al Hoqani et al., 2021). To overcome these limitations, chemical modification through N/S/O heteroatom doping is essential, as it introduces additional active sites such as pyridinic-N, sulfonic, and carboxyl groups which enhance CO_2 binding affinity and improve overall adsorption efficiency and material stability (Kyzas & Bikiaris, 2015; Lu et al., 2022). For instance, κ-carrageenan, a sulfur-rich polysaccharide, was used as a precursor in the hydrothermal synthesis of chitosan-derived CQDs, resulting in N, S co-doping and achieving a high quantum yield of 59.31% (J. Xu et al., 2021). Similarly, lysine and glutamic acid have been employed as N and O sources under microwave radiation, introducing functional

groups that could potentially improve CO_2 adsorption via enhanced surface polarity and interaction with gas molecules (Janus et al., 2019a).

Despite their potential in gas adsorption, the practical application of CQDs is often limited by inherent stability issues. CQDs tend to agglomerate due to their high surface energy, causing loss of accessible active sites and reduced adsorption performance. In addition, many CQDs are highly hygroscopic meaning they readily absorb moisture from the environment (Dua et al., 2023; R. Miao et al., 2017). This moisture uptake can disrupt surface functional groups, weaken pore structure, and negatively alter surface chemistry. In severe cases, CQDs have been reported to absorb enough water to transition into a sticky or viscous liquid-like state, leading to structural collapse and complete loss of their functional properties (R. Miao et al., 2017). These instability issues significantly restrict their handling, storage, and long-term usability in adsorption applications.

Several approaches have been explored to address these limitations, such as embedding CQDs in polymer matrices, supporting them on porous carbon-based materials, or integrating them into inorganic frameworks (Teymoorian et al., 2021; H. Yu et al., 2019). Among these, xerogels have emerged as a promising option due to their highly porous structure, thermal stability, and large surface area, which facilitate gas diffusion and maximize contact with adsorbents Prepared through sol-gel processes followed by ambient drying, xerogels have been successfully employed in various adsorption applications, including pollutant and dye removal, with reported capacities of up to 325 mg/g (Aguilar-Maruri et al., 2024). Incorporating CQDs into xerogels frameworks is therefore expected to enhance their stability and porosity, improving CO_2 adsorption by enhancing CQDs-CO_2 interactions.

1.2 Problem Statement

As of 2024, global CO_2 emissions are projected to reach 41.6 billion tonnes, an increase from 40.6 billion tonnes in 2023 (Z. Liu et al., 2022). The escalating CO_2 emissions pose a pressing global challenge, worsen climate change and necessitating sustainable CO_2 removal methods. Among these, CO_2 adsorption technology has emerged as a promising approach due to its energy efficiency and potential for selective capture. However, many existing adsorbents still face practical limitations, including high energy requirement, low selectivity, and poor moisture tolerance, as

water vapour present in real-world CO_2 streams can compete for active sites and reduce adsorption efficiency (K. H. Kim & Kim, 2023; Rashid & Rafey, 2023; Shamiri & Shafeeyan, 2022). In this context, CQDs derived from shrimp shells and modified with nitrogen (N), sulfur (S), and oxygen (O) heteroatoms offer a promising solution. Despite their potential, the synthesis process, the impact of heteroatom doping, and the efficiency of these modified CQDs for CO_2 capture remain poorly understood.

Chitosan, a derivative of chitin, can be extracted from shrimp shells and serves as a renewable precursor for CQD synthesis. These shells, which are a major component of food waste in the food processing industry, can thus be repurposed to reduce environmental impact (M. Feng et al., 2022). Shrimp-shell-derived chitosan offers a renewable carbon (~44%), oxygen (~40%), and nitrogen (~6.5–8.3%) rich precursor for CQD synthesis, but standalone CQDs suffer from limited functional groups, agglomeration, and instability, which restrict their CO_2 adsorption performance. Although N/S/O heteroatom doping can enhance surface polarity (G. Lim et al., 2016) and introduce active sites that strengthen CO_2 interactions (*(Open Access) Relationship between Surface Hydrophobicity and Composition of Coal (2004) | Zhu Shu-Quan | 1 Citations*, n.d.), most existing studies have not explored the integration of doped CQDs into xerogel matrices, an approach that could overcome these stability issues through structural support and improved porosity (O. Lv et al., 2016; SINGH et al., 2018). As a result, the adsorption behavior of N/S/O-doped CQD-based xerogels (N/S/O-CCQD-X) remains poorly understood, particularly regarding the influence of key operational parameters such as temperature, CO_2 concentration, and flow rate, as well as their equilibrium, kinetic, and thermodynamic characteristics. These knowledge gaps hinder the optimization and practical deployment of biomass-derived adsorbents. Therefore, a systematic investigation is needed to develop a stable, functionalized N/S/O-CCQD-X adsorbent and to elucidate its CO_2 adsorption mechanisms under various conditions for scalable carbon-capture applications.

In this work, chitosan-derived CQDs were synthesized hydrothermally, with N/S/O-heteroatom modification to enhance CO_2 adsorption performance. This study introduces a novel strategy for CO_2 removal by developing N/S/O-doped CQDs derived from chitosan-based shrimp shells (CSS) adsorbent and immobilized within a xerogel matrix (N/S/O-CCQD-X). Through a tailored hydrothermal synthesis method, heteroatom doping using chitosan, thiourea, and KOH was achieved, significantly

enhancing the CO_2 adsorption capacity. This combined approach not only improves adsorption performance but also contributes to waste valorization and supports climate change mitigation efforts.

1.3 Objectives

The main aim of this research is to develop and synthesis N/S/O-doped carbon quantum dots derived from chitosan-based shrimp shells immobilized in xerogel (N/S/O-CCQD-X) adsorbent for efficient CO_2 capture. The following are the measurable objectives:

a) To investigate the effect of xerogel immobilization in stabilizing and enhancing N/S/O-CCQD-X adsorbent for CO_2 removal.
b) To synthesize and characterize physicochemical properties of the N/S/O-CCQD-X adsorbent via a modified hydrothermal method with varying weight ratios of chitosan: thiourea: KOH for high CO_2 removal.
c) To evaluate the effect of adsorption process parameters (adsorption temperature, CO_2 feed concentration, and flow rate) on the CO_2 removal performance using N/S/O-CCQD-X adsorbent.
d) To evaluate the CO_2 adsorption behavior of the N/S/O-CCQD-X adsorbent through isotherms, thermodynamics, and kinetics studies.

1.4 Scope of Study

The first objective focuses on investigating the role of xerogel in enhancing the structural stability and performance of the CQDs adsorbent. The chitosan was extracted from shrimp shells a chemical extraction method involving demineralization, deproteinization, and deacetylation processes. The extracted chitosan was then used to synthesize N/S/O-doped CCQD via hydrothermal treatment at 180°C for 24 hours. Four (4) different CQD-to-solution ratios: CQD-X 1:1, CQD-X 1:10, CQD-X 1:50, and FD CQD-X 1:50 were prepared to understand the stability property of the synthesized adsorbent. The N/S/O-CCQD was incorporated into a xerogel matrix using a sol-gel process, where the gels were aged, molded, and oven-dried at 80°C for 24 hours.

The second objective is the synthesis and characterization of the N/S/O-CCQD-X, using six (6) different doping ratios of chitosan: thiourea: KOH (1:1:3, 1:2:3, 1:3:3, 1:1:2, 1:2:2, and 1:3:2). In this step, the CQDs samples synthesized via hydrothermal method with varying chitosan:thiourea:KOH doping ratios were immobilized into xerogels to improve their structural stability and adsorption performance. The resulting xerogel-based adsorbents were designated as CQD-X 112, CQD-X 122, CQD-X 132, CQD-X 113, CQD-X 123, and CQD-X 133, corresponding to their respective precursor weight ratios. Here, CQD-X refers to the coded sample name, while N/S/O-CCQD-X refers to the final xerogel-based adsorbent developed in this research.

In the next phase, the physicochemical properties of the resulting N/S/O-CCQD-X adsorbent were analyzed using fluorescence spectrophotometer, Fourier Transform Infrared Spectroscopy (FTIR), N_2 sorption-desorption analysis, CHNS/O elemental analysis, Field Emission Scanning Electron Microscopy with Energy Dispersive X-Ray Spectroscopy (FESEM-EDX), Thermal Gravimetric Analysis (TGA), Transmission Electron Microscopy (TEM) and High-Resolution TEM (HRTEM), and X-ray Photoelectron Spectroscopy (XPS).

All samples from objective 1 (CQD-X 1:1, 1:10, 1:50, FD 1:50) and objective 2 (CQD-X 112, 122, 132, 113, 123, 133) were evaluated for CO_2 capture performance using a custom-designed adsorption rig. A 0.5 g of adsorbent was packed into a stainless-steel column with glass wool support and a simulated gas stream (5 wt% CO_2 balanced with N_2) was passed through at a flow rate of 100 mL/min under ambient temperature (30°C). Real-time CO_2 concentrations at the inlet and outlet were monitored using a portable gas analyzer with an electrochemical sensor, calibrated for CO_2 gas. Continuous recording of CO_2 concentration was conducted, and the adsorption test was halted upon reaching a saturated concentration $\frac{C_i}{C_o} = 1.0$.

For the third objective, the study systematically evaluates the effects of temperature, CO_2 concentration, and gas flow rate on CO_2 adsorption performance using the best synthesized ratio of N/S/O-CCQD-X adsorbent. The column temperature was adjusted across five levels: 30, 50, 70, 90, and 110°C. The CO_2 concentration was varied between 2, 4, 6, 8, and 10 wt %, while the gas flow rate at 60, 80,100, 120, and 140 mL/min, following the one-factor-at-a-time (OFAT) approach.

The final objective evaluated the CO_2 adsorption behavior of N/S/O-CCQD-X adsorbent using isotherms, kinetics, and thermodynamic studies. Adsorption isotherms (Langmuir, Freundlich, Temkin, and Redlich-Peterson) were used to determine the equilibrium relationship and maximum adsorption capacity. Kinetic studies, using pseudo-first and pseudo-second-order models, examined the adsorption mechanisms, while thermodynamic analysis investigated the temperature influences. Experimental data were captured across a range of 30 to 110°C to understand the energy dynamics of the adsorption process.

1.5 Significance of Study

This study addresses the urgent global challenge of reducing CO_2 emissions and mitigating climate change by developing N/S/O-doped carbon quantum dots immobilized in xerogels (N/S/O-CQD-X) derived from chitosan-based shrimp shells, a renewable biomass material. This innovative and eco-friendly approach leverages chitosan, an abundant and sustainable resource, to create advanced adsorbents for CO_2 capture. Unlike conventional carbon capture technologies, which often face environmental and cost limitations, this research focuses on enhancing the surface functionalities of CQDs through heteroatom doping (N, S, O) to improve their CO_2 adsorption capacity and selectivity, offering a more sustainable and efficient solution.

The significance of this study lies in bridging a critical research gap in CO_2 capture materials by exploring the synthesis, characterization, and adsorption behavior of N/S/O-CCQD-X. By combining the renewability of biomass-derived CQDs with the stability and high surface area of xerogels, this work addresses key limitations in adsorption performance and durability. Furthermore, the insights gained from isotherm, kinetic, and thermodynamic analyses will advance the understanding of adsorption mechanisms and contribute to the development of cost-effective, high-performance carbon capture technologies.

Looking ahead, the developed N/S/O-CCQD-X material holds immense potential for practical applications in combating greenhouse gas emissions and global warming. Its renewable nature, coupled with enhanced adsorption efficiency and stability, positions it as a promising candidate for large-scale deployment in industries seeking sustainable carbon capture solutions. By paving the way for innovative, biomass-based adsorbents, this research not only addresses current environmental

challenges but also anticipates future needs in the global effort to achieve climate stability and reduce the impacts of climate change.

CHAPTER 2
LITERATURE REVIEW

2.1 Chitosan

Chitin, a naturally abundant polysaccharide with the molecular formula $(C_8H_{13}O_5N)n$, is a key structural component found in the exoskeletons of arthropods and the cell walls of fungi. Structurally similar to cellulose, it is composed of 2-acetamido-2-deoxy-D-glucose (NAG) monomer units linked by β-(1,4) bonds. Chitin often appears as rigid, whitish, nitrogenous microfibrils, contributing to the reinforcement and protection of various organisms, including shrimp, crabs, and cockroaches.

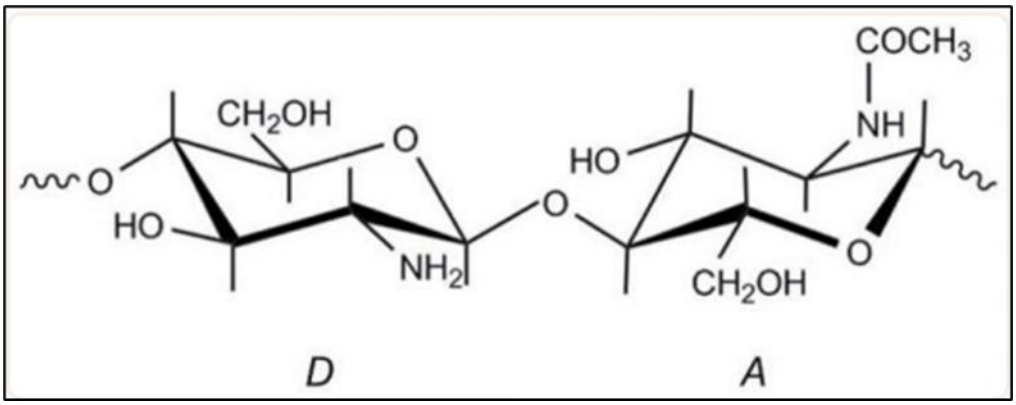

Figure 2.1 Structural Unit of Chitin and Chitosan (Jagtap et al., 2021)

Through deacetylation, chitin is converted into chitosan, an amino polysaccharide with varying degrees of deacetylation. Chitosan is characterized by its solubility in acidic solutions and its higher glucosamine (D) content compared to N-acetylglucosamine (A). Conversely, chitin contains a greater proportion of N-acetylglucosamine (A) (HEMMAMI et al., 2023) . Figure 2.1 illustrates these two structural units: (A) represents N-acetylglucosamine, and (D) represents glucosamine. This distinction between the molecular composition of chitin and chitosan underscores their unique chemical and functional properties.

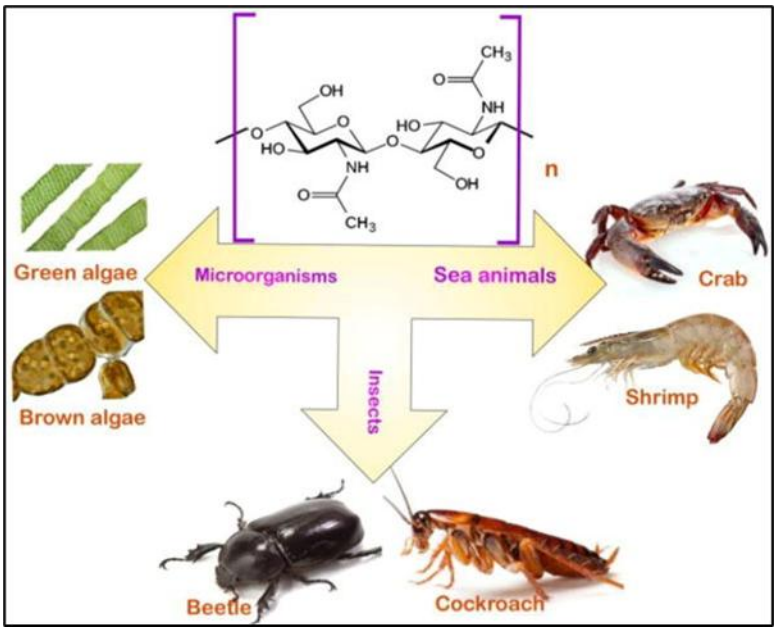

Figure 2.2 Main Natural Sources of Chitin (Chakravarty & Edwards, 2022)

Chitin and chitosan are polysaccharides that share chemical similarities with cellulose, differing only in the absence or presence of nitrogen (N); unlike cellulose, chitin and chitosan contain N (Chakravarty & Edwards, 2022; Sarbon et al., 2015). Chitosan serves as an exemplary basic polysaccharide, a departure from the prevailing nature of neutral or acidic polysaccharides such as cellulose, alginic acid, dextran, agarose, pectin, carrageenan, and agar. Unique properties, including the ability to form films, biocompatibility, biodegradability, non-toxicity, molecular adsorption capabilities, and the generation of polyoxysalts, distinguish chitin and chitosan from other substances. Noteworthy benefits encompass mucoadhesive qualities, wound healing support, antioxidant properties, antifungal and antimicrobial activities, antihyperglycemic effects, anti-inflammatory responses, and potential antitumoral attributes. The elemental composition of the chitosan polymer is carbon (C) (44%), hydrogen (H) (5.92%), nitrogen (N) (7.48%), sulfur (S) (1.92%), oxygen (O) (40.4%), and ash (0.28%) (de Freitas et al., 2021).

2.1.1 Physicohemical Properties of Chitosan from Shrimp Shells

Shrimp shells, an abundant byproduct of the seafood industry, serve as an excellent source of chitin for chitosan production. Comprising 20-30% chitin by dry weight, shrimp shells also contain proteins (30-40%), calcium carbonate (20-50%),

and pigments. The hierarchical structure of shrimp shells consisting of protein-rich outer layers, a mineralized middle layer, and an inner chitinous matrix requires sequential processing (demineralization, deproteinization, and deacetylation) to extract high-purity chitosan. Compared to other crustacean sources, shrimp shell-derived chitosan exhibits superior properties, including higher DDA (typically 70-95%), better solubility in dilute acids, and enhanced biocompatibility. These attributes, coupled with the shells' renewability and low cost, make them an ideal raw material for synthesizing functional materials like carbon quantum dots (CQDs) for CO_2 capture. The use of shrimp shells also aligns with circular economy principles by valorizing marine waste into high-value nanomaterials.

Chitosan, characterized by its unique physical and chemical properties that make it highly versatile for various applications. These properties are influenced by factors such as its molecular structure, degree of deacetylation, and molecular weight. Understanding the physical and chemical attributes of chitosan is essential for optimizing its functionality in fields like biomedicine, agriculture, water treatment, and CO_2 capture. Table 2.1 outlines the key properties of chitosan, which contribute to its widespread use and adaptability.

Table 2.1
Physical and Chemical Properties of Chitosan

Properties	Details	References
Structure	β-(1,4)-linked glucosamine units with amino (-NH_2) groups.	(Abd Rahman & Othman, 2024; HEMMAMI et al., 2023; Lingait et al., 2023)
Solubility	Soluble in dilute acids; depends on deacetylation degree and molecular weight.	(Abd Rahman & Othman, 2024; HEMMAMI et al., 2023)
Charge	Positively charged in acidic solutions.	(Alemu et al., 2023; HEMMAMI et al., 2023; K. Wu et al., 2024)
Biocompatibility	Non-toxic, biodegradable; suitable for medical/environmental uses.	(HEMMAMI et al., 2023; Lingait et al., 2023; Osak et al., 2024; K. Wu et al., 2024)
Film-Forming Ability	Forms flexible, transparent films.	(Khubiev et al., 2023; Yadav et al., 2023)
Molecular Weight	10 kDa - 1,000 kDa; affects viscosity and solubility.	(HEMMAMI et al., 2023; Román-Doval et al., 2023)

Hydrophilicity	Water-absorbing due to -OH/-NH_2 groups.	(Lingait et al., 2023)
Physical Form	Off-white to pale-yellow powder.	(Q. Luo et al., 2019; Ruslan et al., 2020)
Particle size	Nanoscale (10–500 nm) Microscale (1–100 μm)	(*Chitosan Particle and Process Therefor*, 2006; Q. Luo et al., 2019; Ruslan et al., 2020; Wijayadi & Rusli, 2019)
Moisture content	<10%; hygroscopic.	(Liyanage et al., 2022; Q. Luo et al., 2019; Rosa et al., 2010)
Ash content	<1% in high-purity forms.	(Arasukumar et al., 2019; L. Huang et al., 2020; Liyanage et al., 2022; *Preparation Method of Ultralow Ash Content Activated Carbon*, 2019; Ssekatawa et al., 2021)

Chitosan is a natural polysaccharide obtained from chitin, featuring a linear chain of β-(1,4)-linked glucosamine units with free amino functional groups. It exhibits unique solubility in acidic solutions and cationic behavior in low pH environments. The material demonstrates excellent biocompatibility and biodegradability, making it valuable for medical and environmental applications. With molecular weights ranging from 10-1000 kDa, chitosan can form flexible films and shows pronounced hydrophilicity due to its hydroxyl and amine functional groups. Typically appearing as an off-white powder, its particle size (10nm-100μm) and low moisture/ash contents (<10% and <1% respectively) influence its performance in applications requiring purity and controlled reactivity. These properties collectively enable diverse uses from drug delivery to wastewater treatment.

2.1.2 Chitosan Extraction Methods

The extraction of chitosan, a versatile biopolymer, involves both chemical and biological methods, each with unique principles and advantages. Chemical methods, such as the acid-alkali process and ionic liquid extraction, are widely used for their efficiency and scalability (Hosney et al., 2022) . Alternatively, biological methods, including enzymatic extraction and fermentation, offer eco-friendly approaches while preserving chitosan's natural properties. These diverse methods are applied across a

variety of sources, including crustaceans, insects, and fungi, each yielding chitosan with distinct characteristics.

The acid-alkali method is a widely used approach for extracting chitosan from chitin due to its efficiency and simplicity. This process involves three key steps: demineralization, deproteinization, and deacetylation. In demineralization, minerals like calcium carbonate are removed using an acidic solution, such as hydrochloric acid (HCl), under controlled conditions. Deproteinization follows, where proteins are eliminated using alkaline solutions like sodium hydroxide (NaOH). Finally, the deacetylation step converts chitin to chitosan by hydrolyzing acetamide groups through treatment with concentrated NaOH at high temperatures. Factors such as reagent concentration, reaction time, and temperature play a critical role in determining the efficiency and quality of the resulting chitosan (Miron et al., 2022). This method offers several advantages, including cost-effectiveness, scalability, and relatively straightforward implementation, making it suitable for industrial applications. However, it also has notable disadvantages, such as its reliance on harsh chemicals, which can generate wastewater and lead to environmental concerns. Additionally, the use of strong acids and bases may result in partial deacetylation or degradation, which can lower the molecular weight and affect the quality of the final product. To provide a comprehensive overview, Table 2.2 summarizes the acid-alkali extraction methods involved in obtaining chitosan from various natural sources.

Table 2.2
Extraction of Chitosan from Various Sources

Type of precursor	**Method**	**Chitosan extracted (%)**	**References**
Shrimp shells (Litopenaeus vannamei Boone)	Demineralisation, deproteinization, and deacetylation	20.59 – 25.23	(Hosney et al., 2022)
Barnacles (Chelonibia patula)	Demineralisation, deproteinization, and deacetylation	3.11	(Kaya et al., 2014)
Fish scales (catla catla)	Demineralisation, deproteinization, and deacetylation	6	(Durairaj et al., 2018)
Button mushroom, (Agaricus bisporus)	Deproteinization, demineralisation, neutralization, and decolourization	10.5	(Shahadha et al., 2023)

Oyster mushroom (Pleurotus ostreatus)	Deproteinization, demineralisation, neutralization, and decolourization	1.22	(Kalutharage & Rathnasinghe, 2020)
Mud crab shells (Scylla olivicea)	Deproteinization, demineralisation, decolouration, dewatering, and deacetylation	44.57	(Sarbon et al., 2015)

An alternative approach to chitin extraction is the use of ionic liquids (ILs), salts with melting points below 100 °C that contain large organic cations and smaller organic or inorganic anions. Valued for their green solvent properties such as low vapor pressure, thermal stability, low flammability, and recyclability, ILs dissolve crustacean shells by disrupting the hydrogen bond network in chitin, followed by precipitation with an antisolvent like methanol, ethanol, or aqueous solutions. Factors such as crystallinity, molecular weight, and deacetylation degree influence dissolution efficiency, with some ILs capable of dissolving chitin at room temperature, although concerns remain over toxicity and biodegradability (Feroz et al., 2020) . Biological extraction methods, including enzymatic and fermentation approaches, offer milder conditions and can produce high–molecular weight chitin with low deacetylation degrees. Enzymatic methods use proteinases to remove proteins with minimal damage to the chitin chain but often face incomplete deproteination and higher costs (H. Kim et al., 2023), while fermentation methods employ acid- or protease-producing bacteria, sometimes in sequence, to achieve demineralization and deproteination, though they require longer reaction times and complex media preparation. Both biological methods generate supernatants rich in amino acids, adding value despite their respective limitations (Abedin et al., 2023).

In general, the acid/alkali extraction method stands out as one of the most cost-effective approaches for chitin extraction, owing to the relatively low costs of acids and bases involved. This method offers short reaction times, simplicity in reactor requirements, and efficient removal of proteins and minerals, resulting in high-purity chitin, with yields reported as high as 44.57% from mud crab shells (Scylla olivicea) (Sarbon et al., 2015) . However, concerns arise from the environmental toxicity of alkaline residues and the potential for accidental deacetylation and chain degradation under intense reaction conditions (Kozma et al., 2022).

2.1.3 Applications in Industries

Chitosan is widely used in biomedical, pharmaceutical, food, textile, agricultural, and environmental applications due to its biocompatibility, biodegradability, and versatile functional properties. In medicine, it enhances drug delivery systems, supports tissue engineering, and improves mucosal adhesion for targeted therapies. In the food industry, it acts as a natural preservative and antimicrobial agent, extending shelf life. Textile applications include eco-friendly functional finishes, while in agriculture, it promotes plant growth, disease resistance, and sustainable farming. Additionally, chitosan plays a key role in wastewater treatment by adsorbing pollutants and serves as a precursor for CQDs, enabling advanced applications in sensing and CO_2 capture.

Beyond industrial uses, chitosan contributes to environmental sustainability through wastewater remediation and carbon emission mitigation. Its modified forms, such as hydrogels and nanoparticles, enhance pollutant removal efficiency, while chitosan-derived CQDs offer innovative solutions in biomedicine and climate change mitigation . Overall, chitosan's multifunctionality and eco-friendly nature make it a valuable material across diverse fields. A variety of reported applications of chitosan are outlined in Table 2.3.

Table 2.3
Applications of Chitosan in Several Industries

Industry	Applications	References
Pharmaceutical	Drug delivery systems for controlled release and targeted delivery. Vaccine, peptide and protein, and nasal drug delivery.	(Aranaz et al., 2021; Janus et al., 2019a; Kandra & Bajpai, 2020; *(Open Access) Chitosan as Multi Performance Bio Material: Properties and Applications. (2014) | Reyhaneh Azarmi | 1 Citations*, n.d.)
Biomedical	Tissue engineering and regeneration in bone implants and artificial organs. Spinal disc replacement. Wound healing to promote faster recovery and reduce infections. Biodegradable implants for tissue regeneration.	(*(Open Access) Chitosan as Multi Performance Bio Material: Properties and Applications. (2014) | Reyhaneh Azarmi | 1 Citations*, n.d.)

Food	Acts as a natural food preservative. Serves as a coating material by forming films. Inhibits growth of foodborne fungi, yeast, and bacteria. Extends the shelf life of bread. Improves food preservation.	(Barik et al., 2024; Bertrand et al., 2024; Prihanto et al., 2024; Woźniak et al., 2024)
Textiles	Acts as an eco-friendly finishing agent. Enhances textile fibers with antibacterial properties. Improves fabric coloration and dyeing capabilities. Adds anti-wrinkle effects. Provides antistatic functionality to fabrics.	(Elamri et al., 2022; Ghazal et al., 2024; X. Wang et al., 2024)
Agriculture	Enhances plant growth, seed germination, and root development. Boosts crops' immunity against diseases and pests. Improves soil quality, water retention, and nutrient availability. Protects seeds from pathogens and enhances germination rates. Acts as a natural fungicide in crops. Extends the shelf life of fruits and vegetables. Increases crop yields.	(Arshad et al., 2024; Bertrand et al., 2024; *(Open Access) Chitosan as Multi Performance Bio Material: Properties and Applications. (2014) | Reyhaneh Azarmi | 1 Citations*, n.d.; Padamini et al., 2024; Qavami et al., 2017)
Wastewater treatment	Removes heavy metals and organic dyes. Aggregates suspended particles through flocculation. Enhances filtration efficiency in membrane separation processes. Improves pollutant removal. Increases adsorption capacity and surface area. Serves as a sustainable alternative to synthetic chemicals.	(Cuong et al., 2024; Kaur Bhullar et al., 2024; Saiyad et al., 2023a, 2023b; Y. Zhu, 2023)

2.2 Carbon Dioxide (CO_2)

The physical and chemical characteristics of CO_2 play a significant role in its behavior and impact on both the environment and various industrial processes. CO_2 is a colorless, odorless gas at room temperature, heavier than air, and exists as a solid

(dry ice) at temperatures below -78.5°C. It is soluble in water and can form carbonic acid, which dissociates into bicarbonate and carbonate ions. As a greenhouse gas, CO_2 contributes to global warming by trapping heat in the Earth's atmosphere. Additionally, CO_2 is non-flammable, produced during combustion, and reacts with bases to form carbonates. These characteristics are essential for understanding the behavior of CO_2, especially in the context of its role in climate change and its capture in various industrial applications. Table 2.4 summarizes the key physical and chemical characteristics of CO_2, including its molecular properties, phase behavior, and reactivity, which are fundamental to understanding its environmental impact and industrial applications (Aresta & Dibenedetto, 2021; North, 2015; Y. Shen & Lee, 1997).

Table 2.4
Physical and Chemical Characteristics of CO_2

Properties	**Details**
State	Colorless, odorless, and tasteless gas at room temperature.
	Can exist as a solid (dry ice) at low temperatures (below -78.5°C).
Molecular Formula	CO_2
Molecular Weight	44.01 g/mol
Density	Approximately 1.977 g/L at 0°C and 1 atm pressure.
	Heavier than air, which is why CO_2 can accumulate in low-lying areas.
Boiling Point	-78.5°C at 1 atm (sublimation point for solid CO_2).
Freezing Point	-56.6°C at 1 atm (solidification point).
Solubility	Soluble in water, forming carbonic acid (H_2CO_3), though the solubility decreases with increasing temperature.
Compressibility	CO_2 has a higher compressibility compared to lighter gases like He and nitrogen (N_2).
Phase Change	Sublimes directly from solid to gas at -78.5°C (dry ice).
Viscosity and Surface Tension	CO_2 has relatively low viscosity and surface tension.
Reactivity	Non-reactive under standard conditions but can react with water to form carbonic acid (H_2CO_3) and with basic substances to form carbonates.
Acidic Nature	CO_2 is an acidic gas, and when dissolved in water, it forms carbonic acid (H_2CO_3).
Reaction with Bases	Reacts with bases to form carbonates.
Chemical Bonds	CO_2 has a linear molecular structure (C=O), making it stable and non-polar.

2.2.1 Global Greenhouse Gas (GHG) and CO_2 Emissions in Industries

In recent years, the rise in CO_2 emissions from various industries has become a major global concern. Power plants that burn coal and natural gas are some of the biggest sources of CO_2 emissions. The cement industry also contributes significantly during the processing of raw materials. Additionally, the transportation sector, which depends heavily on fossil fuels, adds to the problem (Tuo et al., 2022). Global trends in CO_2 emissions highlight the severity of the issue. Between 1990 and 2023, global greenhouse gas (GHG) emissions increased significantly, with fossil CO_2 emissions rising by 72.1%, methane (CH_4) by 28.2%, and nitrous oxide (N_2O) by 32.4% (Martin, n.d.; Minx et al., 2021). This surge is primarily due to high consumer demand and a slow transition to low-carbon alternatives across key sectors such as energy, industry, buildings, transport, and agriculture. Malaysia's CO_2 emissions reflect this upward trend, with the latest recorded value reaching 283 Mt CO_2 eq in 2023, up from 274 Mt CO_2 eq in 2022—exceeding the global average of 198 Mt CO_2 eq (based on data from 189 countries). This increase underscores Malaysia's growing industrial and energy demands, aligning with broader global emission patterns. Table 2.5 presents global CO_2 emissions from 1990 to 2024, highlighting the steady increase in greenhouse gas output over three decades.

Table 2.5
Global CO_2 Total Emission (Martin, n.d.)

Year	1990	2000	2005	2015	2020	2022	2023
Total Emission (Mton CO_2)	22680.40	25725.44	30044.54	36300.47	36209.86	38548.12	39112.69

Global CO_2 emissions in 2024 are projected to rise to 41.6 billion tonnes, compared to 40.6 billion tonnes in 2023. This includes fossil CO_2 emissions of 37.4 billion tonnes, up 0.8% from 2023, with the remainder attributed to land-use changes like deforestation (*Global Carbon Budget | Fossil Fuel CO_2 Emissions Increase Again in 2024*, n.d.). The largest contributors to these emissions are China, the United States, India, the European Union, Russia, and Brazil, collectively accounting for 62.7% of global GHG emissions (Martin, n.d.; Minx et al., 2021; *(Open Access) Long-Term*

Trend in Global CO2 Emissions (2011) | J G.J. Olivier | 40 Citations, n.d.). Although Europe and North America have achieved moderate decarbonization, the overall global trend reflects persistent growth in emissions, driven by high consumer demand and slow transitions to low-carbon alternatives, underlining the urgent need for robust policies and accelerated transitions toward sustainable, low-carbon practices (Bahman et al., 2023; Friedlingstein et al., 2010; Lamb et al., 2021; Minx et al., 2021).

CO_2, along with other greenhouse gases, traps heat in the atmosphere, causing the Earth's surface to warm. These emissions contribute to the greenhouse gas effect, a process that is a key driver of climate change. As a results, the planet experience rising global temperatures, more frequent extreme weather events, and widespread environmental disruptions. In response to this environmental challenge, various regulations have been implemented globally to curb CO_2 emissions. As part of its commitment to the Paris Climate Accord, Malaysia has pledged to reduce carbon emissions and limit global temperature increases to 1.5°C. The country aims to lower carbon emission intensity by 45% relative to Gross Domestic Product (GDP) by 2030, emphasizing innovation, industrial restructuring, and reduced household emissions. Although Malaysia, as a developing nation, has no binding quantitative targets under the Kyoto Protocol, it actively works to address carbon emissions. The government highlights the need for transparency in global mitigation efforts, financial support, technology transfer, and adherence to the Paris Agreement. To track progress, Malaysia updates its National Determined Contribution (NDC) every five years, showcasing its evolving strategies and commitment to reducing greenhouse gas emissions (Syahindah et al., 2023).

The increasing trend of CO_2 emissions worldwide is a significant environmental concern that has garnered widespread attention in recent decades. Figure 2.3 presents the global greenhouse gas (GHG) emissions by sector from 1990 to 2023, based on data from EDGAR (Martin, n.d.). The chart highlights a consistent upward trend in total GHG emissions over the years, reaching approximately 52,963 Mt CO_2 equivalent in 2023. The power industry remains the dominant contributor, followed by industrial combustion, transport, buildings, and agriculture. The pie chart inset further emphasizes that CO_2 alone accounts for 73.7% of global GHG emissions, underscoring its critical role in climate change.

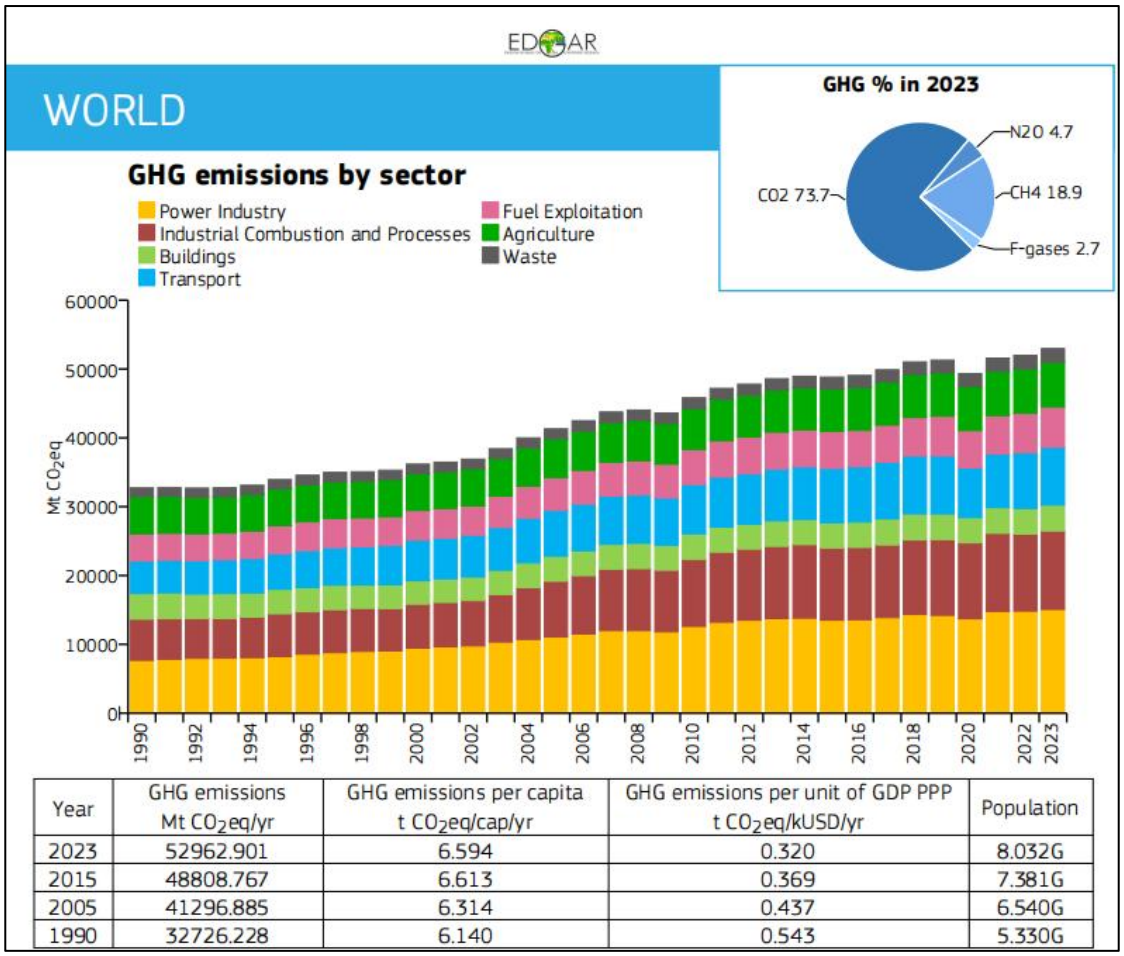

Year	GHG emissions Mt CO_2eq/yr	GHG emissions per capita t CO_2eq/cap/yr	GHG emissions per unit of GDP PPP t CO_2eq/kUSD/yr	Population
2023	52962.901	6.594	0.320	8.032G
2015	48808.767	6.613	0.369	7.381G
2005	41296.885	6.314	0.437	6.540G
1990	32726.228	6.140	0.543	5.330G

Figure 2.3 World GHG Total Emission (Martin, n.d.)

Despite slight improvements in GHG emissions per capita and per unit of GDP since 2005, the overall emissions continue to rise due to global population growth and increasing industrial activities. This trend indicates an urgent need for more aggressive decarbonization strategies across major sectors. Several factors contribute to this escalating trend, reflecting the challenges faced by the global community in addressing climate change as shown in Figure 2.4.

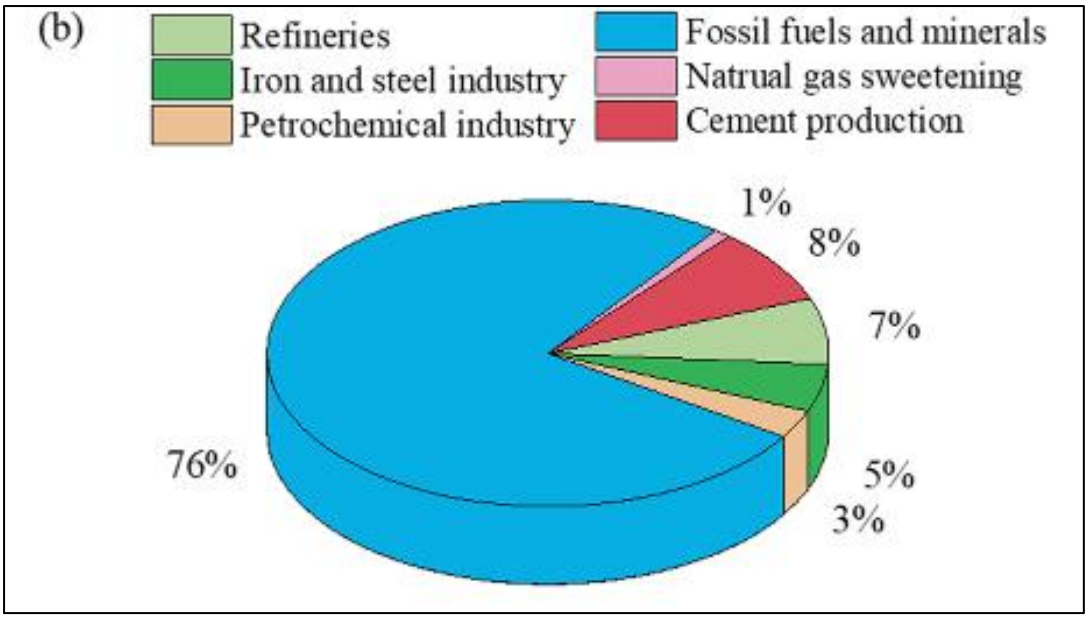

Figure 2.4 Industrial Contribution of each CO_2 Emission Source (Quan et al., 2023)

Figure 2.4 illustrates the industrial contribution of various industrial sectors to global CO_2 emissions. The dominant source is the fossil fuels and minerals sector, which accounts for a substantial 76% of total CO_2 emissions. This is primarily due to extensive combustion of coal, oil, and natural gas for energy generation and industrial processes. Cement production contributes 8%, reflecting the significant CO_2 released during the calcination of limestone. Refineries (7%) and the iron and steel industry (5%) are also notable contributors, given their energy-intensive operations and reliance on carbon-based fuels. The petrochemical industry (3%) and natural gas sweetening processes (1%) add smaller yet important shares. This breakdown highlights the urgent need to focus CO_2 mitigation efforts on fossil fuel combustion and industrial decarbonization to achieve meaningful reductions in greenhouse gas emissions.

Table 2.6
Global Contributions to the Global Trend of CO_2 Emissions

Factors	Details
Industrialization and Economic Growth	Rapid industrialization and economic development in various regions have led to an increased demand for energy, much of which is derived from fossil fuels. The combustion of coal, oil, and natural gas for energy production releases substantial amounts of CO_2 into the atmosphere
Transportation Sector	The growing reliance on automobiles, airplanes, and other modes of transportation contributes significantly to rising CO_2 emissions. The expansion of road networks, increased vehicle ownership, and the use of fossil fuel-

	powered engines contribute to the carbon footprint of the transportation sector
Deforestation	Large-scale deforestation for agriculture, logging, and urbanization reduces the number of trees available to absorb CO_2 through photosynthesis. This contributes to higher atmospheric CO_2 concentrations, as forests play a crucial role in sequestering carbon.
Energy Production	The global dependence on non-renewable energy sources, such as coal and natural gas, for electricity generation remains a primary source of CO_2 emissions. Transitioning to cleaner and renewable energy sources is essential to mitigate this impact.
Increased Industrial Activities	Various industrial processes, including manufacturing, chemical production, and cement manufacturing, release CO_2 as a byproduct. The expansion of industrial activities contributes to higher emissions unless sustainable practices are adopted.
Population Growth	The increasing global population leads to higher energy consumption, increased urbanization, and greater demand for resources. These factors collectively contribute to the rising trend of CO_2 emissions
Inadequate Policy Measures	In some regions, inadequate regulatory frameworks, and policy measures to curb emissions contribute to the persistent increase in CO_2 levels. The lack of stringent environmental policies allows industries to continue emitting significant amounts of greenhouse gases

Table 2.6 presents the trend of CO_2 emissions worldwide, focusing on various contributing factors. It highlights how rapid industrialization and economic growth, particularly in sectors reliant on fossil fuels, have led to an increase in CO_2 emissions (EI Kenawy et al., 2023) . The transportation sector, with its growing reliance on automobiles and airplanes, also plays a significant role, further increasing emissions. Deforestation is another contributing factor, as large-scale agricultural and industrial activities reduce the number of trees capable of absorbing CO_2. Additionally, increased industrial activities, along with the rising global population, have led to higher energy consumption and, consequently, more CO_2 emissions (S. Yang et al., 2023) . Lastly, inadequate policy measures in some regions are hindering efforts to curb emissions, allowing industries to continue emitting significant amounts of greenhouse gases (Bahman et al., 2022).

Addressing the increasing trend of CO_2 emissions requires a comprehensive and coordinated global effort. This includes adopting cleaner technologies, transitioning to renewable energy sources, implementing sustainable land-use practices, and fostering international cooperation to tackle climate change on a

systemic level. The urgency of mitigating CO_2 emissions underscores the importance of prioritizing sustainable development practices and embracing a low-carbon future.

2.2.2 Carbon Capture Technologies

The increasing concentration of atmospheric CO_2 has driven the development of various carbon capture technologies aimed at mitigating emissions from industrial and energy sectors. These technologies differ in their working principles, efficiency, and applicability, offering solutions for diverse emission sources and operational requirements. The selection of an appropriate carbon capture method depends on factors such as cost, energy demand, scalability, and integration feasibility with existing infrastructure.

Table 2.7 compares the major carbon capture technologies, including their CO_2 capture efficiency, advantages, limitations, and key references. The table provides a comprehensive overview of post-combustion capture, pre-combustion capture, oxy-fuel combustion, membrane separation, cryogenic separation, chemical looping combustion (CLC), direct air capture (DAC), carbon capture and storage (CCS), and carbon capture and utilization (CCU). This comparison highlights the trade-offs between technological maturity, energy requirements, and economic viability, offering insights into their potential for large-scale deployment in emission reduction strategies.

Table 2.7
Comparative Analysis of Carbon Capture Technologies: Efficiency, Advantages, and Limitations

Technology	CO_2 Capture Efficiency	Advantages	Limitations	References
Post-Combustion Capture	Up to 90%	Mature technology; suitable for retrofitting existing power plants	High energy consumption for solvent regeneration; solvent degradation	(S. F. Chang et al., 2025; Darabkhani et al., 2023; Meylani et al., 2025)
Pre-Combustion Capture	Up to 90%	Produces hydrogen as a clean fuel; high CO_2 concentration simplifies capture	Requires significant infrastructure changes; complex process integration, high capital costs for gasification infrastructure	(Darabkhani et al., 2023; Law et al., 2024; Meylani et al., 2025)
Oxy-Fuel Combustion	Up to 95%	Produces a CO_2-rich flue gas; reduces	High costs associated with oxygen	(Darabkhani et al., 2023; Meylani et al.,

		nitrogen oxide emissions	production; requires new boiler designs	2025)
Membrane Separation	50–90%	Compact design; lower energy requirements; modular scalability	Lower selectivity and permeability; membrane fouling and degradation	(S. F. Chang et al., 2025; Meylani et al., 2025)
Cryogenic Separation	Up to 95%	High purity CO_2 output; suitable for high CO_2 concentration streams	High energy demand for refrigeration; less effective for low CO_2 concentrations	(Meylani et al., 2025)
Chemical Looping Combustion (CLC)	Up to 100%	Inherent CO_2 separation; high efficiency; reduced NO_x emissions	Technology still in development; complex reactor design	(Meylani et al., 2025)
Direct Air Capture (DAC)	Varies	Captures CO_2 directly from the atmosphere; location-independent	High operational costs; energy-intensive; currently low capture volumes, thermodynamic barriers for low-concentration CO_2.	(Meylani et al., 2025; Vitillo et al., 2022)
Carbon Capture and Storage (CCS)	Up to 90%	Long-term CO_2 storage; applicable to various emission sources	High capital and operational costs; requires suitable geological storage sites	(*5 Potential Benefits of Carbon Capture and Storage (CCS) Technology	Border States*, n.d.; Meylani et al., 2025)
Carbon Capture and Utilization (CCU)	Varies	Converts CO_2 into valuable products; promotes circular economy	Market dependency for CO_2-derived products; potential for CO_2 re-emission	(*5 Potential Benefits of Carbon Capture and Storage (CCS) Technology	Border States*, n.d.; Meylani et al., 2025; Ramirez-Corredores, 2024)

The three primary carbon capture approaches include post-combustion capture (90% efficiency), pre-combustion capture (90% efficiency), and oxy-fuel combustion (95% efficiency) (Darabkhani et al., 2023) . Post-combustion methods, particularly amine scrubbing, dominate existing power plant retrofits but face energy-intensive solvent regeneration challenges (Hamed et al., 2023) . Pre-combustion systems like IGCC plants produce clean hydrogen fuel while capturing CO_2, though requiring substantial infrastructure investment (Law et al., 2024; Teixeira et al., 2022). Oxy-fuel

combustion simplifies CO_2 separation by eliminating nitrogen but demands costly oxygen production (Shammi & Akter, 2024).

Emerging technologies offer complementary solutions: membrane separation (50-90% efficiency) provides modular, low-energy operation but struggles with selectivity (Torres et al., 2024), while cryogenic separation (95% efficiency) delivers high-purity CO_2 at significant energy cost (Torres et al., 2024). Chemical looping combustion achieves near-zero emissions through metal oxide carriers, though reactor complexity persists (Nwabueze & Leggett, 2024). Direct air capture addresses ambient CO_2 but remains energy-intensive (Karayil et al., 2024), with pioneers like Climeworks demonstrating its potential (Barahimi et al., 2023). Storage and utilization strategies complete the value chain. Carbon capture and storage (90% efficiency) securely sequesters CO_2 in geological formations like the Greensand Project's depleted oil fields (Szabados & Poulsen, 2023), while carbon utilization creates valuable products from captured CO_2, albeit with market dependencies (Z. Feng, 2024; Nwabueze & Leggett, 2024).

Among these options, adsorption processes present a versatile alternative, particularly for post-combustion applications. Utilizing porous solid adsorbents like activated carbon, zeolites, or functionalized materials, adsorption offers lower energy requirements compared to liquid absorption systems. The technology's adaptability - from large-scale flue gas treatment to direct air capture - combined with ongoing advances in sorbent materials (e.g., amine-grafted or metal-organic frameworks), positions adsorption as a promising pathway for efficient, scalable carbon capture solutions. Recent developments in pressure/temperature swing adsorption systems further enhance its commercial viability across industrial applications. Advanced adsorbents, such as MOFs and amine-functionalized materials, are designed to optimize these interactions, enabling efficient CO_2 capture under varying conditions.

2.3 Adsorption Principles and Mechanisms

Adsorption is a surface phenomenon where gas molecules (adsorbate, such as CO_2) adhere to a solid material (adsorbent) through physical or chemical interactions (J. Cui, 2022). The process is governed by adsorbate-adsorbent interactions, where molecules accumulate on the surface until reaching equilibrium, a state where the rate of adsorption equals the rate of desorption. The efficiency of adsorption depends on

factors such as surface area, pore structure, and surface chemistry, which influence gas uptake through mechanisms like pore filling and surface binding.

A high surface area provides more active sites for gas molecules to adhere, significantly enhancing adsorption capacity. Materials such as activated carbons and metal-organic frameworks (MOFs) are particularly effective due to their extensive surface areas. Pore structure, including pore size distribution and volume, dictates how gas molecules access and fill the adsorbent. Micropores (<2 nm) are crucial for strong gas trapping at low pressures due to enhanced van der Waals interactions, while mesopores (2–50 nm) facilitate faster diffusion, improving adsorption kinetics (H. Xu et al., 2025) . Surface chemistry determines the nature of adsorbate-adsorbent interactions. Hydrophilic surfaces, for instance, may preferentially adsorb polar gases like CO_2, whereas functional groups (e.g., amines) can enable chemisorption through chemical reactions. Together, these factors govern whether adsorption occurs primarily via pore filling (where gas condenses in pores) or surface binding (where molecules attach to specific active sites), ultimately influencing the overall performance of the adsorbent.

Adsorption occurs primarily via two mechanisms: physisorption (physical adsorption) and chemisorption (chemical adsorption). Physisorption involves weak van der Waals forces, making it reversible and suitable for low-temperature applications, where multilayer adsorption is possible. In contrast, chemisorption involves the formation of strong chemical bonds (covalent or ionic), typically occurring at higher temperatures and resulting in monolayer adsorption, often with irreversible characteristics (Krishnaiah et al., 2014) . Additionally, electrostatic interactions can enhance adsorption, particularly in materials with charged or polar surfaces that attract CO_2 molecules (F. Miao et al., 2026). The choice between these mechanisms depends on operational conditions, desired adsorption capacity, and the feasibility of adsorbent regeneration.

To date, a variety of sorbent materials are available for CO_2 capture, and choosing the most suitable sorbent depends on a detailed set of characteristics, including adsorption capacity, selectivity, rates of adsorption/desorption, temperatures of adsorption/desorption, thermal and mechanical stability, cycling stability, tolerance to moisture, and resistance to other impurities present in the flue gas, along with considerations of production cost.

2.3.1 Adsorption of CO_2

Adsorption is a surface phenomenon in which gas or liquid molecules adhere to the surface of a solid material, driven by physical or chemical interactions. It plays a crucial role in carbon capture technologies, offering a versatile and efficient method for separating CO_2 from gas mixtures. The process is influenced by factors such as adsorbent surface area, pore structure, and the nature of the interaction between the adsorbent and the adsorbate. This subsection explores the fundamental principles and mechanisms of adsorption, focusing on its application for CO_2 capture. Figure 2.5 illustrates the dual mechanisms of CO_2 adsorption on biochar materials, highlighting both physical and chemical adsorption pathways.

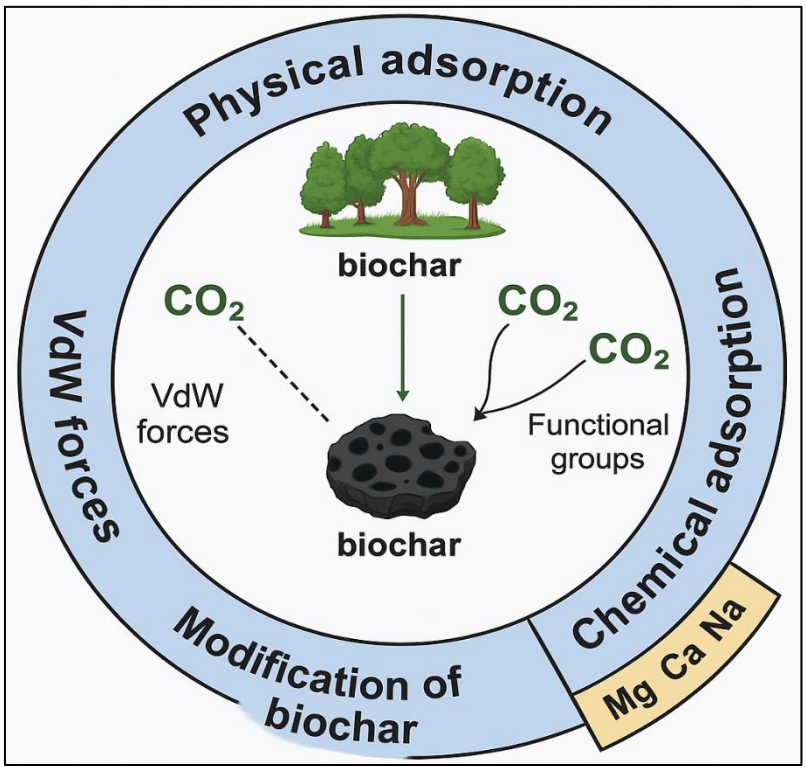

Figure 2.5 Mechanisms of CO_2 Adsorption on Modified Biochar: Physical and Chemical Pathways

CO_2 adsorption theory revolves around the interaction of CO_2 molecules with the surface of a solid adsorbent. The adsorption process can be classified into two types: physical adsorption (physisorption) and chemical adsorption (chemisorption). In physisorption, weak van der Waals forces facilitate the temporary binding of CO_2 to the adsorbent surface, making the process reversible and suitable for applications

requiring regeneration. Conversely, chemisorption involves the formation of stronger chemical bonds between CO_2 molecules and the adsorbent, resulting in higher selectivity but require more energy for regeneration. The process efficiency depends on the adsorbent's structural properties (surface area and pore size) and surface chemistry (functional groups like amines or carboxyl groups), which collectively determine CO_2 affinity and selectivity. Operational conditions such as pressure and temperature significantly influence performance, with higher pressures generally favoring physisorption while chemisorption requires specific temperature optimization. A critical performance metric is the adsorption capacity, reflecting the equilibrium between CO_2 uptake and release, where regenerability - particularly crucial for physisorption systems - ensures sustainable operation. These fundamental principles guide the design of adsorbents for diverse CO_2 capture applications, from industrial emissions to direct air capture, balancing capacity, selectivity and energy efficiency.

In physical adsorption (physisorption), CO_2 molecules interact with the adsorbent surface through weak van der Waals forces and electrostatic interactions, without forming chemical bonds. The process can be represented as: CO_2 (gas) + Adsorbent $\rightarrow$ $CO_2 \cdots$Adsorbent (physically adsorbed), where the dotted lines indicate the weak intermolecular forces (R. T. Yang, 2003). These interactions are typically reversible and depend on the adsorbent's surface properties, such as pore size and polarity. For example, in activated carbon, CO_2 molecules are attracted to the non-polar surface through London dispersion forces, while in polar zeolites, quadrupole-dipole interactions may dominate. The adsorption enthalpy for physisorption is relatively low (typically 20-40 kJ/mol), allowing for easy regeneration through pressure or temperature swings (Sumida et al., 2012). Key studies have characterized these interactions using techniques like volumetric adsorption measurements and infrared spectroscopy, confirming the absence of chemical bond formation during physisorption (D'Alessandro et al., 2010). This mechanism is particularly important in porous materials like metal-organic frameworks (MOFs) and activated carbons, where the large surface area and tunable pore structure enhance physical CO_2 capture capacity (Sumida et al., 2012).

Chemical adsorption (chemisorption) of CO_2 involves strong chemical bonding between CO_2 molecules and the adsorbent surface. A common example is the reaction with amine groups ($-NH_2$), where CO_2 forms either carbamates (in dry conditions) or bicarbonates (in humid conditions) (Sardo et al., 2021) . For metal

oxides like MgO, CO_2 interacts with oxygen vacancies on the surface (Etim et al., 2021a) . These chemical reactions provide high CO_2 selectivity but require more energy to reverse compared to physical adsorption. The type of chemical bond formed depends on the adsorbent material and operating conditions - amines work best at moderate temperatures (30-60°C), while metal oxides often need higher temperatures. Researchers study these reactions using techniques like infrared spectroscopy and computer simulations to design better CO_2 capture materials (Y. Li, Liu, et al., 2024; Sardo et al., 2021) . The main challenge is balancing strong CO_2 binding with the ability to easily regenerate the adsorbent for repeated use.

Understanding these principles allows researchers to design and optimize adsorbents for specific applications, tailoring their properties to achieve high CO_2 adsorption capacity, selectivity, and stability. Ongoing research in this field aims to develop cost-effective and scalable solutions for mitigating CO_2 emissions from various industrial processes.

2.3.2 Adsorbents used in CO_2 Removal

Adsorbents are fundamental to CO_2 capture technologies, as their properties directly impact the efficiency, selectivity, and cost-effectiveness of the adsorption process. A wide range of adsorbents has been explored, from traditional materials like activated carbon and zeolites to advanced options such as metal-organic frameworks (MOFs) and amine-functionalized materials. Each type of adsorbent offers distinct advantages and limitations, with the choice of material depending on the intended application and operating conditions.

In the realm of adsorbents for CO_2 removal, various adsorbents have been extensively studied for their effectiveness in removing CO_2 from gas streams. Activated carbon is a cost-effective and readily available option for CO_2 capture but generally has lower selectivity and capacity compared to zeolites and metal-organic frameworks (MOFs) (Rashid & Rafey, 2023). Zeolites, such as NaY and NaX, exhibit high CO_2 uptake due to their energetically heterogeneous surfaces, especially at low pressures (K. H. Kim & Kim, 2023). Metal-Organic Frameworks (MOFs) stand out for their tunable pore sizes and high CO_2 adsorption capacities, making them highly effective for carbon capture, though further optimization is needed for cost-efficient applications (K. Zhang & Wang, 2024) . Amine-functionalized materials, which

incorporate amine groups into solid adsorbents, allow for chemical interactions with CO_2, effectively combining the advantages of adsorption and absorption. For example, amine-modified MOFs like MIL groups have demonstrated superior performance in separating CO_2 from methane (CH_4) at low pressures (J. Shen et al., 2023).

Overall, selecting the right adsorbent is crucial for optimizing CO_2 capture efficiency, highlighting the importance of continued research to improve performance and reduce costs (Shamiri & Shafeeyan, 2022). As research advances, biomass-based carbon nanostructures are emerging as promising adsorbents due to their versatility and sustainability. Conventional adsorbents, including activated carbon, zeolites, MOFs, and carbon nanomaterials, have been widely studied for CO_2 adsorption, as summarized in Table 2.8.

Table 2.8
Different Types of Adsorbents Reported for CO_2 Capture (Raganati et al., 2021)

Adsorbent	**CO_2 Sorption Capacity**	**Cost/ Scalability**	**Strengths**	**Limitations**	**References**
Natural Zeolites (Zeolite 13X)	6.0–6.2 mmol/g	Low-to-moderate cost, commercially available	High selectivity & regeneration ease	Sensitive to moisture, performance drops with humidity	(Bahmanzadegan & Ghaemi, 2024; Drenchev et al., 2024; Jiang et al., 2024; M. Mambetova et al., 2024; M. M. Mambetova et al., 2023; Mancinelli & Martucci, 2025; Tao et al., 2024; A. G. Yu et al., 2024)
Synthetic Zeolites	4.3 mmol/g	Moderate cost, scalable	Uniform pore structure	Moisture sensitivity, complex synthesis	(Das et al., 2023; Hedayati et al., 2022; Tao et al., 2024)
Activated Carbons	3.3–5.0 mmol/g	Low cost (~$1–5/kg), high scalability	Moisture tolerant, robust	Lower selectivity vs zeolites/MOFs	(Das et al., 2023; Zentou et al., 2025)
Carbon Nanosheets	6.32 mmol/g	Moderate cost; scalable but requires controlled synthesis	High capacity, fast kinetics	Requires high-purity synthesis; structure control costly	(Shi et al., 2021)

MOFs	Up to 5.5–8.0 mmol/g	High cost ($100–500/kg), scaling challenge	Highest surface area & tunability	Moisture & stability issues, high cost	(Ayeleru et al., 2023; W. R. Lee et al., 2014; Zentou et al., 2025)
Amine-Functionalized	4–7 mmol/g	Moderate-high cost	Good selectivity	Amine degradation & regeneration energy	(Das et al., 2023; Yan et al., 2022; Zentou et al., 2025)
Silica Gel	2–3 mmol/g	Moderate cost	Good thermal/mechanical stability	Lower capacity, some high regeneration costs	(Das et al., 2023; You et al., 2022)
Layered Double Hydroxides (LDHs)	1.05 mmol/g	Moderate cost; scalable	Suitable at low CO_2 concentrations (ppm level)	Low capacity (~1 mmol/g); slow kinetics	(Das et al., 2023; X. Zhu et al., 2021)
Metal Oxides (e.g., MgO, CaO)	2.27 mmol/g	Low cost; scalable	Strong chemisorption; good high-temp performance	High regeneration temperature; sintering issues	(*Comparing the Lifespan of Different H_2S Adsorbents*, n.d.; Tao et al., 2024; X. Zhu et al., 2020)
Carbonaceous Xerogels	29.6 mmol/g	Moderate	High surface area potential	Complex synthesis	(*Carbon Capture Could Become Practical with Scalable, Affordable Materials | News | Northwestern Engineering*, n.d.; Carolina Hernández-Galeano et al., 2024; Zentou et al., 2025)
Ion-Exchange Resins	1.75–2.8 mmol/g	Moderate cost; industrially scalable	Fast kinetics; stable over cycles	Low capacity, sensitive to humidity	(*Carbon Capture Could Become Practical with Scalable, Affordable Materials | News | Northwestern Engineering*, n.d.; Shindel et al., 2025; Wei et al., 2018)

Zeolites, including natural types like clinoptilolite and synthetic versions such as zeolite 13X, are among the most widely used CO_2 adsorbents due to their affordability and structural stability. However, their performance is heavily affected by moisture, requiring flue gas to be dried before processing, and while natural zeolites work well in flue gas applications, they often need modifications for direct air capture (DAC). Carbon-based materials like activated carbons and emerging options such as carbon nanosheets offer advantages in terms of cost, scalability, and resistance to humidity, but they generally have lower CO_2 adsorption capacity compared to zeolites unless chemically modified. These adsorbents are less susceptible to moisture due to their typical hydrophobic nature.

On the other hand, metal-organic frameworks (MOFs) like UiO-66 and Mg-MOF-74 demonstrate record-breaking CO_2 uptake (>10 mmol/g) thanks to their ultra-high surface area and customizable pore chemistry. Unfortunately, similar to zeolites, MOFs are highly sensitive to moisture in the feed, where moisture adsorption competes with CO_2, and the presence of other impurities like NOx and SOx poses a poisoning issue. Therefore, a prior drying/purification step for flue gas is necessary before the adsorption process. Unlike zeolites and activated carbons, the majority of MOFs are still synthesized only at the laboratory scale, and the few produced on a larger scale are typically in the form of fine powders.

Amine-functionalized adsorbents, such as polyethyleneimine (PEI)-impregnated silica, combine the benefits of porous supports with strong CO_2 chemisorption, achieving high selectivity and capacity. While amine functionalization enhances CO_2 uptake, challenges persist in achieving a uniform distribution of liquid amines on the porous substrate without pore blockage and in improving thermal/oxidative stability. Among these, amine solutions are the most widely employed industrial chemical absorbents for CO_2 removal due to their high selectivity/affinity for CO_2/N_2. Nevertheless, this approach is associated with drawbacks such as equipment corrosion, high energy requirements for regeneration, and substantial solvent usage.

Currently, zeolites and activated carbons remain the most practical choices for large-scale applications, while MOFs and amine hybrids show great promise but require further development to improve durability and cost-effectiveness. Emerging materials like layered double hydroxides (LDHs) and advanced carbon composites are being explored as potential alternatives that balance performance, stability, and

affordability, though more industrial validation is needed. Ultimately, the best adsorbent depends on specific conditions such as gas composition, humidity, and temperature with hybrid solutions likely playing a key role in future carbon capture technologies.

In conclusion, a variety of adsorbents, including zeolites, carbon-based materials, metal-organic frameworks (MOFs), and amine-functionalized sorbents, have been explored for CO_2 capture applications. Zeolites, both natural and synthetic, offer diverse options, but their sensitivity to moisture requires a prior drying step. Carbon-based materials, aside from carbon nanomaterials, are cost-effective and less affected by moisture, but their unmodified state often results in lower CO_2 adsorption capacity compared to zeolites. MOFs demonstrate remarkable CO_2 adsorption capacity due to tunable pore size and chemistry, but large-scale production remains a challenge. Amines, when functionalized on sorbents, combine the benefits of porous solid adsorbents and solvents, providing high CO_2 adsorption capacity at relatively low costs, yet challenges persist in achieving uniform amine distribution and improving thermal stability. Overall, each adsorbent type presents unique advantages and challenges, highlighting the need for continued research to optimize and scale up these materials for practical CO_2 capture applications.

2.4 Role of Nitrogen, Sulfur, and Oxygen Heteroatom in Carbon-based Adsorbents for CO_2 Removal

The introduction of N/S/O-heteroatoms into carbon-based adsorbents plays a crucial role in enhancing CO_2 adsorption efficiency by modifying the physicochemical properties of the carbon surface. Adsorption site heterogeneity is a significant challenge in CO_2 removal, as it affects the uniformity and efficiency of adsorption (Petrovic et al., 2021). However, doping adsorbents with N, S, and O heteroatoms can address this issue by altering the charge distribution on the carbon surface, facilitating stronger interactions with CO_2 molecules (B. Liu et al., 2022). Table 2.9 summarizes examples of carbon-based adsorbents functionalized with N, S, or O heteroatoms, along with their CO_2 uptake capacities and key performance characteristics reported in previous studies.

Table 2.9
Carbon-based Adsorbents Modified with N, S, or O Heteroatoms for CO_2 Removal

Carbon Adsorbent (type/source)	Dopant (heteroatom)	CO_2 Uptake	Key Performance Highlights	Reference
Activated Carbon (bio-derived, KOH-activated) (from microalgae)	N	4.03 mmol/g (25 °C, 1 bar) 6.68 mmol/g (0 °C)	Very high surface area (~1745 m^2/g) and ultramicroporosity; pyridinic/pyrrolic N (~58%) creates basic sites for CO_2 binding; ultra-high CO_2/N_2 selectivity (~11) at 25 °C; stable uptake over multiple cycles	(H. Luo et al., 2016)
Reduced Graphene Oxide/N-doped Porous Carbon (rGO/NPC)	N	5.77 mmol/g (25 °C, 1 bar)	Composite of rGO and N-rich porous carbon (7.1 wt% N); moderate surface area (865 m^2/g) with abundant micropores; reversible CO_2 uptake; also, excellent electrical performance (for supercapacitors)	(Xiao et al., 2021)
Activated Carbon Fibers (PAN-based) + N-doped CNTs	N	~1.5–1.9 mmol/g (25 °C, 1 bar)	Grafting N-doped carbon nanotubes onto activated carbon fibers introduces additional Lewis-basic (N) sites; moderate CO_2 uptake (~1.5–1.9 mmol/g at 298 K). Faster adsorption kinetics and improved CO_2 affinity due to basic surface functionalities	(Chiang et al., 2017)
Porous Carbon (sulfur-rich coal, KOH-activated)	S	3.46 mmol/g (25 °C, 1 bar)	Very high surface area (2209 m^2/g for optimal sample); in situ sulfur from coal yields thiophenic/–SOx functionalities. Excellent CO_2/N_2 selectivity (~24) and strong cycling/thermal stability. Moderate activation preserves S sites, yielding abundant narrow micropores	(J. Guo et al., 2025)
Activated Carbon (glucose + K-citrate activation)	O	3.57 mmol/g (25 °C, 1 bar)	High oxygen content (enhanced –COOH, –OH groups) from non-corrosive K-citrate activation. Oxygen functional groups markedly strengthen CO_2 adsorption via polar interactions. The O-rich carbon showed higher CO_2/N_2 selectivity than KOH-activated carbon, evidencing the role of oxygen-containing surface sites.	(B. Liu et al., 2018)

N functionalities enhance the basicity of the carbon surface, by introducing basic N-containing functional groups which can improve the interaction with CO_2 molecules. These functional groups promote strong acid-base interactions between the adsorbent and CO_2, a weak acidic molecule, enabling selective and efficient binding of CO_2 (Saha & Kienbaum, 2019). The presence of N-doped functionalities increases the adsorption energy and surface affinity for CO_2 molecules, significantly improving the overall adsorption capacity. The presence of N can also create additional micropores, which can further enhance the surface area available for CO_2 adsorption (Shao et al., 2022a). This combination of enhanced surface activity, improved binding energies, and enhanced surface area makes N doping highly effective for CO_2 adsorption applications (J. X. Chen et al., 2024a).

The incorporation of S atoms promotes the formation of oxidized S-functionalities, which establish strong interactions with CO_2 molecules. These interactions are primarily facilitated by the lone pair of electrons present on sulfur atoms. S doping plays a significant role in enhancing the CO_2 adsorption performance of carbon-based materials by introducing effective active sites and increasing the defect density of the material (Shao et al., 2022a). Additionally, sulfur can contribute to the overall porosity of the material, which is crucial for maximizing the surface area available for gas adsorption (Saha & Kienbaum, 2019). Collectively, the presence of sulfur atoms enhances surface activity, increases surface area availability, and strengthens the CO_2 adsorption performance of the doped material.

O doping plays a complementary role by introducing polar oxygen-containing groups, such as hydroxyl, carbonyl, and carboxyl functionalities, which significantly alter the charge distribution on the carbon surface. These oxygen functionalities increase surface hydrophilicity, further enhancing the adsorbent's affinity toward polar molecules like CO_2 (Etim et al., 2021b) . The introduction of oxygen groups also provides additional active adsorption sites and enhances the surface energy, contributing to greater CO_2 capture performance (Jia et al., 2023).

In conclusion, the incorporation of N, S, and O heteroatoms into carbonaceous materials, such as CQDs derived from chitosan-based shrimp shells, plays a pivotal role in enhancing their CO_2 adsorption performance. These heteroatoms collectively improve the surface chemistry, structural properties, and porosity of the materials, resulting in the creation of active sites and increased adsorption site availability. N doping introduces basic functional groups that enable strong acid-base interactions

with CO_2, while S doping enhances surface polarity and interaction energies through its lone electron pairs and oxidized functionalities. Additionally, oxygen doping modifies the charge distribution and contributes to hydrophilicity, further improving CO_2 adsorption. The synergy between these heteroatoms enhances interaction energies, increases porosity, and enables selective CO_2 adsorption, making these materials highly effective for carbon capture (Gao et al., 2022) . A deeper mechanistic understanding of heteroatom-functionalized CQDs can drive the development of efficient, cost-effective, and sustainable adsorbents for large-scale CO_2 removal applications.

2.5 Carbon Quantum Dots (CQDs)

CQDs, an emerging member of the carbon family, have generated considerable interest owing to their favorable physicochemical properties, such as tunable photoluminescence (PL), high quantum yield (QY), low toxicity, compact size, notable biocompatibility, abundant surface functional groups (e.g., amino, hydroxyl, carboxyl), high stability, and cost-effective synthesis from diverse sources (Khan et al., 2024; Patekar et al., 2024) . These features make CQDs highly versatile for applications in sensing, bioimaging, and environmental remediation. Their performance is strongly influenced by factors such as particle size, surface chemistry, and heteroatom doping, which can enhance surface area, porosity, and functional group composition. Such characteristics are particularly important for CO_2 adsorption, where surface properties and pore structure play a critical role in adsorption capacity and selectivity. Table 2.10 summarizes the key physical and chemical properties of CQDs, providing an overview of their structure, functionality, and performance characteristics.

Table 2.10
Physical and Chemical Properties of CQDs

Properties	Details	References
Size and Structure	2-10 nm particles; amorphous/crystalline hybrid structures with sp^2/sp^3 carbon bonds	(Elugoke et al., 2024; Etefa et al., 2024; Sharma et al., 2024)
Surface Chemistry	Contains -OH, -COOH, $-NH_2$ groups for enhanced functionality	(Elugoke et al., 2024; S. Y. Lim et al., 2014; Yuan et al.,

		2023)
Optical Properties	Tunable photoluminescence; emits light when excited	(Deo et al., 2024; Sankar et al., 2024; Sharma et al., 2024)
Quantum Yield	< 10 % for unmodified/bare CQDs 50–60 % for well-passivated or doped CQDs >90 % in exceptional, highly optimized cases	(Deo et al., 2024)
Stability	Resists heat, light, and chemical degradation	(Sharma et al., 2024)
Biocompatibility	Non-toxic; safe for biological/environmental use	(Deo et al., 2024; Sankar et al., 2024; Sharma et al., 2024)
Modifiability	Can be doped/functionalized for specific applications	(Deo et al., 2024; Elugoke et al., 2024)
Thermal Stability	Can withstand high temperatures without degrading	(Gulati et al., 2023; Kande & Parmar, 2022)
Solubility	Dissolves well in water and organic solvents	(Elugoke et al., 2024; Sankar et al., 2024)
Quantum Confinement	Quantum confinement occurs when the size of the dots is reduced to the nanoscale. This leads to unique optical properties, such as size-tunable photoluminescence	(Gulati et al., 2023; Kande & Parmar, 2022)
Hydrophilicity	Hydrophilic nature due to abundant oxygen-containing groups, enhancing dispersibility in aqueous systems	(Gulati et al., 2023; Kande & Parmar, 2022)
Conductivity	Good electrical conductivity for sensor/energy applications	(Gulati et al., 2023)
Toxicity	Safer than metal-based quantum dots	(Gulati et al., 2023; Kande & Parmar, 2022)

CQDs represent a remarkable class of zero-dimensional nanomaterials with unique structural and functional characteristics. These ultra-small particles, typically ranging from 2-10 nm in size, exhibit a hybrid structure combining both amorphous and crystalline domains through sp^2/sp^3 hybridized carbon bonds, contributing to their exceptional stability and versatility (Xia et al., 2019a). The surface of CQDs is richly decorated with various functional groups including hydroxyl (-OH), carboxyl (-COOH), and amine ($-NH_2$) moieties, which not only enhance their solubility in both aqueous and organic media but also provide numerous sites for further chemical modification and functionalization (Pawar et al., 2019). The surface functionalization

of S-doped CQDs via hydrothermal reaction are illustrated in Figure 2.6, highlighting the presence of abundant hydroxyl, carboxyl, and amine groups on their surface.

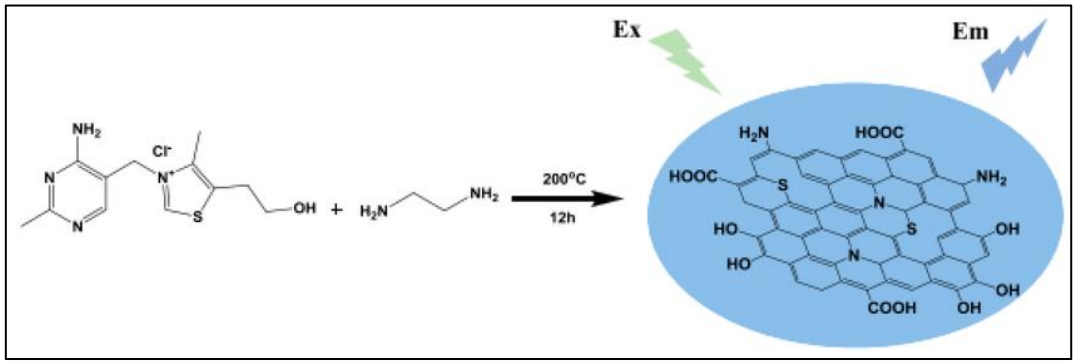

Figure 2.6 Schematic diagram of the synthesis of S-doped CQDs via hydrothermal reaction (Kandasamy, 2019)

One of the most distinctive features of CQDs is their outstanding optical properties. These nanomaterials demonstrate strong, tunable photoluminescence with high quantum yields, meaning they can efficiently absorb and convert light into bright emissions across a spectrum that can be precisely adjusted by controlling synthesis conditions and surface modifications. This property, combined with their excellent photostability and resistance to photobleaching, makes them particularly valuable for applications in bioimaging, optical sensing, and light-emitting devices. Plate 2.1 shows the illustration of chitosan- based CQDs under UV radiation.

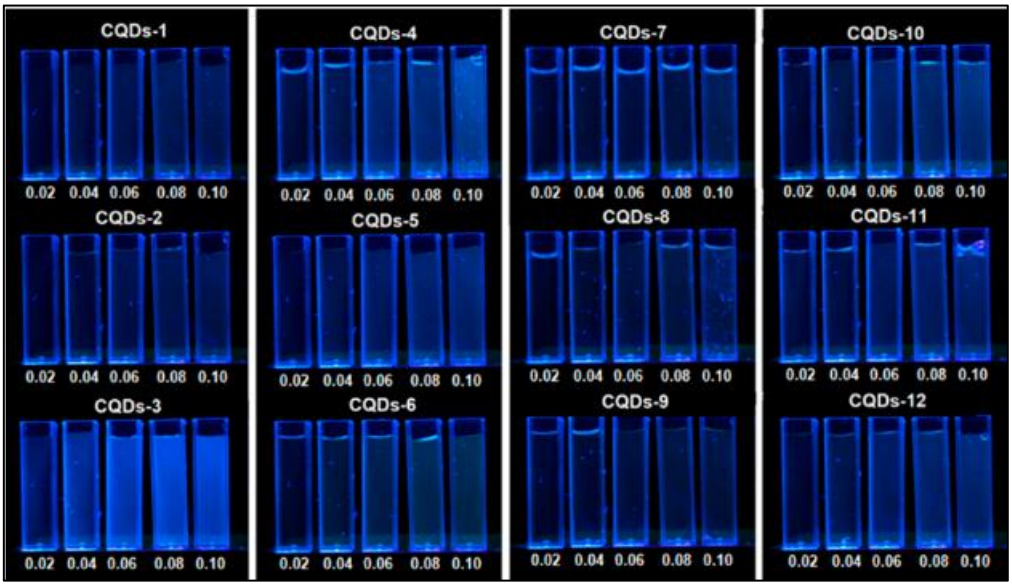

Plate 2.1 Chitosan-based CQDs under UV radiation (Janus et al., 2019b)

The robust nature of CQDs is evident in their impressive chemical and thermal stability. They maintain structural integrity and functionality even when exposed to harsh environmental conditions, elevated temperatures, or strong oxidizing agents. This durability ensures reliable performance in long-term applications ranging from environmental remediation to industrial catalysis. Furthermore, their biocompatibility and low cytotoxicity distinguish them from traditional quantum dots that often contain toxic heavy metals, making CQDs safer alternatives for biomedical applications such as drug delivery, theranostics, and in vivo imaging.

CQDs exhibit interesting electronic properties, including good electrical conductivity that can be fine-tuned through size control and surface functionalization. This characteristic, along with their stable zeta potential that prevents aggregation in colloidal systems, opens up possibilities for their use in energy storage devices, conductive coatings, and electronic sensors. The quantum confinement effect observed in these nanoscale materials gives rise to size-dependent electronic and optical behaviors that can be exploited in quantum computing and optoelectronic applications. The combination of their small size, tunable surface chemistry, exceptional optical characteristics, environmental stability, biocompatibility, and electrical conductivity makes CQDs highly versatile nanomaterials and with significant potential for diverse applications. Their ability to be easily modified through doping or functionalization further expands their potential applications, allowing researchers to tailor their properties for specific technological needs while maintaining the inherent advantages of carbon-based nanomaterials.

2.5.1 CQDs Applications

In recent years, CQDs have emerged as versatile nanomaterials with significant potential across a wide range of industries. Their unique properties, such as excellent photoluminescence, biocompatibility, tunable surface chemistry, and stability, have made CQDs highly suitable for applications in fields including biomedicine, energy, environmental remediation, and sensing technologies. Researchers have explored and documented numerous innovative uses for CQDs, highlighting their ability to address challenges in areas such as drug delivery, bioimaging, pollutant detection, and energy conversion. The diverse applications of

CQDs are summarized in Table 2.11, showcasing their growing impact on modern technology and industrial advancements.

Table 2.11
The Applications of CQDs

Industry	Applications	References
Biomedical	Drug/gene delivery, anticancer studies, tissue engineering, nanomedicine, targeted drug delivery, electrochemical sensing, bioimaging, biosnsing, photothermal and photodynamic therapy	(Ghosal & Ghosh, 2019; Mansuriya & Altintas, 2021; Sharath Shankar et al., 2020)
Sensing technology	Direct fluorescent sensors for metal ions, anions, and molecules	(*CQDs (Carbon Quantum Dots) with High Fluorescence Characteristic as Well as Preparation and Application of CQDs*, 2018a; Meng et al., 2019)
Environmental remediation	Detection of pollutants and contaminants in water and air, wastewater treatment, heavy metals adsorption, and CO_2 capturing	(Ababneh & Hameed, 2021; Emam, 2023)
Textile	Impart luminescent properties to fabrics, enhances the aesthetic appeal of textiles, and provides functionalities such as UV protection and antimicrobial properties	(Emam, 2023)
Food	Utilized in fluorescence sensors for food analysis, identification of food additives, pathogens, heavy metals, nutrients, antibiotics, and insecticide residues	(Sistani & Shekarchizadeh, 2023)
Energy	Supercapacitors, lithium-ion batteries, photovoltaics, hydrogen evolution reaction and oxygen evolution reaction	(Rasal et al., 2021)
Geology	Measurement of rock permeability and porosity	(*CQDs (Carbon Quantum Dots) with High Fluorescence Characteristic as Well as Preparation and Application of CQDs*, 2018a)
Optoelectronic devices	Development of optoelectronic devices, such as light-emitting diodes (LEDs) and solar cells	(*CQDs (Carbon Quantum Dots) with High Fluorescence Characteristic as Well as Preparation and Application of CQDs*, 2018a)

CQDs have found widespread applications across various industries due to their exceptional properties, including high photoluminescence, biocompatibility, and tunable surface functionalities. In the biomedical field, CQDs are extensively used for drug and gene delivery, anticancer therapies, tissue engineering, and nanomedicine. Their capabilities in targeted drug delivery, biosensing, bioimaging, and photodynamic or photothermal therapies make them essential tools for advanced medical diagnostics and treatments. In sensing technology, CQDs serve as fluorescent sensors for detecting metal ions, anions, and molecules with high sensitivity and selectivity, making them invaluable for environmental monitoring and industrial quality control.

In the energy sector, CQDs are employed in the development of supercapacitors, lithium-ion batteries, and photovoltaics. They are also used to facilitate hydrogen evolution and oxygen reduction reactions, contributing to sustainable energy solutions. In geology, CQDs are utilized for measuring rock permeability and porosity, which is critical for geological studies and oil exploration. Furthermore, in optoelectronic devices, CQDs are pivotal for the development of technologies such as light-emitting diodes (LEDs) and solar cells, where their superior luminescent properties enhance efficiency and performance.

CQDs also play a crucial role in environmental remediation, particularly in detecting pollutants, wastewater treatment, heavy metal adsorption, and CO_2 capture, addressing pressing global challenges related to air and water pollution. In the textile industry, CQDs are used to impart luminescent properties to fabrics, enhancing their aesthetic appeal while providing functional advantages such as UV protection and antimicrobial properties. Similarly, in the food industry, CQDs are applied as fluorescence sensors for food analysis, facilitating the detection of pathogens, food additives, heavy metals, nutrients, and pesticide residues, thereby improving food safety and quality control. In summary, the versatile applications of CQDs across industries such as biomedical, environmental, energy, and optoelectronics highlight their growing significance in solving real-world challenges. Their unique combination of biocompatibility, fluorescence, and functional adaptability continues to drive innovation and practical advancements across various scientific and industrial fields.

2.5.2 Synthesis Methods of CQDs

The synthesis of CQDs can generally be divided into two main approaches: top-down and bottom-up methods, each with its unique mechanisms, advantages, and challenges. These approaches play a crucial role in determining the physical and chemical properties of the CQDs, including size, structure, and functional groups, which in turn influence their performance in various applications such as bioimaging, sensing, and CO_2 adsorption.

In the top-down approach, CQDs are derived by breaking down bulk carbon materials, such as graphite, graphene, multi-walled carbon nanotubes, or coal, into smaller nanoscale particles. This is typically achieved through physical or chemical techniques like arc discharge, laser ablation, and electrochemical oxidation (Vibhute et al., 2022) . Arc discharge and laser ablation, for instance, use high energy to fragment larger carbon precursors into CQDs under controlled conditions. Similarly, electrochemical oxidation involves applying a voltage to carbon electrodes submerged in electrolytes to generate CQDs. Although the top-down approach produces high-quality CQDs with well-defined structures, it comes with several limitations, including harsh reaction conditions (high temperatures, pressures, and energy consumption) and complex post-treatment steps for purification and functionalization. These challenges make top-down methods resource-intensive and less appealing for large-scale production, particularly for applications requiring environmentally sustainable solutions.

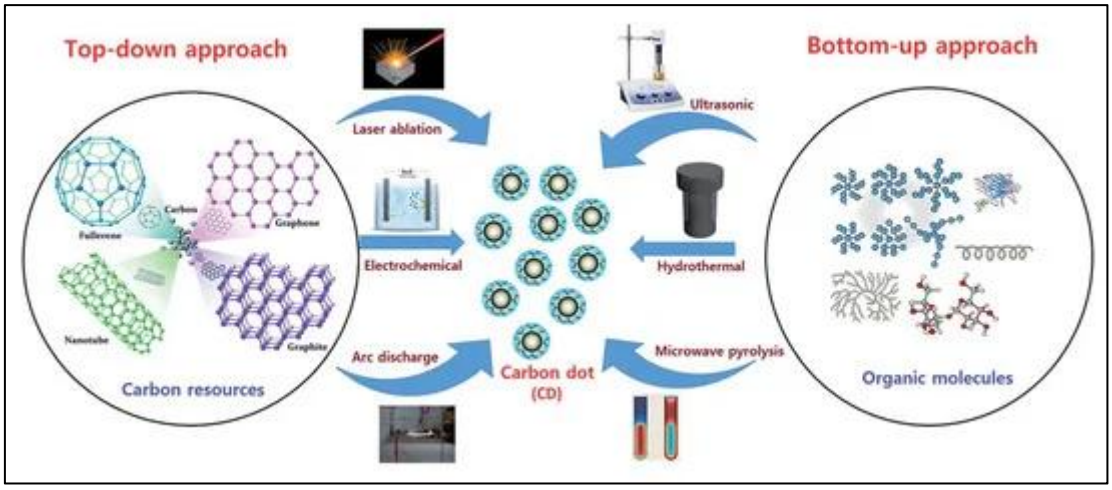

Figure 2.7 Possible synthesis methods of CQDs (Kurian & Paul, 2021)

On the other hand, the bottom-up approach focuses on building CQDs from smaller carbon-rich precursors, such as organic molecules, biomass, and renewable waste materials. These methods rely on external energy sources like microwave heating, thermal treatment, or ultrasonic irradiation to facilitate the carbonization process (Visheratina et al., 2022). Biomolecules like glucose, fructose, citric acid, and agricultural waste are commonly used as raw materials due to their abundance, low cost, and eco-friendly nature. Among bottom-up methods, microwave-assisted synthesis has gained attention for its ability to produce CQDs quickly and efficiently by providing uniform heating. Similarly, hydrothermal and solvothermal techniques involve subjecting carbon precursors to high temperatures and pressures in aqueous or organic solvents, enabling controlled carbonization and functionalization of CQDs. The bottom-up approach is considered superior in terms of sustainability and scalability as it operates under milder conditions, reduces energy consumption, and allows for greater control over CQDs size, shape, and functional groups. This versatility makes bottom-up methods particularly attractive for green synthesis and environmentally sensitive applications (Xia et al., 2019b).

Several methods for synthesizing CQDs will be discussed in this section, each offering unique advantages and applications. These methods include hydrothermal carbonization, which utilizes high temperature and pressure in aqueous environments to produce CQDs, and microwave-assisted synthesis, known for its rapid heating and energy efficiency. Chemical oxidation involves the use of strong oxidizing agents to break down carbon precursors, while pyrolysis carbonization thermally decomposes biomass at high temperatures (400–900°C) in an inert atmosphere to produce CQDs. Ultrasonic methods rely on ultrasonic waves to facilitate carbonization and particle formation, whereas the solvothermal method, similar to hydrothermal synthesis, employs organic solvents to control the size and properties of CQDs. Laser ablation techniques use high-energy lasers to fragment carbon materials into smaller nanoparticles, and electrochemical oxidation generates CQDs through the oxidation of carbon electrodes in electrolytic solutions. Each of these methods provides distinct pathways for CQD synthesis, enabling the production of materials tailored for specific applications in fields like bioimaging, energy, and environmental remediation.

Table 2.12
Advantages and Disadvantages of Common CQDs Synthesis Methods

Synthesis methods	Description	Advantages	Disadvantages	References
Hydrothermal Carbonization	Organic materials are polymerized and carbonized in a sealed vessel under high temperature (120–250°C) and pressure using water as the solvent.	Environmentally friendly, versatile precursor selection, produces CQDs with uniform size and good crystallinity.	Requires long reaction times, high temperatures, and specialized equipment for pressure control.	(Chu et al., 2019; Ferjani et al., 2024; Krishna Saraswat et al., 2024; Meng et al., 2019; Mitra et al., 2013; Nammahachak et al., 2022; Nazibudin et al., 2023; Salim & Irwan, 2024; Zattar et al., 2021)
Microwave-Assisted Synthesis	Carbon-rich precursors are irradiated with microwaves, providing rapid and uniform heating, leading to the synthesis of CQDs in minutes.	Fast reaction times, energy-efficient, controllable particle size, and suitable for large-scale synthesis.	High energy demand, limited control over reaction conditions, and challenges in preventing self-quenching and low quantum yield.	(Ameta et al., 2023; De Medeiros et al., 2019; Gencer et al., 2022; J. Hu et al., 2024; Ibarra-Prieto et al., 2023; Rawat et al., 2024a, 2024b; R. K. Singh et al., 2019; Tran Bao et al., 2024)
Chemical Oxidation	Strong oxidizing agents (e.g., H_2O_2, HNO_3) are used to carbonize and oxidize carbon precursors to produce CQDs.	Simple, fast, and scalable method for large-scale production of CQDs.	Use of toxic chemicals raises environmental concerns, and the resulting CQDs may lack uniform size distribution.	(Krishna Saraswat et al., 2024; Nisha et al., 2024)
Pyrolysis Carbonization	Biomass or carbon precursors are heated at high temperatures (400–900°C) under an inert atmosphere, causing thermal decomposition.	Solvent-free, can process diverse carbon precursors, and produces stable CQDs with significant optical properties.	High energy consumption, requires precise temperature control, and risk of forming undesired carbon	(Bezuneh et al., 2023; X. Li et al., 2015; K. Luo et al., 2024; C. Wang et al., 2022)

			structures.	
Ultrasonic Methods	High-frequency ultrasonic waves generate cavitation bubbles in a solution, leading to localized high temperatures and pressures that facilitate CQDs formation.	Simple, mild reaction conditions, and low energy requirements compared to thermal methods.	Low production yield, limited scalability, and difficulty in achieving uniform particle size.	(*CQDs (Carbon Quantum Dots) with High Fluorescence Characteristic as Well as Preparation and Application of CQDs*, 2018b; H. Huang et al., 2018; R. Kumar et al., 2020; Permadi et al., 2024)
Solvothermal Method	Precursors are dissolved in a solvent and heated in a sealed autoclave at high temperature and pressure, similar to hydrothermal synthesis but with organic solvents.	Produces highly crystalline and monodisperse CQDs, allows better control of particle size and surface functionalization.	Long reaction times, use of organic solvents can pose safety and environmental concerns.	(Huo et al., 2023; Laemont et al., 2024; Palacio-Vergara et al., 2023; Y. Sun et al., 2024)
Laser Ablation Technique	High-powered laser beams are directed onto a solid carbon target immersed in a liquid, vaporizing the target to produce CQDs.	Produces high-purity CQDs with controllable size and minimal chemical contamination.	Expensive equipment, complex procedure, and limited scalability for large-scale production.	(L. Cui et al., 2020; M. Kim et al., 2017; Manikandan & Lee, 2022; Shorgar et al., 2023)
Electrochemical Oxidation	A carbon source is oxidized electrochemically in an electrolyte solution using an electric current to produce CQDs.	Environmentally friendly, scalable, and provides good control over size and functionalization.	Requires specialized equipment, time-consuming, and the yield is often lower compared to other methods.	(Ding et al., 2020; Y. Fu et al., 2018; Y. Li, Liang, et al., 2024; M. Liu et al., 2016; Rocco et al., 2023; D. Wu et al., 2023)

CQDs can be synthesized through various methods, each offering distinct advantages and challenges. Microwave-assisted synthesis provides rapid, energy-

efficient production of nitrogen-doped CQDs (N-CQDs) with high quantum yields (~36.6%) but faces limitations in scalability due to high energy input. Chemical oxidation offers simplicity and speed for large-scale production, though it involves toxic reagents and yields less uniform particles. Pyrolysis carbonization enables solvent-free, high-temperature conversion of biomass into doped CQDs (e.g., N/S-GQDs) but demands precise temperature control to maintain optical properties. Ultrasonic methods leverage cavitation to produce biocompatible CQDs for bioimaging, while solvothermal techniques yield photoluminescent CQDs but require careful parameter optimization to minimize by-products. Laser ablation generates high-purity CQDs with uniform morphology (quantum yields up to 35.4%) but suffers from high costs and scalability issues. Electrochemical oxidation produces carboxyl-rich CQDs for environmental applications but struggles with low yields and stability.

While microwave and laser methods excel in quality control, their energy and cost requirements hinder industrial adoption. Chemical oxidation and pyrolysis prioritize scalability but compromise on homogeneity or environmental safety. Ultrasonic and solvothermal approaches balance biocompatibility and optical performance but need rigorous optimization. Electrochemical synthesis enables precise surface tuning yet remains limited by yield. Despite these trade-offs, CQDs demonstrate versatility in photocatalysis, bioimaging, and sensors, with method selection depending on target properties (e.g., quantum yield, doping) and application constraints (e.g., scalability, toxicity). Future advancements aim to address energy efficiency, yield, and reproducibility across these techniques.

The hydrothermal carbonization (HTC) method is a widely used approach for synthesizing CQDs due to its simplicity, cost-effectiveness, and environmental friendliness. This method involves the thermal degradation and carbonization of organic materials in water at elevated temperatures ranging from 120 to 250°C and under high pressure, facilitating the transformation of biomass into CQDs without requiring strong acids or extensive post-treatment processes. Moreover, the hydrothermal carbonization (HTC) process for generating CQDs operates at a relatively low temperature (180 °C), contributing to energy efficiency. Various biomass sources, such as avocado peels, sweet peppers, glucosamine, and rice husks, have been successfully utilized, producing CQDs with uniform size distributions (typically below 10 nm) and tunable fluorescence properties. By optimizing reaction parameters, the quantum yield (QY) of the synthesized CQDs can be further enhanced.

The resulting CQDs demonstrate significant potential in applications such as photocatalysis, environmental sensing, and pollutant removal, showcasing their versatility and functionality. Overall, the HTC method offers an efficient and sustainable pathway for producing high-quality CQDs while utilizing renewable and waste-derived carbon sources.

2.5.3 Precursors to Synthesis CQDs

CQDs can be synthesized from a wide range of carbon-rich precursors, including agricultural, food, and industrial waste materials. These carbon sources are not only abundant but also eco-friendly, offering a sustainable approach to CQD production while reducing environmental waste. Each source contributes unique properties to the resulting CQDs, influenced by the synthesis method employed, such as hydrothermal, solvothermal, or microwave-assisted techniques. These methods impact the quantum yield (QY), a measure of fluorescence efficiency, and determine the suitability of CQDs for various applications, including sensing, bioimaging, and environmental remediation. Table 2.13 provides an overview of different carbon sources used for CQD synthesis, summarizing their synthesis methods, quantum yields, and key applications.

Table 2.13
Carbon Sources Precursors to Synthesis CQDs

Precursor	Method	Quantum Yield (%)	Application	Reference
Palm kernel shells (PKS)	Microwave irradiation	27.21-43.07	Fluorescent ink, bacteria cells imaging, and metal ion detection	(Balakrishnan et al., 2022)
Eggshell	Biosynthesis Single-step microwave heating	19.98	Selective probe for fluorometric determination of molnupiravir, a COVID-19 antiviral drug	(Deng et al., 2023; Kannouma et al., 2024)
Eggshell membrane (ESM) ashes	Microwave-assisted process	14	Sample detection and biotechnology	(Q. Wang et al., 2012)
Coconut Shell	Hydrothermal carbonization	22.31	Food safety, solar energy harvesting, drug-gene delivery systems, explosive detection, and photocatalytic sensing	(Abinaya et al., 2021)

Orange peel	Hydrothermal carbonization	11.37-12.3	Biosciences and energy sciences: fluorescent indicators and effective catalysts	(Prasannan & Imae, 2013; Surendran et al., 2020)
Orange and lemon peels	Carbonization	16.8% and 15.5%	Sensing approaches for Fe^{3+} and tartrazine determination, intracellular detection of $Fe^{3+,}$ cellular imaging	(Chatzimitakos et al., 2017)
Sugarcane residue	Hydrothermal	17.98	Cytotoxicity assay, hemolysis assay, cellular imaging, and sensing for sunset yellow	(Pandiyan et al., 2020)
Factory tea waste	Hydrothermal treatment	7.1	Biomedical fields, for drug delivery and treatment of disease	(Purkait et al., 2023)
Cranberry beans	Hydrothermal treatment	10.85	Can be utilized as the FL sensor for the selective and sensitive detection of Fe3+ ions	(Zulfajri et al., 2019)
Ginkgo leaves	Hydrothermal treatment	11	Can be used as a novel fluorescence probe that enables both HeLa-cell imaging and sensitive Hg2+ detection.	(Q. Zhang et al., 2019)
Pigeon feather, egg white, egg yolk and manure	Pyrolysis carbonization reactions	24.87% (PCDs-f), 17.48% (PCDs-w), 16.34% (PCDs-y), 33.50% (PCDs-m)	Fluorescent probe for label-free, sensitive and selective detection of Hg^{2+} and Fe^{3+}, imaging of human umbilical vein endothelial cells	(Ye et al., 2017)
Chitosan	Microwave assisted heating	11.5	Cell labelling, diagnostics or controlled drug delivery and release systems	(Janus et al., 2019a)
Chitosan	Simple carbonization	6.28%	Used to detect Cu^{2+} in a mixed solution of different metallic salts, identifying the Cu^{2+} traces in industrial wastewater or solutions	(Trung et al., 2022)

Table 2.13 showcases various carbon sources used in the synthesis of CQDs, highlighting their synthesis methods, quantum yields, and diverse applications. The carbon precursors include natural materials such as agricultural residues (e.g., sugarcane residue and ginkgo leaves), food waste (e.g., orange and lemon peels,

eggshells, and cranberry beans), and animal-derived materials (e.g., pigeon feathers, egg components, and shrimp shell-derived chitosan). These materials emphasize the eco-friendly and sustainable nature of CQDs synthesis, repurposing waste materials into high-value nanomaterials. Among the precursors, palm kernel shells (PKS) and pigeon manure-derived CQDs exhibit the highest QYs (27.21–43.07% and up to 33.50%, respectively), suggesting superior optical properties, likely due to their carbon-rich composition and microwave/pyrolysis methods that enhance crystallinity and surface passivation. In contrast, tea waste and chitosan synthesized via simple carbonization yield lower QYs (7.1% and 6.28%), indicating that less controlled methods may introduce defects or insufficient functionalization. Hydrothermal treatment, used for precursors like coconut shell and ginkgo leaves, consistently produces moderate QYs (11–22.31%), balancing sustainability with performance.

Notably, microwave-assisted methods (e.g., for PKS and chitosan) often achieve higher QYs than hydrothermal routes, possibly due to rapid, uniform heating that reduces aggregation. However, hydrothermal synthesis method is particularly advantageous due to its ability to efficiently carbonize polysaccharide-rich precursors under controlled temperature and pressure, ensuring uniform particle size and enhanced quantum yield. Unlike microwave or pyrolysis methods, hydrothermal synthesis offers better control over surface functionalization, which is critical for biomedical applications such as drug delivery and metal ion sensing. Additionally, this method aligns with green chemistry principles, as it avoids harsh chemicals and enables scalable production of high-quality CQDs.

CQDs derived from renewable precursors demonstrate how waste-to-wealth strategies can meet the demand for functional, environmentally benign nanotechnology solutions. The selection of the hydrothermal method for chitosan not only optimizes performance but also reinforces the commitment to sustainable synthesis practices. Many of these biomass-derived carbon sources, such as chitosan, pigeon feathers, and ginkgo leaves, inherently contain nitrogen, sulfur, and oxygen-rich compounds. During hydrothermal processing, these heteroatom-containing moieties can be retained or incorporated into the CQDs structure, naturally promoting N/S/O-doping. This intrinsic heteroatom modification not only enriches the surface chemistry but also creates abundant active sites for enhanced adsorption, catalysis, and sensing applications, providing a direct transition to the discussion in the following subsection on N/S/O-heteroatom modification of CQDs.

2.6 Heteroatoms in CQDs

CQDs often incorporate heteroatoms such as nitrogen, sulfur, oxygen, phosphorus, and boron, which are introduced either intentionally through doping or naturally via precursor decomposition. The presence and distribution of heteroatoms largely depend on the precursor materials and synthesis conditions, with nitrogen being the most common due to its prevalence in organic and biomass-derived sources. Sulfur and oxygen are frequently incorporated through sulfonated or oxygen-rich precursors, while phosphorus and boron are less common but offer unique electronic modifications. Table 2.14 summarizes the heteroatoms found in CQDs derived from different precursors, along with their corresponding synthesis methods and key parameters.

Table 2.14
Heteroatoms Available in CQDs from Various Precursors

Precursor	Synthesis method	Synthesis parameter	Quantum yield (%)	Heteroatoms created	References
Citric acid + L-cysteine	Hydrothermal	200 °C for 3 h	73	N, S	(Dong et al., 2013)
N-(4-hydroxyphenyl) glycine + boric acid	Hydrothermal	150, 200, 250, 300, 350, and 400 °C for 2.5 h	11.4	N, B	(Jahan et al., 2013)
Pumpkin + H3PO4	Acidic oxidation	90 °C, 1 h	-	P, N	(X. Gong et al., 2015)
Phosphorus tribromide + hydroquinone	Solvothermal	200 °C, 1 h	~25	P	(J. Zhou et al., 2014)
Phytic acid + sodium citrate + ethylenediamine	Hydrothermal	240 °C, 4 h	Not stated	P	(F. Yang et al., 2018)
Citric acid + sodium tetraphenylborate	Hydrothermal	180 °C for 8 h	42	B	(Ma et al., 2020)
Citric acid + urea + DMF	Microwave-assisted	Mass ratio CA:urea 1:2	36	N	(Qu et al., 2014)
Citric acid + linear-structured polyethyleneimine (LPEI)	Hydrothermal	150 °C, 5 h	37.4	N	(J. Liu et al., 2014)
Phytic acid and ethylenediamine	Microwave-assisted	700 W, 8 min	21.65	P	(W. Wang et al., 2013)
MgO, FeCl3·6H2O, 1,10-phenanthroline	Electrolysis	800 °C under argon for 2 h	7.5	Fe-N	(S. Sun et al., 2023)

The incorporation of heteroatoms into CQDs has been widely explored to enhance their physicochemical properties, particularly their optical characteristics and surface reactivity. As shown in Table 2.14, a variety of precursors and synthesis methods have been employed to introduce heteroatoms such as nitrogen (N), sulfur (S), phosphorus (P), and boron (B) into CQDs. Among these, citric acid is frequently used as a carbon source, often combined with heteroatom-rich compounds like L-cysteine, urea, ethylenediamine, or phytic acid to achieve multi-doping.

For instance, the combination of citric acid and L-cysteine via hydrothermal synthesis at 200 °C for 3 hours resulted in N, S co-doped CQDs with a remarkably high quantum yield of 73%. Similarly, N doping using urea or ethylenediamine under hydrothermal or microwave-assisted conditions has consistently produced CQDs with quantum yields up to 37%, highlighting N's significant role in enhancing fluorescence. Phosphorus doping was successfully achieved using phosphorus tribromide, phytic acid, or phosphoric acid-rich biomass like pumpkin with H_3PO_4. These phosphorus-doped CQDs, synthesized mainly via hydrothermal or solvothermal routes, showed moderate quantum yields and are known to contribute to improved charge transfer properties.

Boron-doped CQDs were synthesized using sodium tetraphenylborate, yielding a high quantum yield of 42% under hydrothermal treatment. B co-doping with N using N-(4-hydroxyphenyl) glycine and boric acid also led to dual heteroatom incorporation, though with a lower quantum yield of 11.4%. Interestingly, a unique Fe-N co-doping was achieved through electrolysis of MgO, $FeCl_3 \cdot 6H_2O$, and 1,10-phenanthroline at high temperature (800 °C), demonstrating the feasibility of incorporating transition metals alongside non-metals into CQDs.

In summary, the type and content of heteroatoms doped into CQDs are significantly influenced by the choice of precursor and synthesis conditions. Nitrogen and phosphorus are the most commonly introduced heteroatoms due to their accessibility and the resulting enhancement in CQDs' photoluminescence and surface functionalities. The use of different dopants and combinations offers a tunable strategy to tailor CQD properties for various applications such as sensing, catalysis, and bioimaging.

2.6.1 N/S/O-Heteroatoms Modification of CQDs for CO_2 Removal

N/S/O-heteroatom modification of CQDs plays a pivotal role in enhancing their physicochemical properties for CO_2 capture applications. These heteroatoms can be introduced through various precursors, including biomass, synthetic polymers, and small organic molecules, which influence the electronic structure, surface polarity, and porosity of CQDs. N, commonly derived from amine-rich precursors such as ethylenediamine or urea, enhances basicity and CO_2 adsorption selectivity. Sulfur, often incorporated via sulfonated compounds or thiourea, introduces defect sites and improves surface reactivity, while oxygen-containing groups (e.g., carboxyl, hydroxyl) contribute to polar adsorption sites and hydrophilicity.

Among these precursors, chitosan, a naturally abundant biopolymer rich in N and O stands out as a sustainable and cost-effective carbon source for CQDs synthesis. Utilizing chitosan for CQDs synthesis presents advantages such as cost-effectiveness, an abundant and sustainable source of raw materials, a straightforward synthesis process, and the inherent presence of multiple heteroatoms for potential doping. Given that chitosan lacks sulfur, a supplementary sulfur source is introduced during its chemical modification. The introduction of heteroatoms through doping leads to the formation of small micropores and highly polar adsorption sites on the resulting CQDs.

The incorporation of ternary N, S, and O heteroatoms into chitosan-derived CQDs is expected to enhance the activity of chitosan and broaden its range of applications. Doping agents, such as N or S elements, are essential to augment the fluorescence effect. In the production of CQDs, KOH and thiourea are employed as doping agents. Thiourea doping plays a significant role in enhancing the CO_2 adsorption capacity of carbon-based materials by introducing N and S heteroatoms, which improve the surface chemistry and porosity of the adsorbents. Pure thiourea (CH_4N_2S) contains 82.6% of N and 17.4% of S by weight, corresponding to its molecular formula and molecular weight of 76.14 g/mol (Campopiano et al., 2022). Studies indicate that thiourea-modified porous carbons exhibit high specific surface areas (up to 2581 m^2/g) and optimal micropore volumes, which are crucial for effective CO_2 capture (H. Cui et al., 2022; Nazir et al., 2021). The presence of S element enhances the formation of active sites and increases defect density, while N doping improves adsorption selectivity and interaction strength with CO_2 (J. X. Chen et al., 2024b; Shao et al., 2022b).

Simultaneously, the commonly used activator potassium hydroxide (KOH) is employed to increase the surface area and customize the pore texture of ordered mesoporous carbon. In KOH-impregnated materials, such as rice husk-based activated carbon, the presence of KOH alters surface properties, facilitating both physisorption and chemisorption, which leads to improved CO_2 adsorption capacities (2.1 mmol/g) compared to untreated counterparts (S. Wang et al., 2022). Similarly, KOH activation in the synthesis of N-doped porous carbon results in a high CO_2 adsorption capacity of 3.09 mmol/g, attributed to enhanced interaction between CO_2 and the adsorbent surface (Khalili & Jahanshahi, 2021). Additionally, KOH's role in creating oxygen vacancies in In_2O_3 boosts CO_2 affinity and charge separation, achieving a remarkable adsorption capacity of 2336 cm^3/g (J. Huang et al., 2024). Overall, KOH doping not only increases surface area and porosity but also optimizes the adsorption mechanisms, making it a crucial factor in developing efficient CO_2 adsorbents (X. Chen et al., 2023; Helmi et al., 2023). Recognized as an efficient porogen, KOH produces advanced microporous structures under various activation conditions, including temperature and dosage. A low KOH/carbon ratio leads to the enlargement of created micropores, eventually causing them to merge or transform into mesopores. Conversely, a high KOH/carbon ratio results in an excess of micropores (Y. Lv et al., 2011).

Surface modifications play a significant role in influencing the structure and photoluminescence of CQDs (Thulasi et al., 2019). Functionalizing CQD surfaces can be achieved through either covalent or noncovalent interactions. Covalent interactions involve functional groups reacting with the COOH or NH_2 groups on the surfaces of CQDs. On the other hand, noncovalent interactions, such as interactions between CQDs and particles and the utilization of Van der Waals forces, are employed in the modification process (Pandey & Chusuei, 2021). Table 2.15 provides a summary of previous research focused on surface modifications of chitosan-derived CQDs. These modifications significantly influence the resulting CQDs' properties and performance.

Table 2.15
N/S/O-sources in Surface Modification of Chitosan-derived CQDs

Source/ Modifier	Synthesis method	Synthesis parameter	Quantum yield (%)	Heteroatoms created	References
Acetic acid solution (100 mL, 1%	Hydrothermal carbonization	180 °C for 12 h	35	N	(L. Sun et al., 2021)
Melamine +	Solvothermal	160°C for 4	21	N	(Munusamy

triethanolamine		hours			et al., 2021)
Acrylamide	Microwave-hydrothermal carbonization	220°C for 30-60 minutes	45.9	N	(G. Liu et al., 2019)
Lysine	Microwave radiation	300 W for 3 minutes	11.5	N, O	(Janus et al., 2019a)
Glutamic acid	Microwave radiation	300 W for 5 minutes	7.4	N, O	(Janus et al., 2019a)
κ-carrageenan	Hydrothermal	-	59.31	N, S	(J. Xu et al., 2021)
2,4,6-triaminopyrimidine	Hydrothermal	-	74.9	N	(L. Luo et al., 2018)
Methyl orange (MO)	Hydrothermal carbonization	240 °C for 12 hours	29.4	N, S	(Ren et al., 2023)
Citric acid (CA) and thiosemicarbazide (TSC)	Hydrothermal	-	37.8	N, S	(Chandra et al., 2020)
Citric acid + urea, trizma base, beta-alanine, L-arginine, and EDTA	Continuous hydrothermal flow	-	40	N	(Nguyen et al., 2024)
Citric acid monohydrate + thiourea	Microwave solid-phase pyrolysis	445 W for 50 seconds	23.6	N, S	(T. Liu et al., 2017)
Spent coffee waste	Biomass-assisted synthesis	-	9.4	O	(D. Y. Lee et al., 2024)
Polyethylene glycol (PEG)	Microwave irradiation	500 W at 100 °C	7.84	O	(Y. Zhao et al., 2017)
Citric acid + urea	Microwave	-	75.5	N, O	(Siahcheshm & Heiden, 2022)

Table 2.15 presents a comparative analysis of various synthesis methods and parameters for chitosan-derived CQDs, highlighting their quantum yields (QY) and heteroatom incorporation. The highest QY (75.5%) was achieved using citric acid and urea under microwave synthesis, indicating the efficiency of N and O doping in enhancing fluorescence. Similarly, 2,4,6-triaminopyrimidine yielded a high QY

(74.9%) via hydrothermal synthesis, further emphasizing the role of nitrogen-rich precursors. S-doped CQDs, such as those derived from κ-carrageenan (59.31% QY) and citric acid with thiourea (23.6% QY), demonstrate the potential of S incorporation for improving optical properties. Microwave-assisted methods generally produced higher QYs (e.g., 45.9% for acrylamide) compared to conventional hydrothermal routes, suggesting faster and more efficient synthesis. However, biomass-derived CQDs (e.g., spent coffee waste, 9.4% QY) and PEG-based CQDs (7.84% QY) exhibited lower QYs, likely due to fewer heteroatoms (only O). Overall, N-rich precursors and microwave or solvothermal methods tend to yield CQDs with superior quantum yields, while S and O doping further modulate their properties.

2.6.2 Mechanisms Involved in the Heteroatom Modification

Heteroatom doping introduces functional groups that significantly alter the surface chemistry, electronic structure, and adsorption behavior of carbonaceous materials. These modifications are achieved through various chemical and thermal processes, leading to the creation of active sites and defect structures that play a critical role in improving performance for applications such as CO_2 capture. Understanding the underlying mechanisms of heteroatom incorporation is essential for tailoring materials with superior adsorption, catalytic, and sensing capabilities. This section provides discussion on the mechanisms involved in the heteroatom modification, revealing how heteroatoms doping influences material properties.

Hydrothermal carbonization of organic precursors often yields CQDs whose surface and core incorporate heteroatoms from the feedstock or additives. In particular, N, S and O heteroatoms can enter the carbon network or terminate it as functional groups, strongly tuning the CQDs' optical and electronic properties. The basic mechanism is that under heat and pressure, organic precursors dehydrate and polymerize into aromatic carbon cores, while heteroatom-bearing molecules condense or react to form new bonds. For example, Olla et al. found that heating citric acid with urea produces N-containing cyclic molecules (e.g. citrazinic acid, imidic rings) embedded in the carbon dots (Olla et al., 2023) . In general, N-, S- or O-containing precursors (like urea, thiourea, L-cysteine, chitosan, etc.) decompose to release NH_2, –SH, –OH, carbonyl, and other groups that either crosslink into the graphitic core or stay as surface functionalities. Heteroatom doping has been widely shown to tune the

compositions and structures of CDs and to enhance optical/electronic behavior (Jorns et al., 2021a; C. Sun et al., 2016).

2.6.2.1 Nitrogen Doping Mechanisms

Nitrogen is frequently introduced via amine-rich precursors. Chitosan (a polysaccharide of glucosamine) is a prime example: it is ~7 wt% N and contains $–NH_2$ and –NHCO– groups. When chitosan is carbonized hydrothermally, its C–N backbone partly breaks down and forms N-doped carbon. In fact, chitosan can act as both the C and N source, yielding N-doped CQDs in one step (Villalba-Rodríguez et al., 2022; L. Zhao et al., 2019) . For example, Zhao et al. (2019) hydrothermally treated chitosan alone and obtained ~2 nm N-CQDs with ~6.3% N and ~21% O by XPS. FTIR and XPS showed these N atoms in amine (N–H) and C–N–C environments, and abundant surface $–NH_2$, –OH and –COOH groups (L. Zhao et al., 2019) . Chitosan-based N-CQDs thus contain built-in amine functionalities on the edges ($–NH_2$) as well as graphitic (sp^2) N in the core.

Mechanistically, the amine groups of chitosan can either remain as surface $–NH_2$/–NHCO– groups or incorporate into aromatic rings (forming pyridinic or pyrrolic N) during carbonization. For instance, Olla et al. (2023) showed that urea-derived N doping of citric-acid CQDs results in a decrease of oxygen functional groups and the creation of new N-linked emissive centers (Olla et al., 2023) . In their study, the undoped CDs had many –C=O surface traps, whereas N-doping (via urea) replaced some oxygen groups with N-containing moieties. The N-doped CQDs displayed additional imidic and graphitic C–N features (identified by XPS at ~399–401 eV) and higher fluorescence yield. Nitrogen in CQDs typically appears in multiple bonding configurations – graphitic (C–N–C), pyridinic, pyrrolic and even amine or amide – depending on conditions (Olla et al., 2023; L. Zhao et al., 2019) . Each N type influences the electronic states differently: graphitic N donates electrons into the π-system, pyridinic N contributes lone-pair states, etc. Overall, N-doping introduces additional $\pi \rightarrow \pi^*$ and $n \rightarrow \pi^*$ transitions and often creates mid-gap states that enhance fluorescence quantum yield and shift the emission. In summary, under hydrothermal conditions, N atoms from precursors like urea or chitosan become incorporated either into the aromatic carbon network (as substituted N) or remain as surface functional groups ($–NH_2$, –NHCO–). The result is typical N contents of a few percent (e.g. ~6–

7% in chitosan-CQDs (L. Zhao et al., 2019) and formation of emissive N-centers. Olla et al. noted that N doping causes the decrease in the relative content of O-containing functional groups and the formation of both N-related molecular and surface centers that enhance the quantum yield of the material (Olla et al., 2023). In practice, co-precursors (e.g. ethylenediamine, melamine, amino acids) are often added to boost N-doping and tune the emission. The case of chitosan is instructive: it supplies internal N so that no external N-source is needed, and yields stable, brightly fluorescent N-CQDs with $–NH_2$, –COOH, –OH groups on the surface (L. Zhao et al., 2019).

2.6.2.2 Sulfur Doping Mechanisms

Sulfur heteroatoms are usually introduced via thiol or sulfide compounds (thiourea, L-cysteine, thiamine, sulfates, etc.). In hydrothermal carbonization, S–rich groups either attach to carbon sites or oxidize to sulfoxide/sulfate on the surface. For example, L-cysteine decomposes to leave –C–S– bonds (thiophene-like) and $–SO_x–$ (sulfone/sulfonate) functionalities. XPS of N, S–co-doped CQDs often reveals S2p peaks around 164–166 eV (C–S bonds) and higher 168–169 eV ($C–SO_2/–SO_3$). In garlic-derived CQDs (Sun et al., 2016), which are self-doped by the natural S in garlic, the S was found mainly as covalent C–S (thiophene-S) and some oxidized $–C–SO_x–$ groups (C. Sun et al., 2016). Mechanistically, polysulfide or organosulfur fragments from the precursor insert into the carbon network during the polymerization. S doping often accompanies or cooperates with N. Thiourea, for example, adds both N and S, so co-doped CQDs contain pyridinic/pyrrolic N and thiophene S in the same lattice. These heteroatoms can have synergistic effects: co-doped CQDs frequently show higher quantum yields than singly doped ones. As noted by Kandasamy et al. and others, introducing sulfur alongside N is found to be synergistic for N doping in co-doped CQDs (Kandasamy, 2019). In the garlic-CD example, ethylenediamine was added to boost N, which increased the yield from ~10% to ~20%. In summary, sulfur is incorporated as thiol/thiophene-like C–S bonds and occasionally oxidized forms. In co-doped CQDs one typically sees pyridinic/pyrrolic N (XPS ~400–401 eV) and thiophenic S (XPS ~164–166 eV) (C. Sun et al., 2016). These dopants create new electronic states: for instance, thiophene-S has lone pairs that can contribute mid-gap states, and oxidized S ($–SO_2$, $–SO_3$) adds polar surface traps. The overall effect is to introduce defect states that can quench or enhance emission depending on

environment, and to make the CQD surfaces rich in functional moieties (–C–S–, –SO_3H etc.) that alter chemistry and sensing.

2.6.2.3 Oxygen Doping and Surface Functionalization

Oxygen is inherently present in most carbon dot syntheses (e.g. carboxylic acids, sugars, chitosan have C=O/OH). Oxygen doping typically means increasing the fraction of C–O and C=O groups in the carbon lattice or on edges. During hydrothermal carbonization, oxygen can either remain bound (as hydroxyls, carboxyls, carbonyls) or form ethers/epoxies. Unlike N and S (which often substitute C), O often stays as surface functional groups. For example, chitosan-CQDs contain ~21% surface O in C–O and C=O forms (L. Zhao et al., 2019). Oxygen functional groups strongly affect photoluminescence. Carbonyls (C=O) give rise to n–π* transitions; in many CQDs the blue emission is attributed to surface C=O/COOH traps. In fact, Wang et al. reported that C=O groups on CQD surfaces are considered to be the main emission centers for blue luminescence (Kandasamy, 2019). By contrast, increasing C=O and graphitic-N content was linked to red-shifted (lower-energy) emission. Thus O-doping (in the sense of adding more oxygen content) tends to introduce surface-trap states that often red-shift the emission. Jorns et al. notes that higher carbonyl content correlates with red-emitting CDs, suggesting that oxidation level tunes the band gap (Jorns et al., 2021b). Chemically, oxygen groups also make the CQD surface very reactive: hydroxyls and carboxyls impart water solubility and metal-binding ability. As noted above, chitosan-derived N-CQDs are rich in –OH and –COOH, enabling strong coordination with analytes (L. Zhao et al., 2019). In sensing studies, these oxygen groups are the sites for quenching interactions (e.g. Fe^{3+} complexes with –COOH). Electrically, O-doping (through C–O and C=O) withdraws electron density from the π-system, widening the band gap relative to pure carbon. Overall, heteroatom doping with O (and N, S) changes the electronic structure of the nanoparticle, and therefore the band gaps. In practice, one often sees that adding more O/N/S dopants shifts PL to longer wavelengths (lower gap), consistent with new electronic states introduced by these more electronegative atoms (Jorns et al., 2021b; Kandasamy, 2019).

2.7 Support Structure in Controlling the Instability of CQDs as an Adsorbent

The practical application of CQDs as adsorbents is often hindered by their inherent instability, including tendencies toward agglomeration and sensitivity to environmental factors such as moisture. To overcome these challenges, embedding CQDs within a support matrix has emerged as an effective strategy. Support materials not only enhance the dispersion and stability of CQDs but also improve their mechanical robustness and reusability in adsorption applications.

Various support structures have been explored for immobilizing CQDs, including hydrogels, activated carbon, silica nanoparticles, and polymer scaffolds. Among these, xerogels stand out due to their highly porous architecture, tunable surface chemistry, and exceptional surface area (200–800 m^2/g) (Duceac & Coseri, 2022) . Formed through sol-gel processes followed by ambient drying, xerogels provide an ideal framework for stabilizing CQDs while preserving their optical and adsorptive properties. The interconnected porous network of xerogels prevents CQDs aggregation and enhances accessibility to adsorption sites, making them particularly suitable for applications such as CO_2 capture. Additionally, the mechanical stability of xerogels ensures long-term durability, addressing a key limitation of standalone CQDs.

Other support materials, such as hydrogels, offer flexibility and biocompatibility but may lack the structural rigidity required for certain adsorption processes. Activated carbon provides high surface area but can limit the accessibility of CQDs surfaces due to its microporous nature. Silica nanoparticles and polymer scaffolds, while effective in some cases, may require additional functionalization to optimize CQDs integration. In contrast, xerogels combine high porosity, structural stability, and ease of synthesis, making them a superior choice for stabilizing CQDs in adsorption-based applications. Table 2.16 provides a comparative analysis of different support matrices for CQDs immobilization, highlighting their key characteristics and performance in enhancing the stability and functionality of CQDs-based adsorbents.

Table 2.16
Comparison of Support Matrices for CQDs Immobilization

Support Material	Advantages	Limitations	Suitability for CO_2 Capture	Sorption Capacity	References
Xerogel	High porosity, tunable chemistry, ambient drying	Relatively lower mechanical strength; may require modification for CO_2-specific binding.	Excellent (enhanced gas diffusion and stability)	~0.80 mmol g^{-1} (amine-modified PEG/silica xerogel under pure CO_2)	(Alias et al., 2022a; Deana et al., 2023; H. Fu et al., 2017; Hannachi et al., 2019a; Jaiboon et al., 2014; Mahdi et al., 2024a; Noraini et al., 2022; SEZGIN, 2024)
Hydrogel	High water content, biocompatibility	Lower thermal stability, swelling in humid conditions	Moderate (limited to aqueous systems)	Chitosan–glucose hydrogel: 202 mg Co^{2+}/g at 20 °C (heavy metals)	(Alias et al., 2022a; Kazeminava et al., 2022; Zeng et al., 2021)
Activated Carbon	High surface area; low-cost; wide availability	Pore blocking, limited functionalization	Good (but lacks tailored active sites)	Up to ~3.0 mmol g^{-1} (~44–132 mg/g) under flue gas conditions	(de Freitas et al., 2021; El Jery et al., 2024; Mahdi et al., 2024a)
Silica Nanoparticles	Chemical inertness, thermal stability	Low CO_2 affinity without modification	Poor (requires additional functionalization)	1.14–1.90 mmol g^{-1} (aminated silica xerogels)	(Basaran et al., 2021; Jaiboon et al., 2014; Kajani et al., 2023; Khader et al., 2015)
Polymer Scaffolds	Flexible synthesis; tunable chemistry; tailored affinity for CO_2	Limited porosity, low thermal/chemical stability	Moderate (depends on polymer type)	Imidazolium-based PILs: ~2 mmol CO_2/g (~88 mg/g at 273 K)	(Echeverria Molina et al., 2021; Mindivan & Boz, 2025; Pathak et al., 2023)

The selection of an appropriate support matrix for immobilizing CQDs significantly influences the resulting composite's CO_2 adsorption capacity, structural

integrity, and long-term performance. Hydrogels, while highly biocompatible and capable of absorbing large amounts of water, exhibit limitations in gas-phase CO_2 applications due to their swelling behavior in humid conditions and relatively low thermal stability. Although their direct use in CO_2 gas adsorption is limited, hydrogels have shown promising results in aqueous systems for example, chitosan–glucose hydrogels adsorbing up to 202 mg Co^{2+}/g at 20 °C suggesting their suitability in wastewater treatment rather than flue gas capture. Their poor TGA stability and restricted pore networks further limit their use in high-temperature or dry-gas CO_2 applications.

Activated carbon remains one of the most extensively studied adsorbents due to its high surface area (typically 500–1500 m^2/g), cost-effectiveness, and wide commercial availability. However, its inherent microporosity often limits gas diffusion and adsorption site accessibility. Without functionalization, its affinity for CO_2 is moderate, with typical sorption capacities ranging from 44 to 132 mg/g under flue gas conditions (~3.0 mmol g^{-1}). Despite this, its high thermal stability (confirmed by minimal weight loss in TGA at temperatures up to 600 °C) makes it attractive for cyclic CO_2 capture operations.

Silica nanoparticles, particularly in xerogel form, show improved adsorption performance upon amine functionalization. Literature reports indicate capacities in the range of 1.14–1.90 mmol g^{-1} for aminated silica supports, placing them above unmodified xerogels or activated carbon. The rigid pore framework and chemical inertness of silica provide structural durability, while amine groups enhance CO_2 chemisorption via acid–base interactions. Their high thermal resistance and ability to retain surface area even after grafting make them favorable candidates for long-term operation, although the base material alone has low CO_2 affinity.

Polymer scaffolds offer tunable surface chemistry and flexibility in synthesis, allowing for tailored interactions with CO_2. Imidazolium-based polymeric ionic liquids (PILs), for instance, have achieved adsorption capacities around 2 mmol/g (~88 mg/g at 273 K), showing promise in capturing CO_2 under controlled conditions. However, these polymers typically exhibit limited surface area and lower thermal stability, which restrict their use in harsh industrial settings. Their chemical versatility can, however, be leveraged in hybrid systems where CQDs or other nanostructured adsorbents are embedded to enhance performance.

Among the materials compared, xerogels stand out due to their structural stability, tunable porosity, and synergistic compatibility with heteroatom-doped carbon materials. Their interconnected meso/macroporous network ensures unrestricted CO_2 diffusion to active sites while preventing CQD agglomeration, a critical advantage for maintaining adsorption efficiency in humid environments (Chavhan & Liu, 2025; Güzel Kaya, 2021) . However, xerogels may suffer from moderate mechanical strength and often require further functionalization (e.g., amine doping) to boost CO_2 binding affinity. Studies demonstrate that xerogels derived from silica or carbon frameworks can be further functionalized with amines (e.g., propylene diamine) or metals (e.g., Ca^{2+}), enhancing CO_2 selectivity through acid-base interactions and polar surface modifications (Aquino et al., 2019; Güzel Kaya, 2021). For instance, amine-modified PEG/silica xerogels achieved a CO_2 adsorption capacity of 0.80 mmol/g, outperforming non-porous supports due to their hierarchical pore structure (Güzel Kaya, 2021). Additionally, xerogels synthesized via ambient drying unlike aerogels requiring energy-intensive supercritical drying offer scalable production while retaining high surface areas (200–800 m^2/g) and mechanical robustness (Amaral-Labat et al., 2021; J. Choi et al., 2024) . This combination of stability, tailored porosity, and ease of functionalization positions xerogels as superior supports for scalable CO_2 capture adsorbents, addressing key limitations of alternative materials like hydrogels (swelling issues) or activated carbon (pore blocking) (Asrafali et al., 2025; Chavhan & Liu, 2025).

In summary, xerogels and aminated silica supports show the most balanced performance for CO_2 capture when used as CQD matrices, offering both moderate-to-high adsorption capacities and suitable thermal/mechanical properties. Activated carbon provides a low-cost alternative but lacks surface reactivity, while polymers and hydrogels may be more suited for niche applications involving aqueous systems or mild conditions. The comparative performance across these supports underscores the importance of tuning both the chemical functionality and structural framework to optimize CO_2 capture performance.

2.8 Adsorption Parameters in CO_2 Adsorption

The effectiveness of any adsorption system for carbon dioxide (CO_2) capture is strongly influenced by the operating conditions under which the process is conducted.

Among the most critical parameters are adsorption temperature, CO_2 concentration in the inlet gas stream, and the flow rate of the gas. These factors not only affect the kinetics of CO_2 interaction with the adsorbent surface but also impact equilibrium capacity and breakthrough behavior. Optimizing these variables is essential for designing an efficient and scalable carbon capture system. A literature review of prior research reveals consistent trends across various materials, including activated carbons, metal-organic frameworks (MOFs), and amine-functionalized adsorbents. The following discussion explore the influence of these parameters on CO_2 adsorption based on previously published studies.

Temperature plays a decisive role in CO_2 adsorption, particularly for materials operating via physisorption or weak chemisorption. In general, adsorption is an exothermic process, and elevated temperatures tend to decrease the equilibrium capacity by promoting desorption. For instance, carbon-based sorbents including activated carbon and zeolites exhibit a clear drop in uptake with temperature rising from ~25 °C to 100 °C (Tsiotsias et al., 2023). In fixed-bed breakthrough experiments conducted at 35 °C, 45 °C, and 55 °C, alumina functionalized with DAAB showed superior CO_2 uptake at the lower temperature, with higher adsorption capacities at 35 °C, while performance at 55 °C was notably diminished due to weaker interactions between CO_2 and the amine sites (Krishnaiah et al., 2014) . In addition, TEPA-impregnated silica gel exhibited ~1.9 mmol/g uptake at room temperature, with kinetics and capacity dropping at elevated temperatures (Gu et al., 2022) . These findings align with thermodynamic expectations and match trends seen with CQD-based adsorbents. Thus, it is widely recognized that maintaining adsorption at near-ambient temperatures (25–35°C) can enhance performance while minimizing energy input.

Gas flow rate determines the residence time of CO_2 molecules within the adsorbent bed. At lower flowrates, the extended residence time allows CO_2 molecules to diffuse more effectively into the pores, promoting greater interaction with available binding sites. Conversely, higher flowrates reduce the gas-solid contact duration, potentially resulting in premature breakthrough and lower adsorption capacity due to incomplete utilization of the adsorbent bed. Understanding this relationship is essential for optimizing operating conditions in continuous adsorption processes. Simulation on nanoporous activated carbon confirms that higher feed velocity

correlates with lower adsorption capacity (*(PDF) Computational Fluid Dynamics Simulation of CO2 Adsorption On Nanoporous Activated Carbon: Effect of Feed Velocity*, n.d.). Empirical data from mesoporous alumina (amine-modified) shows CO_2 capacity dropping from 56 to 27 mg/g as flow increases from 90 to 150 mL/min [192]. These findings reinforce the importance of optimizing flow rate to balance mass transfer kinetics and adsorption equilibrium.

The concentration or partial pressure of CO_2 in the feed gas plays a critical role in determining the adsorption behavior within fixed-bed systems. Higher CO_2 concentrations typically provide a greater mass transfer driving force, enhancing initial uptake rates and promoting faster adsorption kinetics. However, numerous studies have reported that excessively high concentrations may inversely affect the total adsorption capacity due to accelerated saturation of available active sites.

For example, dynamic CO_2 breakthrough experiments using porous ionic liquid-based adsorbents demonstrated that while initial uptake was enhanced at elevated concentrations, the overall effective capacity declined. At 1 vol% CO_2, the adsorbent achieved a capacity of 2.44 mmol/g with a prolonged breakthrough time, but as the CO_2 concentration increased, the system experienced quicker saturation, thereby reducing the net adsorption performance (B. Li et al., 2024). Similarly, Salehi et al. observed this inverse relationship while studying benzene and toluene adsorption on carbon fabrics. They found that reducing the inlet concentration extended the breakthrough time and improved the adsorption capacity per gram of adsorbent. In contrast, higher feed concentrations led to quicker saturation and lower measured uptake due to stronger driving forces overwhelming the system's adsorption capacity (Salehi et al., 2025).

Modeling efforts by Estumano et al. further reinforced this phenomenon. Their breakthrough curve analysis for H_2S and CO_2 in fixed-bed columns revealed that model parameters such as maximum adsorption capacity (e.g., in Thomas and Yan models) consistently decreased with increasing inlet concentration. This was attributed to rapid occupation of active sites and competitive interactions at higher concentrations, which, despite faster initial adsorption, limited the total amount of gas captured (Lima et al., 2024). Moreover, in a broader review of competitive biosorption systems, Grosche and Esteves (2025) noted that high adsorbate concentrations tend to exhaust active sites more rapidly, thereby accelerating breakthrough and decreasing fractional uptake. This effect was particularly evident in multi-component systems,

where site competition further reduced capacity at elevated concentrations (Macena et al., 2025).

Collectively, these findings emphasize a consistent mechanistic trend, although higher CO_2 concentrations may boost initial adsorption rates due to enhanced driving forces, they often compromise total adsorption capacity by inducing faster site saturation and limiting the duration of effective adsorption. This underscores the importance of optimizing feed concentration when designing adsorbent systems for CO_2 capture. In summary, literature findings reveal the importance of carefully controlling adsorption process parameters to optimize CO_2 capture efficiency. Lower adsorption temperatures (25–35°C), moderate gas flow rates (80–100 mL/min), and balanced CO_2 concentrations (2–6%) tend to yield superior performance in terms of both kinetics and capacity. These observations provide a strong foundational basis for experimental optimization in lab-scale and pilot-scale CO_2 adsorption systems.

2.9 Adsorption Isotherms for CO_2 Removal

Adsorption isotherms describe the relationship between the amount of adsorbate (such as a gas or liquid) adsorbed onto a solid surface at equilibrium conditions and the pressure or concentration of the adsorbate. Adsorption equilibrium, a foundational aspect of adsorption studies, has been extensively investigated to quantify the adsorbed species under specific conditions. Numerous mathematical forms describe adsorption isotherm models, some rooted in a simplified physical representation of adsorption and desorption, while others are entirely empirical, designed to correlate experimental data.

In this study, diverse adsorption isotherm models were applied to experimental equilibrium data to assess and determine the model that exhibited the most accurate fit. The selection of appropriate adsorption isotherm models is crucial for accurately describing CO_2 capture behavior across different materials. Table 2.17 summarizes various adsorption isotherm models commonly used to analyze gas–solid interactions, highlighting their types, applicability, advantages, limitations, and relevant references.

Table 2.17
Adsorption Isotherm Models

Isotherm Model	Type	Applicability	Equation	Key parameters	Advantages	Limitations	References
Langmuir	Type I (monolayer)	Chemisorption, homogeneous surfaces	$q_e = \frac{q_m K_L P}{1 + K_L P}$	q_e is the adsorbed amount, q_m is the maximum adsorption capacity, K_L is the Langmuir constant, and P is pressure	Simple, widely used for pure CO_2 adsorption	Assumes uniform sites, no multilayer adsorption	(El Jery et al., 2024; Kumar Singh & Anil Kumar, 2018)
Freundlich	Empirical (heterogeneous)	Physisorption, heterogeneous surfaces	$q_e = K_F P^{1/n}$	K_F is the Freundlich constant (related to adsorption capacity) and n indicates adsorption intensity	Accounts for surface heterogeneity	Lacks physical basis, less accurate at high pressures	(El Jery et al., 2024; Ng et al., 2017)
BET (Brunauer-Emmett-Teller)	Type II (multilayer)	Physisorption, porous materials (e.g., MOFs, zeolites)	$\frac{P}{q_e(P_0 - P)} = \frac{1}{q_m C} + \frac{(C-1)P}{q_m C P_0}$	P_0 is saturation pressure and C is the BET constant	Captures multilayer adsorption	Overestimates uptake at high $\frac{P}{P_0}$, limited to non-microporous materials	(Mukhtar et al., 2020)
Redlich-Peterson	Hybrid (Langmuir-Freundlich)	Mixed adsorption (chemisorption + physisorption)	$q_e = \frac{K_{RP} P}{1 + \alpha_{RP} P^{\beta}}$	K_{RP}, α_{RP}, and β ($0 < \beta \leq 1$) are constants. At β=1, it reduces to the Langmuir model	Combines Langmuir & Freundlich features	Requires nonlinear fitting, complex parameterization	(Ng et al., 2017; Piccin et al., n.d.)

Temkin	Chemisorption	Strong chemisorption (e.g., amine-functionalized sorbents)	$q_e = \frac{RT}{b_T}\ln(A_T P$	b_T is the Temkin constant, A_T is the equilibrium binding constant, R is the gas constant, and T is temperature	Accounts for adsorbate-adsorbate interactions	Limited to specific systems, less generalizable	(Ng et al., 2017; Piccin et al., n.d.)
Dubinin-Radushkevich (D-R)	Microporous materials	Ultra-microporous materials (e.g., activated carbons)	$q_e = q_m \exp\left(-B\left[\frac{1}{P}\right]^2\right)$	B is related to adsorption energy. It helps determine the mean free energy of adsorption (E), where E < 8 kJ/mol indicates physisorption and E > 8kJ/mol suggests chemisorption	Useful for pore size analysis	Less accurate at low pressures	(Mukhtar et al., 2020; Ng et al., 2017)
Sips (Langmuir-Freundlich)	Hybrid	Heterogeneous surfaces (e.g., modified zeolites)	$q_e = \frac{q_m (K_S P)^{1/}}{1 + (K_S P)^{1}}$	At low pressures, it behaves like Freundlich, and at high pressures, it approaches Langmuir	Combines Langmuir capacity + Freundlich heterogeneity	Empirical, lacks thermodynamic basis	(Ng et al., 2017)
Kisliuk	Kinetics-based	Adsorption with precursor states (e.g., metal surfaces)	$q_e = \frac{K_K P(1+\alpha}{1 + K_K P}$	K_K is the Kisliuk constant and α accounts for adsorbate mobility	Accounts for surface diffusion effects	Complex, rarely used for CO_2 capture	(Kisliuk, 1957)

The Langmuir model is particularly suitable for chemisorption processes, such as those occurring in amine-grafted materials, as it assumes monolayer adsorption on homogeneous surfaces. However, its applicability becomes limited when dealing with multilayer adsorption scenarios. For physisorption in porous materials like MOFs and zeolites, the BET isotherm is commonly employed due to its ability to account for multilayer adsorption, though it faces challenges when analyzing microporous systems. In cases involving heterogeneous surfaces, such as activated carbons, the Freundlich and Sips isotherms are often preferred as they can better describe the energy distribution of adsorption sites. The Dubinin-Radushkevich (D-R) model proves particularly valuable for characterizing ultra-microporous materials where traditional N_2 adsorption analysis falls short, including certain covalent organic polymers. For more complex adsorption systems, such as amine-functionalized sorbents, the Temkin and Redlich-Peterson models offer improved fitting capabilities by accounting for adsorbate-adsorbate interactions and combining features of both Langmuir and Freundlich approaches, though they require more precise parameterization. These models collectively provide researchers with a toolkit to match the appropriate theoretical framework to their specific material characteristics and adsorption mechanisms. The choice of isotherm depends on the specific characteristics of the adsorption system being studied. Table 2.18 presents a comparison of isotherm model fits and their respective constants for CO_2 adsorption using various precursors, based on recent literature.

Table 2.18
Comparison of Isotherm Model Fits and Constants for CO_2 Adsorption Using Various Precursors

Precursor/ Material	Isotherms model	Constant	References
Palm shell activated carbon impregnated with waste egg-white (ACEW-30)	Langmuir	q_m=2.98 mmol/g K_L=2.311 bar^{-1} R^2=0.999	(Mohammed Hatta et al., 2025)
	Freundlich	K_F=2.713 mmol/g. $bar^{-1/n}$ n=2.51 R^2=0.999	(Mohammed Hatta et al., 2025)

	Tempkin	K_T=22.0 mmol/g.bar b=3.87 kJ/mol R^2=0.998	(Mohammed Hatta et al., 2025)
Rubber seed shell AC (blank and ionic liquid functionalized)	Langmuir	q_m=2.59 mmol/g K_L=3.301 bar R^2=0.987	(Fatima et al., 2023)
	Freundlich	K_F=2.187 mmol/g. $bar^{-1/n}$ n=1.68 R^2=0.989	(Fatima et al., 2023)
	Tempkin	K_T=59.87 mol/g.bar b=130.5 J/mol R^2=0.961	(Fatima et al., 2023)
Coconut-shell AC (virgin, NaOH-impregnated)	Langmuir	q_m=5.39 mmol/g K_L=0.027 bar^{-1} R^2=0.99	(Tangsathitkulchai et al., 2021)
	Freundlich	K_F=0.403 mg/g.$bar^{1/n}$ n=1.98 R^2=0.99	(Tangsathitkulchai et al., 2021)
Rice Husk–Derived Activated Carbon (KOH-activated)	Langmuir	q_m=3.13mmol/g at 0 °C (1 bar) R^2=0.9878	(Nandi et al., 2023)
	Freundlich	q_m=2.24 mmol/g at 25 °C (1 bar) R^2=0.9942	(Nandi et al., 2023)

Across these studies, both Langmuir and Freundlich models generally achieved very high correlation with experimental CO_2 data (R^2 =0.99), reflecting good fits. The Freundlich model often provided slightly better fits (e.g. R^2=0.999 in Hatta et al. (Mohammed Hatta et al., 2025)), indicative of heterogeneous adsorption surfaces. The Langmuir fit also remained strong (R^2 around 0.987–0.999) when monolayer assumptions held. In contrast, Temkin fits (where applied) gave high but somewhat lower R^2 values (e.g. 0.961–0.998), yet still useful for probing heat of adsorption (b

parameter). Notably, Freundlich fits tended to outperform Langmuir at low partial pressures, consistent with multilayer/heterogeneous adsorption (Hatta et al. concluded Freundlich was best). Langmuir fits imply a finite capacity; for instance, the coconut AC reached 5.39 mmol/g under 1 bar, illustrating substantial uptake.

The Temkin constants (b=3–6 kJ/mol) reflect moderately exothermic, primarily physisorption binding. In terms of materials, all precursors (palm shell, rubber seed, coconut shell) yielded comparable high-surface-area carbons. The waste-derived egg-white–impregnated carbon (ACEW-30) and rubber seed AC (both functionalized and blank) showed robust CO_2 uptake with similar q_m (2–5 mmol/g range). Freundlich parameters (n>1) indicate favorable adsorption on these carbons. Overall, Freundlich (and related multi-parameter isotherms) consistently gave the best statistical fits for CO_2, suggesting that the adsorbents' heterogeneous pore structures govern adsorption. Langmuir also fit well for many samples (especially at low coverage), while Temkin provided insight into adsorption energetics. The highest R^2 values (0.999) were routinely achieved with Freundlich or combined models, highlighting their utility in describing CO_2 capture performance on these biomass-derived carbons

2.10 Adsorption Kinetics for CO_2 Removal

Adsorption kinetics involves assessing the adsorption uptake over time under constant pressure or concentration, offering insights into the diffusion of adsorbate within pores (Saleh, 2022) . This research aspect provides valuable information on adsorption rate, adsorbent efficiency, and the mechanisms involved in mass transfer. The study of mass transfer kinetics in adsorption encompasses the following steps (Figure 2.8).

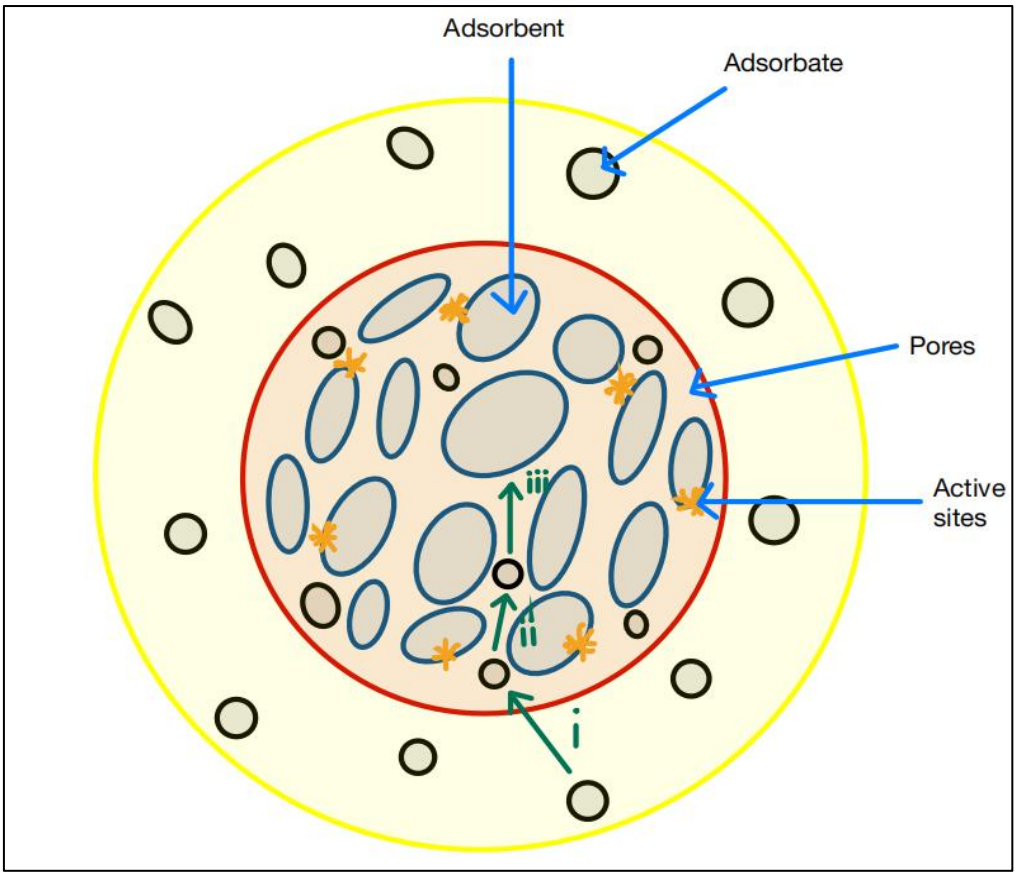

Figure 2.8 The Kinetics of Mass Transfer in Adsorption (Sahoo & Prelot, 2020)

Mass transfer steps	
(i)	External diffusion
(ii)	Internal diffusion
(iii)	Adsorption on active sites

Several commonly used adsorption kinetics models are shown in Table 2.19.

Table 2.19
Kinetic Models for CO_2 Adsorption

Kinetic Model	Equation	Application	Key Parameters	Limitations	References
Pseudo-First Order (PFO)	$\frac{d_{qt}}{d_t} = k1 \quad (q_e - q_t \quad)$	Physisorption-dominated systems (zeolites, ACs)	k_1 (rate constant), q_e	Underestimates initial adsorption rate	(B. Guo et al., 2020; Lalji, Ayubi, Syed, et al., 2024)

Pseudo-Second Order (PSO)	$\frac{d_{qt}}{d_t} = k_2 \quad (q_e - q_t \quad)^2$	Chemisorption (amine-grafted materials)	$k_2, q_e, initial\ rate$ $h = k_2 q_e^2$	Assumes uniform energy sites	(B. Guo et al., 2020; Lalji, Ayubi, Syed, et al., 2024)
Avrami Fractional	$q \quad _t = q_e \quad [1 - e^{-(k_{av}t)^n}]$	Multi-mechanism processes (MOFs, hybrids)	$k_{av}\ (rate\ constant)$, $n\ (order)$	Complex parameter interpretation	(B. Guo et al., 2020; Serna-Guerrero & Sayari, 2010)
Intra-Particle Diffusion (IPD)	$q_t = k_{id} t^{0.5} + C$	Porous materials (MOFs, hierarchical carbons)	$k_{id}(diffusity)$, $C\ (boundary\ layer)$	Requires multi-linear region analysis	(Boonchuay & Worathanakul, 2022; J. Wang & Guo, 2022)
Elovich	$q_t = \frac{1}{\beta} \quad ln(\alpha\beta + 1)$	Heterogeneous surfaces (functionalized sorbents)	$\alpha\ (initial\ rate)$, $\beta\ \left(\frac{activation}{parameter}\right)$	Empirical, no physical meaning of α, β	(B. Guo et al., 2020)
Bangham	$\log(\frac{q_e}{q_e - q_t}$ $= \frac{k_b}{2.303}\log$	Microporous diffusion (zeolites, carbon molecular sieves)	$k_b(porosity\ factor)$	Limited to specific pore structures	(Gor & Bernstein, 2016; Xiaoming et al., 2019)

The kinetics of CO_2 adsorption are fundamental for designing efficient capture systems, with different kinetic models providing insights into the rate-limiting steps and mechanisms. The Pseudo-First Order (PFO) model effectively describes physisorption in materials like zeolites and activated carbons, where surface coverage dominates the process, though it tends to underestimate initial adsorption rates. In contrast, the Pseudo-Second Order (PSO) model better captures chemisorption processes, such as those occurring in amine-functionalized materials, by accounting for electron sharing and covalent bonding kinetics. For porous materials with complex networks, like MOFs, the Intra-Particle Diffusion (IPD) model helps distinguish between surface adsorption and pore diffusion limitations, often revealing multi-stage kinetic behavior.

The Avrami model has gained traction for hybrid adsorbents, where simultaneous physisorption and chemisorption occur, as it accommodates time-dependent rate constants through its fractional order parameter. Meanwhile, the Elovich equation is particularly suited for heterogeneous surfaces, such as nitrogen-doped carbons or defective MOFs, where adsorption energy varies with coverage. The Bangham model offers unique advantages for microporous materials like zeolites and carbon molecular sieves, where pore diffusion controls the adsorption rate. Its logarithmic form effectively describes systems where pore accessibility and size distribution significantly influence kinetics, providing quantitative insights through its porosity factor (k_b).

However, kinetic analysis faces challenges, including the coexistence of multiple rate-limiting steps, oversimplified temperature/pressure dependencies in models, and the frequent neglect of competitive adsorption effects. For comprehensive understanding, researchers increasingly combine multiple kinetic models with advanced characterization techniques like in situ FTIR and breakthrough curve analysis, enabling a more complete picture of adsorption processes from initial surface interactions to saturation. The choice of model ultimately depends on both material properties and specific application conditions, with hybrid approaches often yielding the most accurate predictions for real-world CO_2 capture systems. Table 2.20 summarizes the kinetic models, correlation coefficients (R^2), and corresponding rate constants for CO_2 adsorption using various adsorbents, highlighting the influence of different materials and models on adsorption performance.

Table 2.20
Adsorption Kinetic Parameters and Model Fits for CO_2 Adsorption on Various Materials

Precursor/ Material	Kinetic model applied	R^2 fit	Model Rate Constants	References
Olive mill waste–derived activated carbon	Pseudo-first order (PFO)	0.989	k1: large (KF increases with higher CO_2 concentration)	(Ramos et al., 2025)
0.05 NiO/AC (NiO-impregnated commercial AC)	Pseudo-first order (PFO)	0.938-0.961	k1: 0.0366-0.1196 min^{-1}	(Lahuri et al., 2022)

	Pseudo-second order (PSO)	0.982-0.999	$k2 = 0.0256 - 0.0835\ g.mg^{-1}.min^{-1}$	(Lahuri et al., 2022)
	Intraparticle diffusion	0.759-0.883	$k_{id} = 7.33 - 20.25\ mg.g^{-1}min^{-1/2}$	(Lahuri et al., 2022)
	Elovich	0.934-0.975	$\alpha = 138 - 446\ mg.g^{-1}min^{-1}$ $\beta = 0.0859 - 0.244\ mg.g^{-1}$	(Lahuri et al., 2022)
Rubber-seed shell AC (blank and IL-functionalized)	Pseudo-second order (PSO)	0.998-1.000 (best fit)	$k_2(blank\ AC) = 9.84\ g.min.cm^{-3}$ (25℃), 21.91 ($k_2(IL-AC) = 7.36$ (25℃), 5.23 (40℃)	(Fatima et al., 2023)
CaO-Impregnated Activated Carbon Filter	Pseudo-first order (PFO)	0.7827 - 0.8884	k1: 0.011 – 0.0324 min^{-1}	(Shiue et al., 2017)
	Pseudo-second order (PSO)	0.921 – 0.9806	k2: 0.0777 – 0.4141 . $g^{-1}.min^{-1}$	(Shiue et al., 2017)
	Intra-particle diffusion	0.9771 – 0.9975	ki: 0.2657 – 0.7353 g.$min^{-1/2}$	(Shiue et al., 2017)

Table 2.20 shows that pseudo-second order (PSO) kinetics generally gave the best fits (R^2≈0.98–1.00) for chemisorptive adsorbents, whereas pseudo-first order (PFO) or diffusion models dominated for mainly physisorptive systems. For example, the olive-waste carbon (primarily physical adsorption) was well described by the PFO model (R^2>0.989), consistent with weak CO_2 interactions. In contrast, NiO-impregnated AC (basic sites promoting chemisorption) and IL-functionalized rubber AC required the PSO model (R^2≈0.98–0.999), indicating strong adsorbate–surface binding (e.g. Lahuri et al. report a high activation energy for NiO/AC. Overall, chemisorption-prone materials (amine, metal or IL functionalized) favored PSO fits, while purely physical sorbents often matched PFO or diffusion models. High R^2 values (close to 1) for PSO indicate the dominant mechanism: strong surface binding for PSO and pore diffusion for Bangham. These trends imply that surface chemistry

dictates whether kinetics are reaction-limited (chemisorptive) or transport-limited (physisorptive).

2.11 Thermodynamics for CO_2 Removal

Adsorption processes for CO_2 removal, especially from gas streams like flue gases or natural gases, often involve a detailed consideration of thermodynamics. The adsorption behavior of a substance can be described using thermodynamic parameters, including ΔG (Gibbs free energy change), which can be computed using Equation (2.1) (Piccin et al., n.d.).

$$\Delta G = - RT \ln K_D \tag{2.1}$$

K_D can be obtained by plotting $\frac{q_e}{C_e}$ versus q_e and extrapolating q_e to zero (El Jery et al., 2024) . In accordance with thermodynamics, the Gibbs free energy is expressed as the difference between the adsorption enthalpy (ΔH) and adsorption entropy (ΔS), each multiplied by the temperature. Utilizing this principle, the thermochemical parameters ΔH and ΔS can be ascertained through van't Hoff's plot, as outlined in Equation (2.2).

$$\ln K_D = - \frac{\Delta H}{RT} + \frac{\Delta S}{R} \tag{2.2}$$

Where K_D: thermodynamics equilibrium constant $(L\, g^{-1})$, R: universal gas constant $(8.314\, J\, K^{-1} mol^{-1})$, and T: temperature (K)

Thermodynamics provides a framework for understanding the energy changes, spontaneity, and feasibility of CO_2 adsorption onto solid surfaces. Some key aspects of thermodynamics for CO_2 removal are as shown in Table 2.21.

Table 2.21
Thermodynamic Parameters on Various Adsorbents

Adsorbent Material	Temperature (°C)	ΔH° (kJ/mol)	ΔS° (J/mol·K)	ΔG° (kJ/mol)	Reference
Zeolite-Y-Templated Carbon	30	−4.79	−13.96	−0.56	(Gunawan et al., 2018)
	40	−4.79	−13.96	−0.42	
	50	−4.79	−13.96	−0.28	
Activated Carbon	25	−3.57	30	−5.37	(Almoneef et al., 2021)
	30	−3.57	30	−5.73	
	45	−3.57	30	−6.03	
Functionalized Granular Activated Carbon (GAC-10-500)	25	−17.97	−35	−7.67	(Mashhadimoslem et al., 2022)
	35	−17.97	−35	−7.33	
	45	−17.97	−35	−6.98	
	55	−17.97	−35	−6.64	
Zeolite 13X	25	−11.27	17.57	−16.52	(Hauchhum & Mahanta, 2014)
Zeolite 4A	25	−12.85	−18.50	−7.33	(Hauchhum & Mahanta, 2014)

The thermodynamic equilibrium coefficients obtained at various temperatures and concentrations were utilized to assess adsorption thermodynamics, aiming to confirm potential adsorption mechanisms. A negative enthalpy change (ΔH°) indicates that the adsorption is exothermic, meaning that heat is released during the process. This is typically favorable for adsorption at lower temperatures. Additionally, the magnitude of ΔH° can be used to infer the adsorption mechanism: values less than 20 kJ/mol generally suggest physisorption (weak van der Waals forces), whereas higher values may point to chemisorption, involving stronger chemical bonding between CO_2 molecules and the adsorbent surface.

Negative Gibbs free energy change (ΔG°) values across the tested temperatures indicate that the adsorption process is spontaneous. Furthermore, the entropy change (ΔS°) reflects the degree of randomness at the solid-gas interface. A negative ΔS° implies a decrease in entropy, which typically occurs when gas molecules are confined onto the adsorbent surface, resulting in a more ordered system.

From Table 2.21, Zeolite-Y-templated carbon exhibits negative ΔG° values at all tested temperatures (−0.56 to −0.28 kJ/mol), confirming the spontaneity of CO_2 adsorption. Its ΔH° value of −4.79 kJ/mol indicates a physisorption-dominated process, consistent with weak van der Waals interactions, while the negative ΔS° (−13.96 J/mol·K) suggests decreased molecular randomness upon adsorption, typical

of ordered multilayer formation on porous surfaces. Similarly, activated carbon shows higher spontaneity (ΔG° down to −5.73 kJ/mol) and a positive ΔS° (+30 J/mol·K), implying increased disorder at the interface, potentially due to pore structure heterogeneity and the presence of surface functional groups facilitating CO_2 mobility within the pores. These findings align with previous studies showing that microporous and mesoporous carbonaceous materials combine spontaneous adsorption with textural features that influence entropy change direction and magnitude.

Overall, these thermodynamic indicators help assess both the spontaneity and the adsorption nature of CO_2 capture systems (El Jery et al., 2024) . In summary, thermodynamics plays a pivotal role in optimizing and understanding CO_2 adsorption processes. It provides insights into the energy changes, spontaneity, and efficiency of the adsorption system, aiding in the design and implementation of effective CO_2 removal technologies.

2.12 Summary on Novelty of the Study

Although CQDs have been explored extensively for sensing, imaging, and catalytic applications (*CQDs (Carbon Quantum Dots) with High Fluorescence Characteristic as Well as Preparation and Application of CQDs*, 2018a; Meng et al., 2019) , their use as CO_2 adsorbents remains largely underexplored, especially regarding long-term stability and practical handling. Existing studies rarely address the inherent limitations of CQDs such as agglomeration, moisture sensitivity, and structural instability which severely restrict their standalone adsorption performance (Dua et al., 2023; R. Miao et al., 2017) . This study introduces a novel approach by immobilizing N/S/O-doped CQDs within a xerogel matrix, creating a stable hybrid adsorbent that preserves active functional sites, enhances dispersion, and improves CO_2 affinity. Unlike conventional supports such as silica, activated carbon, or synthetic polymers, the xerogel offers a low-cost, biocompatible, and easily formable support that minimizes CQD aggregation while enabling controlled heteroatom doping. By integrating heteroatom engineering, xerogel stabilization, and detailed adsorption behaviour analysis (isotherms, kinetics, thermodynamics), this work provides a unique and comprehensive strategy that has not been previously reported, demonstrating a promising, waste-derived adsorbent with competitive CO_2 uptake compared to commercial materials.

CHAPTER 3
RESEARCH METHODOLOGY

3.1 Introduction

This chapter outlines the methodology in synthesizing and evaluate N/S/O-doped carbon quantum dots immobilized in xerogel (N/S/O-CCQD-X) for CO_2 removal. This research is divided into four (4) main phases. The first phase is chitosan extraction from shrimp shells, followed by synthesizing the CQDs prior to its immobilization into xerogel structure. Then, in the second phase, the best N/S/O-CCQD-X adsorbent was evaluated using different doping ratio of chitosan: thiourea: KOH. Various analytical techniques, including FTIR, BET, FESEM-EDX, and TGA, are employed to characterize the synthesized N/S/O-CCQD-X adsorbent. In the third phase OFAT approach was used to study the effect of different adsorption process parameters on CO_2 removal. Finally, in the fourth phase, the adsorption behavior of CO_2 was evaluated using isotherm, kinetic, and thermodynamic models.

3.2 Materials and Chemicals

Table 3.1 shows the list of chemicals that are used for extraction of chitosan from shrimp shells and synthesis of CQDs using hydrothermal treatment and CO_2 adsorption experiment.

Table 3.1
List of Materials and Chemicals

Materials/Chemicals/Gas	Purity	Supplier	Function
Shrimp shells	NA-	Nicole Cottage	Chitosan precursor
Hydrochloric acid (HCl)	37%	Merck	Demineralization
Sodium hydroxide (NaOH)	98%	Merck	Deproteinization, deacetylation
Ethanol (C_2H_5OH)	96%	Merck	Decolorization, defatting
Thiourea (CH_4N_2S)	99%	Sigma Aldrich	Doping agent (N/S source)
Potassium hydroxide	85%	Merck	Doping agent (O

(KOH)			functionalization)
Carbon dioxide (CO_2)	10% balanced in N_2	Alpha Gas Solution Sdn. Bhd.	CO_2 Adsorption
Nitrogen (N_2)	99.99	Alpha Gas Solution Sdn. Bhd.	CO_2 Adsorption
Glass wool	NA	NA	Adsorbent support
Sodium alginate $(C_6H_7NaO_6)n$	NA	R&M Chemicals	Xerogel matrix formation
Calcium carbonate ($CaCO_3$)	NA	R&M Chemicals	Xerogel crosslinking agent
Glucono delta-lactone (GDL)	NA	DChemie	Xerogel crosslinking

3.3 Equipment

A range of analytical instruments and experimental tools were used to support the synthesis, characterization, and CO_2 adsorption evaluation in this study. These instruments enabled the assessment of structural, chemical, and adsorption properties of the N/S/O-CCQD-X adsorbents with high accuracy and reliability. Table 3.2 summarizes the equipment, their functions, and their availability.

Table 3.2
List of Equipment

Instruments	**Brand/ Model**	**Function**	**Availability**
Universal Oven	Memmert UNE200	Drying samples	Own by school
Biogas Analyzer	MRU Optima 7	Measure the composition of biogas and other combustion processes, including methane, carbon dioxide, oxygen, and hydrogen sulfide	Own by school
Freeze-dryer	Labconco	Remove moisture from substances by freezing them and then subjecting them to a vacuum, allowing the frozen water to sublimate and leave the material in a dehydrated state.	School of Chemical Engineering, USM
UV-vis Spectrophotometer	Shimadzu UV-1900i	Measurement and analysis of the absorbance properties of CQDs samples	Own by school
Custom continuous fixed bed adsorption rig	-	To conduct CO_2 adsorption experiment using N/S/O-CCQD-X adsorbent	Own by school

Fourier Transform Infrared Spectrum (FTIR)	Thermo Scientific Nicolet iS10	Identify chemical bonds and functional groups present within the adsrobents by analyzing its molecular vibrations	School of Chemical Engineering, USM
N_2 sorption-desorption analysis	ASAP 2020 micromeritics	Determine the surface area and pore size distribution of the adsorbents	Own by school
CHNS/O elemental analyzer	Perkin Elmer	Determines the percentage of Carbon (C), Hydrogen (H), Nitrogen (N), Sulfur (S) and Oxygen (O) present in the adsorbents.	SERC, USM
Field Emission Scanning Electron Microscopy with Energy Dispersive X-Ray Spectroscopy (FESEM-EDX)	Nova Nanosem 450	FESEM provides high-resolution imaging of a material's surface morphology, while EDX determines the elemental composition found within the material's surface.	School of Physics, USM
Thermal Gravimetry Analysis (TGA)	SDT Q600	Measures changes in a material's weight as a function of temperature or time, providing information on its thermal stability and composition.	Own by school
High Resolution Transmission Electron microscope (HRTEM)	Twin S, Tecnai, FEI	Determination of the morphology and microscopic structure of N/S/O-CCQD-X adsorbent (size less than 10nm) with high resolution image	SERC, USM
Fluorescence Spectrophotometer (FS)	Cary Eclipse	Measure the fluorescence emission intensity and spectra of the N/S/O-CCQD-X	INFORMM, USM
X-ray Photoelectron Spectroscopy (XPS)	DLD Ultra XPS, Kratos	Analyzes the surface chemistry of a material, providing information about its elemental composition, chemical states, and electronic structure	SERC, USM

3.4 Overall Flow Chart

Figure 3.1 illustrates the overall workflow of this study, outlining the sequential processes involved from the synthesis of N/S/O-doped CQDs and xerogel immobilization, to characterization, adsorption performance evaluation, and adsorption behavior analysis.

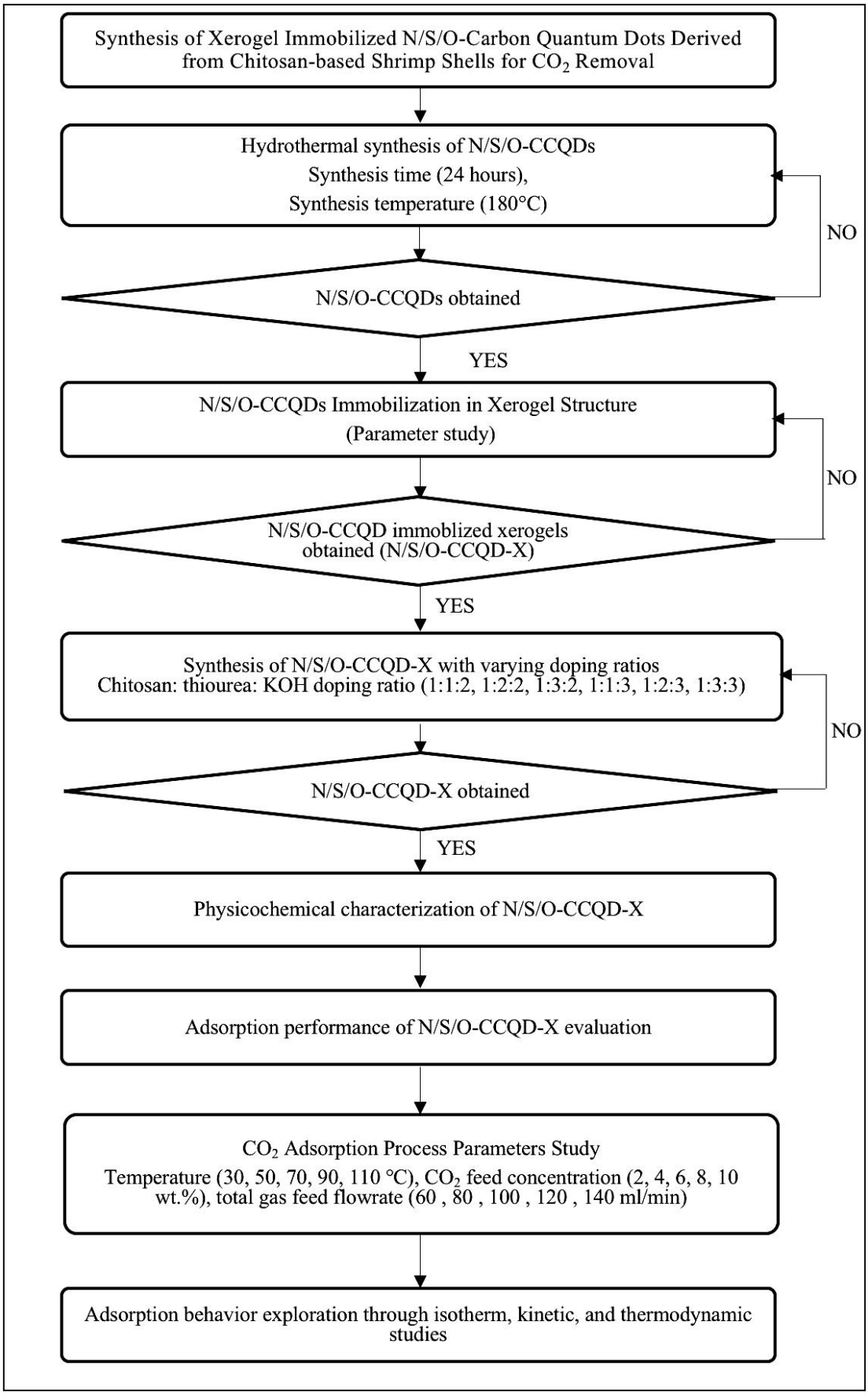

Figure 3.1 Overall Flow Chart of Research Work

3.5 Extraction of Chitosan from Shrimp Shells Waste (CSS)

Chitosan was extracted from shrimp shells waste through a traditional chemical extraction method, including demineralization, deproteination, and deacetylation processes following the method reported by Tong et al. (Tong et al., 2021). The air-dried shrimp shells were first thoroughly cleaned for 3 hours in boiling water to remove any remaining blood, flesh, or impurities. Before being processed into an 80-mesh powder, the shrimp shells were allowed to air dry for 24 hours at 70°C in a universal oven (Memmert UNE200). To achieve demineralization, 100 g of shrimp shells were mixed with 1 L of 1 M HCl. At room temperature, the reaction was constantly agitated for 6 hours at a speed of 250 rpm. The shells were first demineralized, followed by filtration and thorough washing with distilled water until a neutral pH was achieved. After 10 minutes of immersion in ethanol for decolorization and defatting process, the samples were dried in a universal oven at 70°C for 24 hours.

The dried demineralized shells were mixed with 1 M NaOH at a solid-to-liquid ratio of 1g:10mL to undergo deproteination. The mixture was agitated at 80 °C for 3 hours to complete the reaction. The solid was filtered and washed with distilled water until a neutral pH was achieved. The resulting chitin was then immersed in ethanol for 10 minutes and subsequently dried in a universal oven at 70°C for 24 hours. Chitin was deacetylated by reacting 1g solid with 15mL of 12.5 M NaOH. The mixture was first chilled and stored in a freezer at -83°C for 24 hours. It was then heated to 115 °C and agitated at 250 rpm for 4 hours to complete the deacetylation process. After filtration and neutralization with distilled water, the resulting chitosan was dried at 70 °C for 24 hours (Hosney et al., 2022; Janus et al., 2019a; Tong et al., 2021).

3.6 Synthesis of N/S/O-CQD-X Adsorbent

The synthesis of N/S/O-CQD-X involves two main steps, (1) hydrothermal synthesis of N/S/O-CCQDs, followed by (2) immobilization of N/S/O-CCQDs into a xerogel matrix via a sol-gel process to enhance structural stability and adsorption performance.

3.6.1 Synthesis of N/S/O-CCQDs using Hydrothermal Treatment

To produce ternary N/S/O-CCQDs, hydrothermal treatment was applied to the extracted chitosan-based shrimp shells. The chitosan-based shrimp shell powder was thoroughly ground with heteroatom (N, S, O) doping agents, thiourea (N/S source) and KOH (O source and activating agent) at a weight ratio of chitosan:thiourea:KOH (1:1:3) to create the heteroatoms-doped CQDs (Prado et al., 2023; Stachurski et al., 2020) . After dissolving the mixture powder in 100 mL of deionized (DI) water and stirring for 30 minutes, the powder was transferred to a 200 mL Teflon container that was sealed within a stainless-steel autoclave. The mixture is hydrothermally treated for 24 hours at 180°C in an electric oven (Memmert UNE200) (Ababneh & Hameed, 2021) before being cooled to room temperature. Centrifugation (HETTICH EBA 280 model) was used to separate the suspension and hydrochar from the products for 20 minutes at 2000 rpm. The yellow suspension was then filtered via a 0.22 μm filter membrane to obtain conventional CQDs.

3.6.2 N/S/O-CCQDs Immobilization in Xerogel Structure

After the hydrothermal synthesis of N/S/O-CCQDs, the samples are embedded in a xerogel through a sol-gel process, which involves three key stages: sol-gel formation, gel aging, and gel drying. A parameter study was conducted to assess the material properties of CQDs-immobilized xerogels prepared with four (4) different CQD-to-solution ratios: CQD-X 1:1, CQD-X 1:10, CQD-X 1:50, and FD CQD-X 1:50. Table 3.3 summarizes the preparation methods and corresponding abbreviations used for all N/S/O-CCQD-X samples synthesized in the study.

Table 3.3
Preparation Methods and Abbreviations of N/S/O-CCQD-X Samples

CCQDs phase	Sample abbreviation	Preparation method
Aqueous suspensions	CQD-X 1:50	Prepared using 2 mL of CCQDs suspension in a total of 100 mL solution
Aqueous suspensions	CQD-X 1:10	Prepared using 10 mL of CCQDs suspension in a total of 100 mL solution
Aqueous suspensions	CQD-X 1:1	Prepared using 100 mL of CCQDs suspension with no added distilled water

Freeze-dried sample	FD CQD-X 1:50	Prepared using 2 g of freeze-dried CCQDs in a total of 100 mL solution

To begin, 1 g of sodium alginate is completely dissolved in 2 mL of CCQD suspension and 90 mL of distilled water, creating an alginate solution. This solution is prepared 24 hours before sample preparation. Next, 0.2 g of calcium carbonate (CaCO3) powder is added to the alginate solution. The mixture is vigorously stirred at 450 rpm on a hot plate, leading to the formation of a colloidal suspension (sol) through hydrolysis and condensation processes. This sol is then converted into a gel via cross-linking of the calcium carbonate through polymerization.

Once the alginate/$CaCO_3$ mixture becomes homogeneous, 0.3 g of glucono delta-lactone (GDL) is added to initiate the ionization of $CaCO_3$. GDL hydrolyzes into gluconic acid, dissolving the calcium carbonate and alginate particles, which in turn releases calcium ions (Ca^+). These Ca^+ ions cross-link with the alginate polymers, resulting in gel formation. Calcium carbonate was chosen due to its water-insoluble properties, which help control the cross-linking process. To ensure complete polymerization and stable gel formation, the gel undergoes an aging process, where it was kept at ambient temperature for several hours to days, depending on the required stability. Once the gel has aged and stabilized, it is poured into silicone molds to achieve the desired size. The final xerogel is then obtained by drying the gel in an oven at 80°C for 24 hours (Noraini et al., 2022) . The synthesized adsorbent was subsequently tested for CO_2 sorption performance, as detailed in section 3.9.

3.7 Varying Doping Ratios of N/S/O-CCQD-X

Based on the findings from objective 1, the best-performing CCQDs-immobilized xerogel formulation was selected as the standard preparation condition for the next phase (objective 2). In this step, the CCQDs samples synthesized via hydrothermal treatment with varying chitosan:thiourea:KOH doping ratios (1:1:3, 1:2:3, 1:3:3, 1:1:2, 1:2:2, and 1:3:2) were immobilized into xerogels to improve their structural stability and adsorption performance. Following the xerogel preparation step, the synthesized samples are named based on their weight ratios of chitosan, thiourea, and KOH: CQD-X 112, CQD-X 122, CQD-X 132, CQD-X 113, CQD-X 123, and CQD-X 133 (H. Cui et al., 2022; Pełech et al., 2022; J. Singh et al., 2019) . CO_2

sorption experiments were conducted on the synthesized adsorbent, as per the experimental methodology described in Section 3.9.

3.8 Physical Characterization of N/S/O-CCQD-X Adsorbent

In this phase, Thermal Gravimetric Analysis (TGA) assessed the thermal stability and composition of the material through weight loss analysis, while Brunauer-Emmett-Teller (BET) analysis evaluated the surface area and porosity of the adsorbent, key properties influencing adsorption performance. Field Emission Scanning Electron Microscopy with Energy Dispersive X-Ray Spectroscopy (FESEM-EDX) revealed the surface morphology and elemental composition, and High-Resolution Transmission Electron Microscopy (HRTEM) elucidated the nanoscale structural features and particle distribution. Additionally, a fluorescence spectrophotometer characterized the optical properties and fluorescence intensity of the synthesized N/S/O-CCQD-X adsorbent.

3.8.1 Thermal Gravimetry Analysis (TGA)

TGA measured changes in the material's weight as a function of temperature or time, providing critical data on its thermal stability and composition. The sample was heated at a controlled rate (10°C/min) in an inert or oxidative atmosphere, while its weight change was monitored during decomposition, oxidation, or evaporation. A small sample was placed in the TGA furnace, where the temperature was gradually increased under a controlled atmosphere (e.g., nitrogen or air). The recorded weight loss was plotted against temperature or time, revealing key characteristics such as thermal stability, moisture content, and fixed carbon content.

In this study, TGA was performed using a TA Instruments SDT Q600 thermal analyzer under conditions consistent with established literature protocols. The instrument measured weight changes as the sample was heated from ambient temperature up to 1500°C under a controlled inert atmosphere (nitrogen), while simultaneously recording Differential Scanning Calorimetry (DSC) heat flow data (*Thermogravimetric Analysis/Differential Scanning Calorimeter | MATFab Facility - The University of Iowa*, n.d.)

3.8.2 N_2 Sorption-Desorption Analysis

N_2 sorption–desorption analysis was performed using a Micromeritics ASAP 2020 instrument to evaluate the surface area and porosity, which were critical for CO_2 adsorption performance. The procedure began with degassing the sample under vacuum and heating to remove moisture and contaminants. The sample was then cooled to liquid nitrogen temperature (77 K), and nitrogen gas was incrementally introduced to build an adsorption isotherm. From this data, the BET equation was applied to calculate the specific surface area, while pore size distribution and total pore volume were determined using BJH or DFT models (Surface Area and Porosity Analysis Micromeritics ASAP 2020: Physisorption User Notes Micromeritics ASAP 2020: Physisorption User Notes, n.d.).

The ASAP 2020 instrument was designed for accurate and high-resolution measurements. It featured a two-station degas system, independent vacuum lines, and an isothermal jacket for temperature stability, all essential for precise physisorption characterization. The system supported a wide range of pore types, from micropores (0.35–2 nm) to mesopores (2–50 nm), making it well-suited for nanomaterials like CQD xerogels (*ASAP 2020 Plus - Micromeritics*, n.d.).

3.8.3 Field Emission Scanning Electron Microscopy with Energy Dispersive X-Ray Spectroscopy (FESEM-EDX)

Field Emission Scanning Electron Microscopy (FESEM) with Energy Dispersive X-Ray Spectroscopy (EDX) was conducted using a Schottky emitter FEI Nova NanoSEM 450. This system provided ultra-high resolution (down to about 1.4 nm at 1 kV) and included a retractable backscattered detector and an SDD-EDX detector for rapid elemental analysis (*Nanosem Scanning Electron Microscope — Departement Materiaalkunde*, n.d.). The Nova NanoSEM 450 demonstrated excellent performance in imaging both conductive and non-conductive samples under low-vacuum or high-vacuum modes, enabling detailed surface morphology and compositional mapping at the microscale (*FEI Nova NanoSEM | Electron Nanoscopy Instrumentation Facility | Nebraska*, n.d.) . During FESEM analysis, a focused electron beam was emitted to scan the sample surface, producing secondary and backscattered electrons that generated high-resolution images. EDX simultaneously

detected the X-rays emitted when the electron beam excited atoms in the sample, providing elemental composition data. Prior to analysis, the sample was mounted on a conductive substrate and coated with a thin layer of gold or carbon (for non-conductive samples). The FESEM system successfully scanned the sample while EDX concurrently mapped the elemental distribution.

3.8.4 High Resolution Transmission Electron microscope (HRTEM)

HRTEM was employed to examine atomic arrangements and lattice structures within the materials. The technique operated on the principle of electron wave interference, where electrons passing through the sample interacted with atomic planes to generate high-resolution images revealing lattice fringes and crystal structures. For analysis, an ultrathin sample was prepared and positioned in the electron beam path. HRTEM imaging required precise alignment and higher energy to resolve lattice spacings down to 0.1 nm, enabling clear visualization of crystalline features.

HRTEM using the FEI Tecnai G2 F20 S-TWIN (Twin S) instrument offers powerful insight into the atomic-scale structure of materials. Operating with a high-tension field emission gun at 200 kV and utilizing a symmetric S-TWIN lens, this microscope delivers superb resolution with point-to-point detail down to 0.19 nm and information limits near 0.15 nm–allowing researchers to visualize lattice fringes and crystalline defects with clarity (*Tecnai F20 TEM/STEM/AEM - BYU Electron Microscopy Facility*, n.d.).

3.8.5 Fluorescence spectrophotometer

The Cary Eclipse Fluorescence Spectrophotometer was used to measure the fluorescence emission of materials, enabling detailed analysis of their optical properties, including quantum yield. The fluorescence quantum yield (Φ) quantifies a material's light emission efficiency, with 100% being theoretically ideal but unachievable due to non-radiative losses. The Cary Eclipse was widely used in characterizing CQDs due to its high sensitivity, rapid scanning capability, and accurate quantification of fluorescence performance.

A light source (e.g., UV or visible) excites the sample at a specific wavelength, causing it to emit light at a longer wavelength. The emitted fluorescence intensity was detected and recorded. This study used quinine sulfate (Φ=0.54 in 0.1M H_2SO_4) as a reference standard to measure the quantum yield of chitosan-derived CQDs (CCQDs) (Daniel, 2022). The sample was prepared in a liquid or solid form, and its excitation and emission spectra were measured using the spectrophotometer. By comparing the fluorescence intensity to a standard (e.g., quinine sulfate), the quantum yield of the material can be calculated.

Typically, a 100 mg/L quinine sulphate solution was prepared to avoid fluorescence quenching at higher concentrations while ensuring a strong fluorescence signal. This standard solution was then diluted to create concentrations of 0.1 mg/L, 0.2 mg/L, 0.3 mg/L, and 0.4 mg/L for accurate fluorescence measurements (Ghobashy, 2021) . Samples and standards were uniformly diluted in 0.1M H_2SO_4 to ensure comparable measurements. UV-Vis spectroscopy identified 240 nm as the optimal excitation wavelength. Fluorescence spectra were recorded and analyzed using Origin software to calculate integrated emission intensity. Quantum yields were determined by comparing sample and standard absorbance-fluorescence plots using the Equation (3.1). The calibration curves of the standard solution and the CCQDs sample used for quantum yield calculations are provided in the Appendix for reference.

Fluorescence Quantum Yield, φ_x:

$$= \frac{Slope\ Sample}{Slope\ Standard} \times Quantum\ Yield\ Standard, \varphi_{std} \quad (3.1)$$

Where standard: the reference compound (Quinine sulphate dissolved in 0.1 M H_2SO_4)

φstd: 0.54 (reference) (Daniel, 2022; Janus et al., 2019b)

This method enabled systematic comparison of CCQDs with different doping ratios (chitosan:thiourea:KOH), revealing their fluorescence efficiencies for potential sensing or imaging applications. The standardized approach minimized experimental variability while providing reliable quantum yield measurements (Hammi et al., 2020).

3.9 Chemical Characterization of N/S/O-CCQD-X Adsorbent

In this phase, the Fourier Transform Infrared Spectroscopy (FTIR) was used to identify the chemical composition and functional groups present in the adsorbent. CHNS/O elemental analyzer determined the percentages of carbon, hydrogen, nitrogen, sulfur, and oxygen. Finally, X-ray Photoelectron Spectroscopy (XPS) offered detailed information on the surface chemistry, elemental states, and bonding configurations of the doped CCQDs.

3.9.1 Fourier Transform Infrared Spectroscopy (FTIR)

FTIR model Thermo Scientific Nicolet iS10 was used to identify chemical bonds, and functional groups present in a material by analyzing its molecular vibrations. The FTIR technique works by passing infrared light through a sample, where different molecular bonds absorb specific wavelengths of infrared light, resulting in characteristic absorption spectra. This absorption corresponds to the vibrational modes of chemical bonds. To perform FTIR analysis, the sample (solid, liquid, or gas) was prepared as a thin film, pressed into KBr pellets (for solids), or analyzed in its natural state. The spectrum was obtained over a range of wavelengths (4000–400 cm^{-1}), and the peaks observed were matched to known functional groups for identification (*Nicolet IS10 FT-IR - Specification Sheet - Thermo Fisher Scientific*, n.d.).

3.9.2 CHNS/O elemental analyzer

A PerkinElmer 2400 Series II elemental analyzer was employed to determine the percentages of carbon (C), hydrogen (H), nitrogen (N), sulfur (S), and oxygen (O) in the material, which were essential for understanding its elemental composition. In this method, a small, precisely weighed sample (typically 1–15 mg) was combusted in a high-temperature (≈980–2000 °C) oxygen-rich environment, converting the elements into gaseous forms such as CO_2, H_2O, NO_x, and SO_2. These gases were then separated and quantified using thermal conductivity detectors or infrared sensors. The sample was placed in a combustion chamber, where it underwent complete combustion. The resulting gases were analyzed, and the elemental percentages were

calculated based on their composition (*ORGANIC ELEMENTAL ANALYZER (CHNS/O) - Central Research Laboratory Application and Research Center | Eskisehir Osmangazi University*, n.d.).

3.9.3 X-ray Photoelectron Spectroscopy (XPS)

The Kratos Axis Ultra DLD XPS provided information on the elemental composition, chemical states, and electronic properties of the material's surface within the top 2-10 nm. In this technique, the material's surface was irradiated with X-rays, which ejected core electrons from atoms. The energy of these emitted electrons was analyzed to determine both the elemental identity and chemical state of surface species. For analysis, the sample was mounted in a high-vacuum chamber and irradiated with a monochromatic Al-Kα X-ray beam. The resulting photoelectrons were collected and analyzed by a hemispherical electron energy analyzer. Characteristic photoelectron peaks were obtained, corresponding to specific elements and their chemical states, which were subsequently interpreted to determine surface chemistry (*Kratos X-Ray Photoelectron Spectrometer - Axis Ultra DLD*, n.d.; Stockmann et al., 2020).

3.10 CO_2 Removal using Continuous Fixed Bed Adsorption Setup

3.10.1 CO_2 Adsorption Pilot Plant Setup

To evaluate the CO_2 capture performance of the synthesized N/S/O-CCQD-X, a pilot-scale fixed-bed adsorption system was designed and constructed. This custom-built pilot plant simulates industrial adsorption conditions in a controlled laboratory environment, allowing for the systematic investigation of key operational parameters such as temperature, flow rate, and gas composition. The rig integrates essential components such as a stainless-steel adsorption column, flow regulation units, and real-time gas analysis instrumentation to measure breakthrough curves and quantify adsorption capacity. Figure 3.2 illustrates the schematic representation of the current adsorption pilot plant.

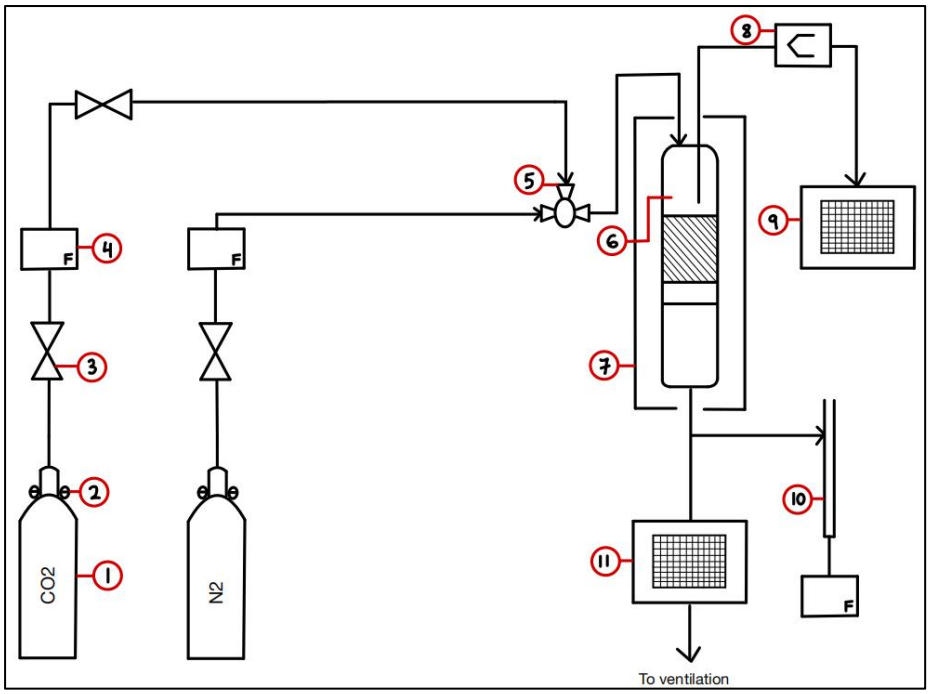

Figure 3.2 Schematic diagram of existing adsorption pilot plant

The CO_2 rig setup, as depicted in Figure 3.2, consisted of an integrated system of components designed for gas adsorption experiments. The system began with a gas cylinder (1) containing CO_2, whose pressure was regulated by a pressure regulator (2) to maintain consistent gas delivery. A control valve (3) adjusted the gas flow, which was precisely measured and controlled by a mass flow controller (4). The gas stream was directed through a 3-way valve (5) for flexible flow path selection. The central component was a stainless-steel adsorption column (6) where the CO_2 capture process occurred. The column was fitted with a heating jacket (7) for temperature control and a k-type thermocouple (8) for continuous temperature monitoring. A digital display unit (9) provided real-time temperature readings throughout the experiments. Following the adsorption column, the effluent gas flow rate was measured using a bubble soap flow meter (10). Finally, the gas composition was analyzed by an online gas analyzer (11) to evaluate adsorption performance. This experimental setup enabled precise control and monitoring of all critical parameters including gas flow rates, adsorption temperatures, and outlet gas compositions, making it ideal for rigorous adsorption studies.

3.10.2 CO_2 Adsorption Experiment

The performance of the N/S/O-CCQDs adsorbents was tested using a custom-designed CO_2 adsorption rig, as illustrated in Figure 3.2. A total of 0.5 g of the synthesized N/S/O-CCQD-X adsorbent was weighed and placed at the center of a stainless-steel fixed-bed column (250 mm length, 9.525 mm diameter), supported at both ends with 0.3 g of borosilicate glass wool. During the experiment, a controlled flow of a CO_2-containing gas mixture (simulated flue gas) was passed through the column at varying flow rates under ambient temperature conditions. The gas composition was regulated using a calibrated mass flow controller (Aalborg) (Kasikamphaiboon & Khunjan, 2018) . The inlet and outlet concentrations of CO_2 were continuously monitored using a portable gas analyzer (MRU Optima 7) equipped with an electrochemical sensor specific for CO_2. Data were recorded every 10 seconds, and the experiment was terminated once breakthrough occurred, defined by the outlet concentration reaching the inlet concentration (Ci/Co = 1.0). The adsorption capacity formula used in the breakthrough analysis comes from the fixed-bed breakthrough quantification approach, where the capacity is calculated from the volumetric flow, time, feed concentration, and mass of adsorbent. The adsorption capacity of the N/S/O-CCQD-X was then calculated using Equation (3.2) and Equation (3.3) (Fernandez et al., 2023) . An actual photograph of the experimental rig setup is provided in the Appendix.

$$q = \frac{Q_f t_t y_f}{m_c} \tag{3.2}$$

$$q_i = 1 - \frac{C_i}{C_0}\left(\frac{Q_F t_b y}{m_s}.\rho_{mix}\right) \tag{3.3}$$

Where;

q: adsorption capacity of fresh adsorbent $\left(\frac{mg}{g}\right)$

Q_f: volumetric feed flow rate $\left(\frac{ml}{min}\right)$

y_f: mole fraction of the adsorbate

t_t: breakthrough time (minute)

m_c: mass of adsorbent (g)

In this study, the fixed-bed adsorption rig was primarily employed to achieve objective 1 and objective 2, which involved evaluating the CO_2 adsorption performance of the synthesized N/S/O-CCQD-X and identifying the most effective synthesis ratio. Objective 1 focused on assessing the stabilizing effect of immobilizing CCQDs in a xerogel matrix, while objective 2 examined how varying the doping ratios influenced the adsorption capacity. Through breakthrough experiments conducted using this setup, adsorption parameters such as breakthrough time, total adsorption capacity, and saturation behavior were quantified across different N/S/O-CCQD-X formulations. These insights enabled a direct comparison of each adsorbent's performance under consistent operating conditions, allowing for the identification of the most efficient material (CQD-X 133) for subsequent parametric studies.

3.10.3 CO_2 Adsorption Process Parameters Study

The third objective focused on systematically evaluating the influence of CO_2 adsorption process parameters; adsorption temperature, CO_2 feed concentration, and total feed gas flow rate on the CO_2 adsorption performance using N/S/O-CCQD-X adsorbents. The column temperature was varied at 30, 50, 70, 90, 110 ℃ (Akpasi & Isa, 2022; Balogun et al., 2021; Suba et al., 2024), CO2 feed concentration was varied at 2, 4, 6, 8, 10 wt.% (Ling et al., 2015; Rahmawati et al., 2019), and the total gas feed flowrate was varied at 60 , 80 , 100 , 120 , and 140 ml/min (Rahmawati et al., 2019) accordingly. The variation of adsorption process parameters is following one factor at a time (OFAT) approach. The OFAT approach used in this study facilitates the isolation of individual parameter effects on performance metrics such as total capacity, breakthrough time, and breakthrough capacity.

The selected temperature range of 30–110 °C reflects typical flue gas temperatures encountered in industrial settings and is frequently used in adsorption studies involving carbon-based materials (Krutka et al., 2013) . Lower temperatures favor physisorption due to reduced desorption tendencies, while higher temperatures provide insights into thermal desorption behavior, allowing a comprehensive understanding of adsorption thermodynamics. Similarly, CO_2 concentrations in the range of 2 to 10 wt.% were chosen to mimic the CO_2 content in diluted gas streams such as indoor air or post-treatment flue gas (J. Wang et al., 2014). This range enables

the assessment of adsorbent performance across varying partial pressures, capturing both low-driving-force and high-capacity regimes. The variation in gas flow rate from 60 to 140 mL/min was based on previous studies employing fixed-bed adsorption columns, where such flow rates are optimal for balancing residence time and mass transfer efficiency (S. Choi et al., 2009). A slower flow ensures adequate contact time between CO_2 molecules and active sites, while a faster flow reveals kinetic limitations due to reduced diffusion time.

3.11 Isotherms studies

The concentration equilibrium relationship within the system was investigated using adsorption isotherms at a constant adsorption temperature of 30 °C. In this study, the experimental conditions were fixed with a total gas feed flow rate of 100 mL/min, while the CO_2 feed concentration was systematically varied at 2, 4, 6, 8, and 10 wt% to evaluate its effect on adsorption behavior. Five different adsorption isotherm models, Langmuir, Freundlich, Temkin, Dubinin-Radushkevich (DR), and Redlich-Peterson (R-P) (El Jery et al., 2024; Piccin et al., n.d.) were applied to the experimental data. Each model offers a unique perspective on the adsorption mechanism, based on different assumptions such as surface homogeneity, multilayer adsorption, or energetic heterogeneity. This comprehensive approach provides a more detailed understanding of the surface characteristics of the N/S/O-CCQD-X adsorbent and the nature of its interaction with CO_2 molecules.

Table 3.4
Summary of Isotherm Models Used in This Work

Isotherm model	**Linear Equation**
Langmuir	$\frac{1}{q_e} = \frac{1}{q_m} + \frac{1}{q_m K_l}\frac{1}{C_e}$
Freundlich	$ln\, q_e = \frac{ln\, C_e}{n} - ln\, K_F$
Temkin	$q_e = \frac{RT}{b}(\, ln\, C_e + ln\, K_T)$
Dubinin-Radushkevich (DR)	$ln\, q_e = ln\, q_{max} - K\epsilon^2$
Redlich-Peterson (R-P)	$ln\left(K_R \frac{C_e}{q_e} - 1\right) = ln\, a_R + \beta\, ln\, C_e$

3.12 Kinetics studies

Furthermore, kinetic evaluations were carried out using N/S/O-CCQD-X adsorbents to better understand the adsorption rate and mechanism for CO_2 capture. The experiments were conducted at a constant adsorption temperature of 30 °C and a fixed CO_2 feed concentration of 5 wt%, while the total gas feed flow rate was varied at 60, 80, 100, 120, and 140 mL/min. Breakthrough data obtained under these conditions were analyzed using pseudo-first order and pseudo-second-order kinetic models to determine the adsorption kinetics. These models help describe how quickly CO_2 molecules are adsorbed onto the surface of the adsorbent and provide insights into whether the adsorption process is governed by physical or chemical interactions.

The pseudo-first-order model operates under the assumption that physisorption limits the adsorption rate, particularly during the initial stages of the process. On the other hand, the pseudo-second-order model posits chemisorption as the rate-limiting mechanism, offering insights into the adsorption behaviour across the entire range of the process. Each model provides a distinct perspective on the dynamics of adsorption, with the pseudo-first-order model capturing the early stages and the pseudo-second-order model offering a comprehensive understanding across the entire adsorption spectrum. The application of these models contributes to unravelling the intricacies of adsorption kinetics and aids in tailoring efficient adsorption processes (Sahoo & Prelot, 2020; Saleh, 2022).

Table 3.5
Kinetic Models used for Adsorption: PFO and PSO

Kinetics model	Equation
pseudo-first order	$ln\left(q_{eq} - q_t\right) = ln\left(q_{eq}\right) - k_1 t$
pseudo-second order	$\frac{t}{q_t} = \frac{1}{k_2 . q_{eq}^2} + \frac{t}{q_{eq}}$

3.13 Thermodynamics studies

The thermodynamic investigation focused on analyzing the influence of temperature on the adsorption system, with experimental data collected using a fixed-bed adsorption column across a temperature range of 30 to 110°C (30, 50, 70, 90, and 110°C). The study maintained consistent experimental conditions, including a CO_2 feed concentration of 5 wt% and the total gas feed flow rate of 100 mL/min, while

only varying the temperature. The thermodynamic equilibrium coefficients obtained at different temperatures were used to evaluate the adsorption thermodynamics, providing insights into the underlying adsorption mechanisms. The adsorption behaviour of a substance can be described using thermodynamic parameters, including ΔG (Gibbs free energy change), which can be computed using Equation (3.4) (Piccin et al., n.d.).

$$\Delta G = - RT \ln K_D \tag{3.4}$$

Where K_D can be obtained by plotting $\frac{q_e}{C_e}$ versus q_e and extrapolating q_e to zero (El Jery et al., 2024) . In accordance with thermodynamics, the Gibbs free energy is expressed as the difference between the adsorption enthalpy (ΔH) and adsorption entropy (ΔS), each multiplied by the temperature. Utilizing this principle, the thermochemical parameters ΔH and ΔS can be ascertained through van't Hoff's plot, as outlined in Equation (3.5).

$$\ln K_D = - \frac{\Delta H}{RT} + \frac{\Delta S}{R} \tag{3.5}$$

K_D: thermodynamics equilibrium constant $\left(\frac{L}{g}\right)$

R: universal gas constant $\left(\frac{\text{L.atm}}{mol.K}\right)$

T: temperature (K)

In summary, thermodynamics plays a pivotal role in optimizing and understanding CO_2 adsorption processes. It provides insights into the energy changes, spontaneity, and efficiency of the adsorption system, aiding in the design and implementation of effective CO_2 removal technologies

CHAPTER 4
RESULTS AND DISCUSSIONS

4.1 Introduction

This chapter presents and discusses the findings of the current research, which are organized into four (4) objectives. The following are the summary of those sections:

a) The first objective presents the parameter study for the efficient synthesis of N/S/O-CCQDs, focusing on achieving stable immobilization within xerogels to produce an effective CO_2 adsorbent.
b) The second objective reports the results of CO_2 adsorption performance of N/S/O-CCQD-X synthesized with varying doping ratios of chitosan: thiourea: KOH (1:1:2, 1:2:2, 1:3:2, 1:1:3, 1:2:3, 1:3:3), followed by comprehensive physicochemical characterization of the resulting adsorbents using various analytical techniques, including FTIR, TGA, BET, FESEM-EDX, CHNS/O, HR-TEM, XPS, and fluorescence spectroscopy. The best-performing adsorbent was selected for further parametric studies to evaluate the influence of key operational factors in the CO_2 adsorption.
c) The third objective discusses the effects of key process parameters – adsorption temperature, CO_2 feed concentration, and gas feed flow rate on the CO_2 adsorption performance using the selected N/S/O-CCQD-X adsorbent.
d) The fourth objective investigates the adsorption mechanism of N/S/O-CCQD-X adsorbent towards CO_2 removal via adsorption isotherms, kinetics analysis, and thermodynamic studies to gain insights into the nature of the adsorption process.

4.2 Role of Xerogel in Stabilizing the N/S/O-CCQD Adsorbent

This study was carried out to investigate the role of xerogel as a support medium in enhancing the stability and performance of N/S/O-CCQD-X for effective

CO_2 adsorption. Immobilization of CCQDs into xerogels was explored as a strategy to improve their structural integrity and adsorption efficiency, providing a robust support material that enhances stability. To achieve this, four types of xerogel samples were prepared: three were immobilized with different volumes of CCQD suspension (2 mL, 10 mL, and 100 mL), while the fourth utilized a freeze-dried CCQDs. The synthesized N/S/O-CCQD-X samples were first evaluated for their CO_2 adsorption performance, followed by comprehensive characterization of their physicochemical properties, to identify the most effective xerogel-based stabilization strategy for producing CCQDs as CO_2 adsorbent.

4.2.1 CO_2 Adsorption Study

In this section, the adsorption capacity of N/S/O-CCQD-X with varying CCQDs configurations is evaluated. The analysis focuses on how different CQD suspension volumes; CQD-X 1:1 (2 mL), CQD-X 1:10 (10 mL), CQD-X 1:50 (100 mL) as well as freeze-dried CQDs (FD CQD-X 1:50) influence the material's CO_2 capture efficiency. The results provide insight into the impact of CCQDs loading on CO_2 adsorption behavior. Figure 4.1 illustrates the CO_2 breakthrough curves for the different N/S/O-CCQD-X samples, showing the change in CO_2 concentration (C/Co) over time during the adsorption process. Table 4.1 summarized the CO_2 adsorption performance of the N/S/O-CCQD-X samples, including key parameters such as breakthrough time, breakthrough capacity, total adsorption time, and total adsorption capacity.

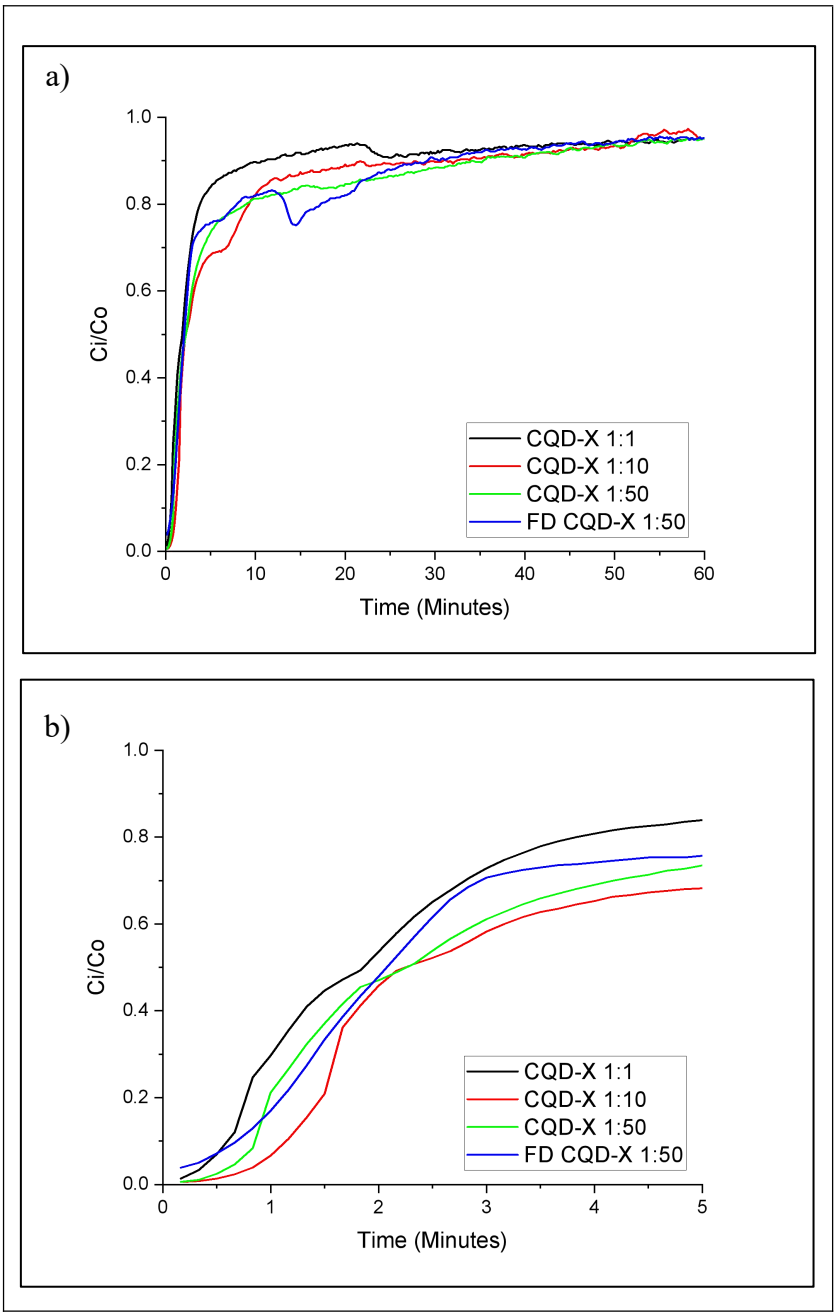

Figure 4.1 a) CO_2 Breakthrough Curves b) Enlarge Image of Breakthrough Curve for CQD-X 1:1, CQD-X 1:10, CQD-X 1:50 and FD CQD-X 1:50

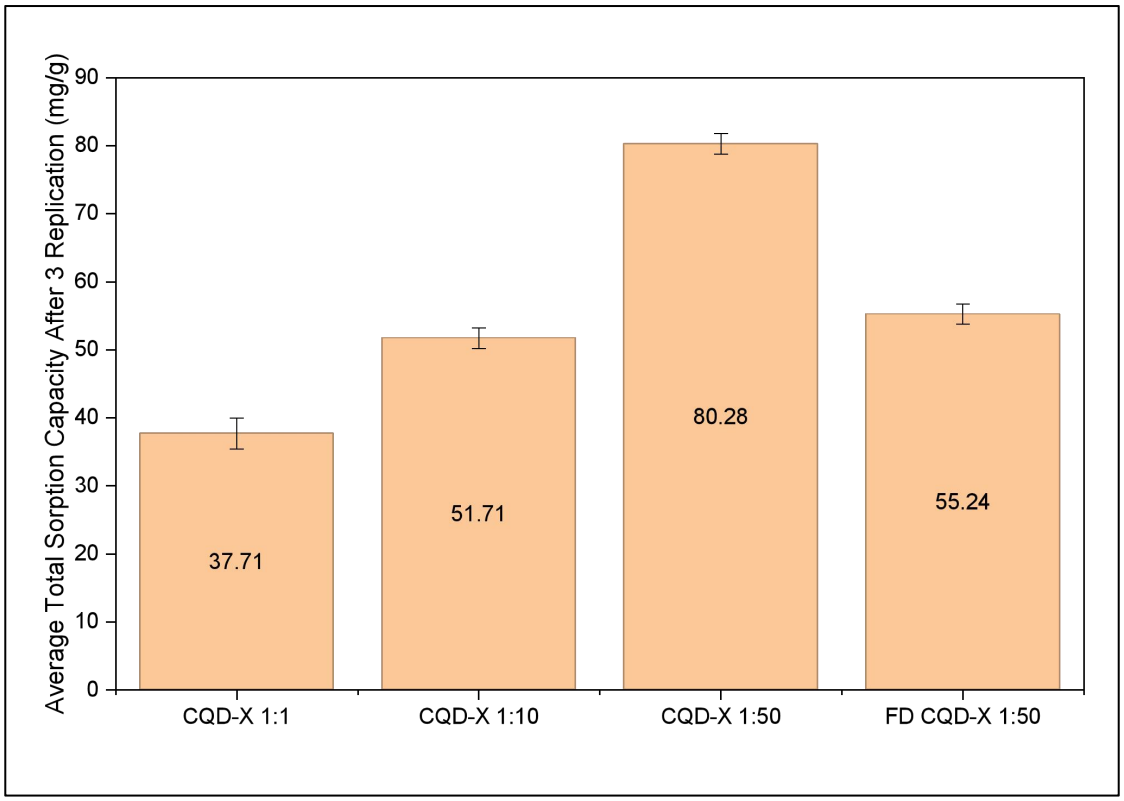

Figure 4.2 Average Total Sorption Capacity with Standard Error Bars

Table 4.1
CO_2 Adsorption Performance of N/S/O-CCQD-X Samples

Samples	Breakthrough time (min)	Breakthrough capacity (mg/g)	Total adsorption time (min)	Average total adsorption capacity (mg/g)	Standard error (SE)
CQD-X 1:1	0.67	0.9478	50.33	37.71	2.2577
CQD-X 1:10	0.83	0.9579	46.33	51.71	1.5087
CQD-X 1:50	1.00	1.1489	34.33	80.28	1.5228
FD CQD-X 1:50	0.83	0.9437	54.50	55.24	1.4796

Table 4.1 presents the CO_2 adsorption performance of N/S/O-CCQD-X samples prepared with different CCQDs-to-solution ratios (1:1, 1:10, and 1:50) and a freeze-dried CCQDs sample (FD CQD-X 1:50). An initial analysis, based on data from a single experimental run, showed inconsistent trends. However, upon revising the results to include all three replicates which also mitigates the potential for human or procedural error such as slight delays in recording breakthrough time, inconsistent packing of the adsorbent bed, or minor variations in setting the flow rate, a consistent

trend emerged. In Figure 4.1a, all samples exhibit a rapid initial rise in C/C_0, indicating fast adsorption during the early stage, followed by a gradual approach to equilibrium. The FD CQD-X 1:50 sample shows a slightly delayed breakthrough compared to the others, suggesting a longer effective adsorption period. Figure 4.1b provides an enlarged view of the initial 5 minutes, showing that CQD-X 1:50 exhibits a comparatively lower C/C_0 profile than the other samples during the early stage of adsorption. This indicates a slower rise in outlet concentration, suggesting improved CO_2 retention relative to the other formulations within this initial period.

Among the samples, CQD-X 1:1 exhibits the shortest breakthrough time (0.67 min) and low breakthrough capacity (0.9478 mg/g), indicating a quicker saturation of adsorption sites and limited initial adsorption performance. The total adsorption time is 50.33 minutes and total capacity (37.71mg/g) is the lowest, suggesting that this ratio is not optimal for CO_2 adsorption. The CQD-X 1:10 sample shows improved performance, with a longer breakthrough time (1.17 min) and a slightly higher breakthrough capacity (0.9579 mg/g). Although its total adsorption time decreases to 46.33 minutes, the total adsorption capacity increases significantly to 51.71 mg/g, indicating enhanced CO_2 retention compared to the CQD-X 1:1 sample. In contrast, the CQD-X 1:50 sample delivers the best performance, achieving the breakthrough time of 1.00 min and the highest breakthrough capacity (1.1489 mg/g). This sample also has the shortest total adsorption time (34.33 minutes) and the highest total capacity (80.28 mg/g), highlighting its superior adsorption behaviour due to the ideal CCQDs-to-solution ratio. For the freeze-dried sample, FD CQD-X 1:50, the breakthrough time (0.83 min) and breakthrough capacity (0.9437 mg/g) are moderate, while the total adsorption time (54.5 min) and total capacity (55. 24 mg/g) are lower than those of the suspension-based CQD-X 1:50 sample. This indicates that while freeze-dried CCQDs are effective, the suspension-based synthesis results in better dispersion and pore structure, leading to superior adsorption efficiency.

The CO_2 adsorption capacity of the CQD-X 1:50 sample, recorded at 80.28 mg/g, surpasses that of the polyurethane (PU)/ionic silica xerogel composites reported in the referenced study, which achieved a maximum of 48.5 mg CO_2/g (dos Santos et al., 2019). This difference can be attributed to variations in the physical and chemical properties of the respective adsorbents. The CQD-X 1:50 sample exhibits a mesoporous structure with a BET surface area of 0.1864 m^2/g and a micropore area of 0.2601 m^2/g. Despite the relatively modest surface area, the presence of both

mesopores and micropores facilitates effective CO_2 adsorption. Additionally, the incorporation of heteroatoms such as nitrogen and sulfur into the CQDs enhances surface functionalities, improving CO_2 affinity. The hydrothermal synthesis method employed for CQD-X 1:50 likely contributes to the development of these advantageous properties. In contrast, the PU/ionic silica xerogel composites incorporate silica xerogels functionalized with room-temperature ionic liquids (RTILs) into a PU matrix. The specific surface area of these composites varies with the type and amount of functionalized xerogel added. Composites prepared with fluorinated RTILs demonstrated higher CO_2 sorption capacities, attributed to increased specific surface areas and enhanced CO_2 affinity due to the presence of fluorinated anions. However, the integration of these xerogels into the PU matrix may lead to filler aggregation, potentially reducing the overall surface area available for adsorption and affecting the mechanical properties of the composites. The superior CO_2 adsorption capacity of CQD-X 1:50 is likely due to the synergistic effects of its mesoporous structure and the presence of nitrogen and sulfur functionalities, which enhance CO_2 interaction. In contrast, while the PU/ionic silica xerogel composites benefit from the inclusion of functionalized xerogels, factors such as filler dispersion and matrix interactions influence their adsorption performance.

4.2.2 Thermal Stability

Thermogravimetric Analysis (TGA) is conducted to investigate the thermal stability and compositional changes of the N/S/O-CCQD-X. This analysis helps in understanding how the N/S/O-CCQD-X withstand high temperatures and identify any weight loss due to decomposition or volatilization of components. Figure 4.3 shows the TGA curve of CQD-X 1:1, CQD-X 1:10, CQD-X 1:50, and FD CQD-X 1:50, while Table 4.2 summarizes the proximate analysis of the samples.

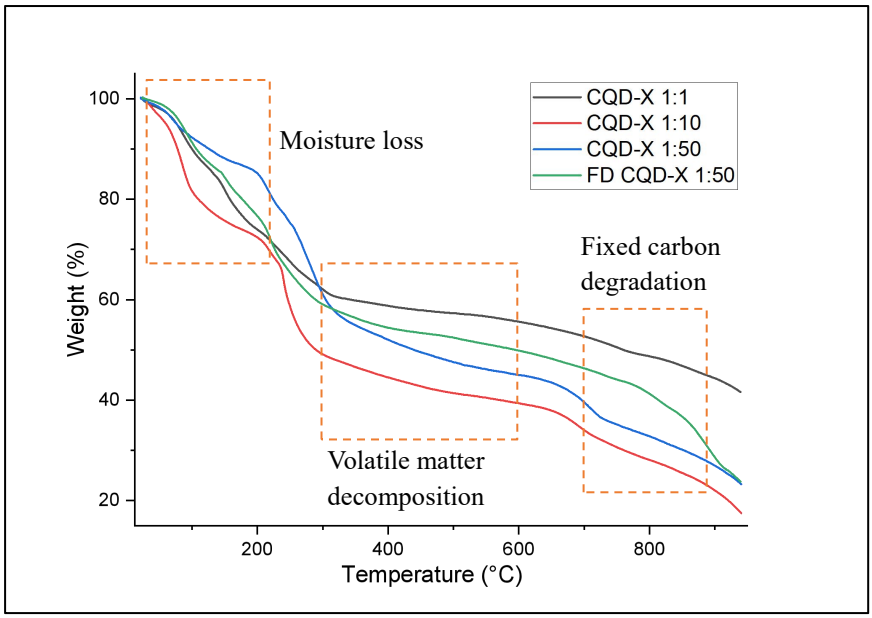

Figure 4.3 TGA curve of N/S/O-CCQD-X samples

Table 4.2
Proximate Analysis of N/S/O-CCQD-X Adsorbents

Sample	Moisture content (%)	Volatile matter (%)	Fixed carbon (%)	Ash content (%)
CQD-X 1:1	15.94	34.62	7.71	41.73
CQD-X 1:10	18.80	44.66	19.06	17.48
CQD-X 1:50	14.55	48.85	13.26	23.34
FD CQD-X 1:50	15.41	41.48	19.35	23.76

The TGA curves reveal distinct weight loss regions that correspond to different stages of decomposition. Similar to the findings by Alias et al., these regions can be categorized into moisture loss, volatile matter decomposition, and fixed carbon degradation. The initial weight loss, occurring between 70°C and 100°C, is attributed to the evaporation of moisture. Among the samples, CQD-X 1:50, with the lowest CCQDs content, shows the least initial weight loss at 103.27°C. In the second region, from 300°C to 700°C, the significant weight loss corresponds to the decomposition of volatile organic components and releasing gases from the CCQDs and xerogel matrix. CQD-X 1:50, with a higher xerogel content, exhibits an earlier onset of degradation compared to CQD-X 1:1 and CQD-X 1:10, suggesting a lower thermal stability due to the composition and concentration of CCQDs within the matrix. CQD-X 1:1 and FD

CQD-X 1:50 show less weight loss and a higher onset temperature of 342.94°C, suggesting better thermal stability. The dense structure of CQD-X 1:1, with the highest CCQDs ratio, likely contributes to its enhanced thermal resistance. The freeze-dried FD CQD-X 1:50, with its altered distribution and interaction of CCQDs due to the freeze-drying process, exhibits a distinct decomposition profile, reflecting changes in its thermal behaviour.

The final stage, between 700°C and 950°C, represents the decomposition of fixed carbon. CQD-X 1:1, with the highest CCQDs content, and FD CQD-X 1:50, the freeze-dried sample, are more thermally stable than the other samples. More thermally stable samples often exhibit a denser structure with fewer pores or smaller pore sizes, contributing to their stable thermal degradation behaviour. CQD-X 1:1 retains a higher residual weight of 40%, with an onset temperature of 760.09°C, suggesting a more stable carbon structure. FD CQD-X 1:50 follows closely with an onset temperature of 729.76°C. Overall, the TGA analysis highlights the significant impact of preparation methods and CCQDs states (aqueous-suspension versus freeze-dried) on the thermal degradation behaviour of N/S/O-CCQD-X samples.

In the study by Alias et al., it was observed that in the first region, the moisture release in xerogel-based EFB occurred earlier than in raw EFB and hydrogel. This was attributed to the increased crystallinity in xerogel, where -OH groups are replaced by intermolecular hydrogen bonds, reducing moisture absorption. Additionally, the weight loss in xerogel was higher due to the breakdown of the alginate backbone and the significant loss of hydroxyl groups. Similarly, a similar trend is observed in the TGA curves of the N/S/O-CCQD-X samples from this research. The CQD-X 1:50 sample, which has the lowest CCQDs content and a more xerogel-like structure, shows earlier moisture loss at 103.27°C. This aligns with the findings in Alias et al.'s study, where xerogel’s structure led to earlier moisture evaporation due to reduced moisture retention. The increased crystallinity in xerogel-like structures, as seen in CQD-X 1:50, supports the early moisture release trend. Moreover, the higher weight loss in the xerogel-based samples, as noted in the Alias et al. study, corresponds to the thermal degradation of the alginate backbone and loss of hydroxyl groups. In the N/S/O-CCQD-X samples, similar behaviour is reflected, particularly in the second region (300°C to 700°C), where significant weight loss due to the decomposition of volatile organic components and the xerogel matrix is observed. The earlier onset of degradation in CQD-X 1:50, compared to samples with higher CCQDs content,

indicates a lower thermal stability similar to the xerogel-based EFB's higher degradation compared to raw and hydrogel forms.

The proximate analysis values do not show a perfect trend because the N/S/O-CCQD-X composites are heterogeneous materials. Differences in formulation change the amount of volatile species and thermally unstable functional groups, so each formulation decomposes differently during heating. Minor variations during synthesis such as mixing uniformity, dispersion of CQDs, drying efficiency, or the amount of residual salts also influence moisture, volatile matter, and fixed carbon content. In addition, small human-related inconsistencies (e.g., weighing, grinding, or sample handling) can contribute to the deviation. Together, these factors make slight non-trend behaviour expected for multi-component carbonaceous composites. (Jadav & Patel, 2023; Poomsawat & Poomsawat, 2023).

The CO_2 adsorption data, when correlated with thermal stability findings, reveal a clear relationship between the CCQDs content, structural integrity, and performance efficiency of the N/S/O-CCQD-X samples. Among all samples, CQD-X 1:50 exhibits the highest total adsorption capacity of 80.28 mg/g, despite having the lowest CCQDs concentration, suggesting that the balance between xerogel matrix and CCQDs enables optimal pore accessibility and gas diffusion. However, this same sample shows lower thermal stability, as evidenced by its earlier degradation onset (103.27°C for moisture loss) and greater mass loss between 300–700°C, indicating a more fragile structure. In contrast, CQD-X 1:1, although showing the lowest total adsorption capacity (37.71 mg/g), exhibits the highest thermal stability, with an onset temperature of 342.94°C for major degradation and a residual weight of 40% at the final decomposition stage. These thermal traits are attributed to its denser structure and higher CCQDs content, which contribute to structural rigidity and slower decomposition. FD CQD-X 1:50, with a freeze-dried matrix, offers a unique balance, it achieves 55.24 mg/g adsorption and a relatively high thermal stability (onset at 729.76°C), suggesting that freeze-drying alters the internal distribution of CCQDs, improving both interaction sites and thermal behavior. These trends align with the study by Alias et al. (Alias et al., 2022b) , where xerogel-like structures facilitated earlier moisture loss and degradation due to increased crystallinity and reduced moisture retention. The comparison emphasizes that while higher CCQDs loading enhances thermal resistance, an optimized xerogel structure particularly in CQD-X 1:50 can significantly improve CO_2 adsorption performance. Thus, tailoring the

preparation method and composition not only fine-tunes the porosity and functionality but also directly impacts both sorption efficiency and thermal stability of the adsorbents.

4.2.3 Physical Surface Characteristics and Morphology

N_2 adsorption-desorption analysis is utilized to evaluate the surface area and porosity of the N/S/O-CCQD-X, which are critical factors affecting its CO_2 adsorption capacity. This analysis provides quantitative data on the specific surface area and pore volume of the CCQDs samples, enabling us to understand how variations in surface properties impact adsorption efficiency. By analysing the N_2 adsorption-desorption data, we can determine how the doping process alters the CCQDs' porosity and surface area, thus affecting its performance as an adsorbent. Figure 4.4 presents the N_2 adsorption-desorption isotherm plot for the CQD-X 1:50 sample, while Table 4.3 provides detailed surface area and pore volume measurements, including single point surface area, BET surface area, Langmuir surface area, micropore area, and micropore volume.

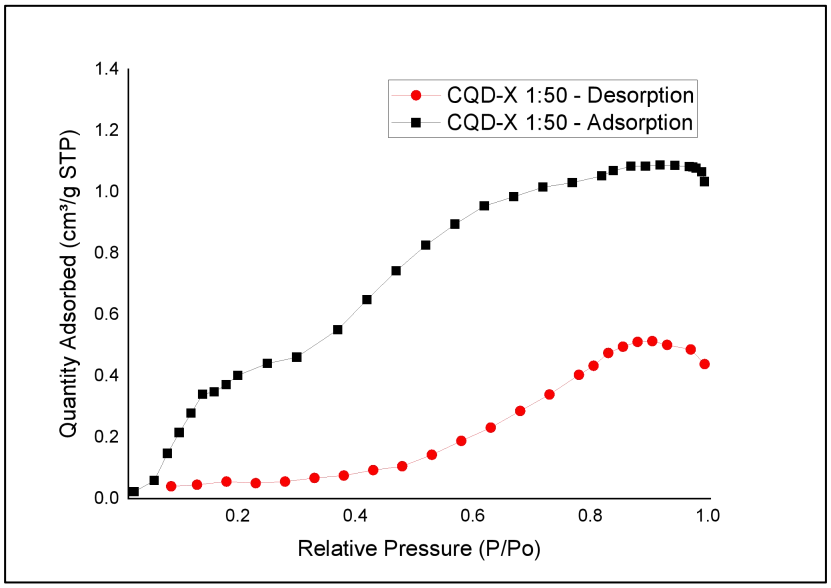

Figure 4.4 N_2 adsorption-desorption isotherm plot for CQD-X 1:50 sample

Table 4.3
Surface Area, Pore Area and Pore Volume of CQD-X 1:50

BET Surface Area, m^2/g	Langmuir Surface Area, m^2/g	Micropore Area, m^2/g	Micropore volume, cm^3/g
0.1864	0.2617	0.2601	0.000156 cm^3/g

The N_2 adsorption-desorption isotherm plot for the CQD-X 1:50 sample exhibits a type IV isotherm with a clear hysteresis loop, characteristic of mesoporous materials, indicating the presence of pores with diameters between 2 and 50 nm (Lan & Zhao, 2022). The hysteresis loop between the adsorption and desorption branches suggests capillary condensation within the mesopores. The gradual increase in nitrogen uptake at lower relative pressures corresponds to the filling of smaller pores, followed by a steep rise at higher pressures due to capillary condensation in larger mesopores. The desorption branch's hysteresis loop, typical of slit-shaped or cylindrical pores, reflects the evaporation of nitrogen gas at a lower pressure than its condensation due to pore geometry and surface tension effects. The surface area and pore characteristics of CQD-X 1:50, determined using the BET theory and t-Plot method, revealed a BET surface area of 0.1864 m^2/g and a micropore area of 0.2601 m^2/g, indicating the presence of both mesopores and micropores, essential for gas adsorption applications like CO_2 capture. In comparison, Mahdi et al. reported higher surface areas for activated carbon (AC) at 868 m^2/g, with a pore size of 1.7532 nm and a pore volume of 0.3805 m^3/g. Their study also highlighted the decrease in surface area, pore size, and pore volume for xerogel-based samples after gelation, with palm kernel shell biochar (PKSB) showing 355.7066 m^2/g surface area, pore size 2.0376 nm, pore volume 0.1820 cm^3/g and palm kernel shell biochar xerogel (PKSBX) only 29.4535 m^2/g surface area, pore size 4.6203 nm, and pore volume 0.0295 m^3/g, attributed to pore blockage and structural shrinkage during hydrogel drying (Mahdi et al., 2024b). This contrast emphasizes that while xerogel structures like CQD-X 1:50 offer sufficient surface area for specific applications, they generally exhibit lower surface areas compared to highly porous materials like activated carbon due to the gelation and drying processes.

Field Emission Scanning Electron Microscopy (FESEM) is employed to examine the surface morphology and structural characteristics of the N/S/O-CCQD-X, particularly focusing on the best-performing adsorbent. The morphology observed in the FESEM results, as shown in Plate 4.1, reveals a porous structure with interconnected pore networks. This morphological feature aligns with the physical surface characteristics indicated by the N_2 adsorption-desorption analysis, supporting the presence of mesoporous architecture favorable for gas diffusion and adsorption. Notably, the CQD-X 1:50 sample demonstrated the highest CO_2 adsorption capacity, with a sorption capacity of 80.28 mg CO_2/g. This strong performance confirms that the

observed porous and structured surface plays a critical role in enhancing the accessibility of active sites, thereby improving CO_2 capture efficiency. The visual and structural assessment underscores the importance of surface architecture in influencing the adsorption behavior of the N/S/O-CCQD-X adsorbent.

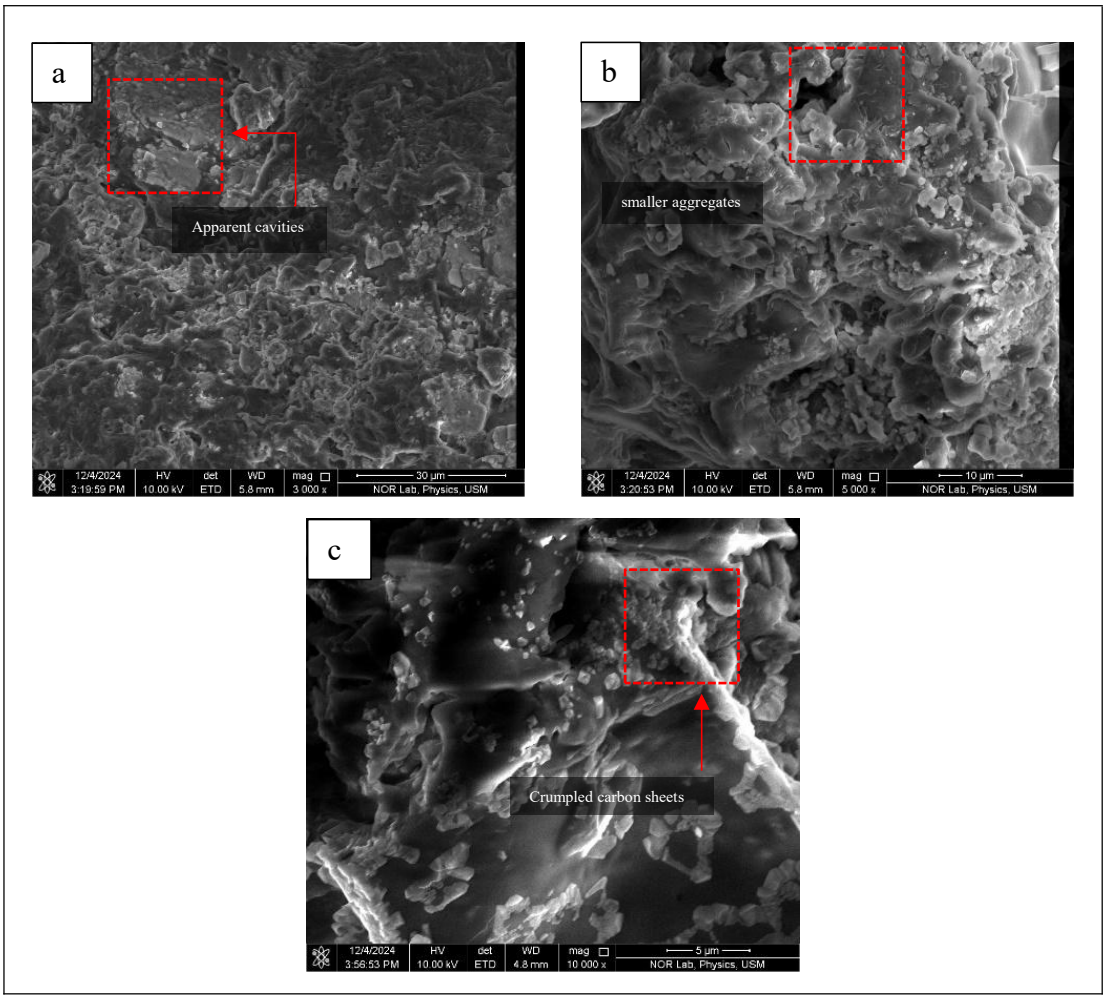

Plate 4.1 FESEM images of CQD-X 1:50 from various magnifications: a) 3000x; b) 5000x; c) 10000x

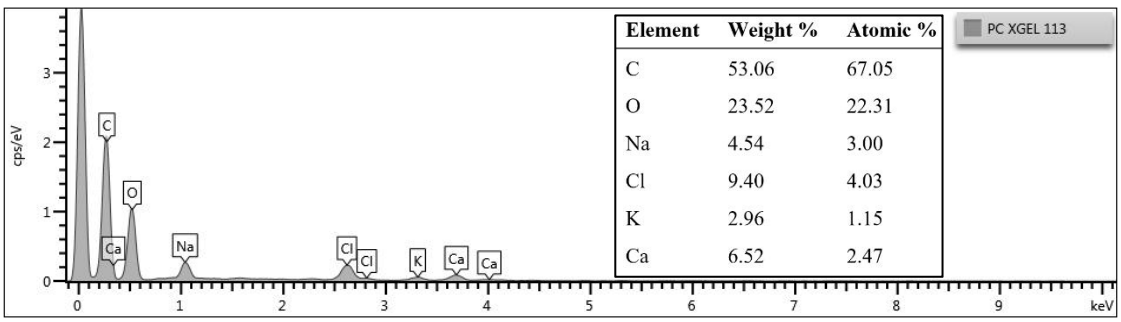

Element	Weight %	Atomic %
C	53.06	67.05
O	23.52	22.31
Na	4.54	3.00
Cl	9.40	4.03
K	2.96	1.15
Ca	6.52	2.47

Figure 4.5 Quantitative analysis of the energy dispersive X-ray (EDX) analysis on CQD-X 1:50 sample

The FESEM images of CQD-X 1:50 at various magnifications (a) 3000x, (b) 5000x, and (c) 10000x provide a detailed view of the surface morphology and structural characteristics of the sample. At all magnifications the CCQD-X 1:50 micrographs show a very irregular and heterogeneous surface. The xerogel matrix structure at 3000× indicates uneven distribution of particles by having a mound-and-valley geometry with apparent cavities. At the 5000X scale, smaller aggregates or clusters of CCQDs are observed, and the surface takes the topology of a network with numerous protrusions and hollows. The surface is highly rough and twisted at 10,000x, and groups of nanoparticles, holes and crumpled sheets of carbon can be observed. In other areas, there are extensive planar terrains that are similar to layers of piled carbonaceous. These structural characteristics indicate that N/S/O doping of the CCQDs changes the xerogel microstructure to form an irregular, accessible surface that enables the catalysis of gas-solid interactions during CO_2 adsorption. Although the FESEM image does not display well-defined mesopores, the observed surface irregularities and interparticle voids imply a texturally open framework that complements the BET findings, which indicate a mesoporous structure with considerable surface area.

There is prior research on such morphologies. For instance, RF xerogels are outlined by Aguilar-Maruri et al. to be “agglomerated in irregular shapes with smooth and striated faces” (Aguilar-Maruri et al., 2024) , and acid-activated carbons were found to have “aggregated and rough surface morphology" with interconnected particles forming surface pores” (Olasehinde & Abegunde, 2020) . It is well known that these highly rough, clumped textures increase the adsorption area: According to Gong et al., rough surfaces coated with nanoparticles “effectively increase the specific surface area” of biochars (W. Gong et al., 2025) . Similarly, xerogel-derived carbons frequently form sheet-like, porous networks, according to Hao et al., who reported a “sheet-like morphology” in N-doped carbon supports that correlates with high porosity (Hao et al., 2023).

Figure 4.5 shows the quantitative analysis of the energy dispersive X-ray (EDX) analysis for the CQD-X 1:50 sample, providing a detailed composition of elements present in the sample, including their weight and atomic percentages. The table lists the major elements detected: carbon (C), oxygen (O), sodium (Na), chlorine (Cl), potassium (K), and calcium (Ca). The findings show a significant presence of carbon (C) and oxygen (O), with weight percentages of 53.06% and 23.52%,

respectively. The high carbon content predominantly originates from the carbon quantum dots, which are formed from chitosan during the synthesis process. The oxygen content is likely due to the presence of various oxygen-containing functional groups such as hydroxyl (–OH), carbonyl (C=O), and carboxyl (–COOH) groups, which are introduced through the oxidation of chitosan and the interaction with other synthesis materials. Sodium (Na) and chlorine (Cl) are detected with weight percentages of 4.54% and 9.4%, respectively. Sodium is likely introduced from the sodium alginate used in the xerogel preparation. The presence of chlorine could be associated with residuals from the thiourea or other synthesis reagents.

The role of sodium alginate is to form a hydrogel network that encapsulates the carbon quantum dots, contributing to the porous structure observed in the FESEM images. Potassium (K) at 2.96% weight is attributed to the KOH used in the doping process. KOH serves as a strong base that helps in the deprotonation and cross-linking during the formation of CCQDs, enhancing their structural integrity and functionality. Potassium can also introduce surface basicity, which can be beneficial for CO_2 adsorption by providing sites for the interaction with acidic CO_2 molecules. Calcium (Ca) with a weight percentage of 6.52% comes from the calcium carbonate ($CaCO_3$) used in the xerogel synthesis. $CaCO_3$ acts as a pore-forming agent, decomposing during the gelation process to form carbon dioxide gas, which helps create a porous structure in the xerogel. This porosity is crucial for enhancing the material's surface area, improving its adsorption capacity for gases and other molecules. Overall, the EDX analysis reflects the incorporation of these synthesis materials into the CQD-X 1:50 sample. The synthesis materials not only define the elemental composition but also significantly influence the structural and functional properties of the resulting adsorbent.

4.2.4 Surface Functional Group

Fourier Transform Infrared Spectroscopy (FTIR) provides detailed insights into the chemical structure and functional groups present in the N/S/O-CCQD-X samples. FTIR analysis was performed for all synthesized samples to identify the specific chemical bonds and functional groups introduced during the doping and immobilization processes. As shown in Figure 4.6, comparison of the FTIR spectra across different samples allows evaluation of how these modifications influence the

chemical structure of the N/S/O-CCQD-X materials, which directly impacts their CO_2 adsorption performance.

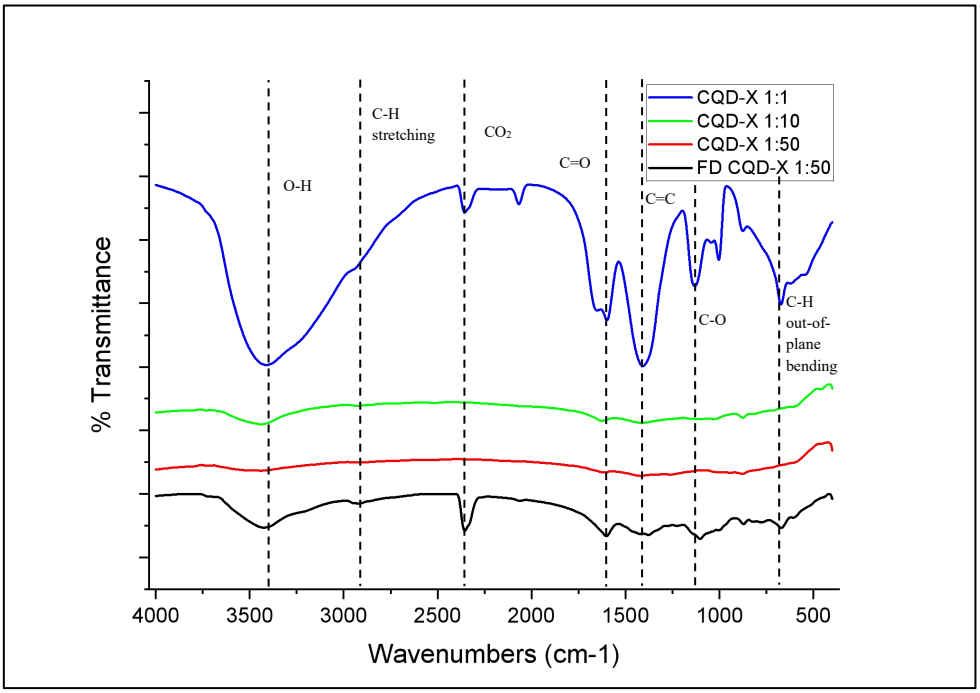

Figure 4.6 FTIR Spectra of N/S/O-CCQD-X with Varying CCQDs Suspensions and Freeze-Dried CCQDs

The FTIR spectra of N/S/O-CCQD-X reveal several functional groups contributing to its adsorption properties. A broad peak in the 3200-3600 cm^{-1} region indicates the presence of hydroxyl (O-H) and amine (N-H) groups, inherent to the chitosan structure. These groups enhance hydrogen bonding capacity, which is crucial for adsorbing polar molecules like CO_2. The peaks in the 2800-3000 cm^{-1} range correspond to aliphatic C-H stretching, highlighting the organic framework of the chitosan backbone and possibly the carbon quantum dots. Peaks observed in the 2300–2400 cm^{-1} region of FTIR spectra are commonly attributed to the asymmetric stretching mode (ν_3) of CO_2. When CO_2 is present in the gas phase or adsorbed on a material surface, an absorption band typically appears in this region around 2350 cm^{-1} due to the CO_2 ν_3 vibration, often seen in studies of gas adsorption by porous materials such as zeolites and related adsorbents (Galhotra et al., 2009). A significant peak between 1650-1750 cm^{-1} points to carbonyl (C=O) groups, likely from oxidized CCQDs or carboxylic groups, which improve adsorption through dipole-dipole interactions. Additionally, C=C stretching in the 1600-1680 cm^{-1} range indicates unsaturated bonds, enhancing π-π interactions with adsorbates. Peaks in the 1000-

1300 cm^{-1} region suggest C-O bonds typical of ethers or alcohols, further aiding in adsorbing polar molecules. C-H bending vibrations in the 600-900 cm^{-1} range point to aromatic or cyclic hydrocarbon rings, suggesting a graphitic structure in the CCQDs, supporting π-π stacking interactions useful for adsorbing aromatic compounds or gases (Hannachi et al., 2019b).

Comparatively, the FTIR spectra of different N/S/O-CCQD-X samples in Figure 4.6 reveal distinct variations influenced by the CCQDs suspension ratios and the material's state (suspension or freeze-dried). Among the samples, CQD-X 1:1, with the highest concentration of CCQDs suspension (100 mL), exhibits the most well-defined and sharp peaks, indicating a higher density of functional groups and better interaction of CCQDs with the xerogel matrix due to the increased CCQDs content. The broad and strong peak in the 3200–3600 cm^{-1} range corresponds to O–H stretching, confirming the presence of hydroxyl groups. Other prominent peaks, such as those around 2900 cm^{-1} (C–H stretching) and 1000–1200 cm^{-1} (C–O stretching), highlight the functional groups associated with CCQDs and the xerogel matrix. The FD CQD-X 1:50 sample, prepared with freeze-dried CCQDs, follows with relatively well-defined peaks. Although the freeze-dried process can lead to slight aggregation of CCQDs, the spectrum demonstrates retained functional groups such as O–H, C–H, and C–O. The broader peaks compared to CQD-X 1:1 suggest reduced uniformity in functional group dispersion, yet the material still shows a good level of structural integration. In contrast, CQD-X 1:10 and CQD-X 1:50, with lower CCQDs suspension concentrations (10 mL and 2 mL, respectively), exhibit progressively less defined peaks.

For CQD-X 1:10, the peaks in the O–H and C–H regions are sharper than those in CQD-X 1:50, indicating better dispersion and interaction due to the moderately higher CCQDs content. This suggests that the CQD-X 1:10 sample retains more distinct functional groups, although there is a reduction in their intensity compared to higher CCQDs content samples, indicating a partial reduction of functional groups. In contrast, CQD-X 1:50 exhibits the least defined peaks, reflecting the impact of its low CCQDs concentration on the visibility of functional groups and structural uniformity, leading to a more significant reduction of functional groups. Overall, the results demonstrate that higher CCQDs concentrations (as in CQD-X 1:1) produce the most well-defined functional groups, while samples with lower CCQDs content or freeze-dried CCQDs show broader and less distinct peaks, likely due to

reduced uniformity, aggregation, or functional group reduction. These findings underscore the influence of the CCQDs-to-solution ratio and the physical state of CCQDs on the structural and chemical properties of the xerogels (Kloos et al., 1999). To further understand the chemical composition of the samples, CHNS elemental analysis was conducted, complementing the FTIR results by quantifying the elemental content and providing information on how the synthesis process impacts the elemental distribution, particularly the carbon, hydrogen, nitrogen, and sulfur content, which correlates with the presence and intensity of functional groups detected in the FTIR spectra, as shown in Table 4.4.

Table 4.4
CHNS elemental analysis of Chitosan and Freeze-dried CCQDs

Sample	Weight(mg)	Carbon (C) wt%	Hydrogen (H) wt%	Nitrogen (N) wt%	Sulfur (S) wt%
Chitosan	2.236	34.00	9.58	7.99	0.62
Freeze-dried CCQDs	1.760	6.38	3.36	4.62	1.09

The CHNS elemental analysis data in Table 4.4 reveals the elemental composition of chitosan and freeze-dried CCQDs. Chitosan shows higher carbon (34.00wt%) and hydrogen (9.58wt%) contents compared to the freeze-dried CCQDs, which have 6.38wt% carbon and 3.36wt% hydrogen. The nitrogen content in freeze-dried CCQDs (4.62wt%) is lower compared to that in chitosan (7.99wt%). But the sulfur content in freeze-dried CCQDs (1.09wt%) is higher than that in chitosan (0.62wt%). This reduction in carbon and nitrogen content in CCQDs is indicative of the carbonization and structural transformation of chitosan during the hydrothermal process, where the organic components are converted into carbon-rich nanoparticles (Song et al., 2018) . The increase in sulfur content in the CCQDs suggests the successful incorporation of thiourea, a sulfur-containing doping agent, into the structure. The hydrogen content reflects the presence of surface functional groups, such as hydroxyl and amine groups, which contribute to the hydrophilicity and stability of the CCQDs. Comparing these results to the relevant literatures, similar trends are observed. Studies such as those by Cui et al. (2022) and Zhou et al. (2022) have demonstrated that incorporating sulfur into CQDs using thiourea as a sulfur source effectively increases the sulfur content within the CQDs. This sulfur doping

enhances the electron-donating capabilities of the CQDs and improves their surface functionalities, making them more effective for applications such as CO_2 capture (H. Cui et al., 2022; H. Zhou et al., 2022). The observed nitrogen content after synthesis aligns with findings by Chang et al. (2022), which indicate that some nitrogen is lost during thermal decomposition, while the remaining nitrogen contributes to heteroatom doping in CQDs. This doping enhances the chemical reactivity and adsorption capacity of CQDs, making them suitable for environmental applications (K. Chang et al., 2022).

The CHNS elemental analysis quantitatively supports the FTIR-identified functional groups and their evolution. The significant reduction in carbon content (34.00 wt% in chitosan → 6.38 wt% in CCQDs) and nitrogen content (7.99 wt% → 4.62 wt%) confirms the carbonization and structural transformation during hydrothermal synthesis, directly explaining the weaker/less defined peaks for C-H, C=O, and N-H groups in FTIR spectra of CCQDs-containing samples. The lower hydrogen content (9.58 wt% → 3.36 wt%) also aligns with reduced O-H/N-H group density observed in FTIR, reflecting the material's altered hydrophilicity. These elemental shifts collectively correlate with the intensity and definition of functional group peaks in FTIR, governing the material's adsorption performance.

4.3 Performance of N/S/O-CCQD-X with Varying Doping Ratios

This section evaluates the adsorption performance of N/S/O-CCQD-X synthesized using different heteroatom doping ratios, aimed at optimizing the functional chemistry required for effective CO_2 capture. The sample used in this section is indeed based on the CQD-X 1:50 formulation. As indicated in the section title, the N/S/O-CCQD-X materials discussed are those synthesised with varying doping ratios. All these samples were derived from the best-performing formulation identified in Objective 1, namely CQD-X 1:50, with the only difference being the adjusted N/S/O doping ratios. This ensures that the influence of doping ratio can be evaluated consistently while maintaining the same base CQD formulation. Six formulations were prepared by varying the weight ratios of chitosan, thiourea, and KOH (1:1:2, 1:2:2, 1:3:2, 1:1:3, 1:2:3, and 1:3:3), generating CCQDs with differing levels of N, S, and O incorporation. These doping variations directly influence the surface basicity, functional group density, and structural properties of the resulting

CQDs, which are critical for enhancing CO_2 adsorption behaviour. The adsorption capacity of each N/S/O-CCQD-X sample was first examined under standardized breakthrough conditions to determine the influence of doping ratio on CO_2 uptake. Subsequent physicochemical characterization was then performed to relate the observed adsorption trends to structural and surface chemistry differences, enabling identification of the optimal dopant composition for maximizing CCQD performance as a CO_2 adsorbent.

4.3.1 CO_2 Adsorption Study

Figure 4.7 shows the CO_2 breakthrough curve of N/S/O-CCQD-X adsorbent synthesized with varying doping ratios of chitosan:thiourea:KOH (1:1:2, 1:2:2, 1:3:2, 1:1:3, 1:2:3, 1:3:3). The adsorption performance was correlated with adsorption data tabulated in Table 4.5. All experiments were conducted under fixed conditions: a CO_2 flow rate of 100 mL/min flow rate, adsorption temperature of 30°C, and 5 wt% of CO_2 feed concentration. The breakthrough curves in Figure 4.7 clearly demonstrate that all N/S/O-CCQD-X samples exhibited CO_2 adsorption capability, with distinct differences in breakthrough behavior and capacity depending on the doping ratio. These variations highlight the influence of precursor composition on the adsorbent's performance.

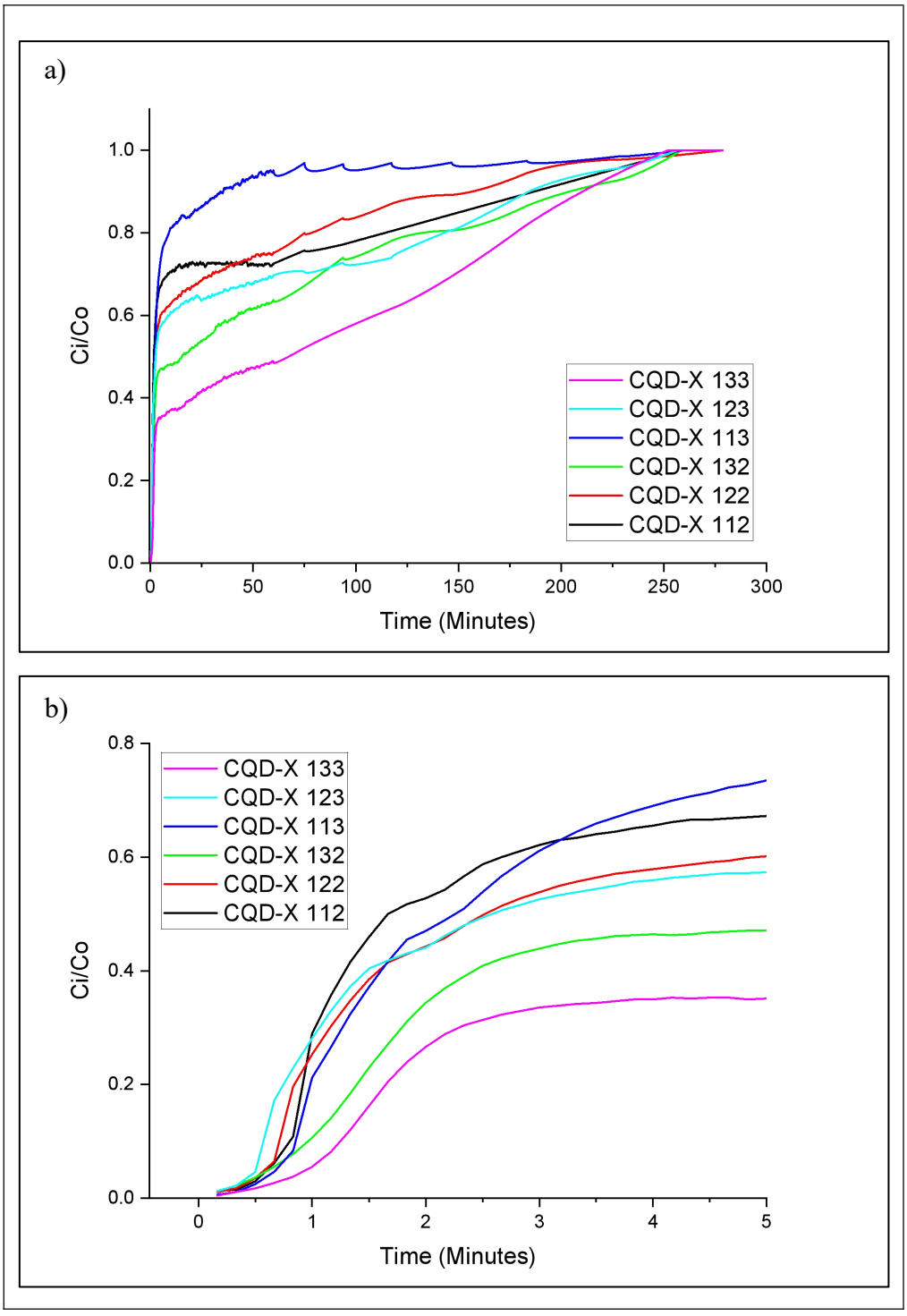

Figure 4.7 a) CO_2 Breakthrough Curve of N/S/O-CCQD-X Adsorbent b) Enlarge Image of Breakthrough Curve N/S/O-CCQD-X Adsorbent

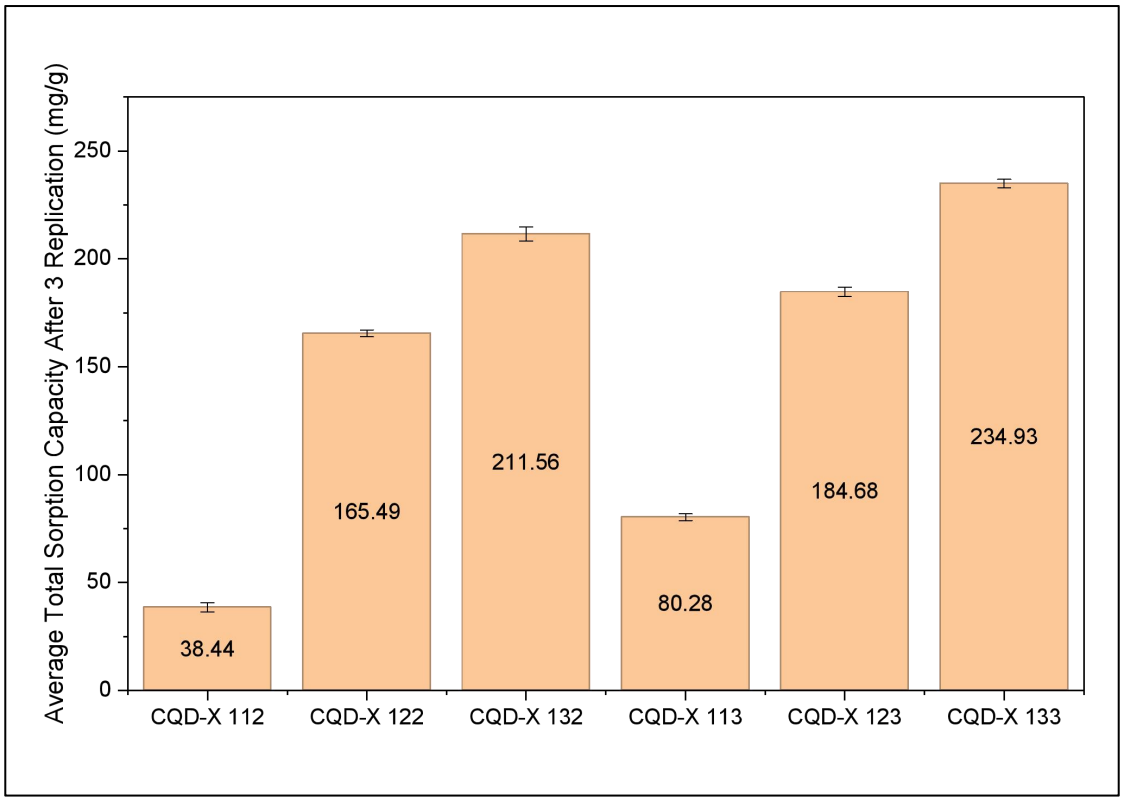

Figure 4.8 Average Total Sorption Capacity with Standard Error Bars

Table 4.5
Breakthrough Time and CO2 Adsorption Capacity of N/S/O-CCQD-X Adsorbents

Sample	Breakthrough time (min)	Breakthrough capacity (mg/g)	Average total adsorption capacity (mg/g)	Standard error (SE)
CQD-X 112	0.833	1.0459	38.44	2.1731
CQD-X 122	0.833	1.2521	165.49	1.5790
CQD-X 132	1	1.5863	211.56	3.1872
CQD-X 113	1	1.1489	80.28	1.5228
CQD-X 123	1	1.3972	184.68	2.1821
CQD-X 133	1.333	1.6955	234.93	1.9724

From the table, the results clearly indicate that increasing the doping ratio from 112 to 133 has a marked effect on the CO_2 adsorption performance of the N/S/O-CCQD-X adsorbents. An initial analysis, based on data from a single experimental run, showed inconsistent trends. However, upon revising the results to include all three replicates which also mitigates the potential for human or procedural error such as slight delays in recording breakthrough time, inconsistent packing of the adsorbent

bed, or minor variations in setting the flow rate, a consistent trend emerged. As the doping ratio increases, the breakthrough time extends from 0.833 minutes for CQD-X 112 to 1.333 minutes for CQD-X 133, while the adsorption capacity dramatically rises from 38.44 mg CO_2/g to 234.93 mg CO_2/g. This trend demonstrates that higher doping ratios, which correspond to increased amounts of thiourea and KOH, enhance the surface functionality and porosity of the adsorbent, thereby creating more active sites available for CO_2 capture. As for the total adsorption capacity, the highest was obtained at CQD-X 133 with 234.93 mg CO_2/g and the lowest was obtained at CQD-X 112 with 38.44 mg CO_2/g.

The breakthrough data indicate that CQD-X 133 exhibits the longest breakthrough time of 1.333 minutes and the highest total adsorption capacity of 234.93 mg/g, underscoring its superior CO_2 adsorption performance. This enhanced efficiency is likely due to the increased presence of thiourea and KOH, which may improve surface functionality and porosity, providing more active sites for CO_2 capture. Conversely, CQD-X 112 demonstrates the shortest breakthrough time (0.833 minutes) and the lowest total adsorption capacity (38.44 mg/g), suggesting a reduced number of active sites for effective CO_2 adsorption and a less developed pore structure. These observations are consistent with studies indicating that higher impregnation ratios of activating agents can enhance the adsorption capacity of carbon-based adsorbents by increasing surface area and pore volume (Min et al., 2023; X. Wang et al., 2022).

Based on these findings, CQD-X 133 was selected for further parametric studies to examine the effects of variables such as temperature, CO_2 concentration, and gas flow rate on adsorption performance. Despite CQD-X 123 exhibiting a slightly higher breakthrough capacity (1.3972 mg/g compared to 1.1701 mg/g for CQD-X 133), the longer breakthrough time and higher total adsorption capacity of CQD-X 133 make it more suitable for practical applications requiring sustained adsorption performance. The balance between adsorption capacity and structural stability in CQD-X 133 positions it as the most promising candidate for optimizing CO_2 capture efficiency.

Moreover, when benchmarked against other well-studied CO_2 sorbents, the superior performance of CQD-X 133 becomes even more apparent. Its total adsorption capacity of 234.93 mg g^{-1} (≈5.34 mmol g^{-1}) far exceeds that of amine-modified PEG/silica xerogels, which reached only 0.80 mmol g^{-1} (≈35.2 mg g^{-1}) thanks to their

hierarchical pore structure (Güzel Kaya, 2021) . Compared with unfunctionalized activated carbons whose typical CO_2 uptakes range from 44 to 132 mg g^{-1} (≈1.0–3.0 mmol g^{-1}) under flue-gas conditions (Echeverria Molina et al., 2021; Mindivan & Boz, 2025; Pathak et al., 2023), CQD-X 133 shows nearly double the highest reported performance. It also outperforms aminated silica supports, which, despite their enhanced surface chemistry, deliver capacities of only 1.14–1.90 mmol g^{-1} (≈50–84 mg g^{-1}) (Echeverria Molina et al., 2021; Mindivan & Boz, 2025; Pathak et al., 2023) . Even advanced imidazolium-based polymeric ionic liquids, noted for their strong chemisorptive interactions, achieve around 2 mmol g^{-1} (≈88 mg g^{-1} at 273 K) (Dani et al., 2016). These comparisons underscore the exceptional sorption capability of CQD-X 133, validating its selection for further parametric studies.

4.3.2 Quantum Yield

Fluorescence quantum yield serves as a critical parameter in evaluating the optical efficiency of CQDs synthesized from chitosan-based shrimp shells. This metric quantifies the material's ability to convert absorbed photons into emitted fluorescence, providing essential insights into its photophysical properties and potential suitability for applications such as CO_2 capture. In this study, the influence of varying chitosan:thiourea:KOH doping ratios on the quantum yield of N/S/O-CCQDs was systematically investigated. The results demonstrate significant variations in fluorescence efficiency across different formulations, highlighting the impact of heteroatom incorporation and synthesis conditions on the optical performance of these biomass-derived nanomaterials. By analyzing these trends, this study establishes key structure-property relationships that contribute to the optimization of N/S/O-CCQDs synthesis for enhanced functional performance.

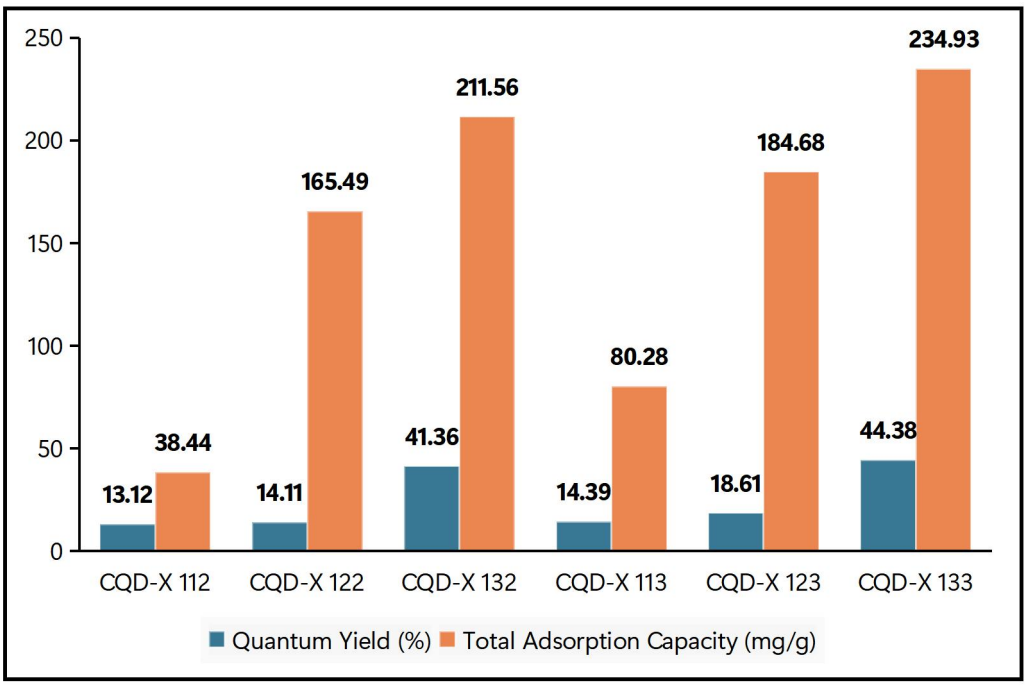

Figure 4.9 The Fluorescence Quantum Yield for Each Sample

The fluorescence quantum yield results demonstrate a clear dependence on the chitosan:thiourea:KOH ratio, with values ranging from 13.12% to 44.38%. The highest quantum yields were achieved with the 1:3:3 ratio (CQD-X 133 at 44.38% and CQD-X 132 at 41.36%), where the increased thiourea and KOH content relative to chitosan significantly enhanced fluorescence efficiency. This improvement can be attributed to several factors: the higher thiourea content provided more nitrogen and sulfur dopants, creating additional emissive sites, while the elevated KOH concentration optimized the reaction conditions for carbon dot formation and heteroatom incorporation. The intermediate 1:2:2 ratio (CQD-X 122 at 14.11%) showed moderate improvement, suggesting that both thiourea and KOH must be present in sufficient quantities to achieve notable effects. The lowest quantum yield was observed with the 1:1:2 ratio (CQD-X 112 at 13.12%), indicating that insufficient thiourea limits doping efficiency even with moderate KOH. Interestingly, samples with 1:1:3 (CQD-X 113 at 14.39%) and 1:2:3 (CQD-X 123 at 18.61%) ratios demonstrated that while increasing KOH alone provides some benefit, it cannot compensate for low thiourea content. These results highlight that thiourea serves as the primary dopant source for fluorescence enhancement, while KOH plays a supporting role in maintaining optimal reaction conditions. The progressive increase in quantum yield with higher thiourea:KOH ratios confirms that effective N/S/O co-doping requires careful balancing of all three components, with the 1:3:3 ratio

emerging as optimal for maximizing fluorescence efficiency through comprehensive heteroatom incorporation and defect passivation. The detailed quantum yield calculation procedure for these samples is provided in the Appendix.

The fluorescence quantum yield results closely parallel the CO_2 sorption performance of the N/S/O-CCQD-X samples, revealing a consistent influence of the chitosan:thiourea:KOH ratio on both optical and adsorption properties. Notably, the CQD-X 133 and CQD-X 132 samples, which exhibited the highest quantum yields (44.38% and 41.36%, respectively), also achieved the highest total CO_2 adsorption capacities, 234.93 mg/g for CQD-X 133 and 211.56 mg/g for CQD-X 132. This suggests that the same structural features enhancing fluorescence, such as increased heteroatom doping and surface defect passivation enabled by higher thiourea and KOH content, also contribute to improved CO_2 capture. The presence of more nitrogen and sulfur dopants creates a greater number of active sites, facilitating both emissive behavior and chemical interaction with CO_2 molecules.

Conversely, samples with lower quantum yields, such as CQD-X 112 (13.12%) and CQD-X 113 (14.39%), correspondingly showed much lower total adsorption capacities, 38.44 mg/g and 80.28 mg/g, respectively. This further supports the notion that limited thiourea content hinders both fluorescent and adsorption performance due to reduced dopant incorporation and pore development. CQD-X 123, with a moderate quantum yield (18.61%), stands out for its high breakthrough capacity (1.3972 mg/g) and considerable total CO_2 uptake (184.68 mg/g), reinforcing the role of balanced doping in enhancing surface reactivity.

The results of this study are consistent with previous findings on the relationship between heteroatom doping, fluorescence behavior, and CO_2 adsorption. In particular, the CQD-X 133 and CQD-X 132 samples, synthesized with a 1:3:3 chitosan:thiourea:KOH ratio, exhibited the highest quantum yields (44.38% and 41.36%, respectively) and the greatest CO_2 sorption capacities (234.93 mg/g and 211.56 mg/g). These outcomes align with reports by Dong et al. and Liu et al., where increased N and S doping led to improved fluorescence due to the formation of abundant emissive centers and defect passivation (Dong et al., 2013) . The current results also reflect trends reported by Hu et al., where enhanced thiourea content significantly elevated quantum yield (Q. Hu et al., 2014). Importantly, the dual role of dopants as luminescent centers and active adsorption sites supports the observed synergy between photoluminescent efficiency and CO_2 uptake. As noted by Liu and

co-workers (H. Liu et al., 2018), heteroatom-induced surface functionalization (e.g., amine, hydroxyl, sulfonic groups) contributes to both radiative recombination and gas-binding interactions. Therefore, this study reinforces the idea that optimizing thiourea and KOH ratios not only tunes optical properties but also enhances adsorption performance, with the 1:3:3 composition emerging as the most effective configuration for maximizing both.

The quantum yield analysis in this study was conducted only up to sample CQD-X 133 because the experimental design and parameter range were predefined and intentionally limited to the six selected doping ratios (1:1:3, 1:2:3, 1:3:3, 1:1:2, 1:2:2, 1:3:2) (H. Cui et al., 2022; Pełech et al., 2022; J. Singh et al., 2019). These formulations were chosen based on the scope of the research objectives, which focused on evaluating the effect of heteroatom doping within this specific range. Although CQD-X 133 exhibited the highest quantum yield, further doping ratios beyond 133 were not included within the scope of this work. Future studies may expand the doping parameter to investigate whether additional ratios could yield even higher quantum yields or improved optoelectronic properties.

4.3.3 Thermal Stability

The thermal stability of N/S/O-CCQD-X samples with varying doping ratios was investigated using thermogravimetric analysis (TGA) to assess how changes in the amount of dopants influence the decomposition behavior and structural robustness of the materials. Evaluating thermal stability is crucial for determining the suitability of these materials for CO_2 adsorption, especially in applications that require repeated heating and regeneration. The TGA curves in Figure 4.10 reveal distinct weight loss stages corresponding to moisture evaporation, decomposition of volatile organic compounds, and degradation of the carbon framework while Table 4.6 shows the proximate analysis of N/S/O-CCQD-X adsorbents. By analyzing these thermal transitions across samples with different doping ratios, this section explores how increased levels of dopants such as thiourea and KOH affect the onset temperature, weight loss patterns, and residual mass, offering valuable insight into the relationship between doping level and material stability.

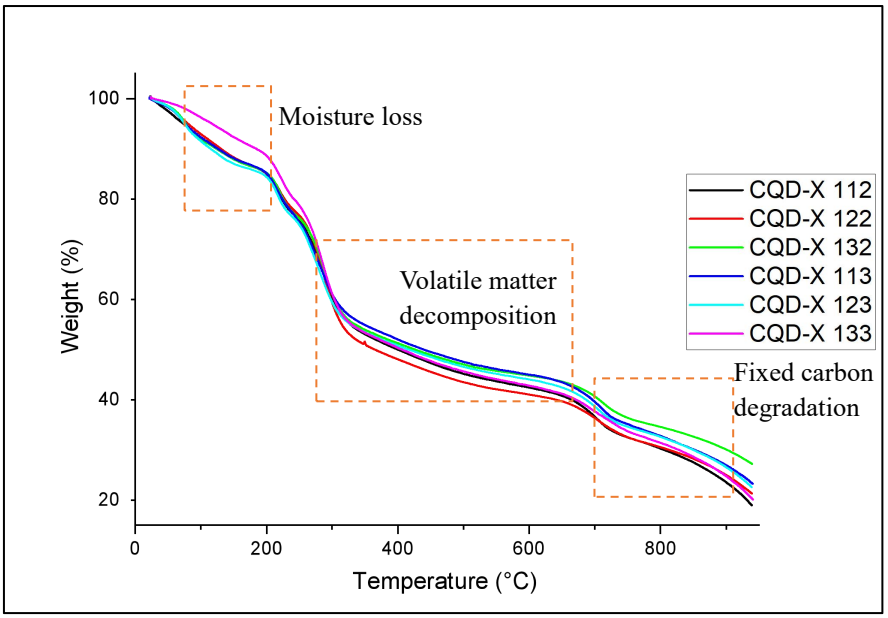

Figure 4.10 Thermogravimetric analysis curve of N/S/O-CCQD-X samples

Table 4.6
Proximate Analysis of N/S/O-CCQD-X Adsorbents

Sample	Moisture content (%)	Volatile matter (%)	Fixed carbon (%)	Ash content (%)
CQD-X 112	15.5	45.68	19.84	18.98
CQD-X 122	15.5	46.82	16.26	21.42
CQD-X 132	15.5	43.3	13.99	27.21
CQD-X 113	15.5	41.94	19.04	23.52
CQD-X 123	15.5	44.37	17.54	22.59
CQD-X 133	11.5	45.33	22.73	20.44

The thermogravimetric analysis and proximate analysis collectively reveal critical insights into the thermal behavior and compositional characteristics of the N/S/O-CCQD-X adsorbents. The initial weight loss (25–200°C) in the TGA profiles corresponds to moisture evaporation, corroborated by the proximate analysis showing consistent moisture content (~11.5–15.5%) across all samples. This uniformity suggests similar hydrophilic properties, likely due to shared precursor chemistry. The second decomposition stage (200–700°C) aligns with volatile matter release, where the proximate analysis quantifies volatile content at 41.94–46.82%. In literature, similar multi-stage behavior is reported: Yu et al. found ~6.7% loss to 200 °C (water

evaporation) and ~40.5% from 200–400 °C (cellulose/lignin breakdown) for nutshell-derived carbon (Y. Yu et al., 2025) , and Kolanowska et al. observed amino-acid CQDs lost most mass in two peaks between 200–350 °C (surface groups) and 300–450 °C (carbon matrix) (Kolanowska et al., 2022) . Our data align with these trends, confirming that Stage I (25–200 °C) is moisture release and Stage II reflects breakdown of carbon dost organics and dopant species.

Across carbon materials, a high fixed-carbon fraction correlates with greater thermal stability. In practice, adsorbent carbons with large fixed-C percentages withstand higher temperatures and retain more char. Notably, CQD-X 133 with the highest fixed carbon (22.73%) and moderate volatiles (45.33%) exhibited superior thermal stability in TGA, retaining the highest residual mass (20.44% ash). By contrast, CQD-X 132/122 (fixed C ≈14–16%) showed larger weight loss. This mirrors the notion that a more carbonized matrix (higher fixed C) yields a sturdier structure. For instance, Adame-Pereira et al. emphasize that carbon adsorbents have a high fixed carbon content, which makes them promising as adsorbent materials (Adame-Pereira et al., 2023). It was observed that CQD-X133's enhanced fixed-C (from the optimized thiourea/KOH doping) leads to superior thermal resistance is fully consistent with these reports (Adame-Pereira et al., 2023; Kolanowska et al., 2022).

The residual weight at 900°C (20–30% ash in proximate analysis) further highlights the role of inorganic constituents in stabilizing the carbon matrix. The balance in CQD-X 133 (moderately low ash with high fixed C) appears optimal: high enough carbonization to provide active sites, yet not so much inorganic filler as to block pores. Heteroatom doping has been shown to modify the structural integrity of carbon materials, where functional groups introduced at moderate dopant levels may volatilize during thermal treatment, reducing the stable carbon residue observed in TGA, whereas at sufficiently high dopant concentrations, stronger carbonization and stable heteroatom–carbon networks can form, increasing fixed carbon content again. This behaviour has been reported in studies of biomass-derived carbon materials with heteroatom doping, where excessive dopants can compromise the carbon framework and pore structure, and where the stability of heteroatom functional groups varies with thermal conditions (G. Li et al., 2025; Rangraz & Heravi, 2021; Y. Sun et al., 2023).

This aligns with reviews advising low ash in adsorbents (Adame-Pereira et al., 2023), and with experimental findings that moderate char yields (20–40%) are typical for stable CQDs (Kolanowska et al., 2022) . The integration of TGA and proximate

analysis demonstrates that doping ratios govern both thermal stability (via fixed carbon) and adsorption capacity. CQD-X 133 emerges as the optimal adsorbent, combining thermal resilience (high fixed carbon, moderate ash) with functional efficacy, validating the strategic role of thiourea/KOH in tailoring carbon dot properties for CO_2 capture. In summary, the TGA/proximate data are in line with previous work on carbon dots and related adsorbents. The observed moisture and volatile losses match established profiles (Kolanowska et al., 2022; Y. Yu et al., 2025), and the clear link between high fixed carbon/low ash and thermal endurance concurs with literature (Adame-Pereira et al., 2023).

Heteroatom doping has been shown to modify the structural integrity of carbon materials, where functional groups introduced at moderate dopant levels may volatilize during thermal treatment, reducing the stable carbon residue observed in TGA, whereas at sufficiently high dopant concentrations, stronger carbonization and stable heteroatom–carbon networks can form, increasing fixed carbon content again. This behaviour has been reported in studies of biomass-derived carbon materials with heteroatom doping, where excessive dopants can compromise the carbon framework and pore structure, and where the stability of heteroatom functional groups varies with thermal conditions (M. S. Lee et al., 2016; Pełech et al., 2022; Sevilla et al., 2013; J. Singh et al., 2019).

4.3.4 Physical Surface Characteristics and Morphology

The N_2 adsorption-desorption analysis was conducted to evaluate the textural properties of the N/S/O-CCQD-X samples, including surface area, pore volume, and pore size distribution. These characteristics are vital in determining the efficiency of CO_2 adsorption, as they directly influence the accessibility and availability of active sites within the material. By examining the isotherms and applying the Brunauer–Emmett–Teller (BET) model, insights into the porosity and structural architecture of the N/S/O-CCQD-X samples were obtained. This section presents a comparative analysis of how varying doping ratios and synthesis conditions impact the development of micro- and mesoporous structures, ultimately affecting the overall CO_2 capture performance of the adsorbents. Figure 4.11 presents the N_2 adsorption-desorption isotherm plots and Table 4.7 shows the surface area, pore area, pore volume and pore size for CQD-X 132, CQD-X 113, CQD-X 123, and CQD-X 133

samples, highlighting the influence of compositional differences on their porosity profiles.

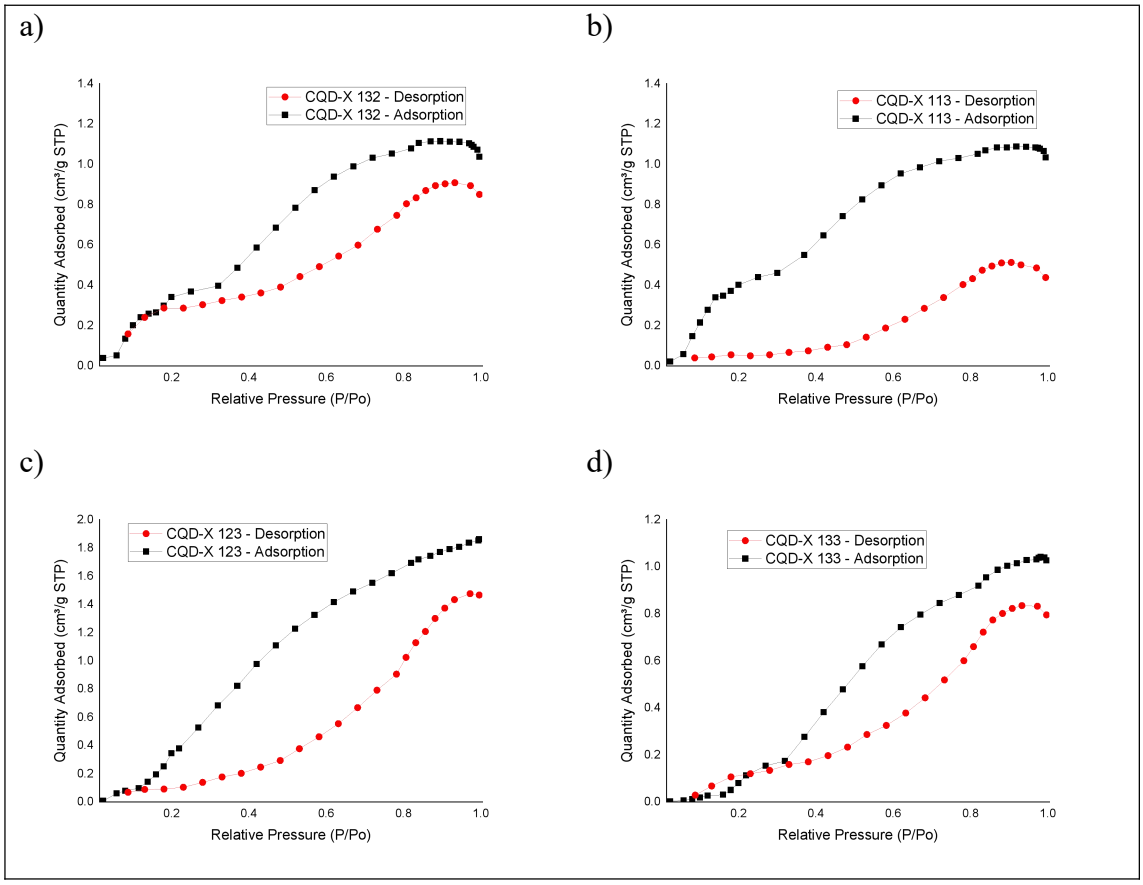

Figure 4.11 N_2 adsorption-desorption isotherm plot of a) CQD-X 132, b) CQD-X 113, c) CQD-X 123, and d) CQD-X 133 sample

Table 4.7
Surface Area, Pore Area, Pore Volume and Pore Size of CQD-X 132, CQD-X 113, CQD-X 123, and CQD-X 133

Sample	BET Surface Area, m^2/g	Langmuir Surface Area, m^2/g	Micropore area, m^2/g	Micropore volume, cm^3/g	Pore size (m^2/g)
CQD-X 132	0.0200	0.0234	0.6518	0.000290	-
CQD-X 113	0.1864	0.2617	0.2601	0.000156	-
CQD-X 133	0.2795	0.4174	0.0112	0.000055	0.071

The N_2 adsorption-desorption isotherm plots for the N/S/O-CCQD-X adsorbent samples (CQD-X 132, CQD-X 113, and CQD-X 133) in Figure 4.11 exhibit

a Type IV isotherm with a pronounced hysteresis loop, characteristic of mesoporous materials. At lower relative pressures ($P/P_0 < 0.1$), a sharp increase in nitrogen adsorption is observed, indicating monolayer adsorption on the surface. This is followed by a gradual rise at higher pressures, signifying multilayer adsorption and eventual capillary condensation within the mesopores. The adsorption-desorption curves reveal a H3-type hysteresis loop, typically associated with slit-like or plate-like mesopores, suggesting that the N/S/O-CCQD-X samples possess aggregated or layered structures rather than well-defined cylindrical pores. The adsorption branch reaches higher values compared to the desorption branch, indicating significant nitrogen uptake, with variations in maximum adsorption quantities across the samples likely due to differences in pore structure, surface area, or functionalization. Additionally, the delayed desorption at higher relative pressures suggests the presence of interconnected pore networks or pore-blocking effects, which can influence the overall adsorption capacity.

The surface textural data in Table 4.7 show clear relationships between textural properties and CO_2 uptake. CQD-X 133 exhibits the largest measured BET surface area (0.2795 m^2/g) and Langmuir surface area (0.4174 m^2/g) and also delivers the highest CO_2 capacity (234.93 mg/g), supporting the general expectation that greater accessible surface area contributes positively to adsorption. However, comparison among the other samples shows that total BET area alone does not fully predict performance.

CQD-X 132, despite a low BET surface area (0.0200 m^2/g), displays measurable micropore contribution (0.6518 m^2/g) and corresponds to a relatively high CO_2 capacity (211.56 mg/g). By contrast, CQD-X 113 which has an intermediate BET area (0.1864 m^2/g) but a very small micropore volume (0.000156 cm^3/g) shows the lowest CO_2 uptake (80.28 mg/g). Taken together, these results indicate that micropore character (volume and the presence of narrow micropores) is a dominant factor for CO_2 capture under the tested breakthrough conditions, while total BET surface area plays a supporting role.

In other words, materials with even modest BET area but with accessible micropores that match CO_2 dimensions can outperform samples with higher BET area but limited microporosity. This interpretation is consistent with studies showing that CO_2 uptake on carbonaceous adsorbents is largely controlled by the volume of narrow micropores (typically <0.8 nm) and that micropore volume often correlates more

directly with low-pressure CO_2 capacity than does broad BET area (M. S. Lee et al., 2016; Sevilla et al., 2013).

The differences in textural properties can be attributed to the extent of CCQDs immobilization within the xerogel matrix. The incorporation of CCQDs tends to block pore channels or alter the gel network, leading to reductions in measurable surface area and porosity, a trend supported by previous studies. For instance, in the development of carbon dots-embedded fluorescent silica xerogels, nitrogen sorption analysis revealed that the resulting materials, while maintaining their mesoporous nature, exhibited variations in pore size, pore volume, and surface area upon the incorporation of carbon dots. These changes are attributed to the partial filling or blocking of the pores by the embedded carbon dots, which can impede access to the internal surface area and reduce the overall porosity of the xerogel (Sarkar et al., 2019).

Similarly, in the synthesis of carbon quantum dot-functionalized aerogels for gas sensing applications, the integration of CQDs into the aerogel matrix led to modifications in the textural properties of the material. The presence of CQDs within the porous network can obstruct pore channels, thereby decreasing the accessible surface area and pore volume, which are critical parameters for adsorption processes (R. Wang et al., 2013). These findings suggest that the incorporation of CCQDs into xerogel matrices can result in decreased surface area and pore volume as summarizes in Table 4.7 due to pore blocking and structural changes within the composite material. Such modifications can adversely affect the material's performance in applications like CO_2 capture, where high surface area and porosity are essential for efficient adsorption.

High-resolution transmission electron microscopy (HRTEM) provides detailed structural and morphological insights into the synthesized N/S/O-CCQD-X materials, including lattice fringes, particle shape, and size distribution.

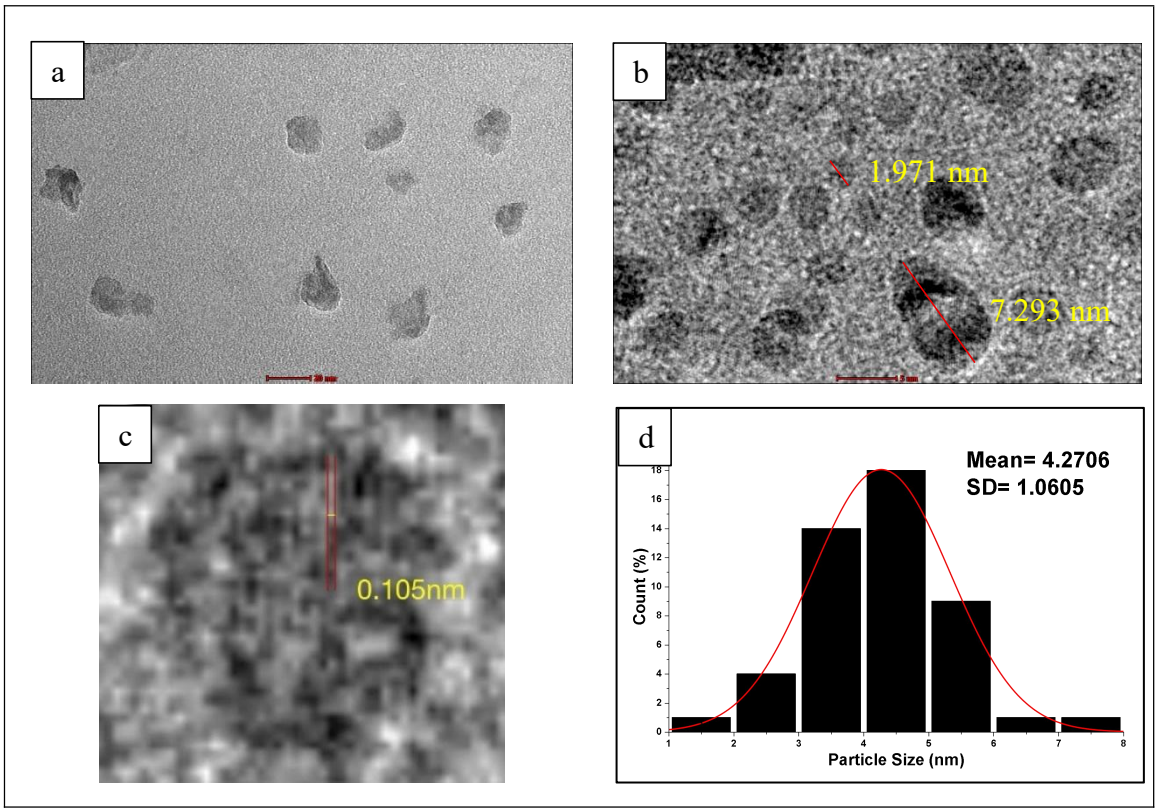

Plate 4.2 HRTEM image of CQD-X 133 at a) 20nm, b) 5nm, c) lattice fringes image, and d) showing particle size distribution histogram with an average diameter of 4.27 ± 1.06 nm.

As illustrated in Plate 4.2a and b, the N/S/O-CCQD-X are observed as uniformly dispersed, nearly spherical particles at the nanoscale, with minimal aggregation across image scales of 20 nm and 5 nm. The particles exhibit a relatively narrow size distribution, ranging from 1.971 to 7.293 nm, indicating controlled synthesis and effective dispersion (Alqahtani et al., 2025) . The appearance of both smaller and larger dots in the HRTEM images suggests slight variations in nucleation and growth processes—where smaller particles likely represent early-stage formation, while larger ones may result from extended growth or localized precursor enrichment. This controlled size heterogeneity, while still within the typical carbon quantum dot range (<10 nm), does not indicate polydispersity but rather reflects a well-regulated synthesis process. Such morphology, featuring small, well-separated spherical particles, is advantageous for adsorption applications, as it ensures high surface area exposure, uniform interaction sites, and consistent packing, favorable characteristics for efficient CO_2 capture (L. Zhang et al., 2023).

In addition, the lattice-resolved imaging, where a distinct lattice fringe is observed in Plate 4.2c shows an interplanar spacing of approximately 0.105 nm. This

indicates a highly crystalline nature of the CQDs, often associated with graphitic domains (Nguyen et al., 2022). By comparison, the standard graphitic (002) spacing is about 0.34 nm, so the much smaller observed spacing likely arises from higher-index graphitic planes or lattice distortions induced by heteroatom doping. Such well-defined lattice fringes reflect an ordered carbon framework, consistent with previous reports of CQDs exhibiting fringes on the order of 0.21–0.22 nm (Nguyen et al., 2022; Ren et al., 2024).

Particle size analysis of the CQD-X 133 sample performed on 48 randomly selected particles in Plate 4.2d, measured using ImageJ software revealed an average particle size of 4.27 ± 1.06 nm. This dimension falls within the typical range for carbon quantum dots (generally <10 nm), confirming the successful synthesis of nanoscale carbon materials (Ren et al., 2024) . The measured size distribution is essentially Gaussian, implying homogeneous particle formation, which is favorable for uniform adsorption behavior in gas capture applications (Nguyen et al., 2022) . Similar particle size distributions have been reported in studies using biomass-derived precursors, such as 5 nm CQDs synthesized from Pista Shell (PSE) agro waste (Manjubaashini et al., 2024) and 4.63 ± 0.87 nm from corn stover precursors (Paneru et al., 2024), supporting the reliability of the current synthesis approach.

Overall, the HRTEM results of CQD-X 133 confirm the formation of monodispersed, crystalline CQDs with lattice fringes indicative of graphitic ordering. The narrow size distribution and observable nanostructure validate the success of the synthesis approach, making these CQDs suitable candidates for applications such as CO_2 capture or sensing, where nanoscale surface functionality plays a vital role (L. Zhang et al., 2023).

The FESEM image of CQD-X 133 (Plate 4.3) further corroborates these findings, revealing a porous, interconnected surface morphology. This physical structure aligns with the BET and pore analysis, confirming that the enhanced CO_2 sorption performance is closely linked to the well-developed surface architecture of CQD-X 133.

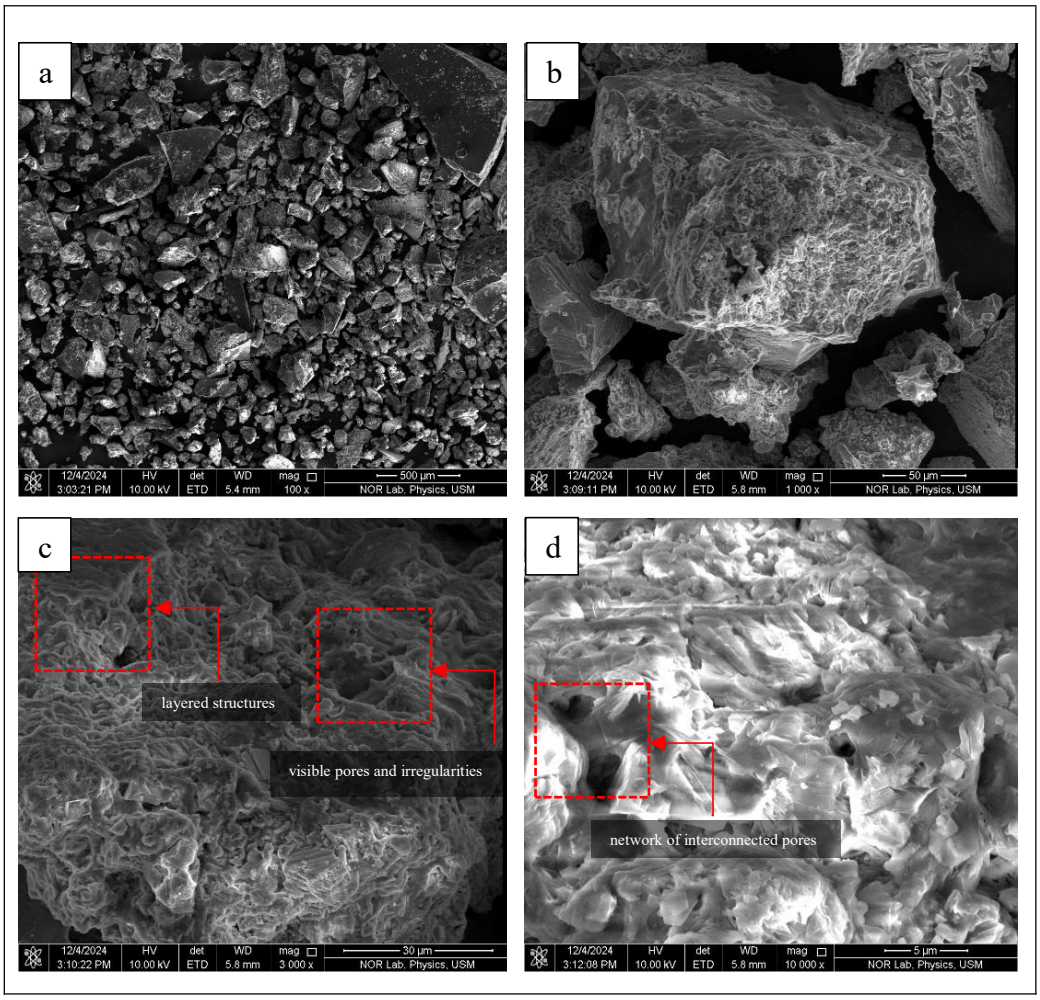

Plate 4.3 FESEM images of CQD-X 133 from various magnifications: a) 100x; b) 1000x; c) 3000x; d) 10000x

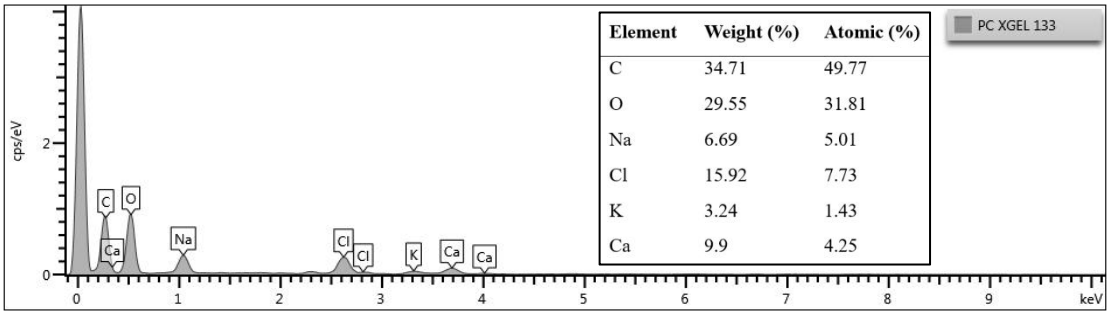

Element	Weight (%)	Atomic (%)
C	34.71	49.77
O	29.55	31.81
Na	6.69	5.01
Cl	15.92	7.73
K	3.24	1.43
Ca	9.9	4.25

Figure 4.12 Quantitative analysis of the energy dispersive X-ray (EDX) analysis on CQD-X 133 sample

The Field Emission Scanning Electron Microscopy (FESEM) image of the CQD-X 133 sample, which exhibits the highest CO_2 adsorption capacity among the tested samples, provides valuable insights into its morphological characteristics. The FESEM analysis reveals a relatively smooth and homogeneous surface morphology, indicative of a uniform distribution of the CCQDs within the xerogel matrix. This

uniformity suggests that the CCQDs are well-integrated into the xerogel structure, potentially facilitating effective interaction sites for CO_2 molecules.

In related studies, the morphology of CQD-based materials has been shown to significantly influence their adsorption capabilities.or instance, a study on natural carbon quantum dots (NCQDs) demonstrated that a spherical morphology with an average size of approximately 17 nm contributed to effective adsorption properties. The FESEM images in this study illustrated a uniform distribution of NCQDs, which was correlated with enhanced adsorption performance (*Nanosensors of Fluorescent Carbon Quantum Dots Derived from Banana Peel: Application in Sr2+ and Co2+ Detection*, n.d.) . Furthermore, the elemental composition of CQD-based adsorbents plays a crucial role in their CO_2 capture efficiency. Energy Dispersive X-ray (EDX) analysis attached to FESEM has been utilized to confirm the presence of elements such as carbon, oxygen, nitrogen, and sulfur in NCQDs. The incorporation of these heteroatoms can introduce functional groups that enhance CO_2 adsorption through various interactions, including hydrogen bonding and dipole–quadrupole interactions.

The smooth and homogeneous surface observed in the FESEM image of CQD-X 133 suggests minimal pore blockage within the xerogel matrix, which is advantageous for gas diffusion and adsorption processes. This morphological feature, combined with the potential presence of functional groups introduced by the N/S/O doping, likely contributes to the superior CO_2 adsorption capacity of the CQD-X 133 sample. In summary, the FESEM analysis of the CQD-X 133 sample indicates a well-integrated and uniform morphology, which, along with its elemental composition, aligns with characteristics found in other effective CQD-based adsorbents. These structural attributes are instrumental in facilitating efficient CO_2 capture, highlighting the potential of CQD-X 133 as a promising material for environmental remediation applications.

4.3.5 Surface Chemistry and Elemental Distribution

Fourier Transform Infrared (FTIR) spectroscopy was employed to investigate the surface chemistry and functional group characteristics of the N/S/O-CCQD-X adsorbents synthesized with varying doping ratios. The presence and intensity of specific vibrational bands provide insight into the incorporation of heteroatoms (N, S, and O) resulting from the different precursor compositions. These findings offer a

deeper understanding of how chemical functionalities contribute to both the optical and adsorption properties of the N/S/O-CCQD-X materials. The comparative FTIR spectra for all synthesized samples are presented in Figure 4.13, highlighting the effect of varying chitosan:thiourea:KOH ratios on the surface chemistry of the adsorbents.

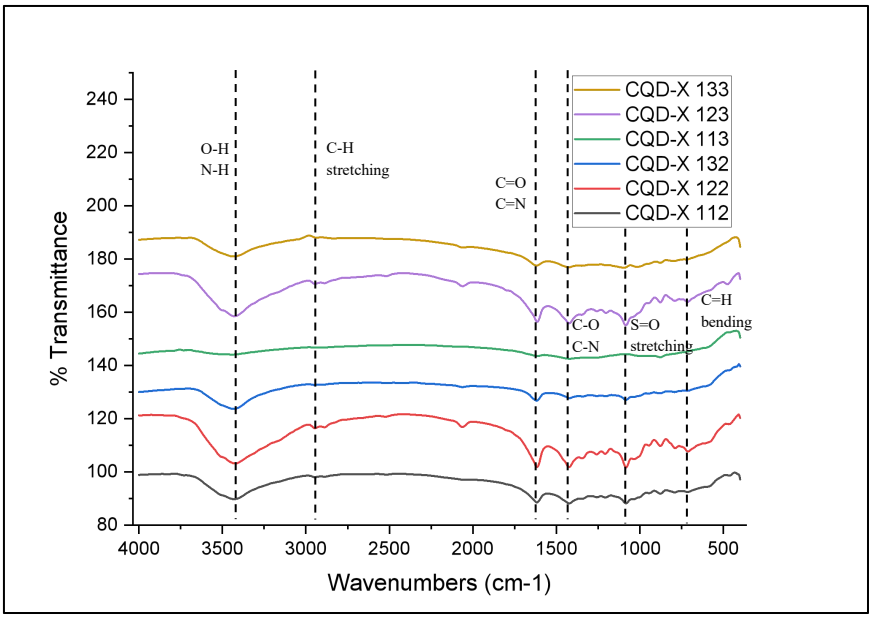

Figure 4.13 FTIR Spectra of N/S/O-CCQD-X with Varying Doping Ratio

The FTIR spectra of the N/S/O-CCQD-X adsorbent samples exhibit several distinct peaks, indicating the presence of various functional groups that contribute to their CO_2 adsorption capabilities. A broad absorption band around 3435 cm^{-1} is commonly attributed to the stretching vibrations of hydroxyl (-OH) and amine (-NH) groups, indicating the presence of these functionalities on the CQDs surface. These groups play a crucial role in enhancing the hydrophilicity and surface reactivity of the CQDs. The peaks observed near 2,900 cm^{-1} are attributed to C–H stretching vibrations, indicating aliphatic hydrocarbons. The peaks observed around 1600–1700 cm^{-1} can be attributed to the presence of both C=N stretching (imine) and C=O (oxygen-containing functional groups) in N/S/O-CCQD-X samples. It suggests a combination of graphitic carbon domains and oxygen-rich functional sites, both of which contribute to CO_2 adsorption. The graphitic domains enhance material stability and conductivity, while the oxygen functional groups increase the adsorption sites available for CO_2 binding.

Additionally, peaks around 1200–1400 cm^{-1} indicate the presence of C–O, C–N, and S=O bonds, confirming the successful doping of oxygen, nitrogen, and sulfur

in the N/S/O-CCQD-X samples. The presence of these functional groups suggests that the N/S/O-CCQD-X materials possess a rich surface chemistry, making them highly interactive with CO_2 molecules. The nitrogen-based functional groups amine (C–N) contribute to chemisorption by forming weak interactions with CO_2, while oxygen-based groups (C–O) enhance physisorption through dipole interactions. These surface functionalities likely result from the chitosan and thiourea doping process, enhancing the overall adsorption efficiency. The absorption bands near 1280 cm^{-1} are linked to C-O stretching vibrations, suggesting the incorporation of oxygen-containing groups such as carboxyl and epoxy groups on the CQDs surface, those around 1000 cm^{-1} correspond to C–S stretching, further verifying the incorporation of sulfur-containing functional groups while the peak at 766 cm^{-1} arises due to the stretching of the C=C bond (Fawaz et al., 2023) The presence of these heteroatoms enhances the basicity of the CQDs, which improves their affinity toward acidic CO_2 molecules.

In comparison, the FTIR spectra of CQDs synthesized from o-phenylenediamine dissolved in toluene exhibit similar functional groups. A broad peak around 3435 cm^{-1} corresponds to O-H and N-H stretching vibrations, indicating the presence of hydroxyl and amine groups. The peak at approximately 1630 cm^{-1} is attributed to C=O stretching vibrations, suggesting the presence of carbonyl groups. Additionally, peaks around 1384 cm^{-1} and 1110 cm^{-1} are associated with C-N and C-O stretching vibrations, respectively, indicating the incorporation of amine and oxygen-containing groups (Marković et al., 2023).

Overall, the FTIR results confirm that the functional groups present in N/S/O-CCQD-X adsorbents such as hydroxyl (–OH), amine ($–NH_2$), carbonyl (C=O), carboxyl (–COOH), and C–N/C–S bonds play critical roles in enhancing both the optical and adsorption properties of the materials. The successful doping with nitrogen, sulfur, and oxygen creates a chemically rich surface that provides abundant active sites for CO_2 interactions through both physisorption and chemisorption mechanisms. This is strongly supported by the observed CO_2 sorption capacities, where samples with more prominent surface functionalities such as CQD-X 133 and CQD-X 132 exhibited the highest adsorption capacities of 234.93 mg/g and 211.56 mg/g, respectively. These samples also demonstrated strong and well-defined FTIR peaks associated with N/S/O functional groups, further confirming the correlation between surface chemistry and adsorption efficiency. Conversely, samples like CQD-X 112, which displayed weaker functional group intensity in the FTIR spectra, showed

significantly lower CO_2 uptake at 38.44 mg/g. This comparison reinforces that heteroatom-rich surface functionalities, particularly those introduced through optimized doping ratios, are key contributors to the improved CO_2 capture performance of N/S/O-CCQD-X materials.

Table 4.8
CHNS elemental analysis of N/S/O-CCQD-X Adsorbents

Sample	Weight(mg)	Carbon%	Hydrogen%	Nitrogen%	Sulfur%
CQD-X 112	2.082	26.69	4.60	0.43	0.45
CQD-X 133	1.920	25.39	4.30	0.81	0.96
Spent CQD-X 133	1.973	26.23	4.45	0.86	1.07

The CHNS elemental analysis of CQD-X 112, CQD-X 133, and the spent CQD-X 133 provides valuable insights into the composition and potential functional properties of the synthesized adsorbents. CQD-X 112 exhibits a carbon content of 26.69%, hydrogen at 4.60%, nitrogen at 0.43%, and sulfur at 0.45%. In comparison, CQD-X 133, which was synthesized using a higher doping ratio, shows a slightly lower carbon content (25.39%) but substantially higher nitrogen (0.81%) and sulfur (0.96%) contents. This indicates more effective incorporation of heteroatoms due to the increased thiourea and KOH content, which enrich the surface with basic functional groups conducive to CO_2 interaction. Correspondingly, this compositional enhancement is reflected in their CO_2 sorption capacities: CQD-X 133 achieved the highest CO_2 uptake of 234.93 mg/g, while CQD-X 112 having the lowest nitrogen and sulfur contents recorded only 38.44 mg/g. This stark contrast supports the role of heteroatom doping in creating more active adsorption sites and improving affinity toward CO_2 molecules.

After the adsorption process, the spent sample of CQD-X 133 is analyzed to assess any changes in its elemental composition. Typically, a decrease in carbon content and alterations in nitrogen and sulfur percentages are observed, with carbon content at 26.23%, hydrogen at 4.45%, nitrogen slightly increasing to 0.86%, and sulfur increasing to 1.07%. The slight variations in nitrogen and sulfur content suggest potential interactions between the CO_2 molecules and the heteroatoms, possibly through chemisorption mechanisms. Comparing these findings with existing literature, a study on chitosan-derived CQDs reported similar elemental compositions, with

significant nitrogen content due to the chitosan precursor (Janus et al., 2019a) . Another research on nitrogen and sulfur co-doped carbon quantum dots demonstrated that the incorporation of these heteroatoms enhances the adsorption properties of the material (Chandra et al., 2020).

These comparisons suggest that the doping strategies employed in CQD-X 112 and CQD-X 133 are effective in modifying the elemental composition to improve CO_2 adsorption performance. In summary, the CHNS elemental analysis data confirm that increased doping with nitrogen and sulfur as implemented in CQD-X 133 directly enhances CO_2 adsorption capacity, validating the synthesis approach and aligning with trends reported in related studies.

To understand the surface chemistry and the nature of the functional groups responsible for CO_2 capture, X-ray photoelectron spectroscopy (XPS) analysis was conducted on the CQD-X 133 sample, which demonstrated the highest CO_2 adsorption capacity (234.93 mg/g). The surface composition and bonding states of carbon, nitrogen, oxygen, sulfur, and calcium atoms in the N/S/O-CCQD-X framework were examined to reveal the distribution of heteroatoms and their corresponding chemical environments. These surface functional groups, particularly nitrogen and oxygen-containing species play a crucial role in enhancing CO_2 adsorption by offering electron-rich sites for chemisorption and polar groups for physisorption.

The higher CO_2 uptake of CQD-X 133 correlates with the observed abundance of pyridinic-N, carboxyl (–COOH), hydroxyl (–OH), and Ca–O functionalities, all of which are favorable for strong CO_2 interactions. The following deconvoluted XPS spectra as shown in Figure 4.14 further elucidate the chemical states of key elements in CQD-X 133 and confirm the successful incorporation of these active functional moieties.

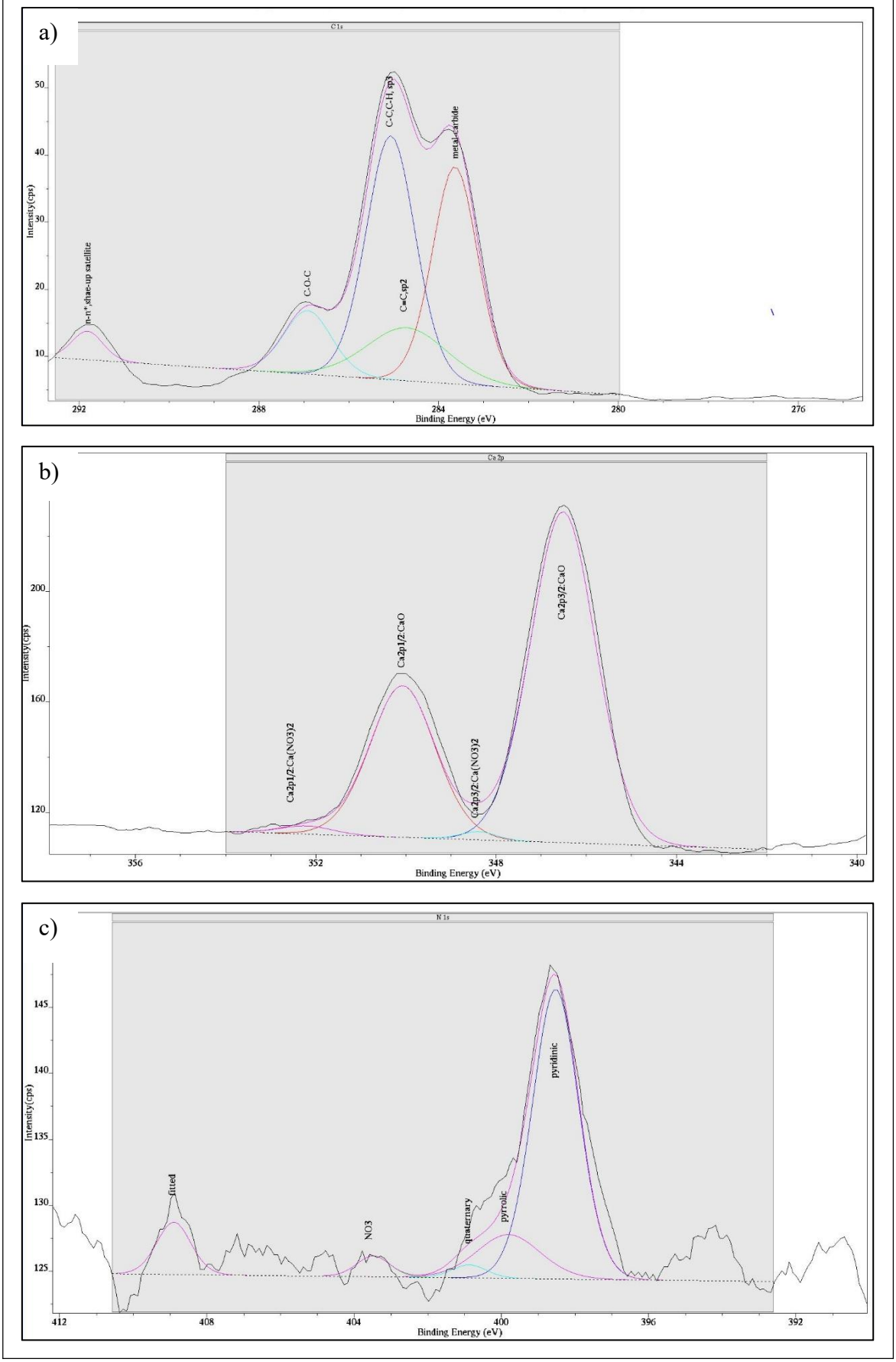
a)
C 1s
Intensity(cps)
Binding Energy (eV)
π-π*,shae-up satellite
C-O,C
C-C,C-H, sp3
CaC,sp2
metal-carbide
b)
Ca 2p
Intensity(cps)
Binding Energy (eV)
Ca2p1/2:Ca(NO3)2
Ca2p1/2:CaO
Ca2p3/2:Ca(NO3)2
Ca2p3/2:CaO
c)
N 1s
Intensity(cps)
Binding Energy (eV)
fitted
NO3
quaternary
pyrrolic
pyridinic

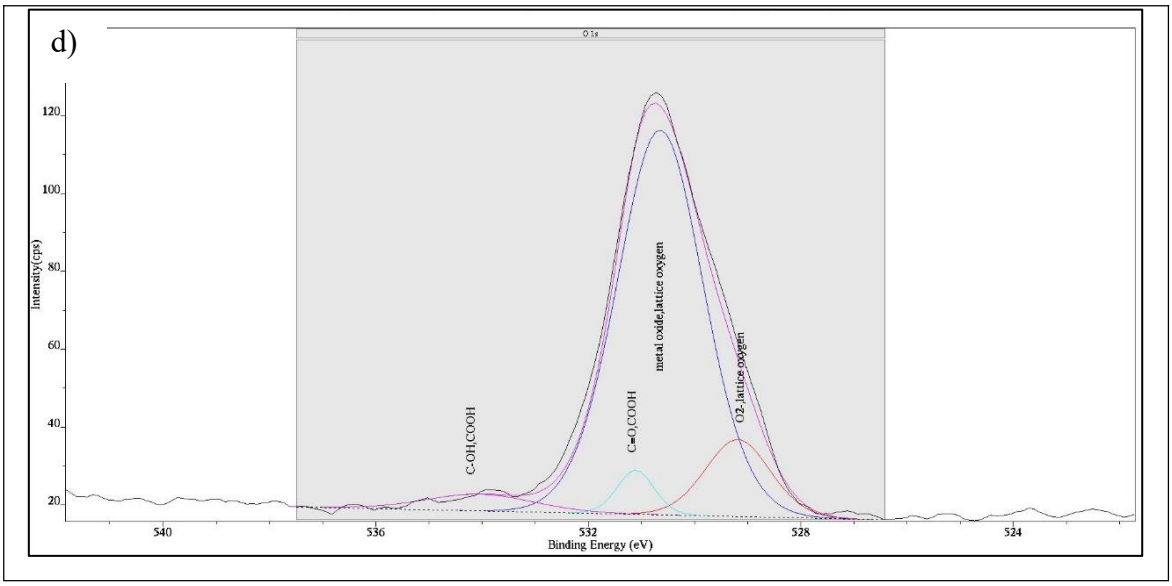

Figure 4.14 a) Deconvoluted C 1s Spectra, b) Deconvoluted Ca 2p Spectra, c) Deconvoluted N 1s Spectra, d) Deconvoluted O 1s Spectra of CQD-X 133

The deconvoluted C 1s X-ray photoelectron spectroscopy (XPS) spectrum of the CQD-X 133 sample reveals several distinct peaks, indicating the presence of different carbon bonding environments on the surface of the material. The dominant peak at approximately 284.4 eV corresponds to sp^2-hybridized carbon atoms (C=C/C–C), which are typical of graphitic or aromatic carbon structures and contribute to the structural stability and conductivity of the CQDs (Nguyen et al., 2022). A second peak around 285.8 eV is assigned to carbon in C–C or C–H bonds (aliphatic or saturated hydrocarbons), suggesting the presence of less conjugated carbon species. The peak at ~286.9 eV is attributed to carbon-oxygen single bonds (C–O–C), indicating the presence of ether or epoxy groups. Another minor peak observed at ~291.8 eV represents π–π* shake-up satellites, typically associated with aromatic systems, confirming the conjugated π structure of the material (*Carbon | XPS Periodic Table - MY*, n.d.) . The presence of these oxygen-containing functional groups confirms successful heteroatom doping and functionalization, which play a key role in improving the CO_2 adsorption performance of the CQD-X 133 adsorbent by providing active sites for chemisorption and enhancing overall surface reactivity.

The deconvoluted Ca 2p XPS spectrum of the CQD-X 133 sample displays two main spin–orbit doublets: Ca $2p_{3/2}$ and Ca $2p_{1/2}$, located approximately at 347.1 eV and 350.6 eV, respectively. These peaks are characteristic of calcium species in a Ca^{2+} oxidation state and confirm the presence of calcium within the N/S/O-CCQD-X xerogel matrix. The primary peaks at ~347.1 eV (Ca $2p_{3/2}$) and ~350.6 eV (Ca $2p_{1/2}$)

are assigned to calcium bonded with oxygen, specifically in the form of Ca–O or calcium carbonate ($CaCO_3$), which is typically introduced during the xerogel formation using calcium carbonate and alginate. These interactions contribute to the structural rigidity and stability of the immobilized CQDs framework. Additional smaller peaks near 348.2 eV and 351.8 eV correspond to Ca 2p signals attributed to calcium bound to nitrogen and oxygen-containing species, such as $Ca(NO_3)_2$ or Ca–N/O complexes. These indicate potential coordination of calcium with heteroatoms present in the doped CQDs, supporting the successful integration of Ca^{2+} into the xerogel structure. The overall presence of calcium and its interaction with oxygen and nitrogen functionalities not only validates the incorporation of calcium during gelation but also suggests a supportive role in enhancing the material's porosity, surface functionality, and possibly CO_2 adsorption performance.

The deconvoluted N 1s XPS spectrum of the CQD-X 133 sample reveals multiple nitrogen configurations, indicating successful nitrogen doping and a diverse nitrogen environment in the material. The main peaks are attributed to pyridinic-N (~398.8 eV), pyrrolic-N (~400.1 eV), and graphitic or quaternary-N (~401.1 eV) (Nguyen et al., 2022). These nitrogen species are commonly found in nitrogen-doped carbon materials, and each plays a distinctive role in enhancing CO_2 adsorption performance. Pyridinic-N (~398.8 eV) is the nitrogen species bonded to two carbon atoms at the edge of graphitic layers and contributes a lone pair of electrons, enhancing basicity and providing active sites for CO_2 chemisorption through acid-base interactions. Pyrrolic-N (~400.1 eV) associated with five-membered rings, pyrrolic nitrogen can interact with CO_2 molecules via electron donor-acceptor mechanisms, aiding in moderate CO_2 affinity. Quaternary or Graphitic-N (~401.1 eV): is a form of nitrogen that replaces a carbon atom within the graphitic plane and contributes to improved electrical conductivity and structural stability, though it has a relatively lower impact on CO_2 capture compared to pyridinic and pyrrolic nitrogen. Minor peaks at higher binding energies suggest the presence of oxidized nitrogen species or nitrate (NO_3^-), possibly introduced during the synthesis or immobilization process. These may also contribute to surface polarity and CO_2 interaction. Overall, the spectrum confirms the presence of multiple nitrogen species in CQD-X 133, supporting the enhanced adsorption properties of the material due to the presence of basic sites favorable for CO_2 interaction.

The deconvoluted O 1s XPS spectrum of the CQD-X 133 sample provides detailed insight into the various oxygen-containing functional groups present on the surface. The spectrum shows multiple distinct peaks, indicating different chemical environments of oxygen atoms. The primary peak centered around 530.1 eV is attributed to metal oxide lattice oxygen, commonly associated with Ca–O bonds formed during the xerogel gelation process using calcium carbonate. This strong presence confirms the structural integration of calcium within the xerogel matrix. Another peak appearing at approximately 531.5 eV corresponds to oxygen in carbonyl or carboxyl (C=O/COOH) groups, which are known to enhance the surface acidity and affinity for CO_2 molecules through dipole–quadrupole interactions. The peak near 532.6 eV is assigned to C–O or C–OH groups, indicating the presence of hydroxyl functionalities that contribute to surface hydrophilicity and can serve as additional interaction sites for CO_2 molecules. A smaller peak at around 533.7 eV suggests the presence of adsorbed water or loosely bound oxygen species on the surface. Overall, the diverse oxygen functionalities observed in the O 1s spectrum confirm the chemical richness and functionalization of the CQD-X 133 sample, which are critical for improving CO_2 adsorption through both physisorption and chemisorption mechanisms. These functional groups not only enhance the surface reactivity but also improve the interaction between the adsorbent and CO_2 molecules.

Overall, doped CQDs often exhibit enhanced CO_2 adsorption due to these surface groups. Oxygen-containing groups (–OH, –COOH) and nitrogen functionalities create a highly polarized, basic surface. For instance, ultrasound-treated biochars with abundant –COOH and –OH (as seen by XPS/FTIR) showed a 9× higher CO_2 uptake than untreated biochars (Quan et al., 2023). XPS-monitored increases in C=O and COOH peaks generally correlate with higher uptake. Nitrogen doping is particularly impactful: pyridinic and pyrrolic N increase the basicity. XPS studies of N-doped carbons (e.g. from chitosan-derived CQDs or activated carbons) find new N 1s peaks (pyridinic, pyrrolic) after doping (Quan et al., 2023), and correspondingly higher CO_2 capacity. Quan et al. (via XPS) identified pyridine-N and pyrrole-N on a chitosan-doped carbon surface, reporting a CO_2 capacity of 5.83 mmol/g at 273 K – significantly above the undoped case (Quan et al., 2023). The authors attribute this to the increased surface alkalinity from N sites. Similarly, sulfur doping (e.g. via ammonium sulfate) introduces sulfoxide/sulfonate groups that XPS confirms and which can interact with CO_2 molecules to raise uptake (Quan et al., 2023). In

summary, XPS-detected surface groups on N/S/O-CCQD-X (–OH, –COOH, C=O, N, S) create acid/base interaction points and dipoles that boost CO_2 uptake. Greater coverage of –COOH and –OH (XPS C=O/O–C=O peaks) enhances physisorption via polar interactions, while pyridinic-N (XPS N1s ~398 eV) provides chemisorptive Lewis base sites (Quan et al., 2023; Shibuya et al., 2022). Thus, XPS characterization of N/S/O-CCQD-X directly identifies the functional moieties responsible for improved CO_2 capture.

4.4 Breakthrough Analysis of CO_2 Removal at Different Adsorption Parameters

Among all formulations tested, CQD-X 133 demonstrated the highest CO_2 adsorption capacity and the most favourable physicochemical characteristics. Therefore, CQD-X 133 was selected as the optimized adsorbent for all subsequent breakthrough studies. The following sections examine how adsorption temperature, CO_2 feed concentration, and flow rate influence its CO_2 removal performance.

4.4.1 Effect of Adsorption Temperature

Temperature is one of the most influential parameters in gas adsorption processes, as it directly affects the adsorbate–adsorbent interactions and adsorption capacity. For CO_2 removal using solid adsorbents such as N/S/O-CCQD-X, the process is typically exothermic; thus, elevated temperatures may reduce adsorption efficiency by weakening the physical and chemical interactions between CO_2 molecules and active surface sites. Conversely, excessively low temperatures may hinder gas diffusion and adsorption kinetics. Therefore, identifying the optimal adsorption temperature is crucial to maximize performance. To evaluate the thermal sensitivity of the N/S/O-CCQD-X adsorbent, breakthrough experiments were conducted at varying temperatures while maintaining constant flow rate and CO_2 concentration. The results are presented in Figure 4.15, which shows the breakthrough curves of the N/S/O-CCQD-X adsorbent at different adsorption temperatures.

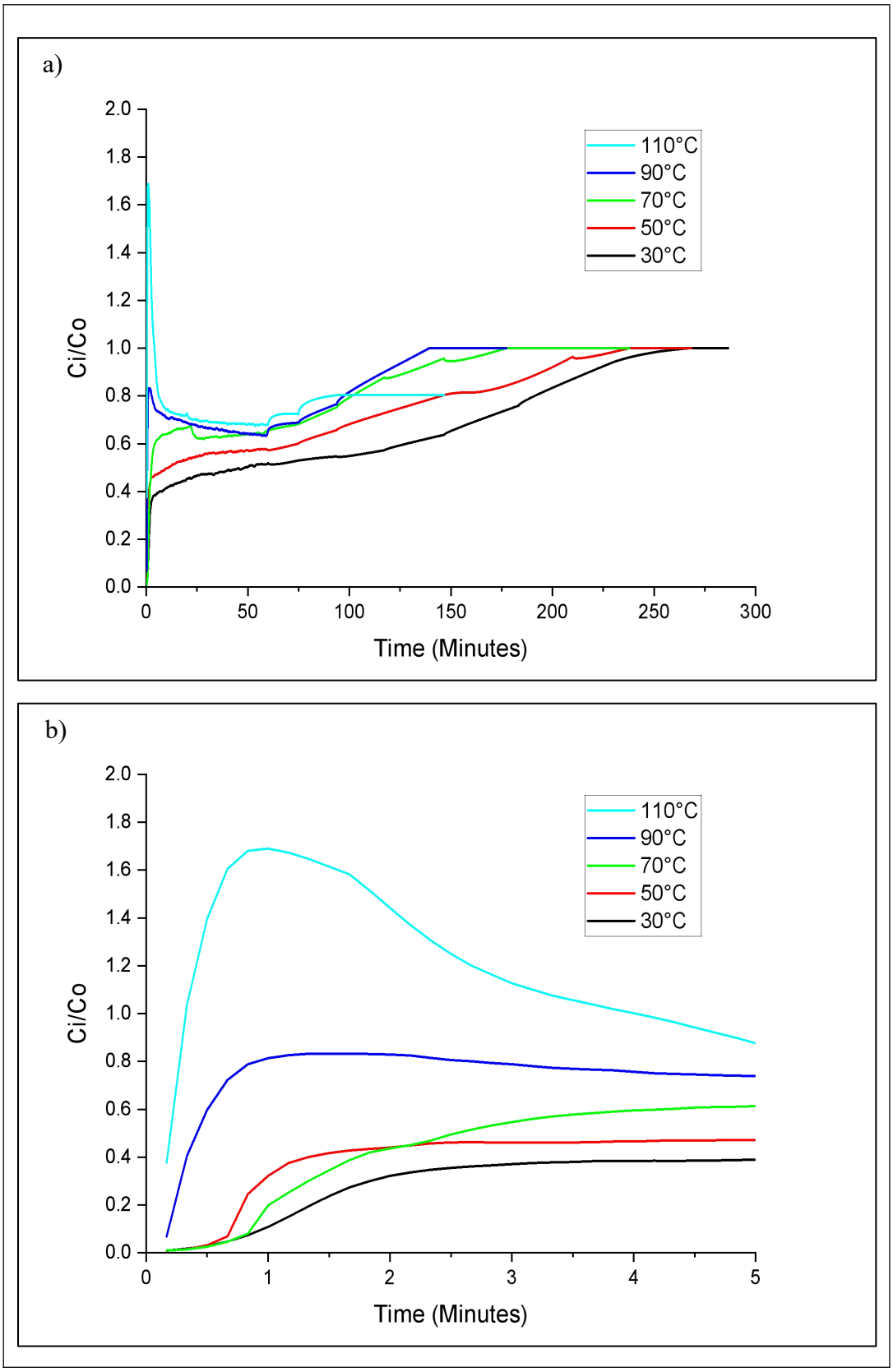

Figure 4.15 a) Breakthrough Curve of N/S/O-CCQD-X Adsorbent at Various Temperature b) Enlarge Image of Breakthrough Curve of N/S/O-CCQD-X Adsorbent at Various Temperature

Table 4.9
N/S/O-CCQD-X Adsorbents Breakthrough Time and Adsorption Capacity at Various Temperature

Temperature (℃)	Breakthrough time (min)	Breakthrough capacity (mg/g)	Total adsorption capacity (mg/g)	Total adsorption time (min)
30	1.00	0.5943	358.80	268.50
50	0.83	0.5911	306.33	238.00
70	0.67	0.5304	202.87	171.00
90	0.33	0.4975	171.85	139.50
110	0.17	0.4715	107.13	93.83

The breakthrough data reveal significant temperature-dependent trends in CO_2 adsorption performance, with 30°C emerging as the optimal condition for maximizing both breakthrough time (1.00 min) and total adsorption capacity (358.80 mg/g). This performance aligns with the exothermic nature of CO_2 adsorption, where lower temperatures enhance adsorbate-adsorbent interactions.

The highest total capacity (358.80 mg/g) and prolonged adsorption time (268.50 min) at 30°C suggest stronger physisorption and efficient pore utilization. The breakthrough capacity (0.5943 mg/g) reflects rapid initial uptake, critical for practical applications. By 110°C, total capacity drops to 107.13 mg/g (70% reduction), and breakthrough time collapses to 0.17 min. This mirrors thermodynamic expectations, where elevated temperatures reduce adsorption affinity due to increased molecular kinetic energy and desorption.

Despite identical breakthrough times at 30°C and 70°C (1.00 min), the total capacity at 70°C is 43% lower (205.53 mg/g). This implies that while initial adsorption kinetics remain competitive at moderate temperatures, sustained performance requires lower thermal energy. At 90–110°C, breakthrough occurs in less than one minute (0.33 min and 0.17 min respectively) with correspondingly low capacities (0.4975–0.4715 mg/g) indicate pore saturation and accelerated desorption, rendering the adsorbent ineffective for continuous capture.

This thermally sensitive behavior aligns well with previous studies. Carbon-based sorbents, including activated carbon and zeolites, have demonstrated decreased CO_2 uptake as temperatures rise from ~25 °C to 100 °C, supporting the notion of temperature-limited physisorption (Tsiotsias et al., 2023) . Similarly, DAAB-

functionalized alumina exhibited its highest CO_2 capacity at 35 °C, while performance significantly decreased at 55 °C due to weakened amine-CO_2 interactions (Krishnaiah et al., 2014). Furthermore, TEPA-impregnated silica gel achieved a CO_2 capacity of approximately 1.9 mmol/g at room temperature, which also declined sharply with increased temperature (Gu et al., 2022).

In the context of carbon quantum dot (CQD)-based adsorbents, similar behavior is reported. Ligero et al. observed decreased CO_2 capacity with increased column temperatures for exothermic systems (Ligero et al., 2023). Broud et al., using simulations, confirmed that CO_2 binds most strongly to CQDs at ambient temperature and that this affinity can be enhanced via heteroatom doping (Broud et al., 2023). Additionally, Kong et al. reported that CQD materials possess abundant surface functional groups whose adsorption performance is highly temperature sensitive (Kong et al., 2024). These findings directly support the observed trend in this study, where CQD-X 133 exhibited reduced CO_2 uptake with increasing temperature, reinforcing the conclusion that physisorption dominates the adsorption mechanism in these materials.

4.4.2 Effect of Gas Feed Flowrate

The gas feed flowrate plays a crucial role in determining the adsorption efficiency and dynamic performance of an adsorbent material. It directly influences the contact time between CO_2 molecules and the active sites on the adsorbent surface, thereby affecting both breakthrough time and total adsorption capacity. A low flow rate allows more time for CO_2 to diffuse into pores and interact with available adsorption sites, while excessively high flow rates reduce contact time, leading to premature breakthrough. The influence of gas feed flowrate on CO_2 capture behavior of the N/S/O-CCQD-X adsorbent is illustrated in Figure 4.16.

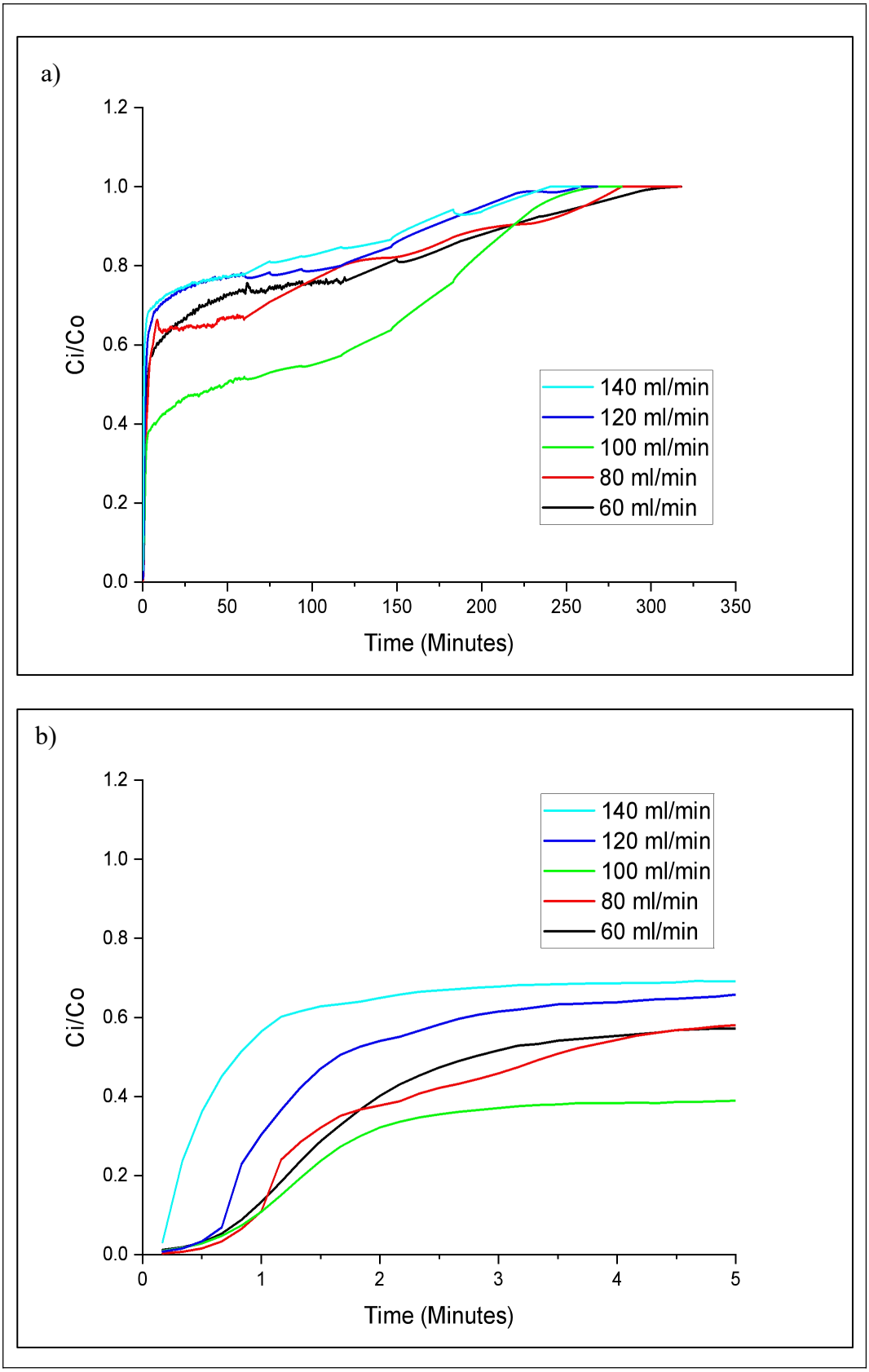

Figure 4.16 a) Breakthrough Curve of N/S/O-CCQD-X Adsorbent at Various Gas Flowrate b) Enlarge Image of Breakthrough Curve of N/S/O-CCQD-X Adsorbent at Various Gas Flowrate

Table 4.10
N/S/O-CCQD-X Adsorbents Breakthrough Time and Adsorption Capacity at Various Gas Flowrate

Gas Flowrate (mL/min)	Breakthrough time (min)	Breakthrough capacity (mg/g)	Total adsorption capacity (mg/g)	Total adsorption time (min)
60	1.00	0.5311	206.81	317.83
80	1.00	0.8453	322.13	282.67
100	1.00	0.5943	358.80	268.50
120	0.83	0.7456	234.30	258.17
140	0.33	0.6050	172.12	240.67

The breakthrough data reveal a complex relationship between gas flow rate and adsorption performance, with 100 mL/min emerging as the optimal flow rate for N/S/O-CCQD-X adsorbents. At this flow rate, the system achieves the highest total adsorption capacity (358.80 mg/g) while maintaining a full 1-minute breakthrough time and moderate breakthrough capacity (0.5943 mg/g). This optimal balance suggests that 100 mL/min provides sufficient contact time between CO_2 molecules and adsorption sites without causing premature saturation or excessive mass transfer limitations.

A progressive increase in flow rate from 60 to 100 mL/min enhances total capacity by 73.5% (from 206.81 to 358.80 mg/g), suggesting improved exploitation of available adsorption sites. The consistent 1-minute breakthrough time across this range implies stable initial adsorption kinetics, likely governed by effective transport of CO_2 to the surface and through the mesoporous channels of the N/S/O-CCQD-X xerogel matrix. However, beyond 100 mL/min, performance declines sharply: total capacity drops to 234.30 mg/g at 120 mL/min and further to 172.12 mg/g at 140 mL/min. This sharp reduction, coupled with a decreased breakthrough time (as low as 0.33 min at 140 mL/min), reflects the impact of insufficient residence time. Excessive flow rates can cause channeling effects, in which CO_2 bypasses available active sites, and mass transfer resistance increases, hindering diffusion-driven adsorption.

The non-monotonic behavior of breakthrough capacity, peaking at 80 mL/min (0.8453 mg/g), highlights the competing effects of flow rate on adsorption kinetics. At 80 mL/min, the system demonstrates the fastest initial uptake but a lower total

capacity than at 100 mL/min, suggesting different rate-limiting mechanisms dominate at different flow regimes. Specifically, while initial physisorption at external sites is enhanced at 80 mL/min, the slower internal diffusion into micropores is better supported at 100 mL/min.

These experimental observations are consistent with findings from prior studies. Simulations of nanoporous activated carbon systems have shown that higher feed velocities lead to reduced adsorption capacities due to limited residence time for equilibrium adsorption to occur (*(PDF) Computational Fluid Dynamics Simulation of CO2 Adsorption On Nanoporous Activated Carbon: Effect of Feed Velocity*, n.d.) . Similarly, in amine-functionalized mesoporous alumina, CO_2 uptake decreased from 56 to 27 mg/g as gas flow increased from 90 to 150 mL/min, confirming that beyond an optimal point, adsorption suffers from mass transfer limitations [192] . Such literature supports the current results, underscoring the importance of optimizing flow rate to ensure effective utilization of both surface and internal pore adsorption mechanisms. In conclusion, the optimal flow rate for N/S/O-CCQD-X adsorbents is 100 mL/min, balancing kinetic accessibility with deep pore utilization, and thereby maximizing total adsorption performance while preserving breakthrough stability.

4.4.3 Effect of CO_2 Feed Concentration

The feed gas concentration of CO_2 plays a pivotal role in influencing the adsorption behavior and efficiency of solid sorbents. Higher CO_2 concentrations generally provide a stronger driving force for mass transfer, potentially enhancing adsorption capacity, but may also accelerate the saturation of active sites, shortening breakthrough time. Conversely, lower concentrations can prolong the breakthrough time but may reduce the total uptake due to limited CO_2 availability. Evaluating the performance of N/S/O-CCQD-X adsorbents under varying CO_2 concentrations is essential for identifying their working limits and optimal operational conditions for real-world flue gas applications. The breakthrough behavior of the adsorbent under different CO_2 concentrations is illustrated in Figure 4.17.

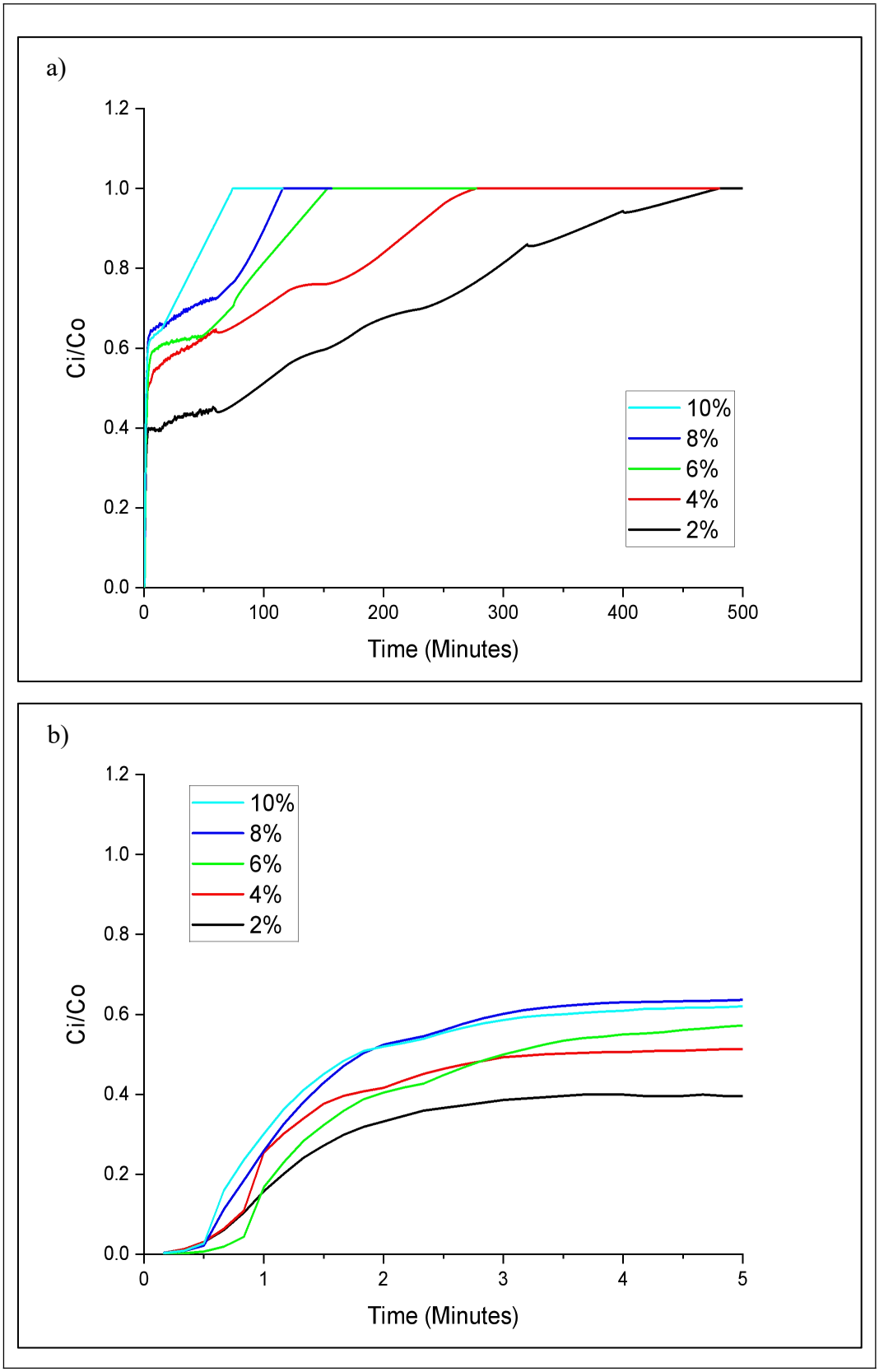

Figure 4.17 a) Breakthrough Curve of N/S/O-CCQD-X Adsorbent at Various CO_2 Concentration b) Enlarge Image of Breakthrough Curve of N/S/O-CCQD-X Adsorbent at Various CO_2 Concentration

Table 4.11
N/S/O-CCQD-X Adsorbents Breakthrough Time and Adsorption Capacity at Various CO_2 Concentration

CO_2 Concentration (%)	Breakthrough time (min)	Breakthrough capacity (mg/g)	Total adsorption capacity (mg/g)	Total adsorption time (min)
2	0.83	0.4344	402.12	480.17
4	0.83	0.7863	360.60	277.50
6	1.00	1.1162	319.57	153.33
8	0.67	1.5523	306.34	115.83
10	0.67	2.1814	264.55	74.00

The breakthrough data demonstrate a clear trade-off between adsorption kinetics and capacity as CO_2 concentration increases from 2% to 10%. At the lowest concentration (2%), the system achieves the highest total adsorption capacity (402.12 mg/g) and longest total adsorption time (480.17 min), indicating superior utilization of adsorption sites under dilute conditions. However, breakthrough capacity is lowest at this concentration (0.4344 mg/g), suggesting slower initial adsorption kinetics due to limited driving force. As concentration increases to 6%, breakthrough capacity more than doubles (1.1162 mg/g) while total capacity decreases by 20.5% (319.75 mg/g), revealing a transition where higher CO_2 availability accelerates initial adsorption but leads to faster saturation of active sites.

The most pronounced changes occur between 6-10% CO_2, where breakthrough capacity nearly doubles (1.1162 to 2.1814 mg/g) but total capacity drops by 17.3% (319.75 to 264.55 mg/g) and total adsorption time collapses by 51.7%. This inverse relationship suggests two competing mechanisms: (1) higher concentrations provide greater mass transfer driving force for rapid initial adsorption (evidenced by increasing breakthrough capacity), while (2) simultaneously promoting faster saturation of adsorption sites (resulting in declining total capacity and adsorption time).

The observed trend in this study, where increasing CO_2 concentration leads to higher breakthrough capacity but lower total adsorption capacity is well supported by literature across various adsorbent types and experimental conditions. For instance, dynamic breakthrough tests on porous ionic liquid-based adsorbents showed that at 1 vol% CO_2, the system achieved a high adsorption capacity of 2.44 mmol/g with

prolonged breakthrough time. However, as CO_2 concentration increased, although initial uptake rates improved, the total effective capacity diminished due to rapid saturation of active sites (B. Li et al., 2024). Similarly, Salehi et al. (2025) reported that for benzene and toluene adsorption on carbon fabrics in fixed-bed columns, higher inlet concentrations led to reduced adsorption capacity per unit mass. They attributed this to quicker saturation under stronger mass transfer driving forces, whereas lower concentrations allowed for extended adsorption and more complete site utilization (Salehi et al., 2025).

Estumano et al. (2024) also observed this trend while modeling H_2S and CO_2 adsorption using several breakthrough models. They found that model-derived parameters such as the Thomas model's maximum adsorption capacity decreased as the feed concentration increased, highlighting how higher concentrations promote faster initial adsorption but ultimately limit total uptake due to accelerated site saturation (Lima et al., 2024). Supporting this, Grosche and Esteves (2025) in their review on competitive biosorption emphasized that higher initial adsorbate levels rapidly exhaust active sites, reducing effective capacity and accelerating breakthrough, particularly under multi-species or high-concentration scenarios (Macena et al., 2025). Collectively, these findings corroborate the dual effect observed in the current work: enhanced initial kinetics at higher concentrations but reduced overall capacity due to shortened adsorption duration and quicker saturation.

4.5 Mechanistic Insights of CO_2 Adsorption using N/S/O-CCQD-X

4.5.1 Prediction of CO_2 Adsorption Isotherms

Understanding the fundamental adsorption behavior of CO_2 on N/S/O-CCQD-X adsorbents requires the application of adsorption isotherm models, which provide mechanistic insights into surface interactions, adsorbate distribution, and site heterogeneity. Isotherms describe how the quantity of CO_2 adsorbed varies with its partial pressure or concentration at a constant temperature, offering a deeper understanding of the physicochemical nature of the adsorption process. Through model fitting, parameters such as maximum adsorption capacity, affinity constants, and interaction energies can be obtained, helping to distinguish between physisorption and chemisorption phenomena. In this study, several widely used isotherm models

were employed to analyze the equilibrium data for N/S/O-CCQD-X, allowing for accurate prediction of adsorption performance under various conditions. Figure 4.18 presents the fitted isotherm curves for CO_2 adsorption on N/S/O-CCQD-X.

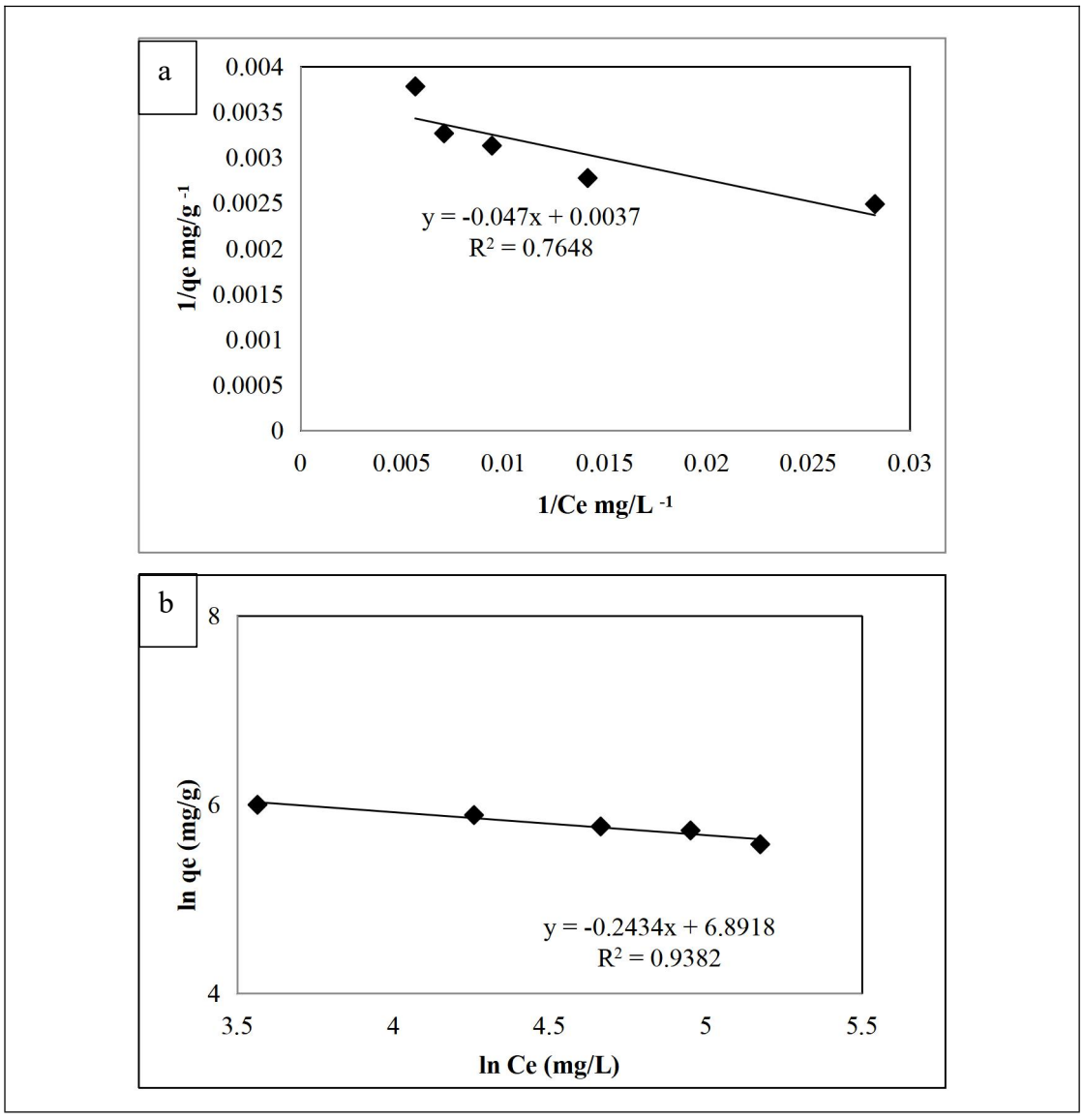

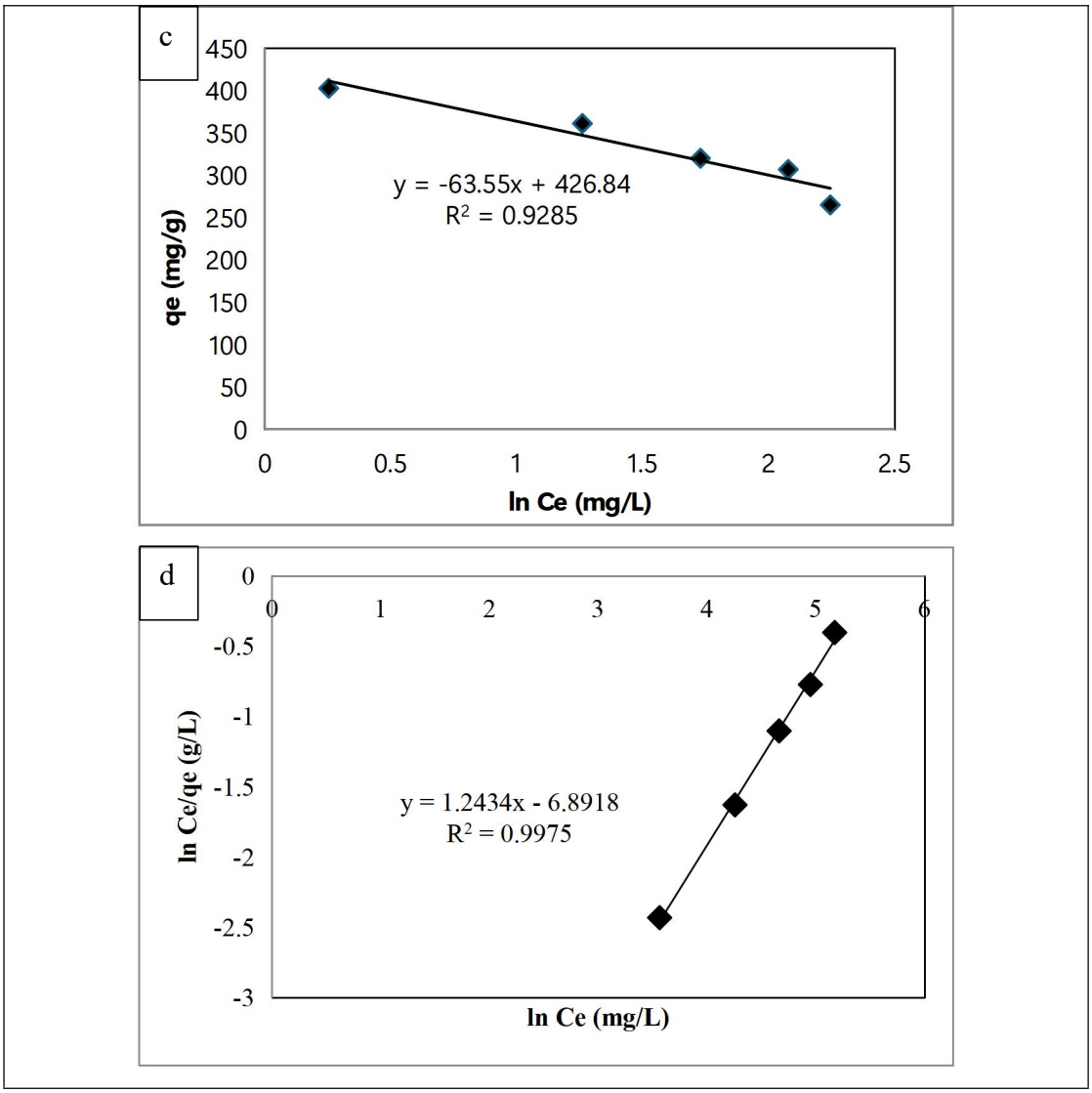

Figure 4.18 a) a) Langmuir Isotherms, b) Freundlich Isotherms, c) Tempkin Isotherms, d) Redlich-Peterson Isotherms

Table 4.12
Isotherms Model Constant and R^2 for N/S/O-CCQD-X towards CO_2 Removal

Isotherms model	Linearization method	Constant	R^2
Langmuir	$\frac{1}{q_e} = \frac{1}{q_m} + \frac{1}{q_m K_l}\frac{1}{C_e}$	$q_m = 270.27\frac{mg}{g}$ $K_l = 0.07872$	0.7648
Freundlich	$ln\, q_e = \frac{ln\, C_e}{n} - ln\, K_F$	$n = -4.11$ $K_F = 984.17$	0.9382
Tempkin	$q_e = \frac{RT}{b}(ln\, C_e + ln\, K_T)$	$b = -39.66$ $K_T = 0.0012$	0.9285

Redlich-Peterson	$\ln\left(\frac{K_R}{q_e}-1\right)=\beta lnC_e-lna_R$	$a_R=0.0099$ $\beta=0.8864$ $K_R=2.9477-14.0214$	0.9975

The Redlich–Peterson model yielded the highest correlation coefficient (R^2 = 0.9975), indicating that it best describes the adsorption equilibrium for this sample. This model combines elements of both Langmuir and Freundlich isotherms, suggesting that the adsorption behavior on CQD-X 133 may involve a heterogeneous surface with both monolayer and multilayer adsorption characteristics. This is likely influenced by the synergistic effect of N/S/O doping and the porous xerogel framework, which enhances both accessibility and reactivity.

Freundlich and Temkin models also show relatively high R^2 values (0.9382 and 0.9285 respectively), implying a degree of surface heterogeneity and interactions between adsorbent and adsorbate. However, they are slightly less accurate than the Redlich–Peterson model in this context. The Langmuir model, with the lowest R^2 (0.7648), appears to be the least suitable, indicating that the assumption of a homogenous monolayer adsorption surface does not fully apply to CQD-X 133.

The Redlich–Peterson model best fits the CO_2 adsorption data for CQD-X 133, suggesting a complex adsorption mechanism involving heterogeneous surface interactions and mixed-mode adsorption behavior. This result supports the advanced functionality of CQD-X 133 as a CO_2 adsorbent due to its heteroatom-doped, structurally varied surface. The strong linearity (R^2 = 0.9975) obtained from the logarithmic transformation of the R–P equation indicates that the adsorption sites on CQD-X 133 exhibit a wide distribution of affinities toward CO_2 molecules. of the active sites. Furthermore, the observed adsorption trend implies that the material does not adhere strictly to monolayer adsorption, as would be expected in the Langmuir model, but rather demonstrates a hybrid mechanism capable of accommodating different adsorption energies and interactions. The CQD-X 133 surface likely includes localized regions of high energy where chemisorption dominates, as well as broader areas with lower energy sites favoring physisorption.

Many adsorption studies of heterogeneous sorbents use the Redlich–Peterson (R–P) isotherm, a three-parameter model that bridges Langmuir (monolayer) and Freundlich (multilayer/heterogeneous) behavior. By construction, R–P can describe

both uniform and heterogeneous surfaces (A. Kumar et al., 2021). In practice, a good fit to R–P often signals mixed-mode adsorption: some sites bind CO_2 strongly (chemisorption) while others hold it weakly (physisorption). For instance, one study of phenacetin removal by copper-organic adsorbents found the best fit for one material was the R–P model ($R^2 \approx 0.975$), and the authors explicitly noted that physisorption and chemisorption participate in the adsorption (Alvine Loris et al., 2022). Similarly, a recent biochar study reported that Langmuir, Freundlich and Redlich–Peterson all fit well, but R–P gave the smallest error (residual variance ~0.001) (López et al., 2024). This implies that the adsorbent had sites of varying energy (heterogeneity), consistent with mixed physical/chemical uptake.

Taken together, the literature suggests that high R^2 fits by R–P and indications of mixed adsorption in CQD–xerogel systems are consistent with the CQD-X 133 observations. In particular, the CQD-X 133 sample's adsorption data best fit the Redlich–Peterson model (with very high R^2), implying a non-uniform surface energy distribution. This matches precedent: heterogeneous carbon-based adsorbents with functionalized surfaces commonly require R–P (or Freundlich) to model equilibrium (A. Kumar et al., 2021; López et al., 2024). Likewise, reports that both physisorption and chemisorption occur (as in (Alvine Loris et al., 2022)) align with the idea that CQD-X 133's CO_2 uptake involves multiple interaction modes. In sum, the CQD-X 133 behavior, strong R–P correlation and inferred mixed-mode uptake is fully in line with published findings for CQDs on porous supports.

4.5.2 Kinetics Study of CO_2 Adsorption

Understanding the kinetics of CO_2 adsorption is essential for evaluating the rate and mechanism by which gas molecules interact with the active sites of an adsorbent. Kinetic modeling provides insights into the adsorption dynamics, helping to determine whether the process is governed by physical or chemical interactions, surface reaction control, or intraparticle diffusion. Among various kinetic models, the pseudo-first order and pseudo-second-order models are widely applied to describe the adsorption behavior in fixed-bed and batch systems. These models offer quantitative frameworks to assess how variables such as flowrate influence the adsorption rate and equilibrium time. In this study, the kinetics of CO_2 adsorption on N/S/O-CCQD-X were analyzed under varying gas flowrates to identify the dominant rate-controlling

mechanism and evaluate the consistency of the kinetic parameters. The experimental data were fitted to both pseudo-first order and pseudo-second-order models to determine the best correlation. The corresponding results are presented in Figure 4.19 (Pseudo-first-order Kinetic Model at Different Gas Flowrates, Figure 4.18 (Pseudo-second-order Kinetic Model at Different Gas Flowrates, and Table 4.13 (Pseudo-first-order and Pseudo-second-order Kinetic Parameters of N/S/O-CCQD-X).

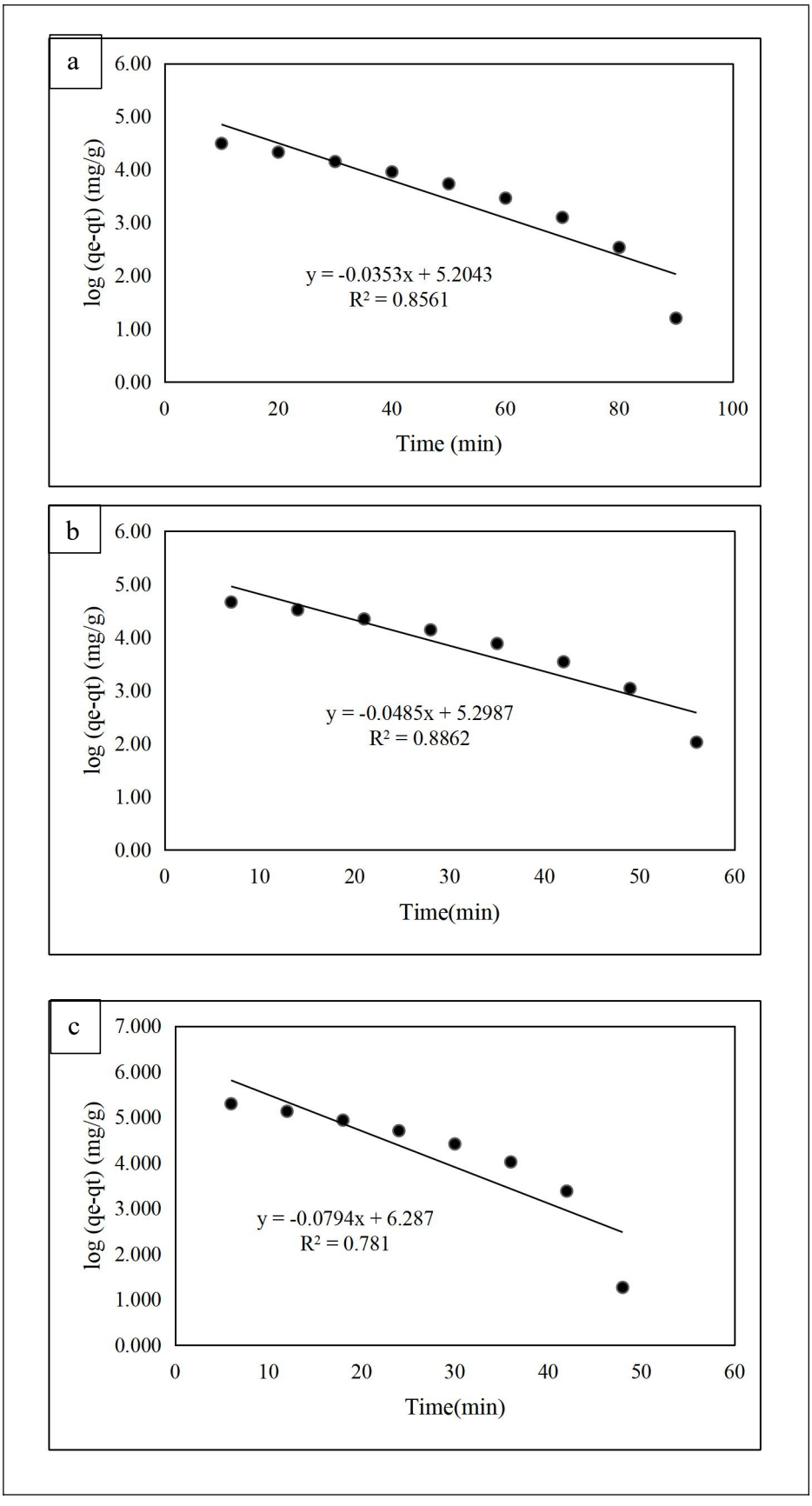
a
log (qe-qt) (mg/g)
6.00
5.00
4.00
3.00
2.00
1.00
0.00
y = -0.0353x + 5.2043
R² = 0.8561
0
20
40
60
80
100
Time (min)
b
log (qe-qt) (mg/g)
6.00
5.00
4.00
3.00
2.00
1.00
0.00
y = -0.0485x + 5.2987
R² = 0.8862
0
10
20
30
40
50
60
Time(min)
c
log (qe-qt) (mg/g)
7.000
6.000
5.000
4.000
3.000
2.000
1.000
0.000
y = -0.0794x + 6.287
R² = 0.781
0
10
20
30
40
50
60
Time(min)

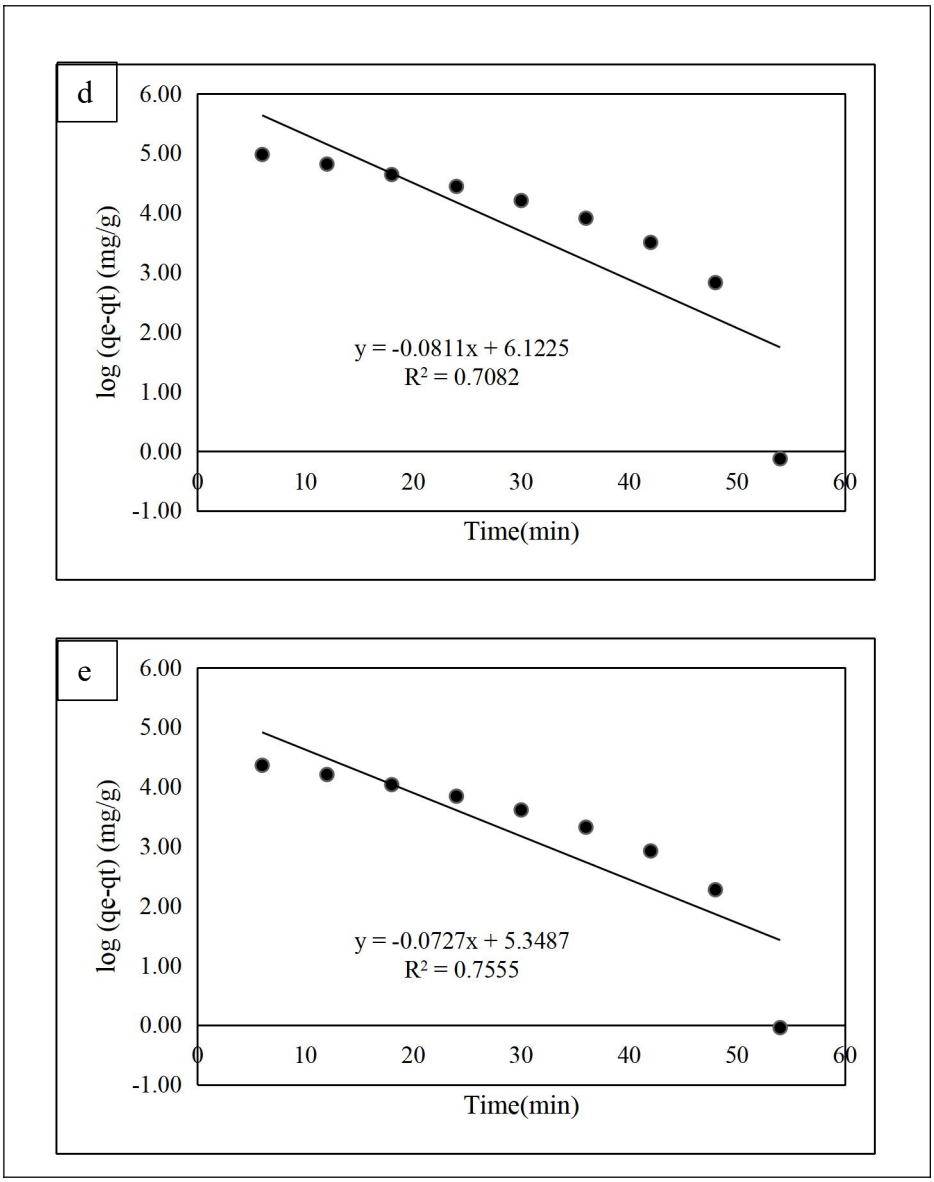

Figure 4.19 Pseudo-first-order Kinetic Model at Different Gas Flowrate a) 60 ml/min, b) 80 ml/min, c) 100 ml/min, d) 120 ml/min, e) 140 ml/min

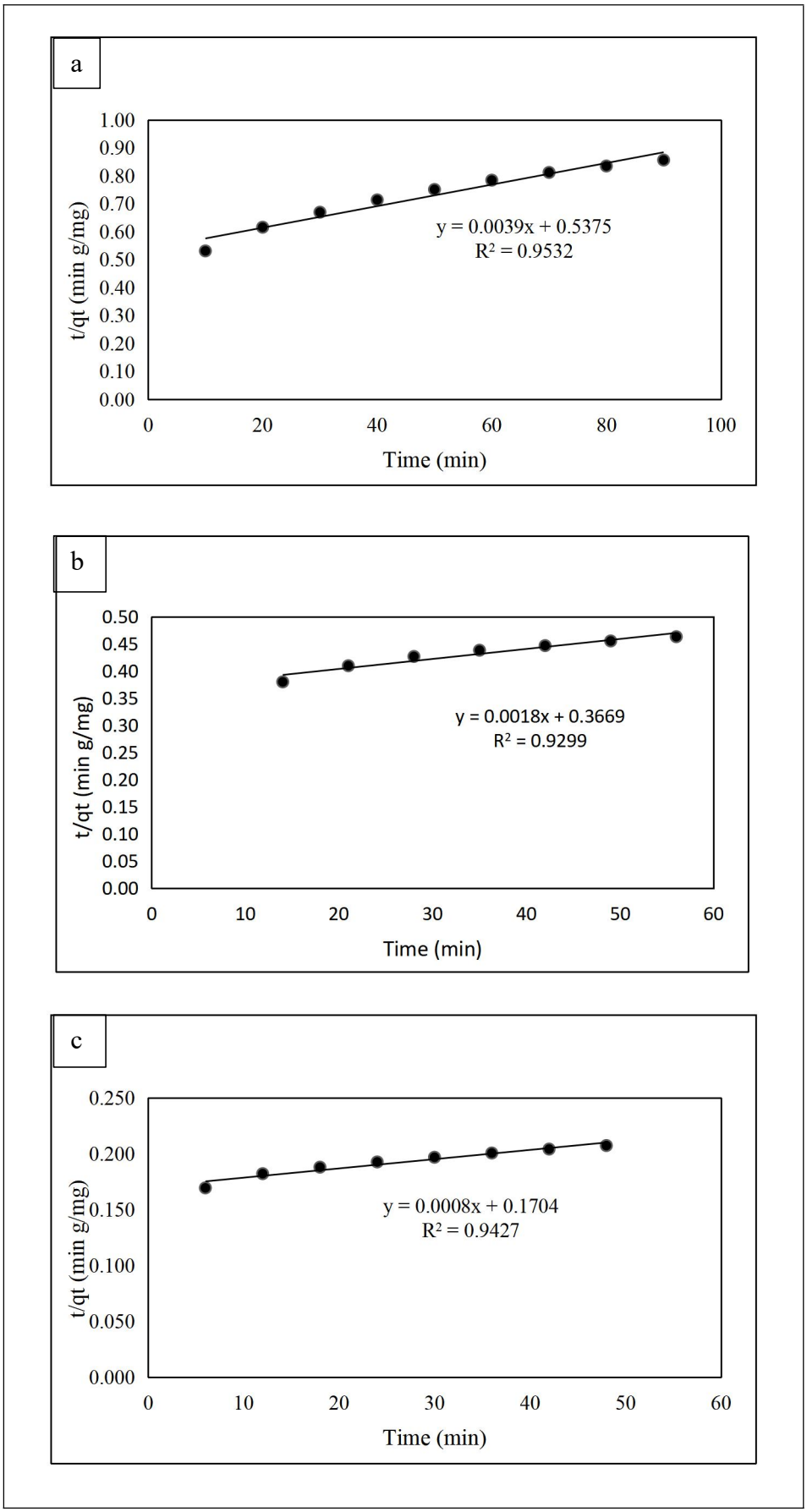
a
1.00
0.90
0.80
0.70
0.60
0.50
0.40
0.30
0.20
0.10
0.00
t/qt (min g/mg)
y = 0.0039x + 0.5375
R² = 0.9532
0
20
40
60
80
100
Time (min)
b
0.50
0.45
0.40
0.35
0.30
0.25
0.20
0.15
0.10
0.05
0.00
t/qt (min g/mg)
y = 0.0018x + 0.3669
R² = 0.9299
0
10
20
30
40
50
60
Time (min)
c
0.250
0.200
0.150
0.100
0.050
0.000
t/qt (min g/mg)
y = 0.0008x + 0.1704
R² = 0.9427
0
10
20
30
40
50
60
Time (min)

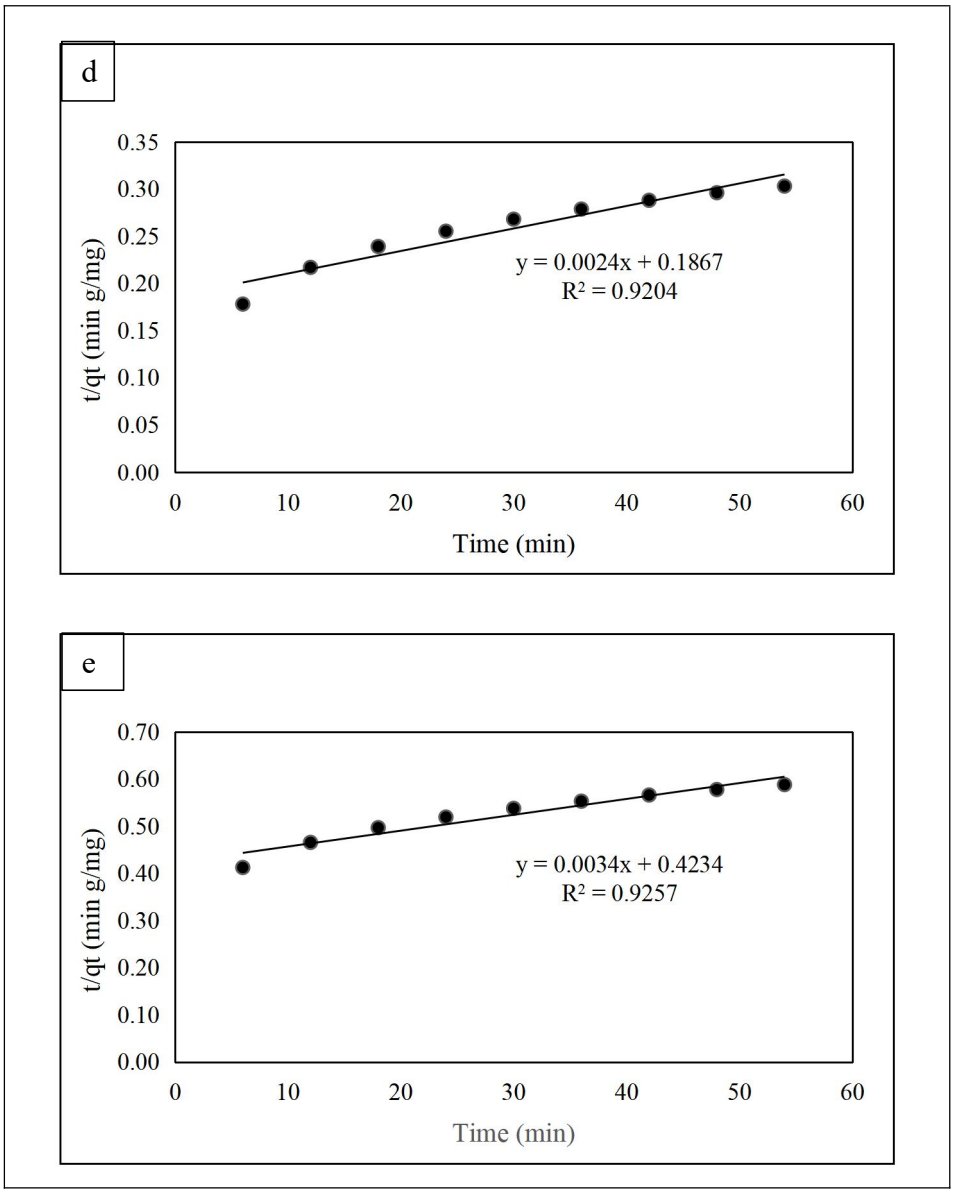

Figure 4.20 Pseudo-second-order Kinetic Model at Different Gas Flowrate a) 60 ml/min, b) 80 ml/min, c) 100 ml/min, d) 120 ml/min, e) 140 ml/min

Table 4.13
Pseudo-first-order and Pseudo-second-order Kinetic Parameters of N/S/O-CCQD-X

Flowrate (ml/min)	Pseudo-first-order			Pseudo-second-order		
	Qe (mg/g)	K_1 (1/min)	R^2	Qe (mg/g)	K_2 (1/min)	R^2
60	182.05	0.0353	0.8561	256.41	2.83E-05	0.9532
80	200.08	0.0485	0.8862	555.56	8.83E-06	0.9299
100	537.54	0.0794	0.7810	1250.00	3.76E-06	0.9427
120	456.00	0.0811	0.7082	416.67	3.09E-05	0.9204
140	210.33	0.0727	0.7555	294.12	2.73E-05	0.9257

The kinetic analysis of CO_2 adsorption on CQD-X 133, as summarized in Table 4.13, clearly shows that the pseudo-second-order (PSO) model provides a significantly better fit than the pseudo-first-order (PFO) model, evidenced by higher correlation coefficients ($R^2 > 0.92$ for PSO compared to 0.7082–0.8862 for PFO). This outcome strongly suggests that chemisorption, involving chemical interactions between CO_2 molecules and surface functional groups, is the dominant mechanism. The exceptionally high Q_e value of 1250 mg/g at the optimal flow rate of 100 mL/min underscores how tuning flow conditions can enhance mass transfer while preserving sufficient contact time, a crucial balance for efficient adsorption (N. Yang et al., 2021).

These findings resonate with the broader literature. For example, amine-functionalized zeolites have frequently been described by PSO kinetics, reinforcing a chemisorption mechanism. In a study by Li et al. on amine-modified zeolites, CO_2 uptake at 70 °C under different flow rates decreased from 4.02 to 3.22 mmol/g as flow increased (S. Li et al., 2023). The authors reported that the PSO model best fitted their kinetic data, confirming chemisorptive control. Similarly, Hubbe et al. reviewed adsorption on cellulosic substrates and noted that PSO kinetics may often arise from diffusion-limited processes or strong site-specific interactions, consistent with the interpretation of this work (Hubbe et al., 2019). Other authors, such as Bae et al., have also found PSO models to best describe CO_2 adsorption on amine-functionalized sorbents, attributing this to the prevalence of chemical binding (Bae et al., 2025; Girimonte et al., 2022).

At lower flowrates (60–80 mL/min), PSO fits were excellent ($R^2 \approx 0.93$–0.95), with moderate Q_e values. As the flowrate increased to 100 mL/min, Q_e reached its peak, indicating that a slight increase in convective mass transfer enhances the availability of active sites for chemisorption. However, as flow sped up further (120–140 mL/min), Q_e and PSO fit parameters dropped somewhat, reflecting mass transfer limitations and reduced contact time, common challenges in dynamic systems under high flow.

In contrast, the PFO model, often associated with physical adsorption (physisorption), showed comparatively lower correlation coefficients across all flowrates, suggesting that the CQD-X 133 material's active surface chemistry (e.g., amines, N/S/O functionalities) plays a key role in enabling chemical interactions with CO_2. These findings align with literature reports on chemisorption-driven CO_2 capture, where the PSO model consistently describes such mechanisms across diverse

adsorbents, including zeolites and amine-modified materials (Alvine Loris et al., 2022; Gunawan et al., 2018; Lalji, Ayubi, Ali, et al., 2024).

4.5.3 Thermodynamics Study of CO_2 Adsorption

Thermodynamic analysis is essential to understanding the nature, feasibility, and energy changes associated with the CO_2 adsorption process on N/S/O-CCQD-X adsorbents. By evaluating parameters such as enthalpy change (ΔH°), entropy change (ΔS°), and Gibbs free energy change (ΔG°), insights can be gained into whether the adsorption is endothermic or exothermic, spontaneous or non-spontaneous, and the degree of randomness at the gas–solid interface. These parameters also help infer the adsorption mechanism, whether it is predominantly physical or chemical in nature. Typically, this analysis involves plotting the Van't Hoff equation to derive ΔH° and ΔS° from the slope and intercept, respectively. A negative ΔG° value across all temperatures would suggest a spontaneous process, while the magnitude of ΔH° distinguishes physisorption (usually < 40 kJ/mol) from chemisorption (> 80 kJ/mol). In this study, the thermodynamic behavior of N/S/O-CCQD-X adsorbents was analyzed over a range of temperatures to assess the influence of thermal conditions on CO_2 capture performance. The results are presented in Figure 4.21 Van't Hoff Plot and summarized in Table 4.14.

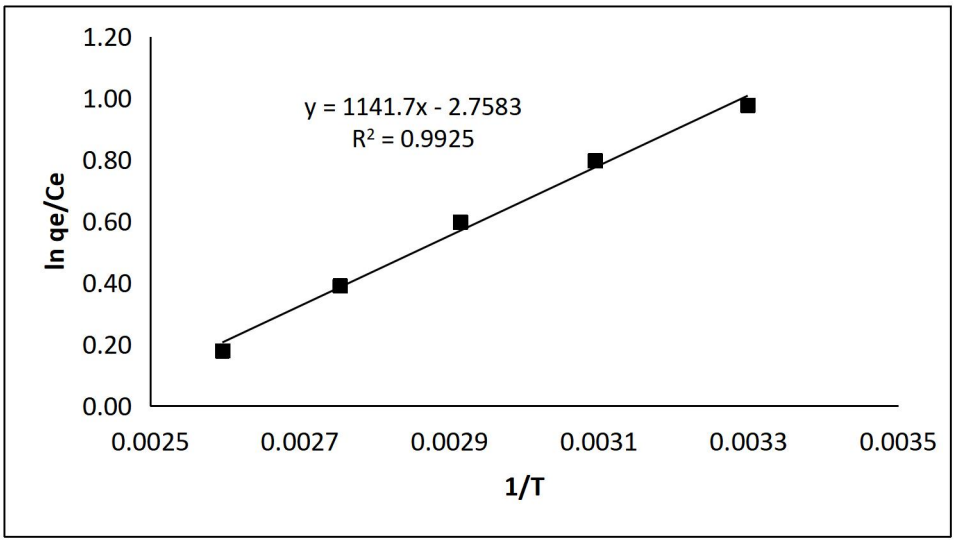

Figure 4.21 Van't Hoff Plot

Table 4.14
Thermodynamics Properties of N/S/O-CCQD-X Adsorbents

Temperature (K)	qe (mg/g)	Ce (mg/L)	$\Delta H\ \left(\frac{kJ}{mol}\right)$	$\Delta S\ \left(\frac{kJ.mol}{K}\right)$	$\Delta G\ \left(\frac{kJ}{mol}\right)$
303.15	234.93				-2.5401
323.15	196.21				-2.0815
343.15	160.72	88.394	-9.4921	-0.02293	-1.6228
363.15	130.65				-1.1642
385.15	105.77				-0.6596

The thermodynamic study of CO_2 adsorption on N/S/O-CCQD-X adsorbents reveals key insights into the nature of the adsorption process. The Van't Hoff plot (Figure 4.21) exhibits a strong linear correlation (R^2 = 0.9925), confirming the reliability of the thermodynamic analysis. The negative values of ΔH (-9.4921 kJ/mol) indicate an exothermic adsorption process, typical of physisorption, where weak van der Waals forces or dipole interactions dominate. The decrease in adsorption capacity (qe) with increasing temperature further supports this, as physisorption is generally less favorable at higher temperatures due to reduced adsorbate-adsorbent interactions. The negative ΔS (-0.02293 kJ/mol·K) suggests a decrease in randomness at the solid-gas interface during adsorption, which is common in localized adsorption processes. The negative ΔG values across all temperatures (-2.5401 to -0.6596 kJ/mol) confirm the spontaneity of the adsorption process, with the magnitude of ΔG decreasing as temperature rises, indicating reduced driving force at higher temperatures.

These findings are consistent with the kinetic results, which demonstrated that the pseudo-second-order model best fit the adsorption data, suggesting chemisorption as the dominant mechanism. However, the adsorption behavior also indicates a potential dual mechanism, where an initial chemisorption phase is followed by an equilibrium state dominated by physisorption. Such behavior is characteristic of heterogeneous adsorbents, which possess diverse surface functionalities and pore structures that support both chemical and physical interactions with CO_2 molecules. This dual interaction mechanism is further supported by Creamer et al. 2015 (Creamer & Gao, 2015)., who reported that materials like metal-organic frameworks (MOFs), zeolites, and biochar exhibit heterogeneous characteristics due to their varied surface chemistry and porosity. These features are crucial for optimizing CO_2 capture

efficiency, as they enable multiple adsorption pathways and enhance overall performance.

4.5.4 Summary of Adsorption Mechanism of CO_2 by N/S/O-CCQD-X

The CO_2 adsorption mechanism of the CQD-X 133 adsorbent can be best described as a mixed-mode process involving both chemisorption and physisorption. Isotherm modeling results reveal that the Redlich–Peterson model provides the best fit (R^2 = 0.9975), indicating a heterogeneous adsorption surface with dual adsorption behavior, combining monolayer and multilayer uptake. This is consistent with the functional complexity of N/S/O-doped CQDs immobilized in xerogel, which possess varied surface energy sites due to rich surface functionalities. Literature on carbon-based and porous adsorbents supports this observation, noting that heterogeneous materials often show best fit with Redlich–Peterson due to their capacity for both physical and chemical adsorption.

Kinetic modeling further supports this interpretation, as the pseudo-second order (PSO) model showed superior correlation ($R^2 > 0.92$), suggesting chemisorption as the dominant rate-limiting mechanism. This implies that chemical interactions between CO_2 molecules and active functional groups particularly those introduced via heteroatom doping (e.g., N, S, O) play a critical role in the adsorption process. The highest Q_e of 1250 mg/g at 100 mL/min highlights the need to balance flow rate for optimal contact between gas molecules and surface binding sites.

Thermodynamic analysis complements the isotherm and kinetic findings. The negative enthalpy change (ΔH = -9.4921 kJ/mol) suggests an exothermic process, characteristic of physisorption, while the spontaneity indicated by negative Gibbs free energy values (ΔG = -2.5401 to -0.6596 kJ/mol) confirms the feasibility of CO_2 capture under the tested conditions. The moderate ΔH value and decreasing adsorption with temperature collectively suggest that although chemisorption initiates CO_2 binding, physisorption dominates at equilibrium supporting a dual mechanism. Figure 4.22 shows the proposed mechanisms of CO_2 adsorption showing active sites interaction.

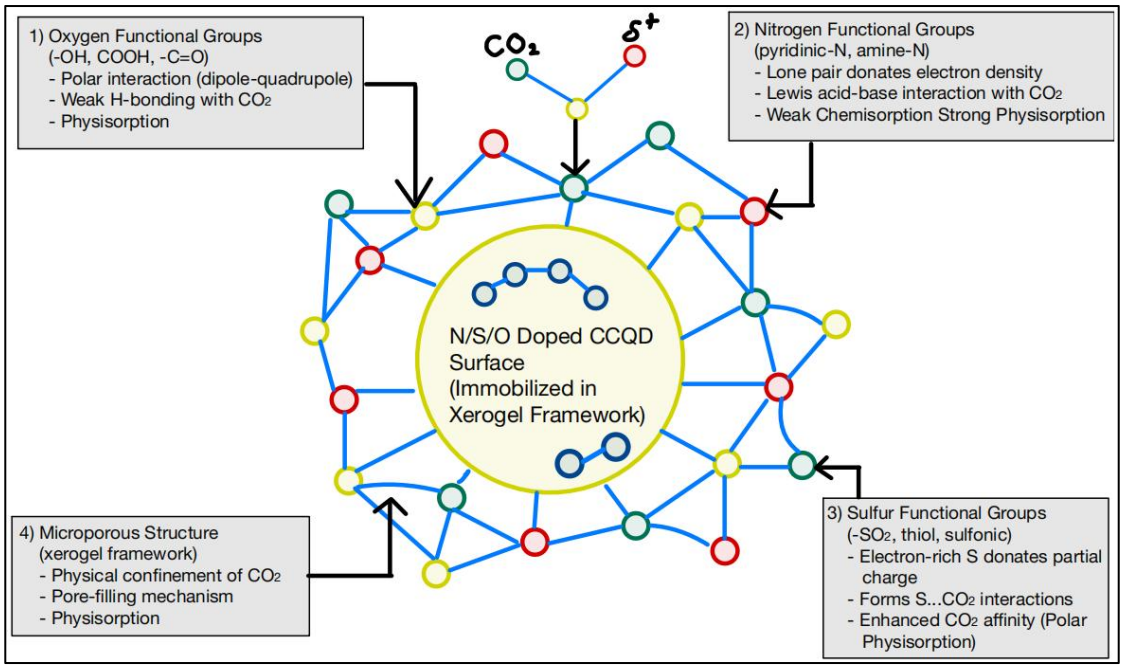

Figure 4.22 Proposed Mechanisms of CO_2 Adsorption

Overall, CQD-X 133 exhibits a complex CO_2 adsorption mechanism facilitated by its heteroatom-doped, structurally heterogeneous surface. The synergy of chemical and physical adsorption pathways enhances capture efficiency and positions this material as a promising candidate for practical carbon capture applications.

CHAPTER 5
CONCLUSIONS AND RECOMMENDATIONS

5.1 Conclusions

This study successfully demonstrated the pivotal role of xerogel immobilization in enhancing the stability, porosity, and mechanical integrity of N/S/O-CCQD-X adsorbents for CO_2 removal. The immobilization process minimized particle aggregation, preserved functional surface sites, and ensured uniform CQD dispersion within the matrix, addressing handling and stability limitations common to powder-form adsorbents. The optimized xerogel formulation (CQD-X 1:50) provided a robust support structure that contributed to improved adsorption efficiency.

The influence of different chitosan:thiourea:KOH ratios on the physicochemical properties of N/S/O-doped CQDs was clearly demonstrated in this study. Using a modified hydrothermal method, CQDs were synthesised from chitosan-based shrimp shells with varied precursor ratios, and comprehensive characterisation (FTIR, XPS, N_2 adsorption–desorption, CHNS, FESEM–EDX, and fluorescence spectroscopy) confirmed successful heteroatom doping and preserved structural features. Among all samples, CQD-X 133 (1:3:3 ratio) exhibited the most favourable characteristics including the highest fixed carbon content, optimal surface chemistry, and the highest quantum yield which collectively resulted in enhanced CO_2 adsorption performance. Overall, the findings show that adjusting precursor ratios is an effective approach to tailor CQD properties for improved CO_2 capture applications.

Adsorption experiments revealed that process parameters significantly impact CO_2 removal. Optimal performance was achieved at 30 °C, 2% CO_2 concentration, and 100 mL/min flow rate, where CQD-X 133 reached a maximum capacity of 402.12 mg/g under low concentration and 358.80 mg/g under standard testing conditions. Higher temperatures and faster flow rates reduced uptake due to the exothermic nature of adsorption and shorter contact times, whereas very low flow rates led to insufficient mass transfer. These findings underscore the necessity of balancing adsorption kinetics and thermodynamics for operational optimization.

Isotherm modeling indicated that the Redlich–Peterson model best described the adsorption process, reflecting a mixed monolayer–multilayer mechanism on a

heterogeneous surface. Kinetic analysis favored the pseudo-second-order model, suggesting chemisorption as the dominant mechanism, while thermodynamic parameters confirmed the spontaneity and exothermicity of CO_2 uptake. The combination of chemisorption and physisorption processes enabled high initial uptake and effective capacity utilization at equilibrium.

In conclusion, the integration of xerogel immobilization, N/S/O-doped CQDs, and optimized process parameters successfully produced an adsorbent with strong CO_2 capture performance, structural stability, and thermal robustness. Among all formulations, CQD-X 133 demonstrated the highest efficiency, confirming that precise control of precursor ratios is essential for maximizing functional group activity and adsorption behavior. Overall, this study establishes a practical and scalable pathway for producing sustainable, biomass-derived adsorbents for post-combustion CO_2 capture.

From an industrial perspective, the use of low-cost shrimp-shell precursors, simple hydrothermal synthesis, and ambient-pressure adsorption conditions makes the material promising for integration into fixed-bed systems, biogas upgrading units, or modular carbon-capture filters. With further scale-up, regeneration studies, and long-term cycling tests, N/S/O-CCQD-X materials hold strong potential for commercialization in low-to-medium-temperature CO_2 capture applications.

5.2 Recommendations

Based on the findings of this research, the following recommendations can be utilized for the development of future studies:

i. Explore other heteroatom dopants: Incorporating elements like phosphorus or boron in addition to N/S/O could further enhance basicity and CO_2 binding affinity.
ii. Study long-term cyclic stability: Perform extended adsorption-desorption cycles to evaluate the reusability and structural stability of the N/S/O-CCQD-X adsorbents under industrially relevant conditions.
iii. Investigate scale-up feasibility: Assess the potential of producing N/S/O-CCQD-X at larger scales, including economic analysis and process integration for real-world CO_2 capture applications.

iv. Model adsorption in mixed-gas systems: Evaluate the N/S/O-CCQD-X performance in syngas simulations containing CO_2, N_2, and moisture to understand competitive adsorption effects.

v. Conduct detailed CO_2 sorption simulations: Employ molecular dynamics (MD) and density functional theory (DFT) simulations to gain atomistic-level insights into CO_2 binding mechanisms, energy profiles, and the role of heteroatom doping on adsorption pathways.

vi. Utilize alternative biomass precursors: Investigate other sustainable feedstocks such as oil palm waste, coconut husks, or other agricultural residues for CQD synthesis to improve resource circularity and potentially tailor material properties.

REFERENCES

5 potential benefits of carbon capture and storage (CCS) technology | Border States. (n.d.). Retrieved May 22, 2025, from https://solutions.borderstates.com/blog/benefits-of-carbon-capture-and-storage/

Ababneh, H., & Hameed, B. H. (2021). Chitosan-derived hydrothermally carbonized materials and its applications: A review of recent literature. In *International Journal of Biological Macromolecules* (Vol. 186, pp. 314–327). Elsevier B.V. https://doi.org/10.1016/j.ijbiomac.2021.06.161

Abd Rahman, S. N. F., & Othman, S. A. (2024). Chitosan Properties: A Preliminary Review. *Journal of Advanced Mechanical Engineering Applications*, *5*(1). https://doi.org/10.30880/JAMEA.2024.05.01.002

Abedin, R. M. A., Abd Elwaly, D. R. M., & Abd El-Salam, A. E. (2023). Production, statistical evaluation and characterization of chitosanase from Fusarium oxysporum D18. *Annals of Microbiology*, *73*(1), 1–14. https://doi.org/10.1186/S13213-023-01731-W/FIGURES/5

Abinaya, K., Rajkishore, S. K., Lakshmanan, A., Anandham, R., Dhananchezhiyan, P., & Praghadeesh, M. (2021). Synthesis and characterization of carbon dots from coconut shell by optimizing the hydrothermal carbonization process. *Journal of Applied and Natural Science*, *13*(4), 1151–1157. https://doi.org/10.31018/jans.v13i4.2916

Adame-Pereira, M., Durán-Valle, C. J., & Fernández-González, C. (2023). Hydrothermal Carbon Coating of an Activated Carbon—A New Adsorbent. *Molecules*, *28*(12), 4769. https://doi.org/10.3390/MOLECULES28124769/S1

Aguilar-Maruri, S. A., Perera-Triana, D., Flórez, E., Forgionny, A., Palestino, G., Gómez-Durán, C. F. A., & Ocampo-Pérez, R. (2024). Highly Adsorptive Organic Xerogels for Efficient Removal of Metformin from Aqueous Solutions: Experimental and Theoretical Approach. *Processes*, *12*(7), 1431–1431. https://doi.org/10.3390/PR12071431

Akpasi, S. O., & Isa, Y. M. (2022). Effect of operating variables on CO2 adsorption capacity of activated carbon, kaolinite, and activated carbon – kaolinite composite adsorbent. *Water-Energy Nexus*, *5*, 21–28. https://doi.org/10.1016/J.WEN.2022.08.001

Alemu, D., Getachew, E., & Mondal, A. K. (2023). Study on the Physicochemical Properties of Chitosan and their Applications in the Biomedical Sector. *International Journal of Polymer Science*, *2023*, 1–13. https://doi.org/10.1155/2023/5025341

Ali Said Al Hoqani, H., Hamed Khalifa Al Shaqsi, N., Amzad Hossin, M., & Abdullah Al Sibani, M. (2021). Structural characterization of polymeric chitosan and mineral from Omani shrimp shells. *Water-Energy Nexus*, *4*, 199–207. https://doi.org/10.1016/J.WEN.2021.11.002

Alias, A. B., Qarizada, D., Malik, N. S. A., Noraini, N. M. R., & Rashid, Z. A. (2022a). Comparison of hydrogel-and xerogel-based sorbent from Empty Fruit Bunch (EFB). *Archives of Materials Science and Engineering*, *118*(2), 49–60. https://doi.org/10.5604/01.3001.0016.2579

Alias, A. B., Qarizada, D., Malik, N. S. A., Noraini, N. M. R., & Rashid, Z. A. (2022b). Comparison of hydrogel-and xerogel-based sorbent from Empty Fruit Bunch (EFB). *Archives of Materials Science and Engineering*, *118*(2), 49–60. https://doi.org/10.5604/01.3001.0016.2579

Almoneef, M. M., Jedli, H., & Mbarek, M. (2021). Experimental study of CO2 adsorption using activated carbon. *Materials Research Express*, *8*(6), 065602. https://doi.org/10.1088/2053-1591/AC05FE

Alqahtani, A., Alqahtani, T., Al Fatease, A., Alshehri, A., & Almrasy, A. A. (2025). Development of N,P-doped carbon quantum dots as a green fluorescent probe for fexofenadine determination: mechanistic studies, Box–Behnken optimization, and pharmacokinetic application. *RSC Advances*, *15*(18), 14545. https://doi.org/10.1039/D5RA01920F

Alvine Loris, D., Donald Raoul, T. T., Cyrille, A. D., Idris-Hermann, K. T., Giscard, D., Alain Clovis, T. D., Gabche, A. S., & Jean, N. (2022). Kinetic and Isotherm Studies of the Adsorption Phenacetin onto Two Copper Porous Coordination Compounds: Nonlinear Regression Analysis. *Journal of Chemistry*, *2022*. https://doi.org/10.1155/2022/2828860

Amaral-Labat, G., Munhoz, M. G. C., da Silva Fonseca, B. C., Boss, A. F. N., de Almeida-Mattos, P., Braghiroli, F. L., Bouafif, H., Koubaa, A., Silva, G. F. B. L. E., & Baldan, M. R. (2021). Xerogel-like Materials from Sustainable Sources: Properties and Electrochemical Performances. *Energies 2021, Vol. 14, Page 7977*, *14*(23), 7977. https://doi.org/10.3390/EN14237977

Ameta, C., Vyas, Y., Chundawat, P., & Dharmendra. (2023). Microwave-assisted synthesis of quantum dots. *Quantum Dots: Fundamentals, Synthesis and Applications*, 115–145. https://doi.org/10.1016/B978-0-12-824153-0.00007-0

Aquino, A. S., Vieira, M. O., Ferreira, A. S. D., Cabrita, E. J., Einloft, S., & de Souza, M. O. (2019). Hybrid Ionic Liquid–Silica Xerogels Applied in CO2 Capture. *Applied Sciences 2019, Vol. 9, Page 2614*, *9*(13), 2614. https://doi.org/10.3390/APP9132614

Aranaz, I., Alcántara, A. R., Civera, M. C., Arias, C., Elorza, B., Heras Caballero, A., & Acosta, N. (2021). Chitosan: An Overview of Its Properties and Applications. *Polymers*, *13*(19). https://doi.org/10.3390/polym13193256

Arasukumar, B., Prabakaran, G., Gunalan, B., & Moovendhan, M. (2019). Chemical composition, structural features, surface morphology and bioactivities of chitosan derivatives from lobster (Thenus unimaculatus) shells. *International Journal of Biological Macromolecules*, *135*, 1237–1245. https://doi.org/10.1016/J.IJBIOMAC.2019.06.033

Aresta, M., & Dibenedetto, A. (2021). Properties of the Carbon Dioxide Molecule. *The Carbon Dioxide Revolution*, 101–121. https://doi.org/10.1007/978-3-030-59061-1_7

Arshad, T., Lihong, W., Najeeb Alawadi, H. F., Mahmood, A., Zia, M. A., Naqve, M., Ali, B., Nawaz, M., Hassan, M. U., Hashem, A., & Abdallah, E. F. (2024). Alleviating adverse effects of environmental stress in plants through chitosan application. *Notulae Botanicae Horti Agrobotanici Cluj-Napoca*, *52*(3), 13538–13538. https://doi.org/10.15835/NBHA52313538

ASAP 2020 Plus - Micromeritics. (n.d.). Retrieved July 18, 2025, from https://micromeritics.com/products/asap-2020-plus/?utm_source=chatgpt.com

Asrafali, S. P., Periyasamy, T., & Bari, G. A. K. M. R. (2025). Advances in Carbon-Based Aerogels for CO2 Capture: Fundamental Design Strategies and Technological Progress. *Gels 2025, Vol. 11, Page 361*, *11*(5), 361. https://doi.org/10.3390/GELS11050361

Astuti, A. R. A., Wenten, I. G., Ariono, D., Sasongko, D., Saputera, W. H., & Khoiruddin, K. (2024). Advances in Carbon Control Technologies for Flue Gas Cleaning. *Separation and Purification Reviews*. https://doi.org/10.1080/15422119.2024.2328080

Ayeleru, O. O., Modekwe, H. U., Onisuru, O. R., Ohoro, C. R., Akinnawo, C. A., & Olubambi, P. A. (2023). Adsorbent technologies and applications for carbon capture, and direct air capture in environmental perspective and sustainable climate action. *Sustainable Chemistry for Climate Action*, *3*, 100029. https://doi.org/10.1016/J.SCCA.2023.100029

Bae, J. Y., Jang, S. G., Cho, J., & Kang, M. (2025). Amine-Functionalized Mesoporous Silica for Efficient CO2 Capture: Stability, Performance, and Industrial Feasibility. *International Journal of Molecular Sciences 2025, Vol. 26, Page 4313*, *26*(9), 4313. https://doi.org/10.3390/IJMS26094313

Bahman, N., Alalaiwat, D., Abdulmohsen, Z., Al Khalifa, M., Al Baharna, S., Al-Mannai, M. A., & Younis, A. (2022). A critical review on global CO2 emission: where do industries stand? *Reviews on Environmental Health*, *0*(0), 681–696. https://doi.org/10.1515/REVEH-2022-0105

Bahman, N., Alalaiwat, D., Abdulmohsen, Z., Al Khalifa, M., Al Baharna, S., Al-Mannai, M. A., & Younis, A. (2023). A critical review on global CO2emission: Where do industries stand? *Reviews on Environmental Health*, *38*(4), 681–696. https://doi.org/10.1515/REVEH-2022-0105/MACHINEREADABLECITATION/RIS

Bahmanzadegan, F., & Ghaemi, A. (2024). Modification and functionalization of zeolites to improve the efficiency of CO2 adsorption: A review. *Case Studies in Chemical and Environmental Engineering*, *9*, 100564. https://doi.org/10.1016/J.CSCEE.2023.100564

Balakrishnan, T., Ang, W. L., Mahmoudi, E., Mohammad, A. W., & Sambudi, N. S. (2022). Formation mechanism and application potential of carbon dots synthesized from palm kernel shell via microwave assisted method. *Carbon Resources Conversion*, *5*(2), 150–166. https://doi.org/10.1016/j.crcon.2022.01.003

Balogun, A. I., Abdulkareem, F. A., Irfan, S. A., & Padmanabhan, E. (2021). The Effective Process Parameters of CO2 Adsorption on Peninsular Malaysia Shale Samples. *SPE/AAPG/SEG Asia Pacific Unconventional Resources Technology Conference, Asia Pacific URTeC 2021*, 1707–1719. https://doi.org/10.15530/AP-URTEC-2021-208386

Barahimi, V., Ho, M., & Croiset, E. (2023). From Lab to Fab: Development and Deployment of Direct Air Capture of CO2. *Energies*, *16*(17). https://doi.org/10.3390/EN16176385

Barik, M., BhagyaRaj, G. V. S., Dash, K. K., & Shams, R. (2024). A thorough evaluation of chitosan-based packaging film and coating for food product shelf-life extension. *Journal of Agriculture and Food Research*, *16*. https://doi.org/10.1016/J.JAFR.2024.101164

Basaran, K., Topcubasi, B. U., & Davran-Candan, T. (2021). Theoretical investigation of CO2adsorption mechanism over amine-functionalized mesoporous silica. *Journal of CO2 Utilization*, *47*, 101492. https://doi.org/10.1016/j.jcou.2021.101492

Bertrand, M., Simonin, S., & Bach, B. (2024). Applications of chitosan in the agri-food sector: A review. *Carbohydrate Research*, *543*, 109219–109219. https://doi.org/10.1016/J.CARRES.2024.109219

Bezuneh, T. T., Fereja, T. H., Li, H., & Jin, Y. (2023). Solid-Phase Pyrolysis Synthesis of Highly Fluorescent Nitrogen/Sulfur Codoped Graphene Quantum Dots for Selective and Sensitive Diversity Detection of Cr(VI). *Langmuir*, *39*(4), 1538–1547. https://doi.org/10.1021/ACS.LANGMUIR.2C02966

Boonchuay, A., & Worathanakul, P. (2022). The Diffusion Behavior of CO2 Adsorption from a CO2/N2 Gas Mixture on Zeolite 5A in a Fixed-Bed Column. *Atmosphere 2022, Vol. 13, Page 513*, *13*(4), 513. https://doi.org/10.3390/ATMOS13040513

Broud, M. T., Samandari, M., Yu, L., Harper, D. P., & Keffer, D. J. (2023). Selective Carbon Dioxide Binding on Carbon Quantum Dots. *Journal of Physical Chemistry C*, *127*(28), 13639–13650. https://doi.org/10.1021/ACS.JPCC.3C02885

Campopiano, O., Jean, D. J., & Ball, L. T. (2022). Thiourea. *Encyclopedia of Reagents for Organic Synthesis*, 1–3. https://doi.org/10.1002/047084289X.RT106.PUB3

Carbon | XPS Periodic Table - MY. (n.d.). Retrieved May 28, 2025, from https://www.thermofisher.com/id/en/home/materials-science/learning-center/periodic-table/non-metal/carbon.html

Carbon Capture Could Become Practical with Scalable, Affordable Materials | News | Northwestern Engineering. (n.d.). Retrieved May 23, 2025, from

https://www.mccormick.northwestern.edu/news/articles/2025/04/carbon-capture-could-become-practical-with-scalable-affordable-materials/

Carolina Hernández-Galeano, J., Serafin, J., Giraldo, L., Murillo-Acevedo, Y., & Carlos Moreno-Piraján, J. (2024). Carbon aerogels in the form of microspheres and their potential application in CO2 adsorption: A thermodynamic and kinetic study. *Journal of Industrial and Engineering Chemistry*, *136*, 475–492. https://doi.org/10.1016/J.JIEC.2024.02.036

Chakravarty, J., & Edwards, T. A. (2022). Innovation from waste with biomass-derived chitin and chitosan as green and sustainable polymer: A review. *Energy Nexus*, *8*, 100149. https://doi.org/10.1016/j.nexus.2022.100149

Chandra, S., Bano, D., Pradhan, P., Singh, V. K., Yadav, P. K., Sinha, D., & Hasan, S. H. (2020). Nitrogen/sulfur-co-doped carbon quantum dots: a biocompatible material for the selective detection of picric acid in aqueous solution and living cells. *Analytical and Bioanalytical Chemistry*, *412*(15), 3753–3763. https://doi.org/10.1007/S00216-020-02629-1

Chang, K., Zhu, Q., Qi, L., Guo, M., Gao, W., & Gao, Q. (2022). Synthesis and Properties of Nitrogen-Doped Carbon Quantum Dots Using Lactic Acid as Carbon Source. *Materials*, *15*(2), 466. https://doi.org/10.3390/MA15020466

Chang, S. F., Chiu, H. H., Jao, H. S., Shang, J., Lin, Y. J., & Yu, B. Y. (2025). Comprehensive evaluation of various CO2 capture technologies through rigorous simulation: Economic, equipment footprint, and environmental analysis. *Carbon Capture Science & Technology*, *14*, 100342. https://doi.org/10.1016/J.CCST.2024.100342

Chatzimitakos, T., Kasouni, A., Sygellou, L., Avgeropoulos, A., Troganis, A., & Stalikas, C. (2017). Two of a kind but different: Luminescent carbon quantum dots from Citrus peels for iron and tartrazine sensing and cell imaging. *Talanta*, *175*, 305–312. https://doi.org/10.1016/J.TALANTA.2017.07.053

Chavhan, M. P., & Liu, X. (2025). Combined effect of hierarchical porosity and surface oxygen functional groups on the performance of carbon xerogels in H2 storage, CO2 capture, and Zn-ion hybrid capacitors. *Journal of Energy Storage*, *122*(September 2024), 116712. https://doi.org/10.1016/J.EST.2025.116712

Chen, J. X., Bao, A., & Siqin, D. (2024a). N/S Dually Doped Nanoporous Carbon for CO2 Adsorption. *ACS Applied Nano Materials*, *7*(10), 12184–12193. https://doi.org/10.1021/ACSANM.4C02198

Chen, J. X., Bao, A., & Siqin, D. (2024b). N/S Dually Doped Nanoporous Carbon for CO2 Adsorption. *ACS Applied Nano Materials*, *7*(10), 12184–12193. https://doi.org/10.1021/ACSANM.4C02198

Chen, X., Liu, W., Sun, Y., Tan, T., Du, C. X., & Li, Y. (2023). KOH-Enabled Axial-Oxygen Coordinated Ni Single-Atom Catalyst for Efficient Electrocatalytic CO2 Reduction. *Small Methods*, *7*(3), 2201311–2201311. https://doi.org/10.1002/SMTD.202201311

Chiang, Y. C., Hsu, W. L., Lin, S. Y., & Juang, R. S. (2017). Enhanced CO2 Adsorption on Activated Carbon Fibers Grafted with Nitrogen-Doped Carbon Nanotubes. *Materials 2017, Vol. 10, Page 511*, *10*(5), 511. https://doi.org/10.3390/MA10050511

Chitosan particle and process therefor. (2006). https://typeset.io/papers/chitosan-particle-and-process-therefor-4tdab4v3bf

Choi, J., Jung, J. C., & Jung, W. (2024). Advances in Carbon Xerogels: Structural Optimization for Enhanced EDLC Performance. *Gels*, *10*(6), 400. https://doi.org/10.3390/GELS10060400

Choi, S., Drese, J. H., & Jones, C. W. (2009). Adsorbent Materials for Carbon Dioxide Capture from Large Anthropogenic Point Sources. *ChemSusChem*, *2*(9), 796–854. https://doi.org/10.1002/CSSC.200900036

Chu, K. W., Lee, S. L., Chang, C. J., & Liu, L. (2019). Recent Progress of Carbon Dot Precursors and Photocatalysis Applications. *Polymers 2019, Vol. 11, Page 689*, *11*(4), 689. https://doi.org/10.3390/POLYM11040689

Comparing the Lifespan of Different H_2S Adsorbents. (n.d.). Retrieved May 23, 2025, from https://www.chemicalproductsokc.com/comparing-the-lifespan-of-different-h%E2%82%82s-adsorbents/

CQDs (carbon quantum dots) with high fluorescence characteristic as well as preparation and application of CQDs. (2018a). https://typeset.io/papers/cqds-carbon-quantum-dots-with-high-fluorescence-1kz6awgmuw

CQDs (carbon quantum dots) with high fluorescence characteristic as well as preparation and application of CQDs. (2018b). https://typeset.io/papers/cqds-carbon-quantum-dots-with-high-fluorescence-1kz6awgmuw

Creamer, A. E., & Gao, B. (2015). *Adsorbents for CO2 Capture*. 25–41. https://doi.org/10.1007/978-3-319-17010-7_3

Cui, H., Xu, J., Shi, J., Yan, N., Zhang, C., & You, S. (2022). N, S co-doped carbon spheres synthesized from glucose and thiourea as efficient CO2 adsorbents. *Journal of The Taiwan Institute of Chemical Engineers*, *138*, 104441–104441. https://doi.org/10.1016/J.JTICE.2022.104441

Cui, J. (2022). Recent Advances in Post-Combustion CO2 Capture via Adsorption Methods. *Highlights in Science, Engineering and Technology*, *6*, 172–181. https://doi.org/10.54097/HSET.V6I.959

Cui, L., Ren, X., Wang, J., & Sun, M. (2020). Synthesis of homogeneous carbon quantum dots by ultrafast dual-beam pulsed laser ablation for bioimaging. *Materials Today Nano*, *12*, 100091. https://doi.org/10.1016/j.mtnano.2020.100091

Cuong, H. N., Kien, N. D., & Hoa, N. Van. (2024). Chitosan-based aerogel microspheres for wastewater treatment. *Vietnam Journal of Chemistry*. https://doi.org/10.1002/VJCH.202400007

D'Alessandro, D. M., Smit, B., & Long, J. R. (2010). Carbon dioxide capture: Prospects for new materials. *Angewandte Chemie - International Edition*, *49*(35), 6058–6082. https://doi.org/10.1002/ANIE.201000431,

Dani, A., Crocellà, V., Magistris, C., Santoro, V., Yuan, J., & Bordiga, S. (2016). Click-based porous cationic polymers for enhanced carbon dioxide capture. *Journal of Materials Chemistry A*, *5*(1), 372–383. https://doi.org/10.1039/C6TA08574A

Daniel, S. (2022). Characterization of carbon dots. *Carbon Dots in Analytical Chemistry: Detection and Imaging*, 43–58. https://doi.org/10.1016/B978-0-323-98350-1.00015-3

Darabkhani, H. G., Varasteh, H., & Bazooyar, B. (2023). Main technologies in CO2 capture. *Carbon Capture Technologies for Gas-Turbine-Based Power Plants*, 19–38. https://doi.org/10.1016/B978-0-12-818868-2.00002-3

Das, A., Peu, S. D., Hossain, M. S., Nahid, M. M. A., Karim, F. R. Bin, Chowdhury, H., Porag, M. H., Argha, D. B. P., Saha, S., Islam, A. R. M. T., Salah, M. M., & Shaker, A. (2023). Advancements in adsorption based carbon dioxide capture technologies- A comprehensive review. *Heliyon*, *9*(12), e22341. https://doi.org/10.1016/J.HELIYON.2023.E22341

de Freitas, F. P., Carvalho, A. M. M. L., Carneiro, A. de C. O., de Magalhães, M. A., Xisto, M. F., & Canal, W. D. (2021). Adsorption of neutral red dye by chitosan

and activated carbon composite films. *Heliyon*, *7*(7). https://doi.org/10.1016/J.HELIYON.2021.E07629

De Medeiros, T. V., Manioudakis, J., Noun, F., Macairan, J. R., Victoria, F., & Naccache, R. (2019). Microwave-assisted synthesis of carbon dots and their applications. *Journal of Materials Chemistry C*, *7*(24), 7175–7195. https://doi.org/10.1039/C9TC01640F

Deana, Q., Nor Mohd, R. N., Azil, B. A., Hamasa, K., & Nurul, S. A. A. (2023). Adsorption of hydrogen sulphide (H2S) using xerogel synthesized from palm kernel shell biochar. *Materials Research Proceedings*, *29*, 109–116. https://doi.org/10.21741/9781644902516-14

Deng, Y., Shen, C., Zhao, W., Zheng, G., Jiao, F., Lou, Q., Liu, K., Shan, C. X., & Dong, L. (2023). Biosynthesis of the Narrowband Deep-Red Emissive Carbon Nanodots from Eggshells. *ACS Sustainable Chemistry & Engineering*, *11*(17), 6535–6544. https://doi.org/10.1021/ACSSUSCHEMENG.2C06892

Deo, S. S., Naser, S. S., Sinha, A., Mohapatra, S. K., Parmar, A. S., Kujawska, M., Verma, S. K., & Tripathy, J. (2024). Biophysical translational posterity of green carbon quantum dots: the unparalleled versatility. *Nanomedicine*, 1–30. https://doi.org/10.1080/17435889.2024.2402682

Ding, X., Niu, Y., Zhang, G., Xu, Y., & Li, J. (2020). Electrochemistry in Carbon-based Quantum Dots. *Chemistry-an Asian Journal*, *15*(8), 1214–1224. https://doi.org/10.1002/ASIA.202000097

Dong, Y., Pang, H., Yang, H. Bin, Guo, C., Shao, J., Chi, Y., Li, C. M., & Yu, T. (2013). Carbon-Based Dots Co-doped with Nitrogen and Sulfur for High Quantum Yield and Excitation-Independent Emission. *Angewandte Chemie*, *125*(30), 7954–7958. https://doi.org/10.1002/ANGE.201301114

dos Santos, L. M., Bernard, F. L., Pinto, I. S., Scholer, H., Dias, G. G., Prado, M., & Einloft, S. (2019). Polyurethane /Ionic Silica Xerogel Composites for CO2 Capture. *Materials Research-Ibero-American Journal of Materials*, *22*. https://doi.org/10.1590/1980-5373-MR-2019-0022

Drenchev, N., Aleksandrov, H. A., Vayssilov, G. N., Shivachev, B., & Hadjiivanov, K. (2024). Why does CaX zeolite have such a high CO2 capture capacity and how is it affected by water? *Separation and Purification Technology*, *349*. https://doi.org/10.1016/J.SEPPUR.2024.127662

Dua, S., Kumar, P., Pani, B., Kaur, A., Khanna, M., & Bhatt, G. (2023). Stability of carbon quantum dots: a critical review. *RSC Advances*, *13*(20), 13845–13861. https://doi.org/10.1039/D2RA07180K

Duceac, I. A., & Coseri, S. (2022). Biopolymers and their derivatives: Key components of advanced biomedical technologies. *Biotechnology Advances*, *61*. https://doi.org/10.1016/j.biotechadv.2022.108056

Durairaj, B., Santhi, R., & Hemalatha, A. (2018). Isolation of chitosan from fish scales of Catla catla and synthesis, characterization and screening for larvicidal potential of chitosan-based silver nanoparticles. *Drug Invention Today |*, *10*.

Echeverria Molina, M. I., Malollari, K. G., & Komvopoulos, K. (2021). Design Challenges in Polymeric Scaffolds for Tissue Engineering. *Frontiers in Bioengineering and Biotechnology*, *9*, 617141. https://doi.org/10.3389/FBIOE.2021.617141/XML/NLM

EI Kenawy, A. M., Al-Awadhi, T., Abdullah, M., Jawarneh, R., & Abulibdeh, A. (2023). A Preliminary Assessment of Global CO2: Spatial Patterns, Temporal Trends, and Policy Implications. *Global Challenges*, *7*(12). https://doi.org/10.1002/GCH2.202300184

El Jery, A., Alawamleh, H. S. K., Sami, M. H., Abbas, H. A., Sammen, S. S., Ahsan, A., Imteaz, M. A., Shanableh, A., Shafiquzzaman, M., Osman, H., & Al-Ansari, N. (2024). Isotherms, kinetics and thermodynamic mechanism of methylene blue dye adsorption on synthesized activated carbon. *Scientific Reports*, *14*(1). https://doi.org/10.1038/s41598-023-50937-0

Elamri, A., Zdiri, K., Bouzir, D., & Hamdaoui, M. (2022). Use of chitosan as antimicrobial, antiviral and antipollution agent in textile finishing. *Vlakna a Textil*, *29*(3), 51–70. https://doi.org/10.15240/TUL/008/2022-3-006

Elugoke, S. E., Uwaya, G. E., Quadri, T. W., & Ebenso, E. E. (2024). Carbon Quantum Dots: Basics, Properties, and Fundamentals. *ACS Symposium Series*, *1465*, 3–42. https://doi.org/10.1021/BK-2024-1465.CH001

Emam, H. E. (2023). Carbon quantum dots derived from polysaccharides: Chemistry and potential applications. *Carbohydrate Polymers*, *324*. https://doi.org/10.1016/J.CARBPOL.2023.121503

Etefa, H. F., Tessema, A. A., & Dejene, F. B. (2024). Carbon Dots for Future Prospects: Synthesis, Characterizations and Recent Applications: A Review (2019–2023). *C*, *10*(3), 60–60. https://doi.org/10.3390/C10030060

Etim, U. J., Zhang, C., & Zhong, Z. (2021a). Impacts of the Catalyst Structures on CO2 Activation on Catalyst Surfaces. *Nanomaterials*, *11*(12), 3265. https://doi.org/10.3390/NANO11123265

Etim, U. J., Zhang, C., & Zhong, Z. (2021b). Impacts of the Catalyst Structures on CO2 Activation on Catalyst Surfaces. *Nanomaterials 2021, Vol. 11, Page 3265*, *11*(12), 3265. https://doi.org/10.3390/NANO11123265

Fatima, S. S., Borhan, A., Ayoub, M., & Ghani, N. A. (2023). Modeling of CO2 Adsorption on Surface-Functionalized Rubber-Seed Shell Activated Carbon: Isotherm and Kinetic Analysis. *Processes 2023, Vol. 11, Page 2833*, *11*(10), 2833. https://doi.org/10.3390/PR11102833

Fawaz, W., Hasian, J., & Alghoraibi, I. (2023). Synthesis and physicochemical characterization of carbon quantum dots produced from folic acid. *Scientific Reports*, *13*(1), 18641. https://doi.org/10.1038/S41598-023-46084-1

FEI Nova NanoSEM | Electron Nanoscopy Instrumentation Facility | Nebraska. (n.d.). Retrieved July 18, 2025, from https://enif.unl.edu/nanosem/?utm_source=chatgpt.com

Feng, M., He, B., Chen, X., Xu, J., Lu, X., Jia, C., & Sun, J. (2022). Separation of chitin from shrimp shells enabled by transition metal salt aqueous solution and ionic liquid. *Journal of the Chemical Industry and Engineering Society of China*, *53*, 133–141. https://doi.org/10.1016/J.CJCHE.2022.01.031

Feng, Z. (2024). Current Research on CO2 Reduction Technology. *Highlights in Science Engineering and Technology*, *90*, 112–116. https://doi.org/10.54097/8Q98CJ44

Ferjani, H., Abdalla, S., Oyewo, O. A., & Onwudiwe, D. C. (2024). Facile synthesis of carbon dots by the hydrothermal carbonization of avocado peels and evaluation of the photocatalytic property. *Inorganic Chemistry Communications*, *160*. https://doi.org/10.1016/J.INOCHE.2023.111866

Fernandez, R. M. D., Estrada, R. J. R., Tomon, T. R. B., Dingcong, R. G., Amparado, R. F., Capangpangan, R. Y., Malaluan, R. M., Dumancas, G. G., Lubguban, A. A., Alguno, A. C., Bacosa, H. P., & Lubguban, A. A. (2023). Experimental Design and Breakthrough Curve Modeling of Fixed-Bed Columns Utilizing a Novel 3D Coconut-Based Polyurethane-Activated Carbon Composite Adsorbent for Lead Sequestration. *Sustainability 2023, Vol. 15, Page 14344*, *15*(19), 14344. https://doi.org/10.3390/SU151914344

Feroz, S., Muhammad, N., Ranayake, J., & Dias, G. (2020). Keratin - Based materials for biomedical applications. *Bioactive Materials*, *5*(3), 496–509. https://doi.org/10.1016/J.BIOACTMAT.2020.04.007

Friedlingstein, P., Houghton, R. A., Marland, G., Hackler, J., Boden, T. A., Conway, T. J., Canadell, J. G., Raupach, M. R., Ciais, P., & Le Quéré, C. (2010). Update on CO2 emissions. *Nature Geoscience*, *3*(12), 811–812. https://doi.org/10.1038/NGEO1022

Fu, H., Ding, X., Ren, C., Li, W., Wu, H., & Yang, H. (2017). Preparation of magnetic porous NiFe2O4/SiO2 composite xerogels for potential application in adsorption of Ce(iv) ions from aqueous solution. *RSC Advances*, *7*(27), 16513–16523. https://doi.org/10.1039/c6ra27219c

Fu, Y., Liu, R., & Zhi, J. (2018). Facile synthesis of graphene quantum dots based on electrochemical method and their application for specific Fe3+ detection. *Advanced Materials Letters*, *9*(9), 614–618. https://doi.org/10.5185/AMLETT.2018.2052

Galhotra, P., Navea, J. G., Larsen, S. C., & Grassian, V. H. (2009). Carbon dioxide (C 16 O 2 and C 18 O 2) adsorption in zeolite Y materials: effect of cation , adsorbed water and particle size. *Energy & Environmental Science*, *2*(4), 401–409. https://doi.org/10.1039/B814908A

Gao, X., Yang, S., Hu, L., Cai, S., Wu, L., & Kawi, S. (2022). Carbonaceous materials as adsorbents for CO2 capture: synthesis and modification. *Carbon Capture Science & Technology*, *3*, 100039. https://doi.org/10.1016/j.ccst.2022.100039

Gencer, O., Çeven, Ö. F., & Ünlü, C. (2022). Triggering excitation independent fluorescence in zinc(II) incorporated carbon dots: Surface passivation of carbon dots with zinc(II) ions by microwave assisted synthesis methods. *Diamond and Related Materials*, *123*. https://doi.org/10.1016/J.DIAMOND.2022.108874

Ghazal, H., Allam, L., Maraae, A., Beltagy, Z., Elshamy, M., Nasser, A., & Abd-Elaal, L. (2024). Chitosan and Its Derivatives in The Functional Processing Of Textiles. *Egyptian Journal of Textile and Polymer Science and Technology*, *0*(0), 0–0. https://doi.org/10.21608/JTCPS.2024.259548.1303

Ghobashy, M. M. (2021). Greener synthesis of carbon dots. *Handbook of Greener Synthesis of Nanomaterials and Compounds: Volume 2: Synthesis at the*

Macroscale and Nanoscale, 219–244. https://doi.org/10.1016/B978-0-12-822446-5.00011-3

Ghosal, K., & Ghosh, A. (2019). Carbon dots: The next generation platform for biomedical applications. *Materials Science and Engineering: C*, *96*, 887–903. https://doi.org/10.1016/J.MSEC.2018.11.060

Girimonte, R., Testa, F., Turano, M., Leone, G., Gallo, M., & Golemme, G. (2022). Amine-Functionalized Mesoporous Silica Adsorbent for CO2 Capture in Confined-Fluidized Bed: Study of the Breakthrough Adsorption Curves as a Function of Several Operating Variables. *Processes 2022, Vol. 10, Page 422*, *10*(2), 422. https://doi.org/10.3390/PR10020422

Global Carbon Budget | Fossil fuel CO_2 emissions increase again in 2024. (n.d.). Retrieved March 19, 2025, from https://globalcarbonbudget.org/fossil-fuel-co2-emissions-increase-again-in-2024/?utm_source=chatgpt.com

Gong, W., Tao, C., Tian, Z., Huang, Z., Lin, H., Qi, C., Yu, Z., & Guo, L. (2025). Characterization and mechanism of phosphorus adsorption from wastewater by lanthanum calcium doped sludge/wheat straw biochar. *Frontiers in Environmental Science*, *13*, 1604542. https://doi.org/10.3389/FENVS.2025.1604542/BIBTEX

Gong, X., Lu, W., Liu, Y., Li, Z., Shuang, S., Dong, C., & Choi, M. M. F. (2015). Low temperature synthesis of phosphorous and nitrogen co-doped yellow fluorescent carbon dots for sensing and bioimaging. *Journal of Materials Chemistry B*, *3*(33), 6813–6819. https://doi.org/10.1039/C5TB00575B

Gor, G. Y., & Bernstein, N. (2016). Revisiting Bangham's law of adsorption-induced deformation: changes of surface energy and surface stress. *Physical Chemistry Chemical Physics*, *18*(14), 9788–9798. https://doi.org/10.1039/C6CP00051G

Gu, Z., Wang, X., Huang, P., Huang, Y., He, X., Wei, X., Yue, J., Jiang, J., & Zhao, C. (2022). Experimental and kinetics investigations of low-concentration CO2 adsorption on several amine-functionalized adsorbents. *Process Safety and Environmental Protection*, *160*, 573–583. https://doi.org/10.1016/J.PSEP.2022.02.047

Gulati, S., Baul, A., Amar, A., Wadhwa, R., Kumar, S., & Varma, R. S. (2023). Eco-Friendly and Sustainable Pathways to Photoluminescent Carbon Quantum Dots (CQDs). *Nanomaterials*, *13*(3), 554–554. https://doi.org/10.3390/NANO13030554

Gunawan, T., Wijiyanti, R., & Widiastuti, N. (2018). Adsorption–desorption of CO 2 on zeolite-Y-templated carbon at various temperatures. *RSC Advances*, *8*(72), 41594–41602. https://doi.org/10.1039/C8RA09200A

Guo, B., Wang, Y., Shen, X., Qiao, X., Jia, L., Xiang, J., & Jin, Y. (2020). Study on CO2 Capture Characteristics and Kinetics of Modified Potassium-Based Adsorbents. *Materials*, *13*(4), 877. https://doi.org/10.3390/MA13040877

Guo, J., Ma, Y. P., Wu, W. J., Cao, X. F., & Fu, Y. P. (2025). One-Step Synthesis of In Situ Sulfur-Doped Porous Carbons for Efficient CO2 Adsorption. *Sustainability (Switzerland)*, *17*(11), 4952. https://doi.org/10.3390/SU17114952/S1

Güzel Kaya, G. (2021). Polyethylene glycol/silica and carbon black/silica xerogel composites as an adsorbent for CO2 capture. *Turkish Journal of Chemistry*, *45*(6), 2013. https://doi.org/10.3906/KIM-2101-45

Hamed, A. M., Kamaruddin, T. N. A. T., Ramli, N., & Wahab, M. F. A. (2023). Design and simulate an amine-based CO2 capture process for a steam methane reforming hydrogen production plant. *IOP Conference Series: Earth and Environmental Science*, *1281*(1). https://doi.org/10.1088/1755-1315/1281/1/012048

Hammi, N., Chen, S., Dumeignil, F., Royer, S., & El Kadib, A. (2020). Chitosan as a sustainable precursor for nitrogen-containing carbon nanomaterials: synthesis and uses. *Materials Today Sustainability*, *10*, 100053. https://doi.org/10.1016/J.MTSUST.2020.100053

Hannachi, Y., Hafidh, A., & Ayed, S. (2019a). Effectiveness of novel xerogels adsorbents for cadmium uptake from aqueous solution in batch and column modes: Synthesis, characterization, equilibrium, and mechanism analysis. *Chemical Engineering Research and Design*, *143*, 11–23. https://doi.org/10.1016/j.cherd.2019.01.006

Hannachi, Y., Hafidh, A., & Ayed, S. (2019b). Effectiveness of novel xerogels adsorbents for cadmium uptake from aqueous solution in batch and column modes: Synthesis, characterization, equilibrium, and mechanism analysis. *Chemical Engineering Research and Design*, *143*, 11–23. https://doi.org/10.1016/j.cherd.2019.01.006

Hao, W., Lee, S. H., & Peera, S. G. (2023). Xerogel-Derived Manganese Oxide/N-Doped Carbon as a Non-Precious Metal-Based Oxygen Reduction Reaction

Catalyst in Microbial Fuel Cells for Energy Conversion Applications. *Nanomaterials*, *13*(22), 2949. https://doi.org/10.3390/NANO13222949/S1

Hauchhum, L., & Mahanta, P. (2014). Carbon dioxide adsorption on zeolites and activated carbon by pressure swing adsorption in a fixed bed. *International Journal of Energy and Environmental Engineering*, *5*(4), 349–356. https://doi.org/10.1007/S40095-014-0131-3/FIGURES/10

Hedayati, A., Delica, B. A., Perez-Gil, S., & Prieto-Fernandez, S. (2022). Evaluation of high-performance adsorbents for separation of CO 2 from industrial effluent gases. *Greenhouse Gases-Science and Technology*, *13*(2), 216–226. https://doi.org/10.1002/GHG.2197

Helmi, M., Moazami, F., Hemmati, A., & Ghaemi, A. (2023). Synthesis and characterization of KOH@Graphene oxide-Fe3O4 as a magnetic composite adsorbent for CO2 capture. *Journal of Physics and Chemistry of Solids*, *178*, 111338–111338. https://doi.org/10.1016/J.JPCS.2023.111338

HEMMAMI, H., BEN AMOR, I., BEN AMOR, A., ZEGHOUD, S., AHMED, S., & ALHAMAD, A. A. (2023). Chitosan, Its Derivatives, Sources, Preparation Methods, and Applications: A Review. *Journal of the Turkish Chemical Society Section A: Chemistry*, *11*(1), 341–364. https://doi.org/10.18596/JOTCSA.1336313

Hosney, A., Ullah, S., & Barčauskaitė, K. (2022). A Review of the Chemical Extraction of Chitosan from Shrimp Wastes and Prediction of Factors Affecting Chitosan Yield by Using an Artificial Neural Network. *Marine Drugs*, *20*(11), 675. https://doi.org/10.3390/md20110675

Hu, J., Tan, W., Wang, C. X., Yan, L. H., Si, J., & Hou, X. (2024). One-step microwave synthesis of high-efficiency solid-state luminescent carbon dots with aggregation-induced emission. *Optical Materials*, *150*. https://doi.org/10.1016/J.OPTMAT.2024.115219

Hu, Q., Paau, M. C., Zhang, Y., Gong, X., Zhang, L., Lu, D., Liu, Y., Liu, Q., Yao, J., & Choi, M. M. F. (2014). Green synthesis of fluorescent nitrogen/sulfur-doped carbon dots and investigation of their properties by HPLC coupled with mass spectrometry. *RSC Advances*, *4*(35), 18065–18073. https://doi.org/10.1039/C4RA02170C

Huang, H., Cui, Y., Liu, M., Chen, J., Wan, Q., Wen, Y., Deng, F., Zhou, N., Zhang, X., & Wei, Y. (2018). A one-step ultrasonic irradiation assisted strategy for the

preparation of polymer-functionalized carbon quantum dots and their biological imaging. *Journal of Colloid and Interface Science*, *532*, 767–773. https://doi.org/10.1016/j.jcis.2018.07.099

Huang, J., Wu, T., Dai, C., Xie, Y., & Zeng, C. (2024). Improved Charge Separation and CO2 Affinity of In2O3 by K Doping with Accompanying Oxygen Vacancies for Boosted CO2 Photoreduction. *Langmuir*. https://doi.org/10.1021/ACS.LANGMUIR.3C03854

Huang, L., Bi, S., Pang, J., Sun, M., Feng, C., & Chen, X. (2020). Preparation and characterization of chitosan from crab shell (Portunus trituberculatus) by NaOH/urea solution freeze-thaw pretreatment procedure. *International Journal of Biological Macromolecules*, *147*, 931–936. https://doi.org/10.1016/J.IJBIOMAC.2019.10.059

Hubbe, M., Azizian, S., & Douven, S. (2019). Implications of apparent pseudo-second-order adsorption kinetics onto cellulosic materials: A review. *BioResources*, *14*(3), 7582–7626. https://doi.org/10.15376/BIORES.14.3.7582-7626

Huo, Y., Xiu, S., Meng, L. Y., & Quan, B. (2023). Solvothermal synthesis and applications of micro/nano carbons: A review. *Chemical Engineering Journal*, *451*, 138572. https://doi.org/10.1016/J.CEJ.2022.138572

Ibarra-Prieto, H. D., Garcia-Garcia, A., Aguilera-Granja, F., Navarro-Ibarra, D. C., & Rivero-Espejel, I. (2023). One-Pot, Optimized Microwave-Assisted Synthesis of Difunctionalized and B–N Co-Doped Carbon Dots: Structural Characterization. *Nanomaterials*, *13*(20). https://doi.org/10.3390/NANO13202753

Jadav, H. L., & Patel, N. (2023). FUEL PRODUCTION FROM BIOMASS AND WASTE PLASTIC (POLYETHYLENE) BY CO-PYROLYSIS PROCESS. In *International Journal of Applied Engineering & Technology Copyrights @ Roman Science Publications Ins* (Vol. 5, Number 4).

Jagtap, P., Patil, K., & Dhatrak, P. (2021). Polyelectrolyte Complex for Drug Delivery in Biomedical Applications: A Review. *IOP Conference Series: Materials Science and Engineering*, *1183*(1), 012007. https://doi.org/10.1088/1757-899x/1183/1/012007

Jahan, S., Mansoor, F., Naz, S., Lei, J., & Kanwal, S. (2013). Oxidative synthesis of highly fluorescent boron/nitrogen Co-doped carbon nanodots enabling

detection of photosensitizer and carcinogenic dye. *Analytical Chemistry*, *85*(21), 10232–10239. https://doi.org/10.1021/AC401949K,

Jaiboon, V., Yoosuk, B., & Prasassarakich, P. (2014). Amine modified silica xerogel for H2S removal at low temperature. *Fuel Processing Technology*, *128*, 276–282. https://doi.org/10.1016/j.fuproc.2014.07.032

Janus, Ł., Piatkowski˛, M., Radwan-Pragłowska, J., Bogdał, D., & Matysek, D. (2019a). Chitosan-based carbon quantum dots for biomedical applications: Synthesis and characterization. *Nanomaterials*, *9*(2). https://doi.org/10.3390/NANO9020274

Janus, Ł., Piatkowski˛, M., Radwan-Pragłowska, J., Bogdał, D., & Matysek, D. (2019b). Chitosan-based carbon quantum dots for biomedical applications: Synthesis and characterization. *Nanomaterials*, *9*(2). https://doi.org/10.3390/nano9020274

Jia, J., Song, H., & Jia, P. (2023). Selective adsorption mechanism of CO2/CH4/N2 multi-component gas mixtures by N/S atoms and functional groups in coal. *Process Safety and Environmental Protection*, *182*, 210–221. https://doi.org/10.1016/J.PSEP.2023.11.079

Jiang, B., Zhang, B., Duan, X., & Xing, Y. (2024). CO2 capture by modified clinoptilolite and its regeneration performance. *International Journal of Coal Science and Technology*, *11*(1). https://doi.org/10.1007/S40789-023-00661-X

Jorns, M., Pappas, D., Tagmatarchis, N., & Kelarakis, A. (2021a). A Review of Fluorescent Carbon Dots, Their Synthesis, Physical and Chemical Characteristics, and Applications. *Nanomaterials 2021, Vol. 11, Page 1448*, *11*(6), 1448. https://doi.org/10.3390/NANO11061448

Jorns, M., Pappas, D., Tagmatarchis, N., & Kelarakis, A. (2021b). A Review of Fluorescent Carbon Dots, Their Synthesis, Physical and Chemical Characteristics, and Applications. *Nanomaterials 2021, Vol. 11, Page 1448*, *11*(6), 1448. https://doi.org/10.3390/NANO11061448

Kajani, A. A., Rafiee, L., Javanmard, S. H., Dana, N., & Jandaghian, S. (2023). Carbon dot incorporated mesoporous silica nanoparticles for targeted cancer therapy and fluorescence imaging. *RSC Advances*, *13*(14), 9491–9500. https://doi.org/10.1039/d3ra00768e

Kalutharage, N. K., & Rathnasinghe, D. L. (2020). A study of chitosan and glucosamine isolated from Sri Lankan local mushroom Schizophyllum

commune and oyster mushroom (Pleurotus ostreatus). *Materials Today: Proceedings*, *23*, 119–122. https://doi.org/10.1016/J.MATPR.2019.07.713

Kandasamy, G. (2019). Recent Advancements in Doped/Co-Doped Carbon Quantum Dots for Multi-Potential Applications. *C 2019, Vol. 5, Page 24*, *5*(2), 24. https://doi.org/10.3390/C5020024

Kande, B., & Parmar, P. (2022). Carbon Quantum Dot and Application: A Review. *Spectrum of Emerging Sciences*, *2*(1), 11–24. https://doi.org/10.55878/SES2022-2-1-3

Kandra, R., & Bajpai, S. (2020). Synthesis, mechanical properties of fluorescent carbon dots loaded nanocomposites chitosan film for wound healing and drug delivery. *Arabian Journal of Chemistry*, *13*(4), 4882–4894. https://doi.org/10.1016/J.ARABJC.2019.12.010

Kannouma, R. E., Kamal, A. H., Hammad, M. A., & Mansour, F. R. (2024). Incorporation of eggshell waste in the preparation of carbon quantum dot nanoprobes for the determination of COVID-19 antiviral drug; molnupiravir. *Microchemical Journal*, *200*. https://doi.org/10.1016/J.MICROC.2024.110397

Karayil, A., Elseragy, A., & Aliyu, A. M. (2024). An Assessment of CO2 Capture Technologies towards Global Carbon Net Neutrality. *Energies*, *17*(6). https://doi.org/10.3390/EN17061460

Kasikamphaiboon, P., & Khunjan, U. (2018). CO2 Adsorption from Biogas Using Amine-Functionalized MgO. *International Journal of Chemical Engineering*, *2018*(1), 1706405. https://doi.org/10.1155/2018/1706405

Kaur Bhullar, N., Sachdev, D., & Kumari, K. (2024). Applications of chitosan based materials in wastewater systems. *Futuristic Trends in Chemical Material Sciences & Nano Technology Volume 3 Book 2*, 239–258. https://doi.org/10.58532/V3BECM2CH17

Kaya, M., Karaarslan, M., Baran, T., Can, E., Ekemen, G., Bitim, B., & Duman, F. (2014). The quick extraction of chitin from an epizoic crustacean species (Chelonibia patula). *Natural Product Research*, *28*(23), 2186–2190. https://doi.org/10.1080/14786419.2014.927469

Kazeminava, F., Javanbakht, S., Nouri, M., Gholizadeh, P., Nezhad-Mokhtari, P., Ganbarov, K., Tanomand, A., & Kafil, H. S. (2022). Gentamicin-loaded chitosan/folic acid-based carbon quantum dots nanocomposite hydrogel films

as potential antimicrobial wound dressing. *Journal of Biological Engineering*, *16*(1). https://doi.org/10.1186/s13036-022-00318-4

Khader, M. M., Al-Marri, M. J., Ali, S., Qi, G., & Giannelis, E. P. (2015). Adsorption of CO₂ on Polyethyleneimine 10k—<i>Mesoporous silica</i> Sorbent: XPS and TGA Studies. *American Journal of Analytical Chemistry*, *06*(04), 274–284. https://doi.org/10.4236/ajac.2015.64026

Khalili, S., & Jahanshahi, M. (2021). Selective CO2 adsorption using N-rich porous carbon derived from KOH-activated polyaniline. *Korean Journal of Chemical Engineering*, *38*(4), 862–871. https://doi.org/10.1007/S11814-020-0691-2

Khan, A. U., Liu, Y., Wang, S., Ullah, M. W., Chen, Q., Zhang, D., Kang, Z., & Mao, B. (2024). Advancements in the green synthesis of carbon dots for sustainable development. *Sustainable Materials and Technologies*, *41*, e01004–e01004. https://doi.org/10.1016/J.SUSMAT.2024.E01004

Khubiev, O. M., Egorov, A. R., Kirichuk, A. A., Khrustalev, V. N., Tskhovrebov, A. G., & Kritchenkov, A. S. (2023). Chitosan-Based Antibacterial Films for Biomedical and Food Applications. *International Journal of Molecular Sciences*, *24*(13), 10738–10738. https://doi.org/10.3390/IJMS241310738

Kim, H., Kim, H., Ahn, Y., Hong, K. B., Kim, I. W., Choi, R. Y., Suh, H. J., & Han, S. H. (2023). The Preparation and Physiochemical Characterization of Tenebrio molitor Chitin Using Alcalase. *Molecules 2023, Vol. 28, Page 3254*, *28*(7), 3254. https://doi.org/10.3390/MOLECULES28073254

Kim, K. H., & Kim, M. H. (2023). Adsorption of CO2, CO, H2, and N2 on Zeolites, Activated Carbons, and Metal-Organic Frameworks with Different Surface Nonuniformities. *Sustainability*, *15*(15). https://doi.org/10.3390/SU151511574

Kim, M., Osone, S., Kim, T., Higashi, H., & Seto, T. (2017). Synthesis of Nanoparticles by Laser Ablation: A Review. *KONA Powder and Particle Journal*, *34*(34), 80–90. https://doi.org/10.14356/KONA.2017009

Kisliuk, P. (1957). The sticking probabilities of gases chemisorbed on the surfaces of solids. *Journal of Physics and Chemistry of Solids*, *3*(1–2), 95–101. https://doi.org/10.1016/0022-3697(57)90054-9

Kloos, R. L., Wineinger, D. M., & Weisshaar, D. E. (1999). QUANTITATIVE ANALYSIS OF A SOLID SOLUTION USING FOURIER TRANSFORM

INFRARED SPECTROMETRY: AN INSTRUMENTAL ANALYSIS EXPERIMENT. In *Proceedings of the South Dakota Academy of Science* (Vol. 78).

Kolanowska, A., Dzido, G., Krzywiecki, M., Tomczyk, M. M., Łukowiec, D., Ruczka, S., & Boncel, S. (2022). Carbon Quantum Dots from Amino Acids Revisited: Survey of Renewable Precursors toward High Quantum-Yield Blue and Green Fluorescence. *ACS Omega*, *7*(45), 41165–41176. https://doi.org/10.1021/ACSOMEGA.2C04751/SUPPL_FILE/AO2C04751_SI_001.PDF

Kong, J., Wei, Y., Zhou, F., Shi, L., Zhao, S., Wan, M., & Zhang, X. (2024). Carbon Quantum Dots: Properties, Preparation, and Applications. *Molecules 2024, Vol. 29, Page 2002*, *29*(9), 2002. https://doi.org/10.3390/MOLECULES29092002

Kozma, M., Acharya, B., & Bissessur, R. (2022). Chitin, Chitosan, and Nanochitin: Extraction, Synthesis, and Applications. *Polymers 2022, Vol. 14, Page 3989*, *14*(19), 3989. https://doi.org/10.3390/POLYM14193989

Kratos X-ray Photoelectron Spectrometer - Axis Ultra DLD. (n.d.). Retrieved July 18, 2025, from https://tmi.utexas.edu/facilities/instrumentation/kratos-x-ray-photoelectron-spectrometer-axis-ultra-dld?utm_source=chatgpt.com

Krishna Saraswat, S., Ahmed Mustafa, M., Kamil Ghadir, G., Kaur, M., Guamán Lozada, D. F., Hasen shuhata alubiady, M., Muzahem Al-Ani, A., Alshahrani, M. Y., Kadhem Abid, M., Salih Jumaa, S., Yahaia Alhameedi, D., & huseen Redhee, A. (2024). Carbon quantum dots: A comprehensive review of green Synthesis, characterization and investigation their applications in bioimaging. *Inorganic Chemistry Communications*, *162*, 112279. https://doi.org/10.1016/J.INOCHE.2024.112279

Krishnaiah, D., Bono, A., Anisuzzama, S. M., Joseph, C., & Khee, T. B. (2014). Carbon Dioxide Removal by Adsorption. *Journal of Applied Sciences*, *14*(23), 3142–3148. https://doi.org/10.3923/JAS.2014.3142.3148

Krutka, H., Sjostrom, S., Starns, T., Dillon, M., & Silverman, R. (2013). Post-combustion CO2 capture using solid sorbents: 1 MW e pilot evaluation. *Energy Procedia*, *37*, 73–88. https://doi.org/10.1016/j.egypro.2013.05.087

Kumar, A., Prasad, S., Saxena, P. N., Ansari, N. G., & Patel, D. K. (2021). Synthesis of an Alginate-Based Fe3O4-MnO2Xerogel and Its Application for the Concurrent Elimination of Cr(VI) and Cd(II) from Aqueous Solution. *ACS*

Omega, *6*(5), 3931–3945. https://doi.org/10.1021/ACSOMEGA.0C05787/SUPPL_FILE/AO0C05787_SI_001.PDF

Kumar, R., Kumar, V. B., & Gedanken, A. (2020). Sonochemical synthesis of carbon dots, mechanism, effect of parameters, and catalytic, energy, biomedical and tissue engineering applications. *Ultrasonics Sonochemistry*, *64*, 105009. https://doi.org/10.1016/J.ULTSONCH.2020.105009

Kumar Singh, V., & Anil Kumar, E. (2018). Comparative Studies on CO2 Adsorption Isotherms by Solid Adsorbents. *Materials Today: Proceedings*, *5*(11), 23033–23042. https://doi.org/10.1016/J.MATPR.2018.11.032

Kurian, M., & Paul, A. (2021). Recent trends in the use of green sources for carbon dot synthesis–A short review. *Carbon Trends*, *3*. https://doi.org/10.1016/J.CARTRE.2021.100032

Kyzas, G. Z., & Bikiaris, D. N. (2015). Recent modifications of chitosan for adsorption applications: A critical and systematic review. In *Marine Drugs* (Vol. 13, Number 1, pp. 312–337). MDPI AG. https://doi.org/10.3390/md13010312

Laemont, A., Matthys, G., Lavendomme, R., & van der Voort, P. (2024). Mild and Scalable Conditions for the Solvothermal Synthesis of Imine-Linked Covalent Organic Frameworks. *Angewandte Chemie International Edition*, e202412420–e202412420. https://doi.org/10.1002/ANIE.202412420

Lahuri, A. H., Yusuf, A. M., Adnan, R., Rahim, A. A., Waheed Tajudeen, N. F., & Nordin, N. (2022). Kinetics and thermodynamic modeling for CO2 capture using NiO supported activated carbon by temperature swing adsorption. *Biointerface Research in Applied Chemistry*, *12*(3), 4200–4219. https://doi.org/10.33263/BRIAC123.42004219

Lalji, S. M., Ayubi, M., Ali, S. I., Rahman, S. ur, & Mustafa, M. (2024). Investigating different kinetic models for CO2 adsorption on amine silica sorbent. *Discover Chemistry*, *1*(1), 71. https://doi.org/10.1007/s44371-024-00077-9

Lalji, S. M., Ayubi, M., Syed, ·, Ali, I., Saad Ur Rahman, ·, & Mustafa, · Muhammad. (2024). Investigating different kinetic models for CO2 adsorption on amine silica sorbent. *Discover Chemistry 2024 1:1*, *1*(1), 1–14. https://doi.org/10.1007/S44371-024-00077-9

Lamb, W. F., Wiedmann, T., Pongratz, J., Andrew, R., Crippa, M., Olivier, J. G. J., Wiedenhofer, D., Mattioli, G., Khourdajie, A. Al, House, J., Pachauri, S., Figueroa, M., Saheb, Y., Slade, R., Hubacek, K., Sun, L., Ribeiro, S. K., Khennas, S., De La Rue Du Can, S., … Minx, J. (2021). A review of trends and drivers of greenhouse gas emissions by sector from 1990 to 2018. *Environmental Research Letters*, *16*(7), 073005. https://doi.org/10.1088/1748-9326/ABEE4E

Lan, K., & Zhao, D. (2022). Functional Ordered Mesoporous Materials: Present and Future. *Nano Letters*, *22*(8), 3177–3179. https://doi.org/10.1021/ACS.NANOLETT.2C00902/ASSET/IMAGES/LARGE/NL2C00902_0001.JPEG

Law, L. C., Mastorakos, E., Othman, M. R., & Trakakis, A. (2024). A Thermodynamics Model for the Assessment and Optimisation of Onboard Natural Gas Reforming and Carbon Capture. *Emission Control Science and Technology*, *10*(1), 52–69. https://doi.org/10.1007/S40825-023-00234-Z

Lee, D. Y., Haider, Z., Krishnan, S. K., Kanagaraj, T., Son, S. H., Jae, J., Kim, J. R., Murphin Kumar, P. S., & Kim, H. il. (2024). Oxygen-enriched carbon quantum dots from coffee waste: Extremely active organic photocatalyst for sustainable solar-to-H2O2 conversion. *Chemosphere*, *361*, 142330–142330. https://doi.org/10.1016/J.CHEMOSPHERE.2024.142330

Lee, M. S., Park, M., Kim, H. Y., & Park, S. J. (2016). Effects of Microporosity and Surface Chemistry on Separation Performances of N-Containing Pitch-Based Activated Carbons for CO2/N2 Binary Mixture. *Scientific Reports 2016 6:1*, *6*(1), 23224-. https://doi.org/10.1038/srep23224

Lee, W. R., Hwang, S. Y., Ryu, D. W., Lim, K. S., Han, S. S., Moon, D., Choi, J., & Hong, C. S. (2014). Diamine-functionalized metal-organic framework: Exceptionally high CO 2 capacities from ambient air and flue gas, ultrafast CO2 uptake rate, and adsorption mechanism. *Energy and Environmental Science*, *7*(2), 744–751. https://doi.org/10.1039/C3EE42328J

Li, B., Zeng, S., Jiang, C., Li, G., Bai, L., Xu, F., & Zhang, X. (2024). Dynamic breakthrough performance of low concentration CO2 adsorption in fixed-bed column with porous amino acid ionic liquid composites. *Separation and Purification Technology*, *349*, 127901. https://doi.org/10.1016/J.SEPPUR.2024.127901

Li, G., He, J., & Yao, J. (2025). A Review of Recent Advances in Biomass-Derived Porous Carbon Materials for CO2 Capture. *C 2025, Vol. 11, Page 92*, *11*(4), 92. https://doi.org/10.3390/C11040092

Li, S., Jia, S., Nagasaka, T., Bai, H., & Yang, L. (2023). CO2 Adsorption Properties of Amine-Modified Zeolites Synthesized Using Different Types of Solid Waste. *Sustainability (Switzerland)*, *15*(13), 10144. https://doi.org/10.3390/SU151310144/S1

Li, X., Chang, J., Xu, F., Wang, X., Lang, Y., Gao, Z., Wu, D., & Jiang, K. (2015). Pyrolytic synthesis of carbon quantum dots, and their photoluminescence properties. *Research on Chemical Intermediates*, *41*(2), 813–819. https://doi.org/10.1007/S11164-013-1233-X/METRICS

Li, Y., Liang, J., Li, J., Liao, L., Guo, J., & Jia, J. (2024). Tuning the carboxyl content of carbon quantum dots by an electrochemical exfoliation method to enhance Fenton-like reactions for contaminants removal in a wide pH range. *Journal of Environmental Chemical Engineering*, *12*(2). https://doi.org/10.1016/J.JECE.2024.112008

Li, Y., Liu, X., & Guo, Q. (2024). Adsorption Mechanisms of CO2 on Macroporous Ion-Exchange Resin Organic Amine Composite Materials by the Density Functional Theory. *ACS Omega*, *9*(15), 17541. https://doi.org/10.1021/ACSOMEGA.4C00587/SUPPL_FILE/AO4C00587_SI_001.PDF

Ligero, A., Calero, M., Martín-Lara, M. Á., Blázquez, G., Solís, R. R., & Pérez, A. (2023). Fixed-bed CO2 adsorption onto activated char from the pyrolysis of a non-recyclable plastic mixture from real urban residues. *Journal of CO2 Utilization*, *73*. https://doi.org/10.1016/J.JCOU.2023.102517

Lim, G., Lee, K. B., & Ham, H. C. (2016). Effect of N-Containing Functional Groups on CO2 Adsorption of Carbonaceous Materials: A Density Functional Theory Approach. *Journal of Physical Chemistry C*, *120*(15), 8087–8095. https://doi.org/10.1021/ACS.JPCC.5B12090

Lim, S. Y., Shen, W., & Gao, Z. (2014). Carbon quantum dots and their applications. *Chemical Society Reviews*, *44*(1), 362–381. https://doi.org/10.1039/C4CS00269E

Lima, H. B. S., Sousa, A. P. S. de, Silva, W. B. da, Costa, D. S. da, Rodrigues, E. C., & Estumano, D. C. (2024). Parameter Estimation of Breakthrough Curve

Models in the Adsorption Process of H2S and CO2 Using the Markov Chain Monte Carlo Method. *Applied Sciences (Switzerland)*, *14*(16), 6956. https://doi.org/10.3390/APP14166956/S1

Ling, J., Ntiamoah, A., Xiao, P., Webley, P. A., & Zhai, Y. (2015). Effects of feed gas concentration, temperature and process parameters on vacuum swing adsorption performance for CO2 capture. *Chemical Engineering Journal*, *265*, 47–57. https://doi.org/10.1016/J.CEJ.2014.11.121

Lingait, D., Rahagude, R., Gaharwar, S. S., Das, R. S., Verma, M. G., Srivastava, N., Kumar, A., & Mandavgane, S. (2023). A review on versatile applications of biomaterial/polycationic chitosan: An insight into the structure-property relationship. *International Journal of Biological Macromolecules*, *257*, 128676–128676. https://doi.org/10.1016/J.IJBIOMAC.2023.128676

Liu, B., Li, H., Ma, X., Chen, R., Wang, S., & Li, L. (2018). The synergistic effect of oxygen-containing functional groups on CO2 adsorption by the glucose–potassium citrate-derived activated carbon. *RSC Advances*, *8*(68), 38965–38973. https://doi.org/10.1039/C8RA05523H

Liu, B., Yu, L., Wang, H., Ma, X., Zeng, Z., & Li, L. (2022). Experimental and molecular perspective on VOCs adsorption and separation: Study of the surface heterogeneity and oxygen functionalizing. *Chemical Engineering Journal*, *435*, 135069. https://doi.org/10.1016/j.cej.2022.135069

Liu, G., Li, B., Liu, Y., Feng, Y., Jia, D., & Zhou, Y. (2019). Rapid and high yield synthesis of carbon dots with chelating ability derived from acrylamide/chitosan for selective detection of ferrous ions. *Applied Surface Science*, *487*, 1167–1175. https://doi.org/10.1016/J.APSUSC.2019.05.069

Liu, H., Zhang, Y., & Huang, C. (2018). Development of nitrogen and sulfur-doped carbon dots for cellular imaging. *Journal of Pharmaceutical Analysis*, *9*(2), 127. https://doi.org/10.1016/J.JPHA.2018.10.001

Liu, J., Liu, X., Luo, H., & Gao, Y. (2014). One-step preparation of nitrogen-doped and surface-passivated carbon quantum dots with high quantum yield and excellent optical properties. *RSC Advances*, *4*(15), 7648–7654. https://doi.org/10.1039/C3RA47577H

Liu, M., Xu, Y., Niu, F., Gooding, J. J., & Liu, J. (2016). Carbon quantum dots directly generated from electrochemical oxidation of graphite electrodes in alkaline

alcohols and the applications for specific ferric ion detection and cell imaging. *Analyst*, *141*(9), 2657–2664. https://doi.org/10.1039/C5AN02231B

Liu, T., Cui, Z. W., Zhou, J., Wang, Y., & Zou, Z. G. (2017). Synthesis of Pyridinic-Rich N, S Co-doped Carbon Quantum Dots as Effective Enzyme Mimics. *Nanoscale Research Letters*, *12*(1), 375–375. https://doi.org/10.1186/S11671-017-2149-Y

Liu, Z., Deng, Z., Davis, S. J., Giron, C., & Ciais, P. (2022). Monitoring global carbon emissions in 2021. *Nature Reviews Earth & Environment*, *3*(4), 217–219. https://doi.org/10.1038/S43017-022-00285-W

Liyanage, C. S., Gonapinuwala, S. T., Fernando, C. A. N., & De Croos, M. D. S. T. (2022). Physico-chemical properties of chitosan extracted from Whiteleg shrimp (Litopenaeus vannamei) processing shell waste in Sri Lanka. *Sri Lanka Journal of Aquatic Sciences*, *27*(2), 107. https://doi.org/10.4038/SLJAS.V27I2.7600

López, J. M. C., Martínez, J. J., Brijaldo, M. H., & Acevedo, S. (2024). CO2 adsorption in biochars obtained from soursop (Anonna muricata) seeds by chemical activation with metallic salts. *Adsorption*, *30*(7), 1865–1880. https://doi.org/10.1007/S10450-024-00528-W/FIGURES/13

Lu, Q., Eid, K., & Li, W. (2022). Heteroatom-Doped Porous Carbon-Based Nanostructures for Electrochemical CO2 Reduction. *Nanomaterials 2022, Vol. 12, Page 2379*, *12*(14), 2379. https://doi.org/10.3390/NANO12142379

Luo, H., Zhu, C. C., Tan, Z. C., Bao, L. W., Wang, J. J., Miao, G., Kong, L. Z., & Sun, Y. H. (2016). Preparation of N-doped activated carbons with high CO2 capture performance from microalgae (Chlorococcum sp.). *RSC Advances*, *6*(45), 38724–38730. https://doi.org/10.1039/C6RA04106J

Luo, K., Li, W., Luo, X., Kang, X., & Wen, Y. (2024). Solvent-free pyrolysis synthesis of solid-state fluorescent carbon dots: Optical properties and latent fingerprint imaging. *Diamond and Related Materials*, *142*. https://doi.org/10.1016/J.DIAMOND.2024.110837

Luo, L., Wang, P., Wang, Y., & Wang, F. (2018). pH assisted selective detection of Hg(II) and Ag(I) based on nitrogen-rich carbon dots. *Sensors and Actuators B: Chemical*, *273*, 1640–1647. https://doi.org/10.1016/J.SNB.2018.07.090

Luo, Q., Wang, Y., Han, Q., Ji, L., Zhang, H., Fei, Z., & Wang, Y. (2019). Comparison of the physicochemical, rheological, and morphologic properties of chitosan

from four insects. *Carbohydrate Polymers*, *209*, 266–275. https://doi.org/10.1016/j.carbpol.2019.01.030

Lv, O., Tao, Y., Qin, Y., Chen, C., Pan, Y., Deng, L., Liu, L., & Kong, Y. (2016). Highly fluorescent and morphology-controllable graphene quantum dots-chitosan hybrid xerogels for in vivo imaging and pH-sensitive drug carrier. *Materials Science and Engineering C*, *67*, 478–485. https://doi.org/10.1016/j.msec.2016.05.031

Lv, Y., Zhang, F., Dou, Y., Zhai, Y., Wang, J., Liu, H., Xia, Y., Tu, B., & Zhao, D. (2011). A comprehensive study on KOH activation of ordered mesoporous carbons and their supercapacitor application. *Journal of Materials Chemistry*, *22*(1), 93–99. https://doi.org/10.1039/C1JM12742J

Ma, Y., Chen, A. Y., Huang, Y. Y., He, X., Xie, X. F., He, B., Yang, J. H., & Wang, X. Y. (2020). Off-on fluorescent switching of boron-doped carbon quantum dots for ultrasensitive sensing of catechol and glutathione. *Carbon*, *162*, 234–244. https://doi.org/10.1016/J.CARBON.2020.02.048

Macena, M., Pereira, H., Cruz-Lopes, L., Grosche, L., & Esteves, B. (2025). Competitive Adsorption of Metal Ions by Lignocellulosic Materials: A Review of Applications, Mechanisms and Influencing Factors. *Separations 2025, Vol. 12, Page 70*, *12*(3), 70. https://doi.org/10.3390/SEPARATIONS12030070

Mahdi, H. H., Saleh, A. M., Alias, A. B., Jawad, A. H., Salman, S. D., Qarizada, D., Mostafa, M. M., Saleh, N. M., & Abdulqader, M. A. (2024a). Synthesis and Characterization of Xerogel Derived from Palm Kernel Shell Biochar and Comparison with Commercial Activated Carbon. *Journal of Ecological Engineering*, *25*(6). https://doi.org/10.12911/22998993/183719

Mahdi, H. H., Saleh, A. M., Alias, A. B., Jawad, A. H., Salman, S. D., Qarizada, D., Mostafa, M. M., Saleh, N. M., & Abdulqader, M. A. (2024b). Synthesis and Characterization of Xerogel Derived from Palm Kernel Shell Biochar and Comparison with Commercial Activated Carbon. *Journal of Ecological Engineering*, *25*(6). https://doi.org/10.12911/22998993/183719

Mambetova, M., Dossumov, K., & Yergaziyeva, G. (2024). The Influence of Mg, Na, and Li Oxides on the CO2 Sorption Properties of Natural Zeolite. *Processes*, *12*(11), 2592–2592. https://doi.org/10.3390/PR12112592

Mambetova, M. M., Yergaziyeva, G. Y., & Zhoketayeva, A. B. (2023). Physicochemical characteristics and carbon dioxide sorption properties of

natural zeolites. *Gorenie i Plazmohimiâ*, *21*(2), 81–87. https://doi.org/10.18321/CPC21(2)81-87

Mancinelli, M., & Martucci, A. (2025). Exploring the Potential of Zeolites for Sustainable Environmental Applications. *Sustainable Chemistry 2025, Vol. 6, Page 9*, *6*(1), 9. https://doi.org/10.3390/SUSCHEM6010009

Manikandan, V., & Lee, N. Y. (2022). Green synthesis of carbon quantum dots and their environmental applications. *Environmental Research*, *212*, 113283. https://doi.org/10.1016/j.envres.2022.113283

Manjubaashini, N., Bargavi, P., & Balakumar, S. (2024). Carbon quantum dots derived from agro waste biomass for pioneering bioanalysis and in vivo bioimaging. *Journal of Photochemistry and Photobiology A: Chemistry*, *454*. https://doi.org/10.1016/J.JPHOTOCHEM.2024.115702

Mansuriya, B. D., & Altintas, Z. (2021). Carbon Dots: Classification, Properties, Synthesis, Characterization, and Applications in Health Care—An Updated Review (2018–2021). *Nanomaterials*, *11*(10). https://doi.org/10.3390/NANO11102525

Marković, Z. M., Budimir, M. D., Danko, M., Milivojević, D. D., Kubat, P., Zmejkoski, D. Z., Pavlović, V. B., Mojsin, M. M., Stevanović, M. J., & Marković, B. M. T. (2023). Structural, optical, and bioimaging characterization of carbon quantum dots solvothermally synthesized from o-phenylenediamine. *Beilstein Journal of Nanotechnology*, *14*, 165. https://doi.org/10.3762/BJNANO.14.17

Martin, R. (n.d.). *GHG EMISSIONS OF ALL WORLD COUNTRIES JRC SCIENCE FOR POLICY REPORT*. https://doi.org/10.2760/0115360

Mashhadimoslem, H., Safarzadeh Khosrowshahi, M., Jafari, M., Ghaemi, A., & Maleki, A. (2022). Adsorption Equilibrium, Thermodynamic, and Kinetic Study of O2/N2/CO2 on Functionalized Granular Activated Carbon. *ACS Omega*, *7*(22), 18409–18426. https://doi.org/10.1021/ACSOMEGA.2C00673/ASSET/IMAGES/LARGE/AO2C00673_0013.JPEG

Meng, W., Bai, X., Wang, B., Liu, Z., Lu, S., & Yang, B. (2019). Biomass-Derived Carbon Dots and Their Applications. In *Energy and Environmental Materials* (Vol. 2, Number 3, pp. 172–192). John Wiley and Sons Inc. https://doi.org/10.1002/eem2.12038

Meylani, V., Busaeri, N., Radjasa, O. K., Hiron, N., & Mutiara, F. (2025). Comprehensive Review of Carbon Capture Technologies for Climate Change Mitigation. *Indonesian Journal of Energy*, *8*(1), 62–74. https://doi.org/10.33116/IJE.V8I1.211

Miao, F., Jia, J., Chen, X., Lu, H., Liu, X., Tu, Y., & Wu, D. (2026). CO2 adsorption behavior and characterization model on inorganic mineral pore surfaces: a molecular simulation study compared with organic pores. *Fuel*, *404*, 136415. https://doi.org/10.1016/J.FUEL.2025.136415

Miao, R., Zhang, S., Liu, J., & Fang, Y. (2017). Zinc-Reduced CQDs with Highly Improved Stability, Enhanced Fluorescence, and Refined Solid-State Applications. *Chemistry of Materials*, *29*(14), 5957–5964. https://doi.org/10.1021/ACS.CHEMMATER.7B01580

Min, H., Zhang, K., Guo, Z., Chi, F., Fu, L., Li, B., Qiao, X., Wang, S., Cao, S., Wang, B., & Ma, Q. (2023). N-rich chitosan-derived porous carbon materials for efficient CO2 adsorption and gas separation. *Frontiers in Chemistry*, *11*, 1333475. https://doi.org/10.3389/FCHEM.2023.1333475/FULL

Mindivan, F., & Boz, B. (2025). A scaffold material: Reduced graphene oxide and carbon quantum dots filled polycaprolactone nanofibers. *Diamond and Related Materials*, *153*, 112039. https://doi.org/10.1016/J.DIAMOND.2025.112039

Minx, J. C., Lamb, W. F., Andrew, R. M., Canadell, J. G., Crippa, M., Döbbeling, N., Forster, P. M., Guizzardi, Di., Olivier, J., Peters, G. P., Pongratz, J., Reisinger, A., Rigby, M., Saunois, M., Smith, S. J., Solazzo, E., & Tian, H. (2021). A comprehensive and synthetic dataset for global, regional and national greenhouse gas emissions by sector 1970-2018 with an extension to 2019. *Earth System Science Data*, *13*(11), 5213–5252. https://doi.org/10.5194/ESSD-13-5213-2021

Miron, A., Sarbu, A., Zaharia, A., Sandu, T., Iovu, H., Fierascu, R. C., Neagu, A. L., Chiriac, A. L., & Iordache, T. V. (2022). A Top-Down Procedure for Synthesizing Calcium Carbonate-Enriched Chitosan from Shrimp Shell Wastes. *Gels*, *8*(11). https://doi.org/10.3390/gels8110742

Mitra, S., Chandra, S., Pathan, S. H., Sikdar, N., Pramanik, P., & Goswami, A. (2013). Room temperature and solvothermal green synthesis of self passivated carbon quantum dots. *RSC Advances*, *3*(10), 3189–3193. https://doi.org/10.1039/C2RA23085B

Mohammed Hatta, N. S., Hussin, F., Gew, L. T., & Aroua, M. K. (2025). Isotherms, Thermodynamics and Regeneration Studies of CO2 Adsorption on Activated Carbon Impregnated With Waste-Sourced Natural Amino Acids. *Greenhouse Gases: Science and Technology*. https://doi.org/10.1002/GHG.2354

Mukhtar, A., Mellon, N., Saqib, S., Lee, S. P., & Bustam, M. A. (2020). Extension of BET theory to CO2 adsorption isotherms for ultra-microporosity of covalent organic polymers. *SN Applied Sciences*, *2*(7), 1–4. https://doi.org/10.1007/S42452-020-2968-9/TABLES/1

Munusamy, S., Sawminathan, S., Arumugham, T., Casales Díaz, M., Godavarthi, S., & Kesarla, M. K. (2021). N-Doped Carbon Dots Derived from Melamine and Triethanolamine for Selective Sensing of Fe3+ Ions. *Journal of Nanomaterials*, *2021*. https://doi.org/10.1155/2021/8275987

Nammahachak, N., Aup-Ngoen, K. K., Asanithi, P., Horpratum, M., Chuangchote, S., Ratanaphan, S., & Surareungchai, W. (2022). Hydrothermal synthesis of carbon quantum dots with size tunability via heterogeneous nucleation. *RSC Advances*, *12*(49), 31729–31733. https://doi.org/10.1039/D2RA05989D

Nandi, R., Jha, M. K., Guchhait, S. K., Sutradhar, D., & Yadav, S. (2023). Impact of KOH Activation on Rice Husk Derived Porous Activated Carbon for Carbon Capture at Flue Gas alike Temperatures with High CO2/N2 Selectivity. *ACS Omega*, *8*(5), 4802–4812. https://doi.org/10.1021/ACSOMEGA.2C06955/ASSET/IMAGES/LARGE/AO2C06955_0012.JPEG

Nanosem scanning electron microscope — Departement Materiaalkunde. (n.d.). Retrieved July 18, 2025, from https://www.mtm.kuleuven.be/oude-website/equipment_old/microscopy/nanosem?utm_source=chatgpt.com

Nanosensors of Fluorescent Carbon Quantum Dots Derived from Banana Peel: Application in Sr2+ and Co2+ Detection. (n.d.). Retrieved February 4, 2025, from https://austinpublishinggroup.com/biosensors-bioelectronics/fulltext/ajbb-v7-id1041.php?utm_source=chatgpt.com

Nazibudin, N. A., Zainuddin, M. F., & Abdullah, C. A. C. (2023). Hydrothermal Synthesis of Carbon Quantum Dots: An Updated Review. *Journal of Advanced Research in Fluid Mechanics and Thermal Sciences*, *101*(1), 192–206. https://doi.org/10.37934/ARFMTS.101.1.192206

Nazir, G., Rehman, A., & Park, S. J. (2021). Role of heteroatoms (nitrogen and sulfur)-dual doped corn-starch based porous carbons for selective CO2 adsorption and separation. *Journal of CO2 Utilization*, *51*, 101641. https://doi.org/10.1016/j.jcou.2021.101641

Ng, K. C., Burhan, M., Shahzad, M. W., & Ismail, A. Bin. (2017). A Universal Isotherm Model to Capture Adsorption Uptake and Energy Distribution of Porous Heterogeneous Surface. *Scientific Reports 2017 7:1*, *7*(1), 1–11. https://doi.org/10.1038/s41598-017-11156-6

Nguyen, K. G., Baragau, I. A., Gromicova, R., Nicolaev, A., Thomson, S. A. J., Rennie, A., Power, N. P., Sajjad, M. T., & Kellici, S. (2022). Investigating the effect of N-doping on carbon quantum dots structure, optical properties and metal ion screening. *Scientific Reports*, *12*(1), 1–12. https://doi.org/10.1038/S41598-022-16893-X;SUBJMETA=1017,301,357,551,639;KWRD=QUANTUM+DOTS,SYNTHESIS+AND+PROCESSING

Nguyen, K. G., Huš, M., Baragau, I. A., Bowen, J., Heil, T., Nicolaev, A., Abramiuc, L. E., Sapelkin, A., Sajjad, M. T., & Kellici, S. (2024). Engineering Nitrogen-Doped Carbon Quantum Dots: Tailoring Optical and Chemical Properties through Selection of Nitrogen Precursors. *Small*, *20*(24), e2310587–e2310587. https://doi.org/10.1002/SMLL.202310587

Nicolet iS10 FT-IR - Specification Sheet - Thermo Fisher Scientific. (n.d.). Retrieved July 18, 2025, from https://knowledge1.thermofisher.com/Molecular_Spectroscopy/Fourier_Transform_%28FT%29_Infrared_%28IR%29_and_Near_Infrared_%28NIR%29/Nicolet_Spectrometers/Nicolet_iS10_Spectrometer/Nicolet_iS10_FT-IR_-_Specification_Sheet?

Nisha, K., Sharma, U., Singh, A., Maurya, K. K., Kumari, S., Kumari, S., Khan, K., & Shukla, H. K. (2024). *Synthesis of Carbon Quantum Dots for Excellent Energy Density in Supercapacitors: A Comprehensive Review*. https://doi.org/10.20944/PREPRINTS202406.1932.V1

Noraini, N. M. R., Alias, A. B., Qarizada, D., Azman, F. A. M., Rashid, Z. A., & Hasan, M. R. C. (2022). Synthesis and Characterization of Xerogel from Palm Kernel Shell Biochar. *Journal of Mechanical Engineering*, *11*(Special Issue 1), 211–226. https://doi.org/10.24191/jmeche.v11i1.23599

North, M. (2015). What is CO2? Thermodynamics, Basic Reactions and Physical Chemistry. *Carbon Dioxide Utilisation: Closing the Carbon Cycle: First Edition*, 3–17. https://doi.org/10.1016/B978-0-444-62746-9.00001-3

Nwabueze, Q. A., & Leggett, S. (2024). Advancements in the Application of CO2 Capture and Utilization Technologies—A Comprehensive Review. *Fuels*, *5*(3), 508–532. https://doi.org/10.3390/FUELS5030028

Olasehinde, E. F., & Abegunde, S. M. (2020). Preparation and characterization of a new adsorbent from raphia taedigera seed. *Research on Engineering Structures and Materials*, *6*(2), 167–182. https://doi.org/10.17515/resm2019.139ma0713

Olla, C., Cappai, A., Porcu, S., Stagi, L., Fantauzzi, M., Casula, M. F., Mocci, F., Corpino, R., Chiriu, D., Ricci, P. C., & Carbonaro, C. M. (2023). Exploring the Impact of Nitrogen Doping on the Optical Properties of Carbon Dots Synthesized from Citric Acid. *Nanomaterials*, *13*(8), 1344. https://doi.org/10.3390/NANO13081344/S1

(Open Access) Chitosan as Multi Performance Bio Material: Properties and Applications. (2014) | Reyhaneh Azarmi | 1 Citations. (n.d.). Retrieved December 10, 2024, from https://typeset.io/papers/chitosan-as-multi-performance-bio-material-properties-and-3ktnur7sx2

(Open Access) Long-term trend in global CO2 emissions (2011) | J G.J. Olivier | 40 Citations. (n.d.). Retrieved November 20, 2024, from https://typeset.io/papers/long-term-trend-in-global-co2-emissions-18k9jfm3gw

(Open Access) Relationship between Surface Hydrophobicity and Composition of Coal (2004) | Zhu Shu-quan | 1 Citations. (n.d.). Retrieved February 1, 2024, from https://typeset.io/papers/relationship-between-surface-hydrophobicity-and-composition-1euw4j6wm5

ORGANIC ELEMENTAL ANALYZER (CHNS/O) - Central Research Laboratory Application and Research Center | Eskisehir Osmangazi University. (n.d.). Retrieved July 18, 2025, from https://arum.esogu.edu.tr/en/Sayfa/Index/36/organic-elemental-analyzer-chnso?utm_source=chatgpt.com

Osak, P., Łosiewicz, B., & Nowińska, D. (2024). Chitosan as a drug carrier. *Progress on Chemistry and Application of Chitin and Its Derivatives*, *29*, 30–43. https://doi.org/10.15259/PCACD.29.003

Padamini, R., Bhumita, P., Hazarika, S., NM, R., Gowda, G. R. V., Chaturvedi, K., Panigrahi, C. K., & Karanwal, R. (2024). Exploring the Role of Chitosan: A Natural Solution for Plant Disease and Insect Management. *Archives of Current Research International*, *24*(6), 102–116. https://doi.org/10.9734/ACRI/2024/V24I6769

Palacio-Vergara, M., Álvarez-Gómez, M., Gallego, J., & López, D. (2023). Biomass solvothermal treatment methodologies to obtain carbon quantum dots: A systematic review. *Talanta Open*, *8*, 100244. https://doi.org/10.1016/J.TALO.2023.100244

Pandey, R. R., & Chusuei, C. C. (2021). Carbon nanotubes, graphene, and carbon dots as electrochemical biosensing composites. *Molecules*, *26*(21). https://doi.org/10.3390/MOLECULES26216674

Pandiyan, S., Arumugam, L., Srirengan, S. P., Pitchan, R., Sevugan, P., Kannan, K., Pitchan, G., Hegde, T. A., & Gandhirajan, V. (2020). Biocompatible Carbon Quantum Dots Derived from Sugarcane Industrial Wastes for Effective Nonlinear Optical Behavior and Antimicrobial Activity Applications. *ACS Omega*, *5*(47). https://doi.org/10.1021/acsomega.0c03290

Paneru, R., Kang, X., Budhathoki, S., Chen, Z., Yang, Q., Tjeng, S. T., Dai, Q., Wang, W., Tang, J., & Fan, M. (2024). *Enhancement Effect of Biomass-Derived Carbon Quantum Dots (Cqds) on the Performance of Dye-Sensitized Solar Cells (Dsscs)*. https://doi.org/10.2139/SSRN.4849238

Patekar, K., Patil-Sankpal, P., Bandgar, S., Patil, S., Udugade, B., Patil, V., Mohite, K., Hajare, A., Patil, S., & Nadaf, S. (2024). Emerging applications of chitosan-based nanomaterials. *Chitosan-Based Hybrid Nanomaterials*, 125–136. https://doi.org/10.1016/B978-0-443-21891-0.00007-X

Pathak, R., Punetha, V. D., Bhatt, S., & Punetha, M. (2023). Multifunctional role of carbon dot-based polymer nanocomposites in biomedical applications: a review. *Journal of Materials Science*, *58*(15), 6419–6443. https://doi.org/10.1007/S10853-023-08408-4/METRICS

Pawar, S., Togiti, U. K., Bhattacharya, A., & Nag, A. (2019). Functionalized Chitosan-Carbon Dots: A Fluorescent Probe for Detecting Trace Amount of Water in Organic Solvents. *ACS Omega*, *4*(6), 11301–11311. https://doi.org/10.1021/acsomega.9b01208

(PDF) Computational Fluid Dynamics Simulation of CO2 Adsorption On Nanoporous Activated Carbon: Effect of Feed Velocity. (n.d.). Retrieved July 16, 2025, from https://www.researchgate.net/publication/286301720_Computational_Fluid_Dynamics_Simulation_of_CO2_Adsorption_On_Nanoporous_Activated_Carbon_Effect_of_Feed_Velocity

Pełech, I., Staciwa, P., Sibera, D., Pełech, R., Sobczuk, K. S., Kayalar, G. Y., Narkiewicz, U., & Cormia, R. (2022). CO2 Adsorption Study of Potassium-Based Activation of Carbon Spheres. *Molecules 2022, Vol. 27, Page 5379*, *27*(17), 5379. https://doi.org/10.3390/MOLECULES27175379

Permadi, A., Shitophyta, L. M., & Satar, I. (2024). One-step phase transferring method on preparing CuInS2/ZnS QDs dispersion via ultrasonic treatment for bioimaging. *International Journal of Advances in Applied Sciences*, *13*(1), 73–83. https://doi.org/10.11591/IJAAS.V13.I1.PP73-83

Petrovic, B., Gorbounov, M., & Masoudi Soltani, S. (2021). Influence of surface modification on selective CO2 adsorption: A technical review on mechanisms and methods. *Microporous and Mesoporous Materials*, *312*, 110751. https://doi.org/10.1016/J.MICROMESO.2020.110751

Piccin, J. S., Dotto, G. L., & Pinto, L. A. A. (n.d.). *ADSORPTION ISOTHERMS AND THERMOCHEMICAL DATA OF FD&C RED N° 40 BINDING BY CHITOSAN*. *28*(02), 295–304. Retrieved www.abeq.org.br/bjche

Poomsawat, W., & Poomsawat, S. (2023). Pyrolysis kinetic behavior of composite polypropylene-biomass solid fuels derived via co-hydrothermal carbonization process. *Thermal Science and Engineering Progress*, *43*, 101953. https://doi.org/10.1016/J.TSEP.2023.101953

Prado, M. B., Truong, N. T., & Wanekaya, A. K. (2023). Improving the quantum yield of nitrogen-doped carbon dots by varying dopant ratios and pH. *Sensors and Actuators Reports*, *6*, 100165. https://doi.org/10.1016/J.SNR.2023.100165

Prasannan, A., & Imae, T. (2013). One-Pot Synthesis of Fluorescent Carbon Dots from Orange Waste Peels. *Industrial & Engineering Chemistry Research*, *52*(44), 15673–15678. https://doi.org/10.1021/IE402421S

Preparation method of ultralow ash content activated carbon. (2019). https://typeset.io/papers/preparation-method-of-ultralow-ash-content-activated-carbon-2x8jtd0ogd

Prihanto, A. A., Nurdiani, R., & Afifah, J. (2024). Potential Application of Chitosan from Fishery Waste. *Current Innovations in Chemical and Materials Sciences Vol. 4*, 152–176. https://doi.org/10.9734/BPI/CICMS/V4/6636E

Purkait, M. K., Haldar, D., & Debnath, B. (2023). Technological Advancements in Product Valorization of Tea Waste. *Technological Advancements in Product Valorization of Tea Waste*, 1–213. https://doi.org/10.1016/C2021-0-03501-X

Qavami, N., Naghdi Badi, H., Labbafi, M., Mehregan, M., Tavakoli, M., & Mehrafarin, A. (2017). Overview on Chitosan as a valuable ingredient and biostimulant in pharmaceutical industries and agricultural products. *The Journal of Supercomputing*, *15*(1), 83–91. https://doi.org/10.15547/TJS.2017.01.014

Qu, S., Liu, X., Guo, X., Chu, M., Zhang, L., & Shen, D. (2014). Amplified spontaneous green emission and lasing emission from carbon nanoparticles. *Advanced Functional Materials*, *24*(18), 2689–2695. https://doi.org/10.1002/ADFM.201303352;SUBPAGE:STRING:ACCESS

Quan, C., Zhou, Y., Wang, J., Wu, C., & Gao, N. (2023). Biomass-based carbon materials for CO2capture: A review. In *Journal of CO2 Utilization* (Vol. 68). Elsevier Ltd. https://doi.org/10.1016/j.jcou.2022.102373

Raganati, F., Miccio, F., & Ammendola, P. (2021). Adsorption of Carbon Dioxide for Post-combustion Capture: A Review. *Energy and Fuels*, *35*(16), 12845–12868. https://doi.org/10.1021/acs.energyfuels.1c01618

Rahmawati, Y., Nurkhamidah, S., Susianto, S., Listiyana, N. I., Rahmatullah, M. A., & Hardian, I. M. (2019). Effect of Activated Alkanolamine for CO2 Absorption using Hollow Fiber Membrane Contactor. *IOP Conference Series: Materials Science and Engineering*, *543*(1). https://doi.org/10.1088/1757-899X/543/1/012080

Ramirez-Corredores, M. M. (2024). Sustainable production of CO2-derived materials. *Npj Materials Sustainability 2024 2:1*, *2*(1), 1–21. https://doi.org/10.1038/s44296-024-00041-9

Ramos, P. B., Mamani, A., Sardella, M. F., Arencibia, A., Sanz, R., Sanz-Pérez, E. S., Bavio, M. A., & Erans, M. (2025). Olive Mill Waste-Derived Activated Carbon for CO2 Capture Using Realistic Conditions. *Energy and Fuels*, *39*(11), 5442–5452.

https://doi.org/10.1021/ACS.ENERGYFUELS.4C04880/SUPPL_FILE/EF4C04880_SI_001.PDF

Rangraz, Y., & Heravi, M. M. (2021). Recent advances in metal-free heteroatom-doped carbon heterogonous catalysts. *RSC Advances*, *11*(38), 23725–23778. https://doi.org/10.1039/D1RA03446D

Rasal, A. S., Yadav, S., Yadav, A., Kashale, A. A., Manjunatha, S. T., Altaee, A., & Chang, J. Y. (2021). Carbon Quantum Dots for Energy Applications: A Review. *ACS Applied Nano Materials*, *4*(7), 6515–6541. https://doi.org/10.1021/ACSANM.1C01372

Rashid, H., & Rafey, A. (2023). Solid adsorbents for carbon dioxide capture: a review. *Chemistry and Ecology*, *39*(7), 1–17. https://doi.org/10.1080/02757540.2023.2227622

Rawat, J., Sharma, H., & Dwivedi, C. (2024a). Microwave-assisted synthesis of carbon quantum dots and their integration with TiO2 nanotubes for enhanced photocatalytic degradation. *Diamond and Related Materials*, *144*, 111050. https://doi.org/10.1016/J.DIAMOND.2024.111050

Rawat, J., Sharma, H., & Dwivedi, C. (2024b). Microwave-assisted synthesis of carbon quantum dots and their integration with TiO2 nanotubes for enhanced photocatalytic degradation. *Diamond and Related Materials*, *144*, 111050–111050. https://doi.org/10.1016/J.DIAMOND.2024.111050

Ren, H., Labidi, A., Sun, J., Allam, A. A., Ajarem, J. S., Abukhadra, M., & Wang, C. (2023). *Green and facile synthesis of N,S co-doped carbon quantum dots with a high product yield for selective detection of Hg2+ in aqueous system*. https://doi.org/10.21203/RS.3.RS-2930575/V1

Ren, H., Qi, F., Feng, X., Liu, J., & Zhao, Y. (2024). Facile Synthesis of Fluorescent Carbon Quantum Dots with High Product Yield Using a Solid-Phase Strategy. *Molecules*, *29*(22), 5317. https://doi.org/10.3390/MOLECULES29225317/S1

Rocco, D., Moldoveanu, V. G., Feroci, M., Bortolami, M., & Vetica, F. (2023). Electrochemical Synthesis of Carbon Quantum Dots. *ChemElectroChem*, *10*(3). https://doi.org/10.1002/CELC.202201104

Román-Doval, R., Torres-Arellanes, S. P., Tenorio-Barajas, A. Y., Gómez-Sánchez, A., & Valencia-Lazcano, A. A. (2023). Chitosan: Properties and Its Application in Agriculture in Context of Molecular Weight. *Polymers*, *15*(13), 2867–2867. https://doi.org/10.3390/POLYM15132867

Rosa, G. S., Moraes, M. A., & Pinto, L. A. A. (2010). Moisture sorption properties of chitosan. *LWT*, *43*(3), 415–420. https://doi.org/10.1016/j.lwt.2009.09.003

Ruslan, N. S., Mohtar, N., Rahiman, S. S. F., & Gazzali, A. M. (2020). The influence of preparation factors on physical characteristics of chitosan nanoparticles. *Journal of Physical Science*, *31*(3), 47–60. https://doi.org/10.21315/JPS2020.31.3.4

Saha, D., & Kienbaum, M. J. (2019). Role of oxygen, nitrogen and sulfur functionalities on the surface of nanoporous carbons in CO2 adsorption: A critical review. *Microporous and Mesoporous Materials*, *287*, 29–55. https://doi.org/10.1016/j.micromeso.2019.05.051

Sahane, P., Nalawade, P., Bhamare, J., Vaishnav, S., Jagtap, U., & Bhosale, A. (2024). Industry - Specific Carbon Emission Reduction Techniques: A Comprehensive Survey. *8th International Conference on I-SMAC (IoT in Social, Mobile, Analytics and Cloud), I-SMAC 2024 - Proceedings*, 414–420. https://doi.org/10.1109/I-SMAC61858.2024.10714592

Sahoo, T. R., & Prelot, B. (2020). Adsorption processes for the removal of contaminants from wastewater: The perspective role of nanomaterials and nanotechnology. *Nanomaterials for the Detection and Removal of Wastewater Pollutants*, 161–222. https://doi.org/10.1016/B978-0-12-818489-9.00007-4

Saiyad, M., Shah, N., Joshipura, M., Dwivedi, A., & Pillai, S. (2023a). Cationic Chitosan in Wastewater Treatment. *Proceedings of the International Conference on Frontiers in Desalination, Energy, Environment and Material Sciences for Sustainable Development*, 142–146. https://doi.org/10.21467/PROCEEDINGS.161.16

Saiyad, M., Shah, N., Joshipura, M., Dwivedi, A., & Pillai, S. (2023b). Chitosan and its derivatives in wastewater treatment application. *Materials Today: Proceedings*. https://doi.org/10.1016/J.MATPR.2023.10.157

Saleh, T. A. (2022). Kinetic models and thermodynamics of adsorption processes: classification. *Interface Science and Technology*, *34*, 65–97. https://doi.org/10.1016/B978-0-12-849876-7.00003-8

Salehi, R., Dadashian, F., Abedi, M., & Eliassi, A. (2025). Adsorption studies of benzene and toluene in gas phase onto activated carbon fabrics in fixed bed column. *Heliyon*, *11*(2). https://doi.org/10.1016/J.HELIYON.2025.E42071

Salim, L. O. A., & Irwan, I. (2024). Overview of Biomass Hydrothermal Techniques for Carbon Quantum Dots Synthesis: Mini Review. *Asian Journal of Environmental Research*, *1*(1), 01–04. https://doi.org/10.69930/AJER.V1I1.16

Sankar, H., S, S., & Damodharan, N. (2024). Advancements in Nanomedicine: Carbon Quantum Dots for Drug Delivery. *International Journal of Chemical and Biochemical Science*, *25*(19). https://doi.org/10.62877/110-IJCBS-24-25-19-110

Sarbon, N. M., Sandanamsamy, S., Kamaruzaman, S. F. S., & Ahmad, F. (2015). Chitosan extracted from mud crab (Scylla olivicea) shells: Physicochemical and antioxidant properties. *Journal of Food Science and Technology*, *52*(7), 4266–4275. https://doi.org/10.1007/s13197-014-1522-4

Sardo, M., Afonso, R., Juźków, J., Pacheco, M., Bordonhos, M., Pinto, M. L., Gomes, J. R. B., & Mafra, L. (2021). Unravelling moisture-induced CO2 chemisorption mechanisms in amine-modified sorbents at the molecular scale. *Journal of Materials Chemistry. a*, *9*(9), 5542. https://doi.org/10.1039/D0TA09808F

Sarkar, T., Rawat, K., Solanki, P. R., & Bohidar, H. B. (2019). Carbon dots-embedded fluorescent silica xerogel. *Colloids and Surfaces A: Physicochemical and Engineering Aspects*, *583*. https://doi.org/10.1016/J.COLSURFA.2019.123844

Serna-Guerrero, R., & Sayari, A. (2010). Modeling adsorption of CO2 on amine-functionalized mesoporous silica. 2: Kinetics and breakthrough curves. *Chemical Engineering Journal*, *161*(1–2), 182–190. https://doi.org/10.1016/J.CEJ.2010.04.042

Sevilla, M., Parra, J. B., & Fuertes, A. B. (2013). Assessment of the role of micropore size and N-doping in CO2 capture by porous carbons. *ACS Applied Materials & Interfaces*, *5*(13), 6360–6368. https://doi.org/10.1021/AM401423B

SEZGIN, D. (2024). Xerogel of fast kinetics and high adsorption capacity for cationic dye removal. *Sigma Journal of Engineering and Natural Sciences – Sigma Mühendislik ve Fen Bilimleri Dergisi*, 189–197. https://doi.org/10.14744/sigma.2022.00019

Shahadha, A. F., Al-Aubadi, I. M., & Merzah, N. R. (2023). Preparation of Chitosan from Agaricus bisporus Brown Stems and Studying some Its Physicochemical and Functional Properties. *IOP Conference Series: Earth and Environmental Science*, *1259*(1), 012070. https://doi.org/10.1088/1755-1315/1259/1/012070

Shamiri, A., & Shafeeyan, M. S. (2022). Evaluation of adsorbent materials for carbon dioxide capture. *Materialwissenschaft Und Werkstofftechnik*, *53*(11), 1392–1409. https://doi.org/10.1002/MAWE.202100332

Shammi, M., & Akter, B. (2024). CO2 sequestration for conventional utilization and industrial application. *Decarbonization Strategies and Drivers to Achieve Carbon Neutrality for Sustainability*, 299–319. https://doi.org/10.1016/B978-0-443-13607-8.00011-0

Shao, J., Ma, C., Zhao, J., Wang, L., & Hu, X. (2022a). Effective nitrogen and sulfur co-doped porous carbonaceous CO2 adsorbents derived from amino acid. *Colloids and Surfaces A: Physicochemical and Engineering Aspects*, *632*, 127750–127750. https://doi.org/10.1016/J.COLSURFA.2021.127750

Shao, J., Ma, C., Zhao, J., Wang, L., & Hu, X. (2022b). Effective nitrogen and sulfur co-doped porous carbonaceous CO2 adsorbents derived from amino acid. *Colloids and Surfaces A: Physicochemical and Engineering Aspects*, *632*, 127750–127750. https://doi.org/10.1016/J.COLSURFA.2021.127750

Sharath Shankar, S., Ramachandran, V., Raj, R. P., Sruthi, T. V., & Sameer Kumar, V. B. (2020). Carbon Quantum Dots: A Potential Candidate for Diagnostic and Therapeutic Application. *Nanobiomaterial Engineering: Concepts and Their Applications in Biomedicine and Diagnostics*, 49–70. https://doi.org/10.1007/978-981-32-9840-8_3

Sharma, E., Thakur, V., & Singh, K. (2024). Carbonaceous Quantum Dots and Their Application in Environmental Remediation. *Nanomaterials: An Approach Towards Environmental Remediation*, 56–78. https://doi.org/10.2174/9789815223613124010006

Shen, J., Wang, X., & Chen, Y. (2023). Adsorbents for adsorption separation of CO_2 and CH_4: A literature review. *Canadian Journal of Chemical Engineering*, *101*(12), 7115–7133. https://doi.org/10.1002/CJCE.24942

Shen, Y., & Lee, M. L. (1997). Physicochemical properties and chromatographic performance of carbon dioxide in packed capillary column solvating gas chromatography. *Chromatographia*, *46*(9), 537–544. https://doi.org/10.1007/BF02496373

Shi, W., Zhang, Q., Liu, S., Su, S., Chang, B., & Yang, B. (2021). Copper ions-assisted inorganic dynamic porogen of graphene-like multiscale microporous

carbon nanosheets for effective carbon dioxide capture. *Journal of Colloid and Interface Science*, *600*, 670–680. https://doi.org/10.1016/J.JCIS.2021.04.146

Shibuya, R., Takeyasu, K., Guo, D., Kondo, T., & Nakamura, J. (2022). Chemisorption of CO2on Nitrogen-Doped Graphitic Carbons. *Langmuir*, *38*(47), 14430–14438. https://doi.org/10.1021/ACS.LANGMUIR.2C01987

Shindel, B., Hegarty, J., Estradioto, J. D., Barsoum, M. L., Yang, M., Farha, O. K., & Dravid, V. P. (2025). Platform Materials for Moisture-Swing Carbon Capture. *Environmental Science and Technology*. https://doi.org/10.1021/ACS.EST.4C11308

Shiue, A., Hu, S. C., Chang, S. M., Ko, T. Y., Hsieh, A., & Chan, A. (2017). Adsorption Kinetics and Breakthrough of Carbon Dioxide for the Chemical Modified Activated Carbon Filter Used in the Building. *Sustainability 2017, Vol. 9, Page 1533*, *9*(9), 1533. https://doi.org/10.3390/SU9091533

Shorgar, N., Bhati, I., & Jhalora, P. (2023). Laser ablation synthesis of quantum dots. *Quantum Dots: Fundamentals, Synthesis and Applications*, 53–75. https://doi.org/10.1016/B978-0-12-824153-0.00004-5

Siahcheshm, P., & Heiden, P. (2022). High quantum yield carbon quantum dots as selective fluorescent turn-off probes for dual detection of Fe2+/Fe3+ ions. *Journal of Photochemistry and Photobiology A-Chemistry*, *435*, 114284–114284. https://doi.org/10.1016/J.JPHOTOCHEM.2022.114284

SINGH, I., ARORA, R., DHIMAN, H., PAHWA, R., SINGH, I., ARORA, R., DHIMAN, H., & PAHWA, R. (2018). Carbon Quantum Dots: Synthesis, Characterization and Biomedical Applications. *Turkish Journal of Pharmaceutical Sciences*, *15*(2), 219–230. https://doi.org/10.4274/TJPS.63497

Singh, J., Bhunia, H., & Basu, S. (2019). Adsorption of CO2 on KOH activated carbon adsorbents: Effect of different mass ratios. *Journal of Environmental Management*, *250*. https://doi.org/10.1016/J.JENVMAN.2019.109457

Singh, R. K., Kumar, R., Singh, D. P., Savu, R., & Moshkalev, S. A. (2019). Progress in microwave-assisted synthesis of quantum dots (graphene/carbon/semiconducting) for bioapplications: a review. *Materials Today Chemistry*, *12*, 282–314. https://doi.org/10.1016/J.MTCHEM.2019.03.001

Sistani, S., & Shekarchizadeh, H. (2023). Applications of Quantum Dots in the Food Industry. *Quantum Dots - Recent Advances, New Perspectives and Contemporary Applications*. https://doi.org/10.5772/INTECHOPEN.107190

Song, J., Zhao, L., Wang, Y., Xue, Y., Deng, Y., Zhao, X., & Li, Q. (2018). Carbon Quantum Dots Prepared with Chitosan for Synthesis of CQDs/AuNPs for Iodine Ions Detection. *Nanomaterials 2018, Vol. 8, Page 1043*, *8*(12), 1043. https://doi.org/10.3390/NANO8121043

Ssekatawa, K., Byarugaba, D. K., Wampande, E. M., Moja, T. N., Nxumalo, E., Maaza, M., Sackey, J., Ejobi, F., & Kirabira, J. B. (2021). Isolation and characterization of chitosan from Ugandan edible mushrooms, Nile perch scales and banana weevils for biomedical applications. *Scientific Reports*, *11*(1). https://doi.org/10.1038/S41598-021-81880-7

Stachurski, C. D., Click, S. M., Wolfe, K. D., Dervishogullari, D., Rosenthal, S. J., Kane, G., Bcd, J., & Cliffel, D. E. (2020). *Optical and electrochemical tuning of hydrothermally synthesized nitrogen-doped carbon dots †*. https://doi.org/10.1039/d0na00264j

Stockmann, J. M., Radnik, J., Bütefisch, S., Busch, I., Weimann, T., Passiu, C., Rossi, A., & Unger, W. E. S. (2020). A new test specimen for the determination of the field of view of small-area X-ray photoelectron spectrometers. *Surface and Interface Analysis*, *52*(12), 890–894. https://doi.org/10.1002/SIA.6831

Suba, M., Verdeș, O., Borcănescu, S., & Popa, A. (2024). Effect of Temperature on CO2 Adsorption onto Amine-Functionalized KIT-6 Adsorbents. *Molecules 2024, Vol. 29, Page 3172*, *29*(13), 3172. https://doi.org/10.3390/MOLECULES29133172

Sumida, K., Rogow, D. L., Mason, J. A., McDonald, T. M., Bloch, E. D., Herm, Z. R., Bae, T. H., & Long, J. R. (2012). Carbon dioxide capture in metal-organic frameworks. *Chemical Reviews*, *112*(2), 724–781. https://doi.org/10.1021/CR2003272/ASSET/CR2003272.FP.PNG_V03

Sun, C., Zhang, Y., Wang, P., Yang, Y., Wang, Y., Xu, J., Wang, Y., & Yu, W. W. (2016). Synthesis of Nitrogen and Sulfur Co-doped Carbon Dots from Garlic for Selective Detection of Fe3+. *Nanoscale Research Letters*, *11*(1), 1–9. https://doi.org/10.1186/S11671-016-1326-8/FIGURES/6

Sun, L., Zhang, H., Wang, Y., Xiong, Z., Zhao, X., & Xia, Y. (2021). Chitosan-derived N-doped carbon dots for fluorescent determination of nitrite and bacteria

imaging. *Spectrochimica Acta - Part A: Molecular and Biomolecular Spectroscopy*, *251*. https://doi.org/10.1016/j.saa.2021.119468

Sun, S., Bao, W., Yang, F., Yan, X., Sun, Y., Zhang, G., Yang, W., & Li, Y. (2023). Electrochemical synthesis of FeNx doped carbon quantum dots for sensitive detection of Cu2+ ion. *Green Energy & Environment*, *8*(1), 141–150. https://doi.org/10.1016/J.GEE.2021.04.005

Sun, Y., Jia, J., Liu, Z., Liu, Z., Huo, L., Zhao, L., Zhao, Y., & Yao, Z. (2023). Heteroatom-doped biochar devised from cellulose for CO2 adsorption: a new vision on competitive behavior and interactions of N and S. *Biochar 2023 5:1*, *5*(1), 76-. https://doi.org/10.1007/S42773-023-00275-1

Sun, Y., Zhang, D., Ren, G., Zhou, S., Tian, L., & Zhou, L. (2024). One-step solvothermal synthesis of Na-doped carbon quantum dots and concomitant photochromic small molecules. *Chemical Physics Letters*, *840*, 141114–141114. https://doi.org/10.1016/J.CPLETT.2024.141114

Surendran, P., Lakshmanan, A., Vinitha, G., Ramalingam, G., & Rameshkumar, P. (2020). Facile preparation of high fluorescent carbon quantum dots from orange waste peels for nonlinear optical applications. *Luminescence*, *35*(2), 196–202. https://doi.org/10.1002/BIO.3713

Surface Area and Porosity Analysis Micromeritics ASAP 2020: Physisorption User notes Micromeritics ASAP 2020: Physisorption User notes. (n.d.).

Syahindah, S., Azlan, S., Raida, N., Rahman, A., & Mohamad, M. (2023). Carbon Emission in Malaysia: Trends and Initiatives of Government. *International Journal of Academic Research in Accounting, Finance and Management Sciences*, *13*(1), 318–329. https://doi.org/10.6007/IJARAFMS/V13-I1/15879

Szabados, A., & Poulsen, S. R. (2023). The CCS greensand project: CO2 pilot injection and monitoring. *Baltic Carbon Forum*, *2*, 11–12. https://doi.org/10.21595/BCF.2023.23608

Tangsathitkulchai, C., Naksusuk, S., Wongkoblap, A., Phadungbut, P., & Borisut, P. (2021). Equilibrium and Kinetics of CO2 Adsorption by Coconut Shell Activated Carbon Impregnated with Sodium Hydroxide. *Processes 2021, Vol. 9, Page 201*, *9*(2), 201. https://doi.org/10.3390/PR9020201

Tao, Z., Tian, Y., Wu, W., Liu, Z., Fu, W., Kung, C.-W., & Shang, J. (2024). Development of zeolite adsorbents for CO2 separation in achieving carbon

neutrality. *Npj Materials Sustainability 2024 2:1*, *2*(1), 1–16. https://doi.org/10.1038/s44296-024-00023-x

Tecnai F20 TEM/STEM/AEM - BYU Electron Microscopy Facility. (n.d.). Retrieved July 18, 2025, from https://microscopy.byu.edu/tecnai-f20-tem-stem-aem?utm_source=chatgpt.com

Teixeira, P., Bacariza, C., Correia, P., Pinheiro, C. I. C., & Cabrita, I. (2022). Hydrogen Production with In Situ CO2 Capture at High and Medium Temperatures Using Solid Sorbents. *Energies*, *15*(11), 4039–4039. https://doi.org/10.3390/EN15114039

Teymoorian, T., Hashemi, N., Mousazadeh, M. H., & Entezarian, Z. (2021). N, S doped carbon quantum dots inside mesoporous silica for effective adsorption of methylene blue dye. *SN Applied Sciences*, *3*(3), 1–14. https://doi.org/10.1007/S42452-021-04287-Z/TABLES/6

Thermogravimetric Analysis/Differential Scanning Calorimeter | MATFab Facility - The University of Iowa. (n.d.). Retrieved July 18, 2025, from https://matfab.research.uiowa.edu/using-lab/instruments-depth/thermogravimetric-analysisdifferential-scanning-calorimeter

Thulasi, K. M., Sindhu, T. M., & Kizhakkekilikoodayil Vijayan, B. (2019). Effect of Surface Modification on SILAR Deposited CdS Quantum Dot Sensitized Hydrothermally Synthesised Titania Nanostructure. *Materials Today: Proceedings*, *9*, 645–652. https://doi.org/10.1016/J.MATPR.2018.10.388

Tong, S., Buntong, B., Sophal, L., Vann, S., & Acedo, A. (2021). Effects of Chemical Extraction Methods on Physicochemical Properties of Shrimp Chitosan. *IJERD-International Journal of Environmental and Rural Development*, 12–14. https://www.strategyr.com/market-report-chitin-and-chitosan-

Torres, F. B., Gutierrez, J. P., Ruiz, L. A., Bertuzzi, M. A., & Erdmann, E. (2024). Carbon dioxide capture by using hybrid system. parametric sensitivity analysis and environmental and energy evaluation. *Latin American Applied Research*, *54*(3), 425–430. https://doi.org/10.52292/J.LAAR.2024.3280

Tran Bao, T., Tran Ngoc, B., Tran Tien, D., Tran Dong, D., Vu Duy, T., Chu Thi, H., Pham Gia, B., Nguyen Thi Anh, H., & Pham Thi Ngoc, M. (2024). Synthesis of nitrogen-doped carbon quantum dots (N-CQDs) using microwaveassisted hydrothermal method for tyramine determination. *Tạp Chí Kiểm Nghiệm và An*

Toàn Thực Phẩm, *7*(3), 155–167. https://doi.org/10.47866/2615-9252/VJFC.4347

Trung, L. G., Subedi, S., Dahal, B., Truong, P. L., Gwag, J. S., Tran, N. T., & Nguyen, M. K. (2022). Highly efficient fluorescent probes from chitosan-based amino-functional carbon dots for the selective detection of Cu2+ traces. *Materials Chemistry and Physics*, *291*. https://doi.org/10.1016/j.matchemphys.2022.126772

Tsiotsias, A. I., Georgiadis, A. G., Charisiou, N. D., & Goula, M. A. (2023). CO2 Physisorption over an Industrial Molecular Sieve Zeolite: An Experimental and Theoretical Approach. *Materials*, *16*(20), 6656. https://doi.org/10.3390/MA16206656

Tuo, S. J., Li, C., Brou, E. F., Kassi, D. F., & Gnangoin, Y. T. (2022). Estimating the carbon dioxide emission levels of G7 countries: A count data approach. *Energy and Environment*, 0958305X2211434-0958305X2211434. https://doi.org/10.1177/0958305X221143416

Vibhute, A., Patil, T., Gambhir, R., & Tiwari, A. P. (2022). Fluorescent carbon quantum dots: Synthesis methods, functionalization and biomedical applications. *Applied Surface Science Advances*, *11*, 100311. https://doi.org/10.1016/J.APSADV.2022.100311

Villalba-Rodríguez, A. M., González-González, R. B., Martínez-Ruiz, M., Flores-Contreras, E. A., Cárdenas-Alcaide, M. F., Iqbal, H. M. N., & Parra-Saldívar, R. (2022). Chitosan-Based Carbon Dots with Applied Aspects: New Frontiers of International Interest in a Material of Marine Origin. *Marine Drugs*, *20*(12). https://doi.org/10.3390/MD20120782

Visheratina, A., Hesami, L., Wilson, A. K., Baalbaki, N., Noginova, N., Noginov, M. A., & Kotov, N. A. (2022). Hydrothermal synthesis of chiral carbon dots. *Chirality*. https://doi.org/10.1002/CHIR.23509

Vitillo, J. G., Eisaman, M. D., Aradóttir, E. S. P., Passarini, F., Wang, T., & Sheehan, S. W. (2022). The role of carbon capture, utilization, and storage for economic pathways that limit global warming to below 1.5°C. *IScience*, *25*(5), 104237. https://doi.org/10.1016/J.ISCI.2022.104237

Wang, C., Yang, M., Shi, H., Yao, Z., Liu, E., Hu, X., Guo, P., Xue, W., & Fan, J. (2022). Carbon quantum dots prepared by pyrolysis: Investigation of the

luminescence mechanism and application as fluorescent probes. *Dyes and Pigments*, *204*, 110431. https://doi.org/10.1016/J.DYEPIG.2022.110431

Wang, J., & Guo, X. (2022). Review on the Intraparticle Diffusion Adsorption Kinetics Model: Interpretation, Solving Methods and Applications. *SSRN Electronic Journal*. https://doi.org/10.2139/SSRN.4120203

Wang, J., Huang, L., Yang, R., Zhang, Z., Wu, J., Gao, Y., Wang, Q., O'Hare, D., & Zhong, Z. (2014). Recent advances in solid sorbents for CO2 capture and new development trends. *Energy & Environmental Science*, *7*(11), 3478–3518. https://doi.org/10.1039/C4EE01647E

Wang, Q., Liu, X., Zhang, L., & Lv, Y. (2012). Microwave-assisted synthesis of carbon nanodots through an eggshell membrane and their fluorescent application. *Analyst*, *137*(22), 5392–5397. https://doi.org/10.1039/C2AN36059D

Wang, R., Li, G., Dong, Y., Chi, Y., & Chen, G. (2013). Carbon quantum dot-functionalized aerogels for NO2 gas sensing. *Analytical Chemistry*, *85*(17), 8065–8069. https://doi.org/10.1021/AC401880H/SUPPL_FILE/AC401880H_SI_001.PDF

Wang, S., Lee, Y. R., Won, Y., Kim, H., Jeong, S. E., Wook Hwang, B., Ra Cho, A., Kim, J. Y., Cheol Park, Y., Nam, H., Lee, D. H., Kim, H., & Jo, S. H. (2022). Development of high-performance adsorbent using KOH-impregnated rice husk-based activated carbon for indoor CO2 adsorption. *Chemical Engineering Journal*, *437*, 135378–135378. https://doi.org/10.1016/J.CEJ.2022.135378

Wang, W., Li, Y., Cheng, L., Cao, Z., & Liu, W. (2013). Water-soluble and phosphorus-containing carbon dots with strong green fluorescence for cell labeling. *Journal of Materials Chemistry B*, *2*(1), 46–48. https://doi.org/10.1039/C3TB21370F

Wang, X., Luo, L., Yang, C., Wang, Q., Wang, P., Xu, B., & Yu, Y. (2024). Disulfide bond network crosslinked flexible multifunctional chitosan coating on fabric surface prepared by the chitosan grafted with thioctic acid. *International Journal of Biological Macromolecules*, *263*, 130431–130431. https://doi.org/10.1016/J.IJBIOMAC.2024.130431

Wang, X., Zeng, W., Kong, X., Xin, C., Dong, Y., Hu, X., & Guo, Q. (2022). Development of Low-Cost Porous Carbons through Alkali Activation of Crop

Waste for CO2Capture. *ACS Omega*, *7*(50), 46992–47001. https://doi.org/10.1021/ACSOMEGA.2C06109/ASSET/IMAGES/LARGE/AO2C06109_0013.JPEG

Wei, M., Yu, Q., Duan, W., Zuo, Z., Hou, L., & Dai, J. (2018). CO2 adsorption and desorption performance of waste ion-exchange resin-based activated carbon. *Environmental Progress & Sustainable Energy*, *37*(2), 703–711. https://doi.org/10.1002/EP.12743

Wijayadi, L. J., & Rusli, T. R. (2019). Characterized and synthesis of chitosan nanoparticle as nanocarrier system technology. *IOP Conference Series: Materials Science and Engineering*, *508*(1), 012143. https://doi.org/10.1088/1757-899X/508/1/012143

Woźniak, M., Młodziejewska, J., Stefanowska, K., Mrówczyńska, L., Sip, A., Dobrucka, R., & Ratajczak, I. (2024). Chitosan-Based Films with Essential Oil Components for Food Packaging. *Coatings*, *14*(7), 830–830. https://doi.org/10.3390/COATINGS14070830

Wu, D., Zhu, J., & Fu, L. (2023). Quantum leap for electroanalysis: graphene dots take electrochemical sensing to the next level. *International Journal of Environmental Analytical Chemistry*. https://doi.org/10.1080/03067319.2023.2278752

Wu, K., Yan, Z., Wu, Z., Li, J., Zhong, W., Ding, L., Zhong, T., & Jiang, T. (2024). Recent Advances in the Preparation, Antibacterial Mechanisms, and Applications of Chitosan. *Journal of Functional Biomaterials*, *15*(11), 318–318. https://doi.org/10.3390/JFB15110318

Xia, C., Zhu, S., Feng, T., Yang, M., & Yang, B. (2019a). Evolution and Synthesis of Carbon Dots: From Carbon Dots to Carbonized Polymer Dots. *Advanced Science*, *6*(23), 1901316. https://doi.org/10.1002/ADVS.201901316;WGROUP:STRING:PUBLICATION

Xia, C., Zhu, S., Feng, T., Yang, M., & Yang, B. (2019b). Evolution and Synthesis of Carbon Dots: From Carbon Dots to Carbonized Polymer Dots. *Advanced Science*, *6*(23). https://doi.org/10.1002/ADVS.201901316

Xiao, J., Wang, Y., Zhang, T. C., & Yuan, S. (2021). rGO/N-porous carbon composites for enhanced CO2 capture and energy storage performances. *Journal of Alloys and Compounds*, *857*. https://doi.org/10.1016/J.JALLCOM.2020.157534

Xiaoming, N., Liu, Z., Jianping, W., & Zhao, Y. (2019). Experimental study of the kinetics of the adsorption of nitrogen by coal containing different amounts of water. *Anais Da Academia Brasileira de Ciências*, *91*(3), e20180434. https://doi.org/10.1590/0001-3765201920180434

Xu, H., Xu, L., Wang, Z., Wei, F., & Zhang, M. (2025). Diffusion-adsorption synergistic mechanism in the adsorption of hierarchical porous carbon for antibiotics removal from water. *Colloids and Surfaces A: Physicochemical and Engineering Aspects*, *711*, 136327. https://doi.org/10.1016/J.COLSURFA.2025.136327

Xu, J., Wang, Y., Sun, L., Qi, Q., & Zhao, X. (2021). Chitosan and κ-carrageenan-derived nitrogen and sulfur co-doped carbon dots "on-off-on" fluorescent probe for sequential detection of Fe3+ and ascorbic acid. *International Journal of Biological Macromolecules*, *191*, 1221–1227. https://doi.org/10.1016/j.ijbiomac.2021.09.165

Yadav, M., Kaushik, B., Rao, G. K., Srivastava, C. M., & Vaya, D. (2023). Advances and challenges in the use of chitosan and its derivatives in biomedical fields: A Review. *Carbohydrate Polymer Technologies and Applications*, *5*, 100323–100323. https://doi.org/10.1016/J.CARPTA.2023.100323

Yan, H., Zhang, G., Xu, Y., Zhang, Q., Liu, J., Li, G., Zhao, Y., Wang, Y., & Zhang, Y. (2022). High CO2 adsorption on amine-functionalized improved macro-/mesoporous multimodal pore silica. *Fuel*, *315*. https://doi.org/10.1016/J.FUEL.2022.123195

Yang, F., He, X., Wang, C., Cao, Y., Li, Y., Yan, L., Liu, M., Lv, M., Yang, Y., Zhao, X., & Li, Y. (2018). Controllable and eco-friendly synthesis of P-riched carbon quantum dots and its application for copper (II) ion sensing. *Applied Surface Science*, *448*, 589–598. https://doi.org/10.1016/J.APSUSC.2018.03.246

Yang, N., Xue, R., Huang, G., Ma, Y., & Wang, J. (2021). CO2 Adsorption Performance and Kinetics of Ionic Liquid-Modified Calcined Magnesite. *Nanomaterials 2021, Vol. 11, Page 2614*, *11*(10), 2614. https://doi.org/10.3390/NANO11102614

Yang, R. T. (2003). Adsorbents: Fundamentals and Applications. *Adsorbents: Fundamentals and Applications*. https://doi.org/10.1002/047144409X

Yang, S., Wang, X., Ge, Z., & Ma, M. (2023). *Global per-capita CO 2 emission trends and the driving forces for shifts in the center of gravity*. https://doi.org/10.21203/RS.3.RS-2597065/V1

Ye, Q., Yan, F., Luo, Y., Wang, Y., Zhou, X., & Chen, L. (2017). Formation of N, S-codoped fluorescent carbon dots from biomass and their application for the selective detection of mercury and iron ion. *Spectrochimica Acta Part A: Molecular and Biomolecular Spectroscopy*, *173*, 854–862. https://doi.org/10.1016/J.SAA.2016.10.039

You, J., Qin, J., Du, C., Fu, J., & Cheng, S. (2022). CO2-assisted fabrication of silica gel adsorbent in honeycomb rotary wheels for air dehumidification. *Frontiers in Chemistry*, *10*, 1038095. https://doi.org/10.3389/FCHEM.2022.1038095

Yu, A. G., Lee, Z. H., Pang, C. Y., & Issabayeva, G. (2024). PRELIMINARY STUDY ON PERFORMANCE OF Zn-DOPED ZEOLITE IN LOW-TEMPERATURE CO2 ADSORPTION. *Malaysian Journal of Science*, *43*(sp1), 33–37. https://doi.org/10.22452/MJS.VOL43SP1.6

Yu, H., Zhu, W., Zhou, H., Liu, J., Yang, Z., Hu, X., & Yuan, A. (2019). Porous carbon derived from metal–organic framework@graphene quantum dots as electrode materials for supercapacitors and lithium-ion batteries. *RSC Advances*, *9*(17), 9577–9583. https://doi.org/10.1039/C9RA01488H

Yu, Y., Ouyang, Y., Xu, F., Wang, T., Wei, X., Wang, T., & Yao, Y. (2025). Green synthesis of carbon quantum dots from nutshells for enhanced performance in dye-sensitized solar cells. *RSC Advances*, *15*(10), 7938. https://doi.org/10.1039/D4RA08649J

Yuan, T., Yuan, F., Sui, L., Zhang, Y., Li, Y., Li, X., Tan, Z., & Fan, L. (2023). Carbon Quantum Dots with Near-Unity Quantum Yield Bandgap Emission for Electroluminescent Light-Emitting Diodes. *Angewandte Chemie*, *135*(20), e202218568. https://doi.org/10.1002/ANGE.202218568

Zattar, A. P. P., Fajardo, G. L., de Mesquita, J. P., & Pereira, F. V. (2021). Luminescent carbon dots obtained from chitosan: a comparison between different methods to enhance the quantum yield. *Fullerenes Nanotubes and Carbon Nanostructures*, *29*(6), 414–422. https://doi.org/10.1080/1536383X.2020.1854742

Zeng, H., Hu, Z., Peng, C., Deng, L., & Liu, S. (2021). Effective adsorption and sensitive detection of cr(Vi) by chitosan/cellulose nanocrystals grafted with

carbon dots composite hydrogel. *Polymers*, *13*(21). https://doi.org/10.3390/polym13213788

Zentou, H., Hoque, B., Abdalla, M. A., Saber, A. F., Abdelaziz, O. Y., Aliyu, M., Alkhedhair, A. M., Alabduly, A. J., & Abdelnaby, M. M. (2025). Recent advances and challenges in solid sorbents for CO2 capture. *Carbon Capture Science & Technology*, *15*, 100386. https://doi.org/10.1016/J.CCST.2025.100386

Zhang, K., & Wang, R. (2024). A critical review on new and efficient adsorbents for CO2 capture. *Chemical Engineering Journal*, *485*. https://doi.org/10.1016/J.CEJ.2024.149495

Zhang, L., Xiao, S. J., & Huang, C. Z. (2023). Large-scale Synthesis of Carbon Dots for Pollutant Adsorption and Photodegradation. *Green Development of Photoluminescent Carbon Dots*, 88–106. https://doi.org/10.1039/9781837671205-00088

Zhang, Q., Zhang, X., Bao, L., Wu, Y., Jiang, L., Zheng, Y., Wang, Y., & Chen, Y. (2019). The application of green-synthesis-derived carbon quantum dots to bioimaging and the analysis of mercury(II). *Journal of Analytical Methods in Chemistry*, *2019*. https://doi.org/10.1155/2019/8183134

Zhao, L., Wang, Y., Zhao, X., Deng, Y., & Xia, Y. (2019). Facile Synthesis of Nitrogen-Doped Carbon Quantum Dots with Chitosan for Fluorescent Detection of Fe3+. *Polymers 2019, Vol. 11, Page 1731*, *11*(11), 1731. https://doi.org/10.3390/POLYM11111731

Zhao, Y., Zuo, S., & Miao, M. (2017). The effect of oxygen on the microwave-assisted synthesis of carbon quantum dots from polyethylene glycol. *RSC Advances*, *7*(27), 16637–16643. https://doi.org/10.1039/C7RA01804E

Zhou, H., Ren, Y., Li, Z., He, W., & Li, Z. (2022). Selective Detection of Fe3+ by Nitrogen–Sulfur-Doped Carbon Dots Using Thiourea and Citric Acid. *Coatings 2022, Vol. 12, Page 1042*, *12*(8), 1042. https://doi.org/10.3390/COATINGS12081042

Zhou, J., Shan, X., Ma, J., Gu, Y., Qian, Z., Chen, J., & Feng, H. (2014). Facile synthesis of P-doped carbon quantum dots with highly efficient photoluminescence. *RSC Advances*, *4*(11), 5465–5468. https://doi.org/10.1039/C3RA45294H

Zhu, X., Ge, T., Yang, F., Lyu, M., Chen, C., O'Hare, D., & Wang, R. (2020). Efficient CO2 capture from ambient air with amine-functionalized Mg–Al mixed metal oxides. *Journal of Materials Chemistry A*, *8*(32), 16421–16428. https://doi.org/10.1039/D0TA05079B

Zhu, X., Lyu, M., Ge, T., Wu, J., Chen, C., Yang, F., O'Hare, D., & Wang, R. (2021). Modified layered double hydroxides for efficient and reversible carbon dioxide capture from air. *Cell Reports Physical Science*, *2*(7). https://doi.org/10.1016/J.XCRP.2021.100484

Zhu, Y. (2023). Application of chitosan-based materials in wastewater treatment. *Highlights in Science Engineering and Technology*, *69*, 489–497. https://doi.org/10.54097/HSET.V69I.12403

Zulfajri, M., Gedda, G., Chang, C.-J., Chang, Y.-P., & Huang, G. G. (2019). *Cranberry Beans Derived Carbon Dots as a Potential Fluorescence Sensor for Selective Detection of Fe 3+ Ions in Aqueous Solution*. https://doi.org/10.1021/acsomega.9b01333

APPENDICES

APPENDIX 1

Table 5.1
Absorbance and Calculated Area of Standard Sample

Concentration (mg/L)	Absorbance	Area
0.1	0.017	161.2193
0.2	0.028	246.7905
0.3	0.039	254.01275
0.4	0.047	351.31531

Table 5.2
Absorbance and Calculated Area of CQD-X 112

Concentration (mg/L)	Absorbance	Area
0.1	0.009	130.15958
0.2	0.011	242.25124
0.3	0.019	284.31016
0.4	0.035	333.26153

Table 5.3
Absorbance and Calculated Area of CQD-X 122

Concentration (mg/L)	Absorbance	Area
0.1	0.018	168.38322
0.2	0.032	188.9152
0.3	0.041	192.93668
0.4	0.054	316.74965

Table 5.4
Absorbance and Calculated Area of CQD-X 132

Concentration (mg/L)	Absorbance	Area
0.1	0.023	150.97525
0.2	0.034	171.10509
0.3	0.058	201.20912

0.4	0.070	307.08747

Table 5.5
Absorbance and Calculated Area of CQD-X 113

Concentration (mg/L)	Absorbance	Area
0.1	0.012	175.22994
0.2	0.021	229.28108
0.3	0.022	554.10757
0.4	0.031	606.52932

Table 5.6
Absorbance and Calculated Area of CQD-X 123

Concentration (mg/L)	Absorbance	Area
0.1	0.013	122.3237
0.2	0.030	156.62734
0.3	0.043	171.97903
0.4	0.058	175.69747

Table 5.7
Absorbance and Calculated Area of CQD-X 133

Concentration (mg/L)	Absorbance	Area
0.1	0.019	154.81947
0.2	0.032	231.09788
0.3	0.045	260.90877
0.4	0.060	286.21003

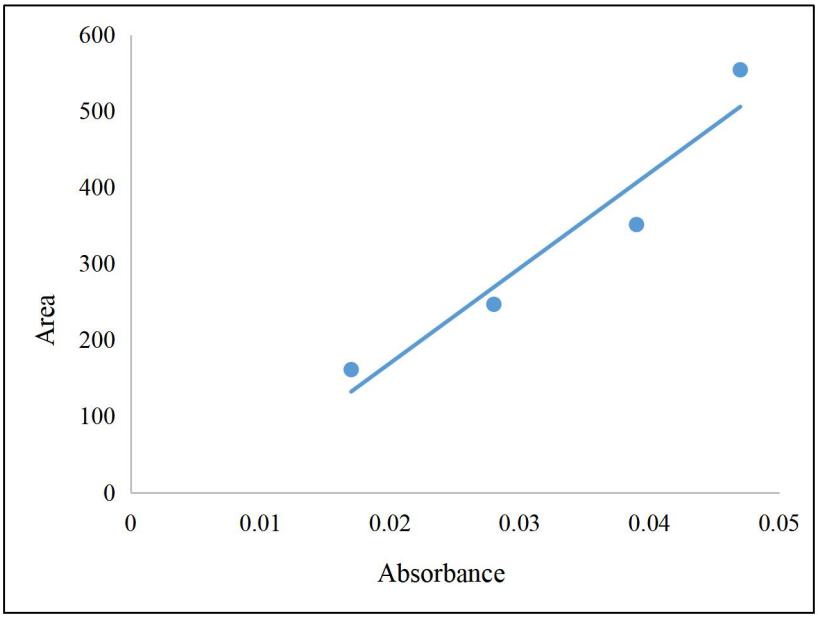

Figure 5.1 Linear Graph of Absorbance vs Area for Standard Sample

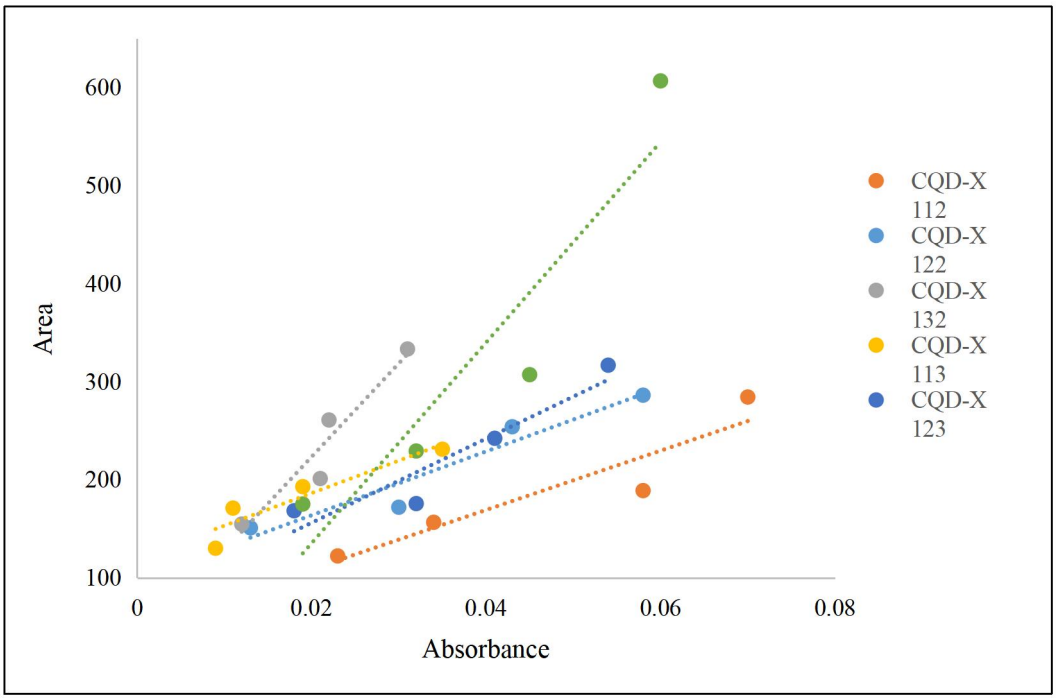

Figure 5.2 Linear Graph of Absorbance vs Area for N/S/O-CCQD-X Samples Synthesized at Different Doping ratio

Table 5.8
Data of Linear Graph for Each CQDs Sample

Sample	Slope	Interception	R2	Fluorescence Quantum Yield
Standard	12443	-79.159	0.9223	-

CQD-X 112	3022.4	48.259	0.8729	0.1312
CQD-X 122	3251.7	98.732	0.9258	0.1411
CQD-X 132	9530.7	32.641	0.92	0.4136
CQD-X 113	3316.9	119.96	0.8641	0.1439
CQD-X 123	4287.9	70.334	0.8825	0.1861
CQD-X 133	10227	-69.316	0.8718	0.4438

APPENDIX 2

Figure 5.3 CO_2 Adsorption Pilot Plant

Sample calculation of breakthrough capacity for the sample CQD-X 1:1:

Total gas flowrate (O_2 & N_2):	100 ml/min
Concentration of CO_2 at equilibrium:	5.15 %
Total time to reach equilibrium:	60 min
CO_2 flowrate:	50 ml/min

P:	$1.0325\ x10^5\ Pa$
R:	$8314.34\ \frac{m^3 Pa}{kgmol.K}$
T:	303.15 K
ρCO_2 :	$1.98\ \frac{kg}{m^3}$
ρN_2 :	$1.2506\ \frac{kg}{m^3}$

To calculate the adsorption capacity, use formula:

$$q_i = 1 - \frac{C_i}{C_0}\left(\frac{Q_F t_b y}{m_s}.\rho_{mix}\right)$$

To find y:

$$y_{CO2} = \frac{n_{CO2}}{n_{N2} + n_{CO2}}$$

To find n:

$$PV = nRT$$
$$n = \frac{PV}{RT}$$

To find V:

$$VCO_2 = flowrate\ CO_2\ x\ C_i\ x\ t$$
$$= 50\ x\ 0.0062\ x\ 0.667$$
$$= 0.207\ ml$$
$$= 2.07\ x10^{-7} m^3$$

$$VN_2 = Total\ flowrate - CO_2\ flowrate$$
$$= 100 - (50\ x\ 0.0062)x\ 0.667$$
$$= 66.46\ ml$$
$$= 6.646\ x10^{-5} m^3$$
$$nCO_2 = \frac{1.0325\ x10^5\ x\ 2.07\ x10^{-7}}{8314.34\ x\ 303.15}$$
$$= 8.466\ x10^{-9}$$

$$nN_2 = \frac{1.0325\ x10^5\ x\ 6.646\ x10^{-5}}{8314.34\ x\ 303.15}$$
$$= 2.722\ x10^{-6}$$
$$y_{CO2} = \frac{8.466\ x10^{-9}}{2.722\ x10^{-6} + 8.466\ x10^{-9}}$$

$$= 0.02575$$

To find ρ_{mix}:

$$\rho_{mix} = \frac{\rho_1 V_1 + \rho_2 V_2}{V_1 + V_2}$$

$$= \frac{1.98(2.07\ x10^{-7}) + 1.2506(6.646\ x10^{-5})}{2.07\ x10^{-7} + 6.646\ x10^{-5}}$$

$$= 1.2529 \frac{kg}{m^3}$$

$$= 1.2529\ \frac{mg}{ml}$$

Finally,

$$q = 1 - \frac{0.62}{5.15}\left(\frac{100\ x\ 0.667\ x\ 0.02575\ x\ 1.2529}{0.5}\right)$$

$$= 0.9478$$

The adsorption capacity of CQD-X 1:1 at breakthrough time (t = 0.67 minute) is 0.9478 mg CO_2/g. In order to obtain the total adsorption capacity, the adsorption capacities recorded from t = 0.167 minute (corresponding to the first data point, as CO_2 concentration was recorded every 10 seconds) up to the point of equilibrium must be summed.

AUTHOR'S PROFILE

Nur Ainaa Binti Mohd Hasyim Chan earned her Bachelor of Chemical Engineering (Environment) with Honours in 2023 from Universiti Teknologi Mara (UiTM), Permatang Pauh Campus, where she was recognized with the Vice Chancellor Award and a Gold Award at the Penang International Invention, Innovation, and Design (PIID 2023). Currently serving as a Graduate Research Assistant while pursuing her Master of Science in Chemical Engineering, she specializes in developing innovative CO_2 adsorption solutions using carbon quantum dots (CQDs) derived from chitosan-based shrimp shells. Her research focuses on synthesizing and characterizing CQDs, with particular emphasis on heteroatom doping and xerogel immobilization to enhance their stability and adsorption efficiency. She employs advanced analytical techniques including FTIR, TGA, BET, CHNS, FESEM-EDX, Fluorescence Spectroscopy, HRTEM, and XPS to evaluate the material properties. Her published work, "Characteristics of Carbon Dots Derived from Chitosan-Based Shrimp Shells Deacetylated at Different Temperatures as a Potential CO_2 Adsorbent" (Materials Research Forum, 2025), contributes to the development of sustainable adsorbents for climate change mitigation. She can be contacted at ainaamimi20@gmail.com.

LIST OF ATTENDED CONFERENCE

8th World Engineering, Science and Technology Congress (ESTCON2024), Organizer: Universiti Teknologi PETRONAS (UTP), Venue: Sabah

International Convention Centre (SICC), Kota Kinabalu, Sabah, Malaysia, Date: 10–11 September 2024, Paper Presented: "Characteristics of Carbon Dots Derived from Chitosan-Based Shrimp Shells Deacetylated at Different Temperatures as a Potential CO_2 Adsorbent".

LIST OF PUBLICATION

Chan, N. A. M. H., Nor, N. M., Zaul Kapri, A. S., Osman, M. S., Mohamed, A. R (2025). Characteristics of carbon dots derived chitosan-based shrimp shells deacetylated at different temperatures as a potential CO_2 adsorbent. Materials Research Proceedings, 53, 305-231.

Zaul Kapri, A. S., Nor, N. M., Chan, N. A. M. H., Osman, M. S., Mohamed, A. R (2025). Development of carbon dots from lignocellulose oil palm wastes: A potential CO2 adsorbent. Materials Research Proceedings, 53, 255-272.

LIST OF SUBMITTED PAPER

N. A. M. H. Chan, Nor, N. M., "Evaluating the Feasibility of Chitosan-based Carbon Quantum Dots in Xerogel Matrix for CO_2 Removal". Jurnal Teknologi, submitted.

N. A. M. H. Chan, Zaul Kapri, A. S., Nor, N. M., "N/S/O-Doped Carbon Quantum Dots Immobilized in Xerogel from Chitosan Shrimp Shells for CO_2 Capture". Carbon (Elsevier), submitted.

N. A. M. H. Chan, Zaul Kapri, A. S., Nor, N. M., "Process Parameters and Mechanistic Insights into CO_2 Adsorption on N/S/O-Doped Carbon Quantum Dots Xerogel Derived from Chitosan-Based Shrimp Shell Waste". Journal of Environmental Chemical Engineering, submitted.